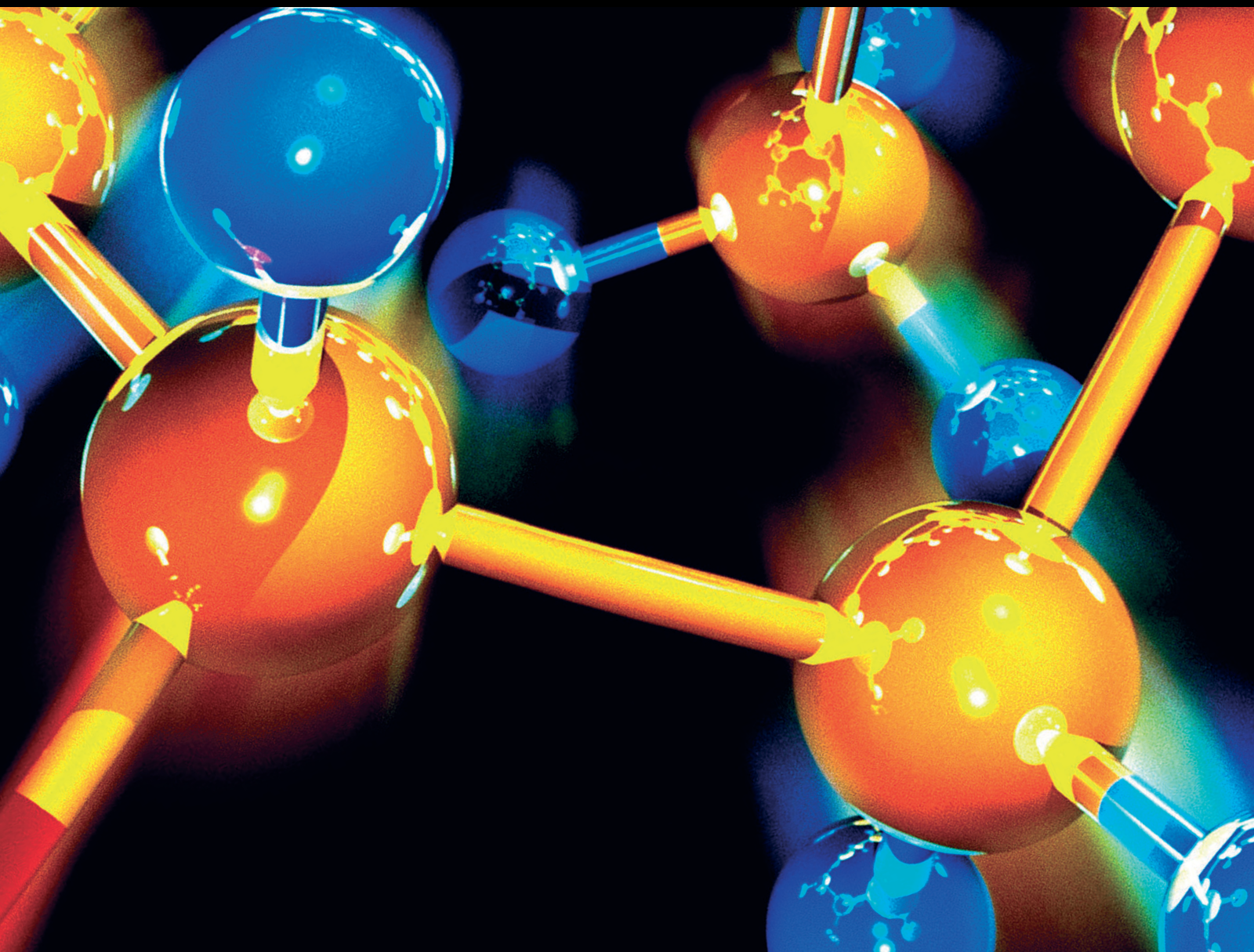# The Development of Novel Biologically Active Small Molecules 2022

Lead Guest Editor: Wagdy Eldehna
Guest Editors: Hatem A. Abdel-Aziz, Mohamed Fares, and Alessio Nocentini

The Development of Novel Biologically Active Small Molecules 2022

The Development of Novel Biologically Active Small Molecules 2022

Lead Guest Editor: Wagdy Eldehna
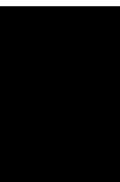Guest Editors: Hatem A. Abdel-Aziz, Mohamed Fares, and Alessio Nocentini

Chief Editor

Kaustubha Mohanty, India

Associate Editors

Mohammad Al-Ghouti, Qatar
Tingyue Gu ⓘ, USA
Teodorico C. Ramalho ⓘ, Brazil
Artur M. S. Silva ⓘ, Portugal

Academic Editors

Jinwei Duan , China
Luqman C. Abdullah ⓘ, Malaysia
Dr Abhilash ⓘ, India
Amitava Adhikary, USA
Amitava Adhikary ⓘ, USA
Mozhgan Afshari, Iran
Daryoush Afzali ⓘ, Iran
Mahmood Ahmed, Pakistan
Islam Al-Akraa ⓘ, Egypt
Juan D. Alché ⓘ, Spain
Gomaa A. M. Ali ⓘ, Egypt
Mohd Sajid Ali ⓘ, Saudi Arabia
Shafaqat Ali ⓘ, Pakistan
Patricia E. Allegretti ⓘ, Argentina
Marco Anni ⓘ, Italy
Alessandro Arcovito, Italy
Hassan Arida ⓘ, Saudi Arabia
Umair Ashraf, Pakistan
Narcis Avarvari ⓘ, France
Davut Avci ⓘ, Turkey
Chandra Azad ⓘ, USA
Mohamed Azaroual, France
Rasha Azzam ⓘ, Egypt
Hassan Azzazy ⓘ, Egypt
Renal Backov, France
Suresh Kannan Balasingam ⓘ, Republic of Korea
Sukanta Bar ⓘ, USA
Florent Barbault ⓘ, France
Maurizio Barbieri ⓘ, Italy
James Barker ⓘ, United Kingdom
Salvatore Barreca ⓘ, Italy
Jorge Barros-Velázquez ⓘ, Spain
THANGAGIRI Baskaran ⓘ, India
Haci Baykara, Ecuador
Michele Benedetti, Italy
Laurent Billon, France

Marek Biziuk, Poland
Jean-Luc Blin ⓘ, France
Tomislav Bolanca ⓘ, Croatia
Ankur Bordoloi ⓘ, India
Cato Brede ⓘ, Norway
Leonid Breydo ⓘ, USA
Wybren J. Buma ⓘ, The Netherlands
J. O. Caceres ⓘ, Spain
Patrizia Calaminici ⓘ, Mexico
Claudio Cameselle ⓘ, Spain
Joaquin Campos ⓘ, Spain
Dapeng Cao ⓘ, China
Domenica Capasso ⓘ, Italy
Stefano Caporali ⓘ, Italy
Zenilda Cardeal ⓘ, Brazil
Angela Cardinali ⓘ, Italy
Stefano Carli ⓘ, Italy
Maria F. Carvalho ⓘ, Portugal
Susana Casal ⓘ, Portugal
David E. Chavez, USA
Riccardo Chelli ⓘ, Italy
Zhongfang Chen ⓘ, Puerto Rico
Vladislav Chrastny ⓘ, Czech Republic
Roberto Comparelli ⓘ, Italy
Filomena Conforti ⓘ, Italy
Luca Conti ⓘ, Italy
Christophe Coquelet, France
Filomena Corbo ⓘ, Italy
Jose Corchado ⓘ, Spain
Maria N. D.S. Cordeiro ⓘ, Portugal
Claudia Crestini, Italy
Gerald Culioli ⓘ, France
Nguyen Duc Cuong ⓘ, Vietnam
Stefano D'Errico ⓘ, Italy
Matthias D'hooghe ⓘ, Belgium
Samuel B. Dampare, Ghana
Umashankar Das, Canada
Victor David, Romania
Annalisa De Girolamo, Italy
Antonio De Lucas-Consuegra ⓘ, Spain
Marcone A. L. De Oliveira ⓘ, Brazil
Paula G. De Pinho ⓘ, Portugal
Damião De Sousa ⓘ, Brazil
Francisco Javier Deive ⓘ, Spain
Tianlong Deng ⓘ, China

Contents

Research Article

Multistaged *In Silico* Discovery of the Best SARS-CoV-2 Main Protease Inhibitors amongst 3009 Clinical and FDA-Approved Compounds

Ibrahim H. Eissa [iD],[1] **Abdulrahman M. Saleh** [iD],[1] **Sara T. Al-Rashood** [iD],[2] **Abdul-Aziz M. M. El-Attar**,[3] **and Ahmed M. Metwaly** [iD][4,5]

[1]*Pharmaceutical Medicinal Chemistry & Drug Design Department, Faculty of Pharmacy (Boys), Al-Azhar University, Cairo 11884, Egypt*

[2]*Department of Pharmaceutical Chemistry, College of Pharmacy, King Saud University, P.O. Box 2457, Riyadh 11451, Saudi Arabia*

[3]*Pharmaceutical Analytical Chemistry Department, Faculty of Pharmacy, Al-Azhar University, Cairo 11884, Egypt*

[4]*Pharmacognosy and Medicinal Plants Department, Faculty of Pharmacy (Boys), Al-Azhar University, Cairo 11884, Egypt*

[5]*Biopharmaceutical Products Research Department, Genetic Engineering and Biotechnology Research Institute, City of Scientific Research and Technological Applications (SRTA-City), Alexandria 21934, Egypt*

Correspondence should be addressed to Ibrahim H. Eissa; ibrahimeissa@azhar.edu.eg and Ahmed M. Metwaly; ametwaly@azhar.edu.eg

As a follow-up to our teamwork's former work against SARS-CoV-2, eight compounds (ramelteon (**68**), prilocaine (**224**), nefiracetam (**339**), cyclandelate (**911**), mepivacaine (**2325**), ropivacaine (**2351**), tasimelteon (**2384**), and levobupivacaine (**2840**)) were revealed as the best potentially active SARS-CoV-2 inhibitors targeting the main protease (PDB ID: 5R84), M^{pro}. The compounds were named in the midst of 3009 FDA and clinically approved compounds employing a multistaged *in silico* method. A molecular fingerprints study with **GWS**, the cocrystallized ligand of the M^{pro}, indicated the resemblance of 150 candidates. Consequently, a structure similarity experiment disclosed the best twenty-nine analogous. Then, molecular docking studies were done against the M^{pro} active site and showed the binding of the best compounds. Next, a 3D-pharmacophore study confirmed the obtained results for the eight compounds by exhibiting relative fit values of more than 90% (except for **68**, 74%, and **2384**, 83%). Levobupivacaine (**2840**) showed the most accurate docking and pharmacophore scores and was picked for further MD simulations experiments (RMSD, RMSF, R$_g$, SASA, and H-H bonding) over 100 ns. The MD simulations results revealed the accurate binding as well as the optimum dynamics of the M^{pro}-levobupivacaine complex. Finally, MM-PBSA studies were conducted and indicated the favorable bonding of the M^{pro}-levobupivacaine complex with a free energy value of −235 kJ/mol. The fulfilled outcomes hold out hope of beating COVID-19 through more *in vitro* and *in vivo* research for the named compounds.

1. Introduction

The WHO noted on March 4, 2022, that the confirmed infections of COVID-19 on a worldwide basis are 440,807,756 humans. In sorrow, 5,978,096 humans among them are dead [1]. Despite the fact that the number of vaccine doses reached 10,585,766,316, the dangerous virus still has the ability to infect vastly [2]. According to these horrible numbers, massive work is demanded from scientists all over the world to find a cure. The routine process of drug discovery and detection is greatly expensive and lasts for a very long time. The usual time needed for new drug discovery is twelve years costing about 2.6 billion USD [3]. On the other hand, drug repurposing is a much faster process [4, 5].

Drug repurposing includes the identification of new biological use or uses for an old drug [6]. The process of drug repositioning was employed successfully in the development of anticancer [7], anti-COVID-19 [8], anti-inflammatory [9] antibacterial [10], antiparasitic [11], and antiviral [12] drugs.

Methods of computational chemistry were used to explore various pharmacokinetic and pharmacodynamic parameters that connect the chemical structure to activity as well as to explore the interaction of ligands with biological proteins such as structure similarity [13], molecular fingerprints [14], QSAR [15], pharmacophores [16], homology models [17], molecular modeling, drug molecular design [18], rational drug design [19], molecular docking [20], MD simulations [21], absorption [22], distribution, metabolism [23], excretion [24], and toxicity properties [25] as well as physicochemical characterization [26] assessment and DFT.

For that reason, our team composed a multiple-phase computational screening approach to name the most effective inhibitor/s for an essential SARS-CoV-2 enzyme in the midst of hundreds or thousands of compounds. Among a set of 310 antiviral natural metabolites, we pointed the most potential inhibitors against various SARS-CoV-2 proteins, including nsp10 [27], helicase [28], the main protease [29, 30], and the papain-like protease [31]. Similarly, the most potential FDA-approved drugs were anticipated against the SARS-CoV-2 nsp16-nsp10 $2'$-o-methyltransferase complex [32] and the SARS-CoV-2 RNA-dependent RNA polymerase [33]. We also expected potential natural inhibitors for the SARS-CoV-2 helicase [34] and RdRp [35].

Viral proteases stand out as promising targets for the development of antiviral treatments, demonstrating efficacy against specific viruses such as the human immunodeficiency virus and hepatitis C virus when targeted by aspartyl and serine proteases, respectively [36]. In the context of SARS-CoV-2, the main protease (M^{pro}) plays a pivotal role in the activation of sixteen functional and nonstructural proteins through the cleavage of the large polyproteins (pp1a and pp1ab). The inhibition of M^{pro} emerges as a strategic approach, causing substantial impairment to the virus and impeding its replication [37]. It is noteworthy that the structural and sequential distinctions between the viral main protease (M^{pro}) and human proteases further emphasize M^{pro} as a viable target for anti-COVID-19 drug discovery [38]. The unique structural properties of the SARS-CoV-2 M^{pro}, coupled with its significant role in the viral life cycle, underscore its potential as a focal point for developing novel and effective therapeutic interventions against COVID-19 [39, 40]. In this work, a set of 3009 clinical and FDA-approved compounds were retrieved from the website of https://Selleckchem.com [41] and has been subjected to multi-staged *in silico* methods to determine the most potent inhibitors targeting SARS-CoV-2 main protease (M^{pro}). The applied methods included molecular structures similarity study against the cocrystallized ligand (**GWS**) of M^{pro} (PDB ID: 5R84) [42] (Figure 1), molecular fingerprints study against the same ligand, molecular docking, molecular dynamics (MD) simulations and MM-PBSA experiments against M^{pro}.

Unfortunately, the *in vitro* and *in vivo* examinations against COVID-19 are not accessible for our team currently.
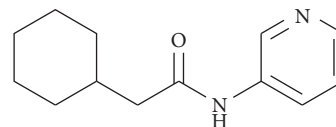
FIGURE 1: Structure of the cocrystallized ligand (**GWS**) of M^{pro} (PDB ID: 5R84).

However, we employed extensive well-structured *in silico* methods to present a sort of strong potential SARS-CoV-2 inhibitors for every scientist who has these facilities aiming at finding a treatment.

2. Results and Discussion

2.1. Filter Using Fingerprints. The cocrystallized ligand is a compound that strongly binds to a specific protein, forming a crystalized complex [43]. This complex provides crucial insights into the nature of interaction, revealing important structural and chemical characteristics that contribute to the strong binding with that protein [44]. The chemical structural features of the cocrystallized ligand serve as a valuable blueprint for designing inhibitors that can effectively bind to the target protein. By examining the structural features and functional groups of the cocrystallized ligand, we can better understand the key elements responsible for its strong binding [45]. We used this knowledge to select compounds similar to **GWS**, aiming to discover potent inhibitors with a high affinity for the M^{pro} protein (Table 1). This approach is rooted in the principle of a structure-activity relationship (SAR), which suggests that compounds with similar chemical structures are likely to have similar biological effects [46]. The molecular finger-prints analysis represented the absence or existence of the next descriptors in the fragments and atoms of the considered compounds and **GWS**: H-bond acceptors [47], H-bond donors [48], charges [49], hybridization [50], positive ionizable atoms [51], negative ionizable atoms [52], halogens [53], and aromatic groups [54], align with the ALogP [55].

2.2. Molecular Similarity. A fundamental distinction between molecular similarity studies and fingerprint studies lies in the depth of molecular information they capture. Molecular similarity studies embrace a wider array of molecular descriptors and properties, facilitating a comprehensive evaluation of structural and chemical resemblances. These studies encompass considerations such as molecular shape, electrostatic characteristics, and pharmacophoric attributes. In contrast, fingerprint studies focus on specific structural motifs encoded in binary fingerprints, presenting a more condensed representation of molecular structures [56]. In a molecular similarity study, a holistic analysis is conducted, wherein the complete structures of the reference compound and the examination set are characterized and juxtaposed, employing descriptors encompassing steric, topological, electronic, or physicochemical attributes [57]. Molecular structural similarity study also belongs to the approaches of ligand-based *in silico* (computational) type

TABLE 1: Fingerprint similarity between the tested compounds and **GWS**.

Comp	Similarity	SA	SB	SC
GWS	1.000	176	0	0
18	0.686	168	69	8
58	0.594	174	117	2
68	0.552	137	72	39
74	0.532	158	121	18
92	0.559	176	139	0
114	0.622	217	173	−41
163	0.629	158	75	18
169	0.609	168	100	8
224	0.517	109	35	67
227	0.583	183	138	−7
252	0.613	168	98	8
266	0.595	194	150	−18
276	0.607	167	99	9
279	0.539	213	219	−37
286	0.530	123	56	53
297	0.562	218	212	−42
325	0.536	118	44	58
339	0.533	122	53	54
393	0.554	163	118	13
400	0.583	123	35	53
417	0.571	192	160	−16
419	0.629	158	75	18
438	0.540	218	228	−42
462	0.531	155	116	21
486	0.512	174	164	2
497	0.514	150	116	26
508	0.573	172	124	4
515	0.567	160	106	16
530	0.584	185	141	−9
552	0.587	145	71	31
560	0.558	201	184	−25
614	0.520	130	74	46
643	0.540	154	109	22
671	0.557	230	237	−54
675	0.562	136	66	40
686	0.564	137	67	39
727	0.608	163	92	13
736	0.522	153	117	23
741	0.538	183	164	−7
756	0.524	177	162	−1
768	0.556	140	76	36
772	0.553	210	204	−34
786	0.530	178	160	−2
829	0.542	156	112	20
843	0.572	158	100	18
854	0.646	159	70	17
855	0.590	207	175	−31
863	0.519	285	373	−109
878	0.512	148	113	28
911	0.551	151	98	25
935	0.520	259	322	−83
970	0.558	203	188	−27
987	0.518	142	98	34
1064	0.608	163	92	13
1069	0.573	172	124	4
1108	0.585	226	210	−50
1113	0.582	114	20	62
1168	0.567	136	64	40
1177	0.512	173	162	3

TABLE 1: Continued.

Comp	Similarity	SA	SB	SC
1178	0.586	190	148	−14
1179	0.564	168	122	8
1186	0.587	138	59	38
1211	0.547	188	168	−12
1253	0.530	151	109	25
1267	0.530	254	303	−78
1284	0.554	206	196	−30
1315	0.548	165	125	11
1320	0.531	155	116	21
1410	0.512	174	164	2
1441	0.523	104	23	72
1443	0.523	104	23	72
1461	0.515	150	115	26
1462	0.535	147	99	29
1463	0.527	97	8	79
1516	0.618	168	96	8
1521	0.523	104	23	72
1551	0.529	208	217	−32
1553	0.514	182	178	−6
1589	0.553	121	43	55
1591	0.549	169	132	7
1604	0.531	170	144	6
1608	0.512	214	242	−38
1622	0.596	121	27	55
1649	0.529	101	15	75
1694	0.547	181	155	−5
1737	0.516	127	70	49
1742	0.595	209	175	−33
1756	0.524	204	213	−28
1805	0.580	170	117	6
1818	0.527	194	192	−18
1822	0.531	241	278	−65
1919	0.564	168	122	8
1955	0.579	169	116	7
1975	0.615	134	42	42
1993	0.547	169	133	7
2023	0.512	127	72	49
2024	0.601	176	117	0
2075	0.606	168	101	8
2091	0.530	96	5	80
2126	0.533	147	100	29
2163	0.682	189	101	−13
2171	0.532	166	136	10
2185	0.550	138	75	38
2205	0.567	174	131	2
2261	0.519	160	132	16
2264	0.584	201	168	−25
2274	0.690	191	101	−15
2296	0.537	110	29	66
2306	0.523	174	157	2
2325	0.602	136	50	40
2333	0.603	185	131	−9
2334	0.632	127	25	49
2351	0.608	158	84	18
2372	0.562	154	98	22
2380	0.614	159	83	17
2384	0.545	126	55	50
2395	0.646	168	84	8
2399	0.530	151	109	25
2403	0.594	168	107	8

TABLE 1: Continued.

Comp	Similarity	SA	SB	SC
2425	0.532	100	12	76
2437	0.576	179	135	−3
2447	0.573	201	175	−25
2478	0.535	168	138	8
2524	0.597	160	92	16
2525	0.578	170	118	6
2530	0.556	155	103	21
2553	0.550	105	15	71
2603	0.604	116	16	60
2622	0.516	214	239	−38
2630	0.539	138	80	38
2638	0.515	152	119	24
2649	0.636	140	44	36
2657	0.633	143	50	33
2660	0.618	168	96	8
2704	0.561	162	113	14
2761	0.528	239	277	−63
2775	0.603	152	76	24
2788	0.521	126	66	50
2790	0.522	186	180	−10
2825	0.516	145	105	31
2839	0.588	143	67	33
2840	0.606	172	108	4
2865	0.542	156	112	20
2877	0.519	217	242	−41
2901	0.565	140	72	36
2917	0.568	147	83	29
2918	0.540	162	124	14
2939	0.523	229	262	−53
3003	0.607	167	99	9

SA: The number bits in both **GWS** and the target. **SB**: The number of bits in the target but not **GWS**. **SC**: The number of bits in **GWS** but not the target. The bold values indicate that the number is based on the number of compounds.

that considered following descriptors; hydrogen bond donors (HBA) [58], acceptors (HBD) [59] partition coefficient (Alog p) [60], molecular weight (M. W) [61], rotatable bonds [62], rings and aromatic rings [63], and molecular fractional polar surface area (MFPSA) [64]. The computation of the mentioned features using Discovery Studio software led to the revelation of the best 29 analogs (Figure 2, and Table 2).

2.3. Docking Studies

2.3.1. Validation of Molecular Docking.
The molecular docking algorithm was initially validated by redocking of the cocrystallized ligand into the active site of the target receptor (SARS-CoV-2 M^{pro} PDB ID: 5R84) with the calculation of root mean square deviation (RMSD) for reliability and reproducibility of the proposed docking algorithm. The redocked ligand showed an RMSD value of 0.56 A indicating a validated docking process (Figure 3).

The binding mode of the cocrystallized ligand (**GWS**) exhibited a binding energy of −6.51 kcal/mol against M^{pro}. The cyclohexyl moiety formed three Pi-Alkyl interactions with His41, Met165, and Met49. Additionally, the amino group in (pyridine-3-yl) acetamide moiety interacted with His163 by one hydrogen bond with a distance of 1.99°A.

Moreover, the amide linker interacted with Glu166 and Asn142 by two hydrogen bonds with distances of 2.04 and 2.72°A, respectively (Figure 4).

The binding mode of compound **68** (Ramelteon) exhibited a binding energy of −6.49 kcal/mol against M^{pro}. The tetrahydro-2H-indeno[5,4-b]furan-8-yl moiety formed three Pi-alkyl interactions with Met49, His41, and Met165. Additionally, the ethyl propionamide moiety formed two hydrogen bonds with Glu166(2.51°A) and Asn142 (2.35°A) (Figure 5).

Compound **224** (Prilocaine) exhibited a binding energy of −6.05 kcal/mol against M^{pro}. The o-tolyl moiety formed three Pi-alkyl and Pi-Pi interactions with Cys145, His163, and Leu141. The amide moiety interacted with Asn142 and Glu166 by two hydrogen bonds with distances of 2.31 and 1.97°A, respectively (Figure 6).

The binding mode of compound **339** (Nefiracetam) exhibited a binding energy of −6.12 kcal/mol against M^{pro}. The 2,6-dimethylphenyl moiety formed three Pi-alkyl interactions with His41 and Met165. The (2-oxopyrrolidin-1-yl) acetamide moiety formed two hydrophobic interactions with His163 and Cys145. Moreover, the central amide moiety interacted with two hydrogen bonds with Asn142 and Glu166 with a distance of 2.42 and 2.01°A, respectively. (Figure 7).

Figure 2: Twenty-nine compounds with good molecular similarity with **GWS**.

Table 2: Molecular descriptors of the examined compounds and **GWS**.

Comp	Alog p	M. Wt	HBA	HBD	Rotatable bonds	Rings	Aromatic rings	MFPSA	Minimum distance
GWS	2.17	218.3	2	1	3	2	1	0.179	0
68	2.83	259.34	2	1	4	3	1	0.143	0.388
163	2.35	275.34	3	1	4	3	1	0.17	0.456
169	3.4	313.86	3	1	5	2	1	0.088	0.733
224	2.26	220.31	2	2	5	1	1	0.157	0.484
286	4.17	250.33	3	1	6	1	1	0.154	0.666
325	2.39	233.7	3	1	4	1	0	0.261	0.732
339	1.44	246.31	2	1	3	2	1	0.182	0.21
400	1.29	232.28	3	2	2	2	1	0.293	0.664
419	2.35	275.34	3	1	4	3	1	0.17	0.456
497	2.86	285.34	3	0	3	3	1	0.132	0.634
552	2.49	207.27	2	1	1	2	0	0.186	0.594
675	3.36	282.81	2	1	2	2	1	0.1	0.532
686	3.91	269.81	2	1	2	2	1	0.074	0.63
829	1.72	289.37	4	1	5	3	1	0.167	0.683
854	2.8	263.38	3	2	4	2	1	0.144	0.526
911	3.64	276.37	3	1	4	2	1	0.149	0.515

TABLE 2: Continued.

Comp	Alog p	M. Wt	HBA	HBD	Rotatable bonds	Rings	Aromatic rings	MFPSA	Minimum distance
1113	4.11	194.27	2	2	5	1	1	0.181	0.643
1186	2.94	246.3	3	1	4	2	1	0.212	0.364
2296	3.25	190.24	2	0	3	2	1	0.131	0.481
2325	2.98	246.35	2	1	2	2	1	0.114	0.362
2334	2.9	259.8	2	1	3	2	1	0.206	0.281
2340	3.04	164.24	1	1	4	1	1	0.104	0.568
2351	3.85	274.4	2	1	4	2	1	0.102	0.563
2384	2.2	245.32	2	1	4	3	1	0.154	0.311
2395	3.02	277.4	3	1	5	2	1	0.1	0.572
2553	4.39	178.27	1	1	4	1	1	0.093	0.714
2840	4.31	288.43	2	1	5	2	1	0.096	0.703
2865	1.72	289.37	4	1	5	3	1	0.167	0.683
2901	4.01	262.34	3	1	3	2	1	0.158	0.517

The bold values indicate that the number is based on the number of compounds.
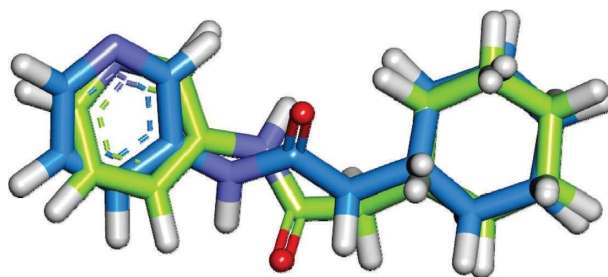
FIGURE 3: Superimposition of the docked and original poses of the cocrystallized ligand of SARS-CoV-2 M^{pro} (PDB ID: 5R84).

Compound **911** (Cyclandelate) exhibited a binding energy of −6.89 kcal/mol against M^{pro}. The trimethyl cyclohexyl moiety formed six hydrophobic interactions with His41, Met49, and Met165. Additionally, the 2-hydroxy-2-phenylacetate moiety formed three hydrogen bonds with Glu166, Asn142, and Leu141 with distances of 1.99, 2.45, and 2.55˚A, respectively (Figure 8).

Compound **2325** (Mepivacaine) exhibited a binding score of −6.19 kcal/mol. The 2,6-dimethyl phenyl moiety formed three Pi-alkyl and Pi-sulfur interactions with His163 and Cys145. The piperidine moiety formed two Pi-alkyl interactions with His41 and Met49. Moreover, the central amide moiety interacted with two hydrogen bonds with Glu166 and Asn142 with a distance of 2.01 and 2.40˚A, respectively (Figure 9).

The binding mode of compound **2351** (Ropivacaine) exhibited an energy binding of −6.38 kcal/mol against M^{pro}. The 2,6-dimethyl phenyl moiety formed three Pi-alkyl and Pi-sulfur interactions with His163 and Cys145. The propylpiperidine moiety formed two Pi-alkyl interactions with His41 and Met49. Moreover, the central amide moiety interacted by two hydrogen bonds with Glu166 and Asn142 with a distance of 2.27 and 2.25˚A, respectively (Figure 10).

The binding mode of compound **2384** (Tasimelteon) exhibited an energy binding of −6.45 kcal/mol-1 against M^{pro}. The 2,3-dihydrobenzofuran-4-yl moiety formed four Pi-alkyl and Pi-Pi interactions with Met49, Met165, and His41. Additionally, it formed one hydrogen bond with Glu166 at a distance of 2.44˚A. The (cyclopropyl methyl) propionamide moiety interacted with Asn142 through one hydrogen bond with a distance of 2.63˚A. Moreover, it was incorporated in four Pi-alkyl interactions with His163, His172, His41, and Cys145 (Figure 11).

Interestingly, the binding mode of compound **2840** (Levobupivacaine) was very similar to that of the cocrystallized ligand (**GWS**) exhibiting a binding energy of −6.65 kcal/mol, slightly bitter that **GWS** (−6.51 kcal/mol) against the M^{pro}. In detail, The 2,6-dimethylphenyl moiety of compound **2840**, in a similar way to the cyclohexyl moiety of **GWS** formed hydrophobic interactions with the same three amino acids; Met49, His41, and Met165. Additionally, the butylpiperidine moiety of compound **2840** interacted with Asn142 by a hydrogen bond with a distance of 2.36˚A. The amide linker of **GWS** interacted with the same amino acid through a hydrogen bond with distances of 2.72˚A. Furthermore, the butylpiperidine moiety of compound **2840** formed one hydrophobic interaction with His163 similar to the amino group in (pyridine-3-yl) acetamide moiety of **GWS**. Finally, the amide linker of compound **2840** formed two hydrogen bonds with Gln189, and Glu166 in a distance of 2.24, and 2.64˚A, respectively. This interaction was similar to that of the amide linker of **GWS** with Glu166 a hydrogen bond with a distance of 2.04˚A. In summary, compound **2840** (Levobupivacaine) exhibited interactions with all the amino acids that the cocrystallized ligand (**GWS**) interacted with. Additionally, there was an extra interaction observed with Gln189 (Figure 12, and Table 3).
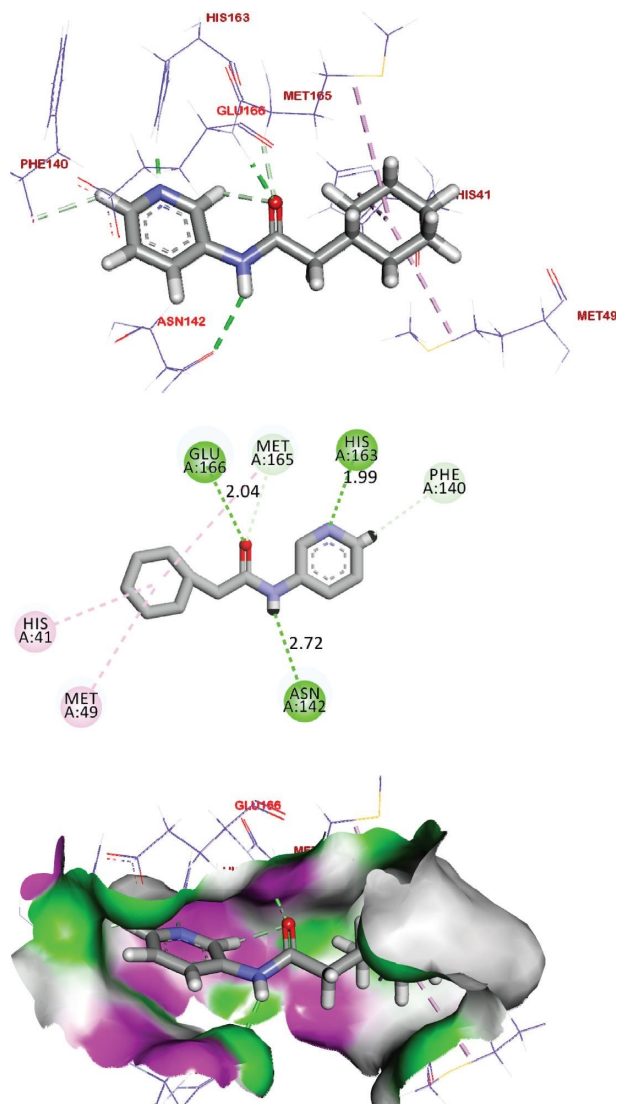
FIGURE 4: Binding mode and mapping surface of **GWS** in the active site of M^pro.

FIGURE 5: Binding mode and mapping surface of compound **68** in the active site of M^pro.

2.4. Pharmacophore Study.

The pharmacophore recognizes the key features in a ligand to interact with a protein target resulting in elicitation or blockage of a certain biological activity. The 3D pharmacophore model determines the essential chemical feature of a metabolite to be active against a specific protein. Additionally, it specifies the 3D geometry of these essential features [65]. The generated 3D model is an important key that can be used to predict definite bioactivity based on the presence or absence of these features [66, 67]. The presented study concerned the optimization of the key pharmacophoric interaction features of the cocrystallized ligand (**GWS**) of the main protease (PDB ID: 5R84) and the consequent examination of the presence of these features in the tested FDA-approved drug to pick the most promising candidates.

2.4.1. Generation of a 3D-Pharmacophore Model.

The generated 3D pharmacophore model consisted of three features: one H-bond donor and two hydrophobic centers

(Figure 13(a)). The generated model was used as a 3D search query to evaluate the tested drugs as possible SARS-CoV-2 main protease inhibitors. The fitting of the cocrystallized ligand against the generated pharmacophore model was illustrated in Figure 13(b).

2.4.2. The Test Set Activity Prediction.

The test set of thirty FDA-approved drugs was mapped to the generated 3D pharmacophore model. As a result, the FDA-approved drugs that verified the essential pharmacophoric features and the fit value were selected as promising candidates.

The results privileged nineteen drugs that have the main essential features of SARS-CoV-2 main protease inhibitors. Surprisingly, the drugs that showed good binding mode against SARS-CoV-2 main protease showed high fit and high relative fit values. In detail, compounds **68** (Fit value = 2.86,
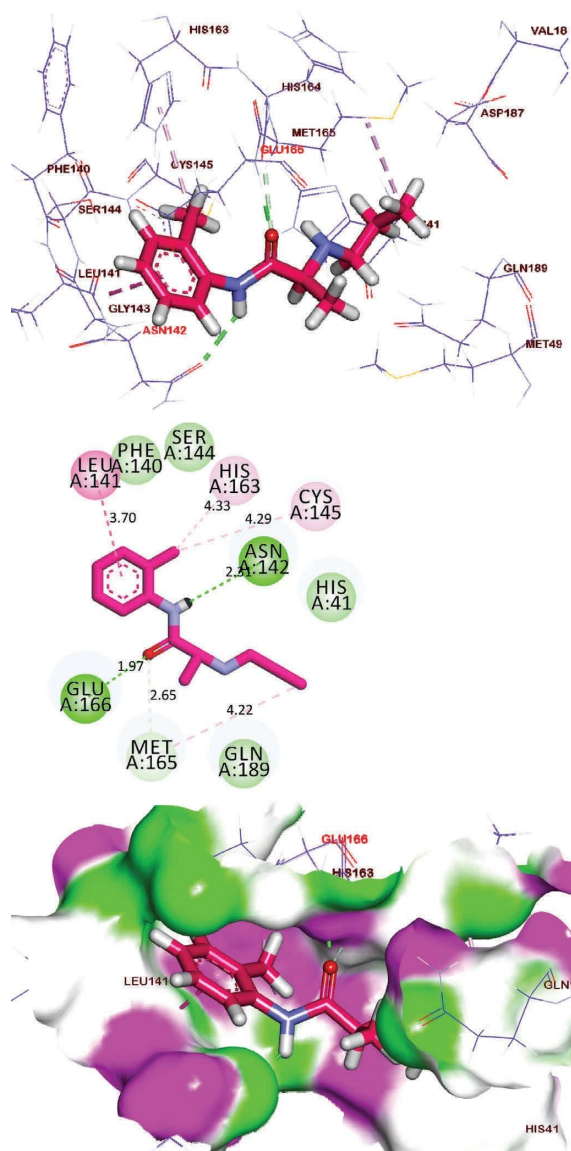
Figure 6: Binding mode and mapping surface of compound **224** in the active site of M^pro.

Relative Fit = 74.48%), **224** (Fit value = 2.75, Relative Fit = 96.15%), **339** (Fit value = 2.56, Relative Fit = 89.51%), **911** (Fit value = 2.81, Relative Fit = 98.25%), **2325** (Fit value = 2.73, Relative Fit = 95.45%), **2351** (Fit value = 2.75, Relative Fit = 96.15%), **2384** (Fit value = 2.38, Relative Fit = 83.22%), and **2840** (Fit value = 2.78, Relative Fit = 97.20%) showed high fit value comparing to the cocrystallized ligand (Fit value = 2.86, Relative Fit = 100%) (Table 4).

Figure 14 shows the mapping of the most promising drugs that showed good fitting value against the generated 3D-pharmacophore and well as good binding mode against SARS-CoV-2 main protease.

In summation, eight compounds were appointed as potential M^pro inhibitors (ramelteon (**68**), prilocaine (**224**), nefiracetam (**339**), cyclandelate (**911**), mepivacaine (**2325**), ropivacaine (**2351**), tasimelteon (**2384**), and levobupivacaine
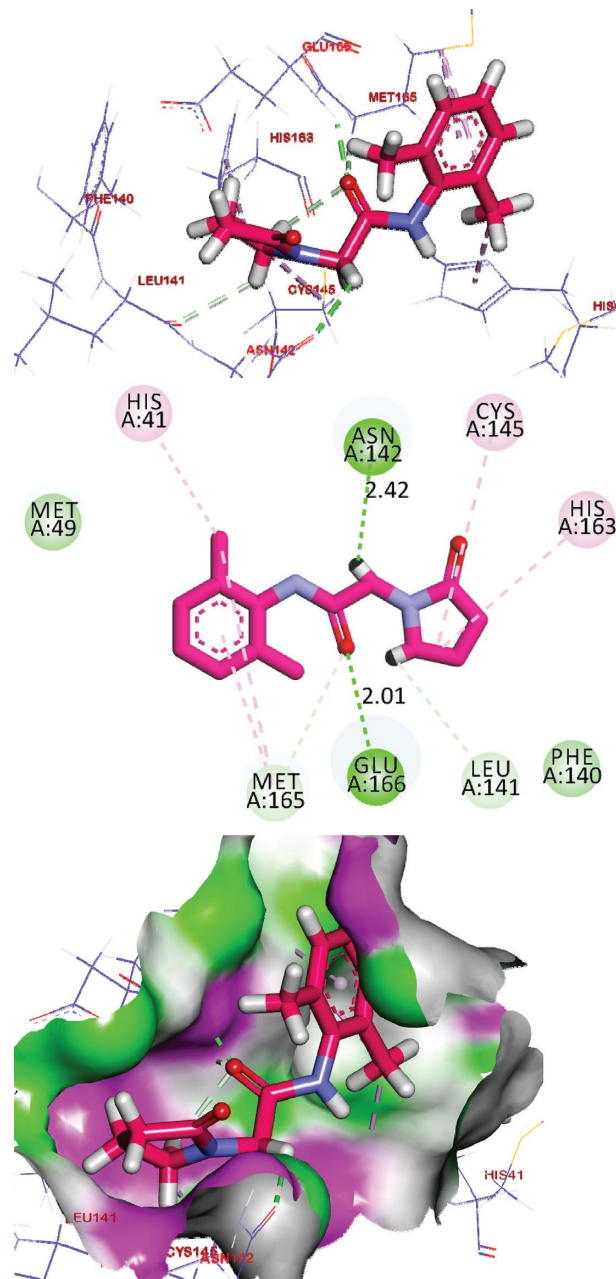
Figure 7: Binding mode and mapping surface of compound **339** in the active site of M^pro.

(**2840**)). levobupivacaine (**2840**) demonstrated identical 3D pharmacophore features to the cocrystallized ligand (**GWS**), encompassing HBD-1, hydrophobic-2, and aromatic ring-3. Notably, levobupivacaine (**2840**) displayed the highest fit value at 2.78, accompanied by the highest relative Fit of 97.20%. Ramelteon, the melatonin agonist, is used to treat insomnia [68]. Interestingly, Ramelteon demonstrated significant *in silico* anti-SARS-CoV-2 activities through binding and inhibition of SARS-CoV-2 RBD and ACE 2 [69]. A drug repositioning study identified prilocaine as a potential candidate against COVID-19 [70]. Stimulatingly, cyclandelate showed *in vitro* inhibitory effect against 1 ribosomal frameshifting of SARS-CoV-2 at a concentration of $2\,\mu$M
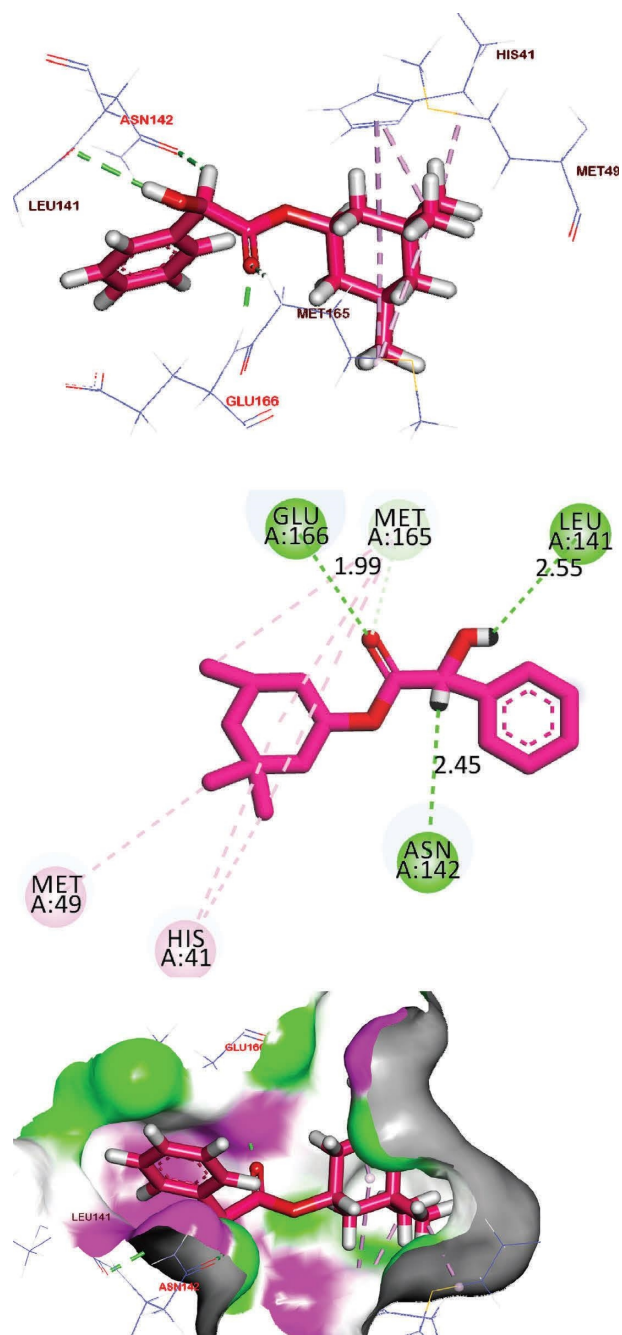
Figure 8: Binding mode and mapping surface of compound **911** in the active site of M^pro.

Figure 9: Binding mode and mapping surface of compound **2325** in the active site of M^pro.

[71]. Additionally, mepivacaine, the local anesthetic, demonstrated an *in vitro* inhibitory effect against Herpes simplex 1 before [72]. Further, tasimelteon displayed significant *in silico* binding with the COVID-19 PLpro [73]. Also, a molecular modeling study suggested the anti-COVID-19 potential of the local anesthetic, levobupivacaine [74]. On the other side, this is the first time to referee an antiviral potentiality for both nefiracetam and ropivacaine. Because several selected compounds are local anesthetics, further studies regarding the route of administration and systemic safety of these drugs are essential.

2.5. Molecular Dynamic Simulations. Molecular dynamics (MD) simulations can be used to examine almost all sorts of big molecules (proteins, nucleic acids, and carbohydrates) of medicinal significance. The MD experiments can supply not only galore energetic records on the considered macromolecules but also a considerable of dynamical structural specifics about the interactions that happen between the ligand and the targeted protein. The acquired information is very beneficial to understand several parameters regarding the protein-ligand interaction [75]. Being an effective guide, MD simulations experiments have been applied widely and successfully in the process of modern drug discovery and discovery [76].

Levobupivacaine (**2840**) demonstrated excellent fitting value against the generated 3D-pharmacophore as well as an ideal binding mode against M^pro. Consequently, it was selected for further molecular dynamic simulations.
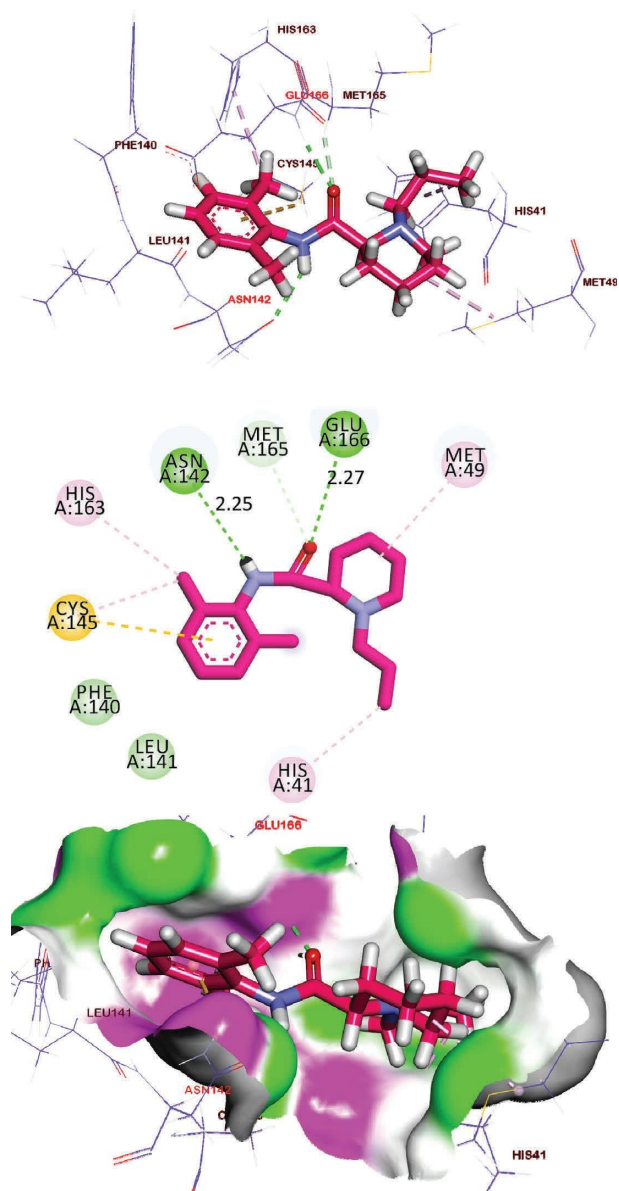
Figure 10: Binding mode and mapping surface of compound **2351** in the active site of M^pro.

Figure 11: Binding mode and mapping surface of compound **2384** in the active site of M^pro.

The dynamic structural changes of the backbone of the levobupivacaine—M^pro complex were calculated on an atomic resolution by RMSD to investigate the stability of the explored complex after binding. Stimulatingly, levobupivacaine—M^pro complex displayed a low value of root mean square deviation (RMSD) exhibiting no major fluctuations (Figure 15(a)). This outcome indicates the stability of the reviewed complex. The flexibility of the levobupivacaine—M^pro complex was diagnosed in terms of root mean square fluctuation (RMSF) to expose the fluctuated regions of M^pro during the simulation. It was confirmed that the binding of levobupivacaine does not change the flexibility of M^pro significantly (Figure 15(b)). To study the compactness of the levobupivacaine—M^pro complex, the radius of gyration (Rg) of M^pro was computed. The Rg of the M^pro was more constant at the end of the experiment than at the starting period (Figure 15(c)). Interaction between levobupivacaine—M^pro complex and the surrounding solvents was estimated by solvent accessible surface area (SASA) over a period of 100 ns. Fortunately, the levobupivacaine—M^pro complex featured a noticeable decrease in the surface area (lower SASA value) than the starting time (Figure 15(d)). Hydrogen bonding through the Levobupivacaine—M^pro complex was estimated over 100 ns. Favorably, the highest number of the M^pro conformations formed up to two hydrogen bonds with the Levobupivacaine over the examined 100 ns (Figure 15(e)).
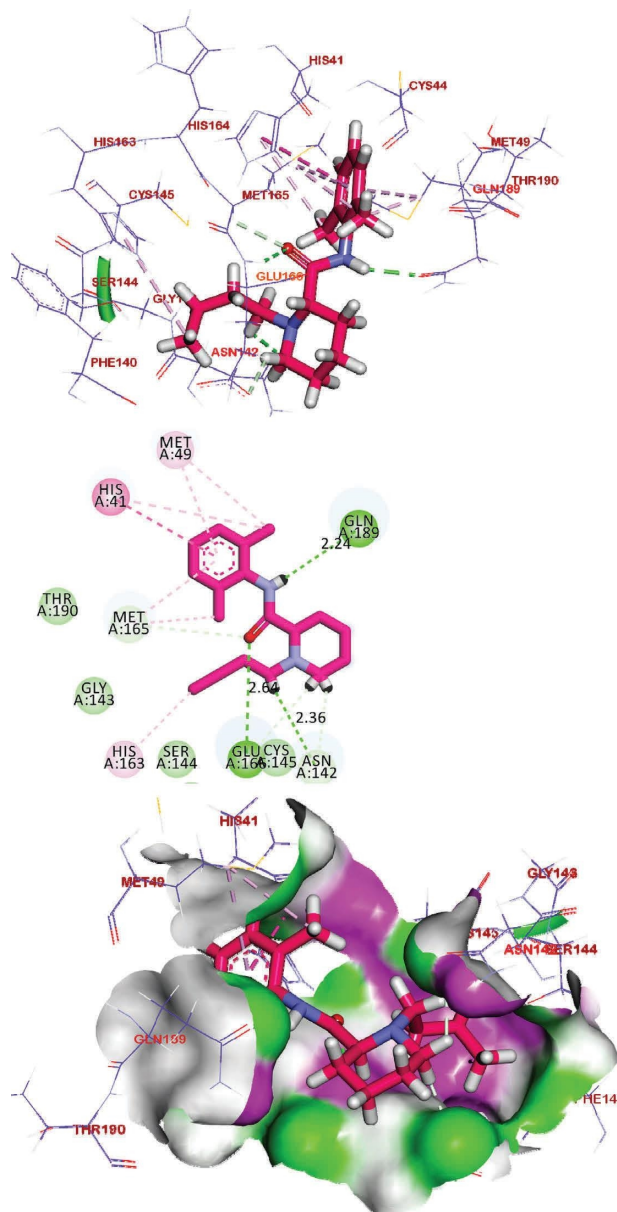
FIGURE 12: Binding mode and mapping surface of compound **2840** in the active site of M^{pro}.

2.6. MM-PBSA. The molecular mechanics Poisson–Boltzmann surface area (MM-PBSA) is a computational technique employed in molecular modeling and computational chemistry to estimate the binding free energy between a ligand and a protein. This method combines molecular mechanics (MM) computations, which elucidate interactions within the complex, with Poisson–Boltzmann (PB) computations, which factor in the electrostatic interactions between the solute and its surrounding solvent environment [77].

In the MM-PBSA approach, the binding free energy (ΔG_bind) is approximated by evaluating the energetic components associated with the complex, the ligand, and the receptor in both bound and unbound states. These components encompass contributions from van der Waals interactions, electrostatic interactions, and alterations in solvation-free energy [78]. MM-PBSA is especially valuable for investigating interactions between proteins and ligands, offering insights into the thermodynamics of binding and aiding in the design of potential drug compounds. It is important to acknowledge, however, that while MM-PBSA provides valuable estimates, it relies on several assumptions and may not capture the complete intricacies of binding processes in all systems [79]. We calculated the binding free energy of the last 20 ns of MD production run of the levobupivacaine—M^{pro} complex with an interval of 100 ps from MD trajectories using the MM/PBSA method. As shown in Figure 16(a), Levobupivacaine displayed an excellent binding free energy of −235 kJ/mol with the M^{pro}. Furthermore, the participation of each amino acid residue of the M^{pro} regarding the binding free energy after the binding with levobupivacaine was computed. The total binding free energy of the levobupivacaine—M^{pro} complex was decomposed into per amino acid residue contribution energy. The output of this study helps to identify the essential amino acid residues in the binding of the levobupivacaine—M^{pro} complex. It was found that GLU-47, ASP-48, GLU-55, ASP-56, GLU-166 and ASP-187 residues of the M^{pro} shared higher than −15 kJ/mol binding energy (Figure 16(b)). It is noteworthy to mention that GLU-166, an essential amino acid, was identified in the interactions of both levobupivacaine and the cocrystallized ligand (**GWS**).

3. Method

3.1. Molecular Similarity Detection. Compound similarity was assessed in Discovery Studio 4.0 using the CHARMM force field and ligand preparation protocol. Compounds were compared to **GWS** with a 5% output adjustment. Default molecular properties were used, including rotatable bonds, rings, aromatic rings, HBA, HBD, ALog p, M. Wt, and MFPSA. The study was operated by Discovery Studio 4.0 software as represented before [80] (additional details in Supplementary data).

3.2. Fingerprint Studies. Compound fingerprints were evaluated against **GWS** using Discovery Studio 4.0. CHARMM force field was initially applied, and compounds were prepared using the ligand protocol. They were then compared to **GWS**. Default molecular properties were used, including various atom parameters. This encompassed charge, hybridization, H-bond features, ionizability, halogenation, aromaticity, or none of the above. Additionally, ALogP category of atoms was considered. The study was operated by Discovery Studio 4.0 software as represented before [81] (additional details in Supplementary data).

3.3. Docking Studies. The crystal structure of M^{pro} was obtained from Protein Data Bank. The docking investigation was accomplished using MOE2014. The study was operated by MOE and Discovery Studio 4.0 software [82] as represented before (additional details in Supplementary data).

TABLE 3: Docking binding energy (kcal/mol) of the tested compounds against M^{pro} (PDB ID: 5R84).

Serial	Compounds	Name	RMSD value (Å)	Docking score (kcal/mol)	No. of H-bonds	No. of hydrophobic bonds
1	**GWS**		0.56	−6.51	3	3
2	**68**	Ramelteon	1.45	−6.49	2	3
3	**163**	Rolipram	1.68	−5.64	1	2
4	**169**	Venlafaxine hydrochloride	1.20	−5.98	1	3
5	**224**	Prilocaine	1.19	−6.05	2	4
6	**286**	Gemfibrozil	1.29	−6.23	3	6
7	**325**	Lomustine	1.11	−5.98	2	2
8	**339**	Nefiracetam	1.23	−6.12	2	5
9	**400**	Aminoglutethimide	1.13	−5.73	0	2
10	**419**	S-(+)-Rolipram	0.91	−6.35	1	3
11	**497**	Piperine	0.89	−6.23	1	3
12	**552**	Ciclopirox	1.56	−5.65	2	0
13	**675**	Mepivacaine hydrochloride	0.78	−6.05	2	3
14	**686**	Meptazinol hydrochloride	1.11	−5.78	0	3
15	**829**	Hyoscyamine	1.40	−6.15	1	3
16	**854**	Desvenlafaxine	1.23	−5.64	2	2
17	**911**	Cyclandelate	1.38	−6.89	3	6
18	**1113**	Hexylresorcinol	0.67	−5.80	1	3
19	**1186**	Loxoprofen	0.88	−6.40	2	1
20	**2296**	3-n-Butylphathlide	0.85	−5.64	0	3
21	**2325**	Mepivacaine	0.85	−6.19	2	5
22	**2334**	Tiletamine Hydrochloride	1.09	−5.80	0	3
23	**2340**	Fenipentol	0.95	−5.78	1	0
24	**2351**	Ropivacaine	1.36	−6.38	2	5
25	**2384**	Tasimelteon	0.89	−6.45	2	8
26	**2395**	Venlafaxine	1.41	−6.44	2	3
27	**2553**	Amylmetacresol	1.25	−5.66	1	2
28	**2840**	Levobupivacaine	0.75	−6.65	3	7
29	**2865**	Atropine	1.36	−6.01	1	3
30	**2901**	Homosalate	0.89	−5.36	0	6

The bold values indicate that the number is based on the number of compounds.

(a)

(b)
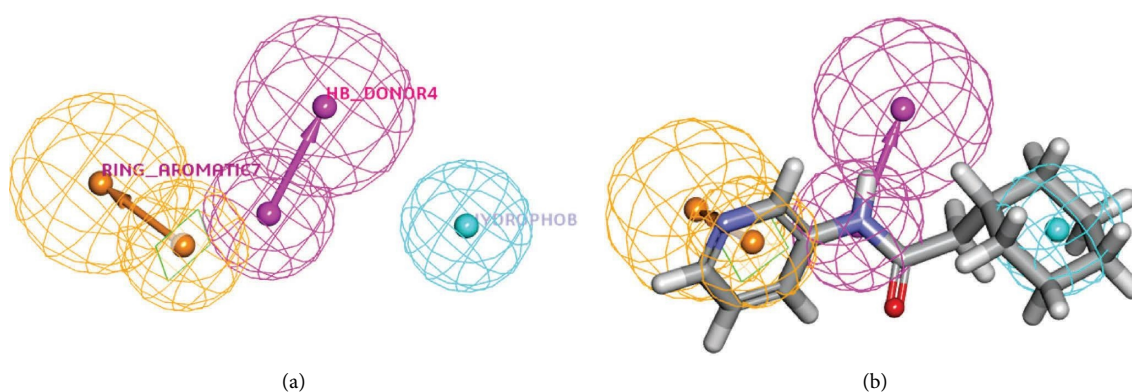
FIGURE 13: (a) The generated 3D-pharmacophore geometry with three features; one H-bond donor (pink color) and two hydrophobic centers (blue). (b) Mapping of the cocrystallized ligand on the generated pharmacophore (Fit value = 2.86).

3.4. Pharmacokinetic Profiling. LigandScout software was used to generate a 3D pharmacophore model based on **GWS** binding against M^{pro}. The Espresso algorithm was employed. The best model, which includes features such as hydrogen bond acceptors, donors, aromatic rings, and hydrophobic elements while excluding a volume sphere, was selected from the ten generated models. Model validation was performed using ROC Curve and AUC analysis with default parameters in LigandScout. Discovery Studio 4.0 was used (see method part in Supplementary data).
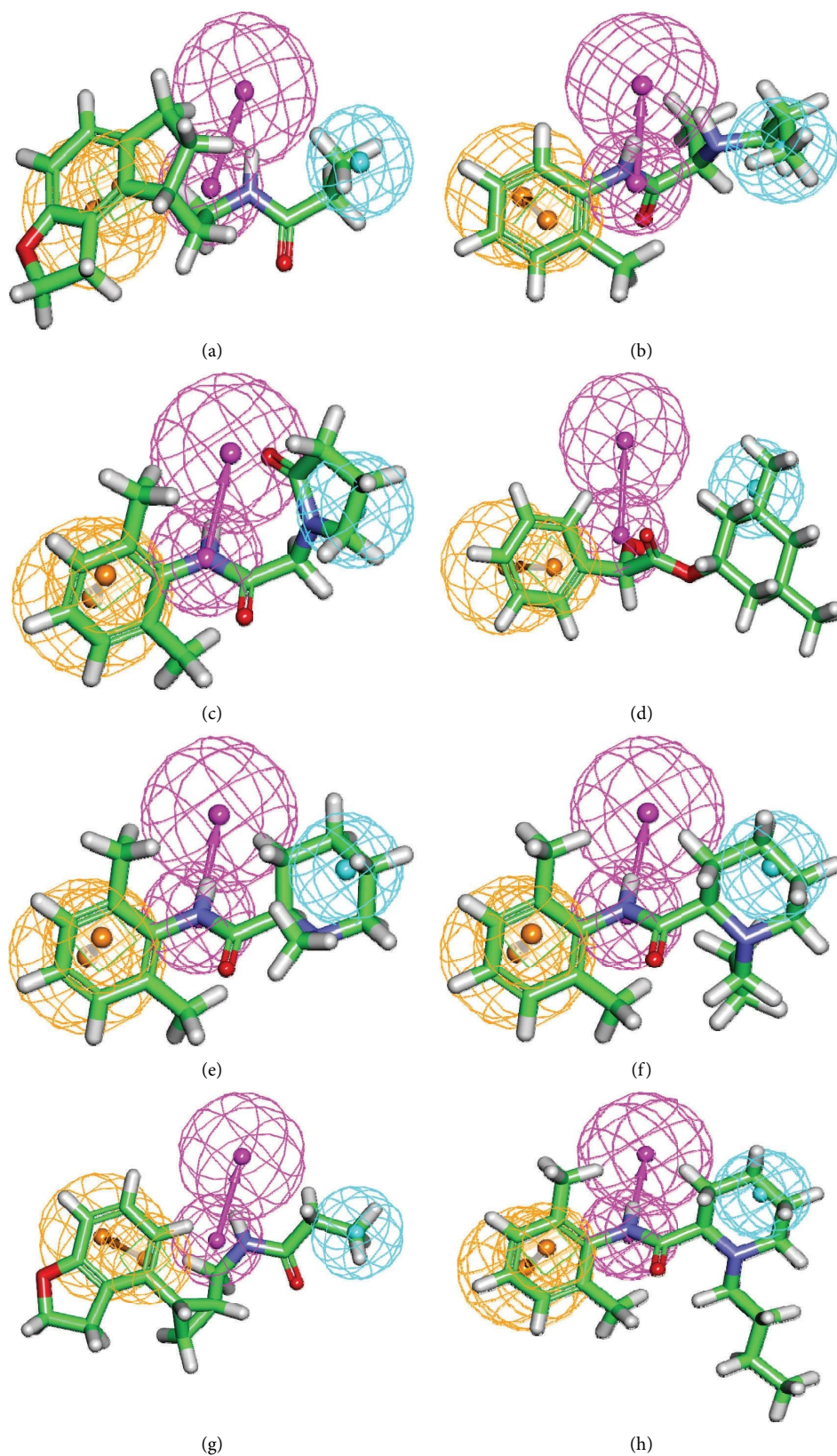
Figure 14: Mapping of the tested metabolites on the generated pharmacophore (a) compounds **68** (Fit value = 2.86, Relative Fit = 74.48%), (b) **224** (Fit value = 2.75, Relative Fit = 96.15%), (c) **339** (Fit value = 2.56, Relative Fit = 89.51%), (d) **911** (Fit value = 2.81, Relative Fit = 98.25%), (e) **2325** (Fit value = 2.73, Relative Fit = 95.45%), (f) **2351** (Fit value = 2.75, Relative Fit = 96.15%), (g) **2384** (Fit value = 2.38, Relative Fit = 83.22%), and (h) **2840** (Fit value = 2.78, Relative Fit = 97.20%).

(a)

(b)

(c)

(d)

(e)

—— Protein
—— Ligand
—— Complex
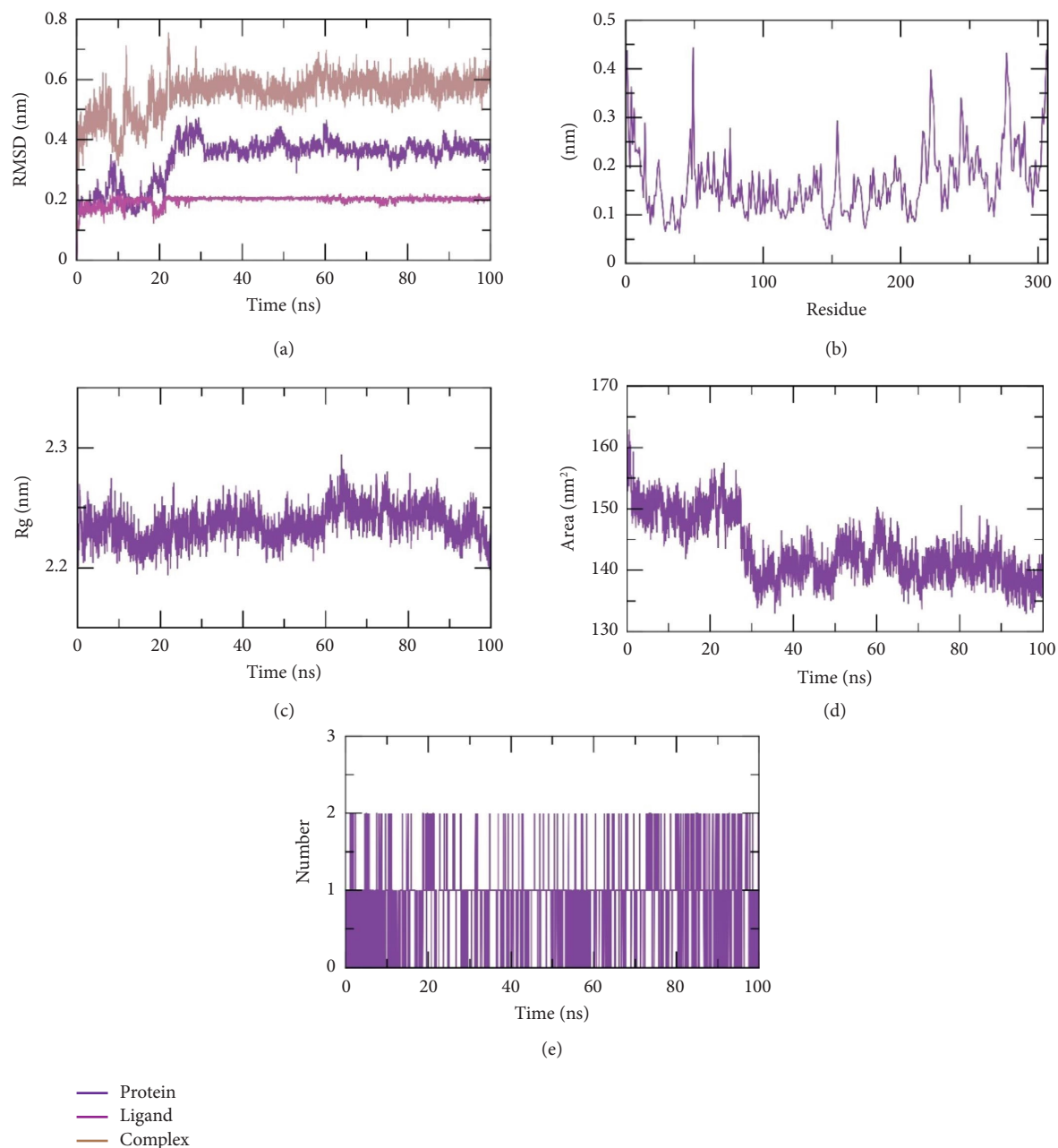
FIGURE 15: M D simulations outcomes; (a) RMSD values, (b) RMSF, (c) R_g, (d) SASA, and (e) H-bonding between levobupivacaine—M^{pro} complex over 100 ns of the MD run.

TABLE 4: Fit value and relative fit of the tested metabolites and (**GWS**).

	Comp	Mapped features	Fit value[a]	Relative Fit[b] (%)
1	Cocrystallized ligand	HBD-1, Hydrophobic-2, Aromatic ring-3	2.86	100.00
2	**68**	HBD-1, Hydrophobic-2, Aromatic ring-3	2.13	74.48
3	**169**	HBD-1, Hydrophobic-2, Aromatic ring-3	1.66	58.04
4	**224**	HBD-1, Hydrophobic-2, Aromatic ring-3	2.75	96.15
5	**339**	HBD-1, Hydrophobic-2, Aromatic ring-3	2.56	89.51
6	**675**	HBD-1, Hydrophobic-2, Aromatic ring-3	2.73	95.45
7	**829**	HBD-1, Hydrophobic-2, Aromatic ring-3	2.30	80.42
8	**854**	HBD-1, Hydrophobic-2, Aromatic ring-3	1.76	61.54
9	**911**	HBD-1, Hydrophobic-2, Aromatic ring-3	2.81	98.25
10	**1113**	HBD-1, Hydrophobic-2, Aromatic ring-3	2.66	93.01

TABLE 4: Continued.

	Comp	Mapped features	Fit value[a]	Relative Fit[b] (%)
11	**2325**	HBD-1, Hydrophobic-2, Aromatic ring-3	2.73	95.45
12	**2334**	HBD-1, Hydrophobic-2, Aromatic ring-3	1.61	56.29
13	**2340**	HBD-1, Hydrophobic-2, Aromatic ring-3	2.76	96.50
14	**2351**	HBD-1, Hydrophobic-2, Aromatic ring-3	2.75	96.15
15	**2384**	HBD-1, Hydrophobic-2, Aromatic ring-3	2.38	83.22
16	**2395**	HBD-1, Hydrophobic-2, Aromatic ring-3	1.62	56.64
17	**2553**	HBD-1, Hydrophobic-2, Aromatic ring-3	2.49	87.06
18	**2840**	HBD-1, Hydrophobic-2, Aromatic ring-3	2.78	97.20
19	**2865**	HBD-1, Hydrophobic-2, Aromatic ring-3	2.30	80.42
20	**2901**	HBD-1, Hydrophobic-2, Aromatic ring-3	2.58	90.21

[b]Relative fit = (fit value of a metabolite/fit value of (**GWS**)) X 100. The bold values indicate that the number is based on the number of compounds.

(a)

(b)
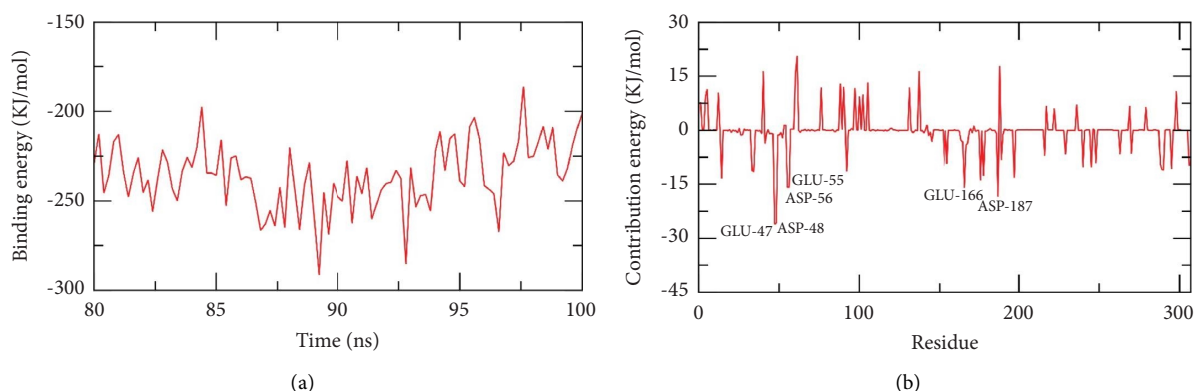
FIGURE 16: MM-PBSA outcomes of levobupivacaine—M^{pro} complex.

3.5. Molecular Dynamics Simulation. The system was prepared using the web-based CHARMM-GUI [83–85] interface utilizing CHARMM36 force field [86] and NAMD 2.13 [87] package. The TIP3P explicit solvation model was used (additional details in Supplementary data).

3.6. MM-PBSA Studies. The g_mmpbsa package of GRO-MACS was utilized to calculate the MM/PBSA (additional details in Supplementary data).

4. Conclusion

In conclusion, our study identified eight promising compounds (ramelteon, prilocaine, nefiracetam, cyclandelate, mepivacaine, ropivacaine, tasimelteon, and levobupivacaine) as potential inhibitors against SARS-CoV-2 main protease (M^{pro}). These compounds were selected from a pool of 3009 FDA and clinically approved compounds using a rigorous *in silico* approach. Further analysis through molecular fingerprints, structure similarity, and molecular docking studies confirmed their potential. Levobupivacaine exhibited the highest docking and pharmacophore scores, leading to extensive molecular dynamics simulations. The results demonstrated stable binding and optimal dynamics of the M^{pro}-Levobupivacaine complex over 100 ns. MM-PBSA studies reaffirmed the strong interaction with a free energy value of −235 kJ/mol.

These findings provide a promising foundation for further *in vitro* and *in vivo* research on these compounds in the fight against COVID-19.

Data Availability

The data used to support the findings of this study are included within the article.

Conflicts of Interest

The authors declare that they have no conflicts of interest.

Acknowledgments

Supplementary Materials

Detailed methodologies covering fingerprints, molecular similarity, molecular docking, pharmacophore, MD simulations, and MM-PBSA studies. (*Supplementary Materials*)

References

[1] Who, "WHO coronavirus (COVID-19) dashboard," 2022, https://covid19.who.int/.

[2] Q. Wang, L. Yang, H. Jin, and L. Lin, "Vaccination against COVID-19: a systematic review and meta-analysis of acceptability and its predictors," *Preventive Medicine*, vol. 150, Article ID 106694, 2021.

[3] H. S. Chan, H. Shan, T. Dahoun, H. Vogel, and S. Yuan, "Advancing drug discovery via artificial intelligence," *Trends in Pharmacological Sciences*, vol. 40, no. 10, 2019.

[4] A. Talevi and C. L. Bellera, "Challenges and opportunities with drug repurposing: finding strategies to find alternative uses of therapeutics," *Expert Opinion on Drug Discovery*, vol. 15, no. 4, pp. 397–401, 2020.

[5] V. Parvathaneni, N. S. Kulkarni, A. Muth, and V. Gupta, "Drug repurposing: a promising tool to accelerate the drug discovery process," *Drug Discovery Today*, vol. 24, no. 10, pp. 2076–2085, 2019.

[6] S. Pushpakom, F. Iorio, P. A. Eyers et al., "Drug repurposing: progress, challenges and recommendations," *Nature Reviews Drug Discovery*, vol. 18, no. 1, pp. 41–58, 2019.

[7] P. Nowak-Sliwinska, L. Scapozza, and A. Ruiz i Altaba, "Drug repurposing in oncology compounds, pathways, phenotypes and computational approaches for colorectal cancer," *Biochimica et Biophysica Acta (BBA) Reviews on Cancer*, vol. 1871, no. 2, pp. 434–454, 2019.

[8] T. U. Singh, S. Parida, M. C. Lingaraju, M. Kesavan, D. Kumar, and R. K. Singh, "Drug repurposing approach to fight COVID-19," *Pharmacological Reports*, vol. 72, no. 6, pp. 1479–1508, 2020.

[9] J. Hong and M. Bang, "Anti-inflammatory strategies for schizophrenia: a review of evidence for therapeutic applications and drug repurposing," *Clinical Psychopharmacology and Neuroscience*, vol. 18, no. 1, pp. 10–24, 2020.

[10] A. K. Konreddy, G. U. Rani, K. Lee, and Y. Choi, "Recent drug-repurposing-driven advances in the discovery of novel antibiotics," *Current Medicinal Chemistry*, vol. 26, no. 28, pp. 5363–5388, 2019.

[11] D.-A. Shirley, I. Sharma, C. A. Warren, and S. Moonah, "Drug repurposing of the alcohol abuse medication disulfiram as an anti-parasitic agent," *Frontiers in Cellular and Infection Microbiology*, vol. 11, Article ID 633194, 2021.

[12] J. Trivedi, M. Mohan, and S. N. Byrareddy, "Drug repurposing approaches to combating viral infections," *Journal of Clinical Medicine*, vol. 9, no. 11, p. 3777, 2020.

[13] S. Ranjan, R. Devarapalli, S. Kundu et al., "Isomorphism: `molecular similarity to crystal structure similarity' in multicomponent forms of analgesic drugs tolfenamic and mefenamic acid," *IUCrJ*, vol. 7, no. 2, pp. 173–183, 2020.

[14] A. T. Baidya, K. Ghosh, S. A. Amin et al., "In silico modelling, identification of crucial molecular fingerprints, and prediction of new possible substrates of human organic cationic transporters 1 and 2," *New Journal of Chemistry*, vol. 44, no. 10, pp. 4129–4143, 2020.

[15] Y. Shi, "Support vector regression-based QSAR models for prediction of antioxidant activity of phenolic compounds," *Scientific Reports*, vol. 11, no. 1, pp. 8806–8809, 2021.

[16] M. O. Idris, A. A. Yekeen, O. S. Alakanse, and O. A. Durojaye, "Computer-aided screening for potential TMPRSS2 inhibitors: a combination of pharmacophore modeling, molecular docking and molecular dynamics simulation approaches," *Journal of Biomolecular Structure and Dynamics*, vol. 39, no. 15, pp. 5638–5656, 2021.

[17] Y. Lu and M. Li, "A new computer model for evaluating the selective binding affinity of phenylalkylamines to T-Type Ca2+ channels," *Pharmaceuticals*, vol. 14, no. 2, p. 141, 2021.

[18] A. Zhanzhaxina, Y. Suleimen, A. M. Metwaly et al., "In vitro and in silico cytotoxic and antibacterial activities of a diterpene from cousinia alata schrenk," *Journal of Chemistry*, vol. 2021, Article ID 5542455, 11 pages, 2021.

[19] R. Jalmakhanbetova, E. B. Elkaeed, I. H. Eissa, A. M. Metwaly, and Y. M. Suleimen, "Synthesis and molecular docking of some grossgemin amino derivatives as tubulin inhibitors targeting colchicine binding site," *Journal of Chemistry*, vol. 2021, Article ID 5586515, 10 pages, 2021.

[20] A. M. Metwaly, V. O. Imieje, A. A. Zaki et al., "Antileishmanial derivatives of humulene from Asteriscus hierochunticus with in silico tubulin inhibition potential," *Records of Natural Products*, vol. 16, no. 2, pp. 150–171, 2021.

[21] M. O. Rafi, K. Al-Khafaji, T. T. Tok, and M. S. Rahman, "Computer-based identification of potential compounds from Salviae miltiorrhizae against Neirisaral adhesion A regulatory protein," *Journal of Biomolecular Structure and Dynamics*, vol. 40, no. 10, pp. 4301–4313, 2020.

[22] D. R. Parmar, J. Y. Soni, R. Guduru et al., "Discovery of new anticancer thiourea-azetidine hybrids: design, synthesis, in vitro antiproliferative, SAR, in silico molecular docking against VEGFR-2, ADMET, toxicity, and DFT studies," *Bioorganic Chemistry*, vol. 115, Article ID 105206, 2021.

[23] Y. M. Suleimen, A. M. Metwaly, A. E. Mostafa et al., "Isolation, crystal structure, and in silico aromatase inhibition activity of ergosta-5, 22-dien-3β-ol from the fungus gyromitra esculenta," *Journal of Chemistry*, vol. 2021, Article ID 5529786, 10 pages, 2021.

[24] R. G. Yousef, H. M. Sakr, I. H. Eissa et al., "New quinoxaline-2 (1 H)-ones as potential VEGFR-2 inhibitors: design, synthesis, molecular docking, ADMET profile and anti-proliferative evaluations," *New Journal of Chemistry*, vol. 45, no. 36, pp. 16949–16964, 2021.

[25] H. H. Amer, S. H. Alotaibi, A. H. Trawneh, A. M. Metwaly, and I. H. Eissa, "Anticancer activity, spectroscopic and molecular docking of some new synthesized sugar hydrazones, Arylidene and α-Aminophosphonate derivatives," *Arabian Journal of Chemistry*, vol. 14, no. 10, Article ID 103348, 2021.

[26] A. Husain, A. Farooqui, A. Khanam et al., "Physicochemical characterization of C-phycocyanin from Plectonema sp. and elucidation of its bioactive potential through in silico approach," *Cellular and Molecular Biology*, vol. 67, no. 4, pp. 68–82, 2022.

[27] I. H. Eissa, M. M. Khalifa, E. B. Elkaeed, E. E. Hafez, A. A. Alsfouk, and A. M. Metwaly, "In silico exploration of potential natural inhibitors against SARS-Cov-2 nsp10," *Molecules*, vol. 26, no. 20, p. 6151, 2021.

[28] E. B. Elkaeed, I. H. Eissa, A. M. Saleh, B. A. Alsfouk, and A. M. Metwaly, "Computer-aided drug discovery of natural antiviral metabolites as potential SARS-CoV-2 helicase inhibitors," *Journal of Chemical Research*, vol. 48, no. 1, 2024.

[29] E. B. Elkaeed, R. G. Yousef, H. Elkady et al., "New anticancer theobromine derivative targeting EGFR(WT) and EGFR(T790M): design, semi-synthesis, in silico, and in vitro anticancer studies," *Molecules*, vol. 27, no. 18, p. 5859, 2022.

[30] E. B. Elkaeed, I. H. Eissa, H. Elkady et al., "A multistage in silico study of natural potential inhibitors targeting SARS-CoV-2 main protease," *International Journal of Molecular Sciences*, vol. 23, no. 15, p. 8407, 2022.

[31] E. B. Elkaeed, A. M. Metwaly, M. S. Alesawy, A. M. Saleh, A. A. Alsfouk, and I. H. Eissa, "Discovery of potential SARS-CoV-2 papain-like protease natural inhibitors employing a multi-phase in silico approach," *Life*, vol. 12, no. 9, p. 1407, 2022.

[32] I. H. Eissa, M. S. Alesawy, A. M. Saleh et al., "Ligand and structure-based in silico determination of the most promising SARS-CoV-2 nsp16-nsp10 2 o-methyltransferase complex inhibitors among 3009 FDA approved drugs," *Molecules*, vol. 27, no. 7, p. 2287, 2022.

[33] E. B. Elkaeed, H. Elkady, A. Belal et al., "Multi-phase in silico discovery of potential SARS-CoV-2 RNA-dependent RNA polymerase inhibitors among 3009 clinical and FDA-approved related drugs," *Processes*, vol. 10, no. 3, p. 530, 2022.

[34] A. M. Metwaly, A. Elwan, A.-A. M. M. El-Attar, S. T. Al-Rashood, and I. H. Eissa, "Structure-based virtual screening, docking, ADMET, molecular dynamics, and MM-PBSA calculations for the discovery of potential natural SARS-CoV-2 helicase inhibitors from the traditional Chinese medicine," *Journal of Chemistry*, vol. 2022, Article ID 7270094, 23 pages, 2022.

[35] E. B. Elkaeed, B. A. Alsfouk, T. H. Ibrahim et al., "Computer-assisted drug discovery of potential natural inhibitors of the SARS-CoV-2 RNA-dependent RNA polymerase through a multi-phase in silico approach," *Antiviral Therapy*, vol. 28, no. 5, 2023.

[36] A. A. Agbowuro, W. M. Huston, A. B. Gamble, and J. D. Tyndall, "Proteases and protease inhibitors in infectious diseases," *Medicinal Research Reviews*, vol. 38, no. 4, pp. 1295–1331, 2018.

[37] Q.-S. Du, S.-Q. Wang, Y. Zhu et al., "Polyprotein cleavage mechanism of SARS CoV Mpro and chemical modification of the octapeptide," *Peptides*, vol. 25, no. 11, pp. 1857–1864, 2004.

[38] A. Hegyi and J. Ziebuhr, "Conservation of substrate specificities among coronavirus main proteases," *Journal of General Virology*, vol. 83, no. 3, pp. 595–599, 2002.

[39] P.-H. Liang, "Characterization and inhibition of SARS-coronavirus main protease," *Current Topics in Medicinal Chemistry*, vol. 6, no. 4, pp. 361–376, 2006.

[40] S. Ullrich and C. Nitsche, "The SARS-CoV-2 main protease as drug target," *Bioorganic and Medicinal Chemistry Letters*, vol. 30, no. 17, Article ID 127377, 2020.

[41] Fda-approved Drug Library, https://www.selleckchem.com/screening/fda-approved-drug-library.html, 2021.

[42] A. Douangamath, D. Fearon, P. Gehrtz et al., "Crystallographic and electrophilic fragment screening of the SARS-CoV-2 main protease," *Nat Commun*, vol. 11, no. 1, pp. 1–11, 2020.

[43] A. L. Carvalho, J. Trincão, and M. J. J. L. Romão, "protocols," *X-ray Crystallography in Drug Discovery*, Springer, Berlin, Germanypp. 31–56, 2010.

[44] A. M. Hassell, G. An, R. K. Bledsoe et al., "Crystallization of protein–ligand complexes," *Acta Crystallographica Section D Biological Crystallography*, vol. 63, no. 1, pp. 72–79, 2007.

[45] D. Vidal, R. Garcia-Serna, and J. Mestres, "Ligand-based approaches to in silico pharmacology," in *Chemoinformatics and Computational Chemical Biology*, pp. 489–502, Springer, Berlin, Germany, 2011.

[46] G. Schneider, Y. Tanrikulu, and P. Schneider, "Self-organizing Molecular Fingerprints: A Ligand-Based View on Drug-like Chemical Space and Off-Target Prediction," *Future Med Chem*, vol. 1, 2009.

[47] M. A. Spackman and J. J. McKinnon, "Fingerprinting intermolecular interactions in molecular crystals," *CrystEngComm*, vol. 4, no. 66, pp. 378–392, 2002.

[48] H. Chu, Q.-X. He, J. Wang, Y. Hu, Y.-Q. Wang, and Z.-H. Lin, "In silico design of novel benzohydroxamate-based compounds as inhibitors of histone deacetylase 6 based on 3D-QSAR, molecular docking, and molecular dynamics simulations," *New Journal of Chemistry*, vol. 44, no. 48, pp. 21201–21210, 2020.

[49] C. Ieritano, J. L. Campbell, and W. S. Hopkins, "Predicting differential ion mobility behaviour in silico using machine learning," *Analyst*, vol. 146, no. 15, pp. 4737–4743, 2021.

[50] M. Taha, N. H. Ismail, M. Ali et al., "Molecular hybridization conceded exceptionally potent quinolinyl-oxadiazole hybrids through phenyl linked thiosemicarbazide antileishmanial scaffolds: in silico validation and SAR studies," *Bioorganic Chemistry*, vol. 71, pp. 192–200, 2017.

[51] K. Heikamp and J. R. Bajorath, "How do 2D fingerprints detect structurally diverse active compounds? Revealing compound subset-specific fingerprint features through systematic selection," *Journal of Chemical Information and Modeling*, vol. 51, no. 9, pp. 2254–2265, 2011.

[52] F. A. D. M. Opo, M. M. Rahman, F. Ahammad, I. Ahmed, M. A. Bhuiyan, and A. M. Asiri, "Structure based pharmacophore modeling, virtual screening, molecular docking and ADMET approaches for identification of natural anti-cancer agents targeting XIAP protein," *Scientific Reports*, vol. 11, no. 1, pp. 4049–4117, 2021.

[53] J. Duan, S. L. Dixon, J. F. Lowrie, and W. Sherman, "Analysis and comparison of 2D fingerprints: insights into database screening performance using eight fingerprint methods," *Journal of Molecular Graphics and Modelling*, vol. 29, no. 2, pp. 157–170, 2010.

[54] M. Sastry, J. F. Lowrie, S. L. Dixon, and W. Sherman, "Large-scale systematic analysis of 2D fingerprint methods and parameters to improve virtual screening enrichments," *Journal of Chemical Information and Modeling*, vol. 50, no. 5, pp. 771–784, 2010.

[55] T. Kogej, O. Engkvist, N. Blomberg, and S. Muresan, "Multifingerprint based similarity searches for targeted class compound selection," *Journal of Chemical Information and Modeling*, vol. 46, no. 3, pp. 1201–1213, 2006.

[56] P. Willett, "Molecular similarity approaches in chemoinformatics: early history and literature status," *Frontiers in Molecular Design and Chemical Information Science-Herman Skolnik Award Symposium*, ACS Publications, Jürgen Bajorath, 2016.

[57] G. Maggiora, M. Vogt, D. Stumpfe, and J. Bajorath, "Molecular similarity in medicinal chemistry: miniperspective," *Journal of Medicinal Chemistry*, vol. 57, no. 8, pp. 3186–3204, 2014.

[58] T. Altamash, A. Amhamed, S. Aparicio, and M. Atilhan, "Effect of hydrogen bond donors and acceptors on CO2 absorption by deep eutectic solvents," *Processes*, vol. 8, no. 12, p. 1533, 2020.

[59] Y. Wan, Y. Tian, W. Wang, S. Gu, X. Ju, and G. Liu, "In silico studies of diarylpyridine derivatives as novel HIV-1 NNRTIs using docking-based 3D-QSAR, molecular dynamics, and pharmacophore modeling approaches," *RSC Advances*, vol. 8, no. 71, pp. 40529–40543, 2018.

[60] M. Turchi, Q. Cai, and G. Lian, "An evaluation of in-silico methods for predicting solute partition in multiphase complex fluids–A case study of octanol/water partition coefficient," *Chemical Engineering Science*, vol. 197, pp. 150–158, 2019.

[61] K. M. Sullivan, S. J. Enoch, J. Ezendam, K. Sewald, E. L. Roggen, and S. Cochrane, "An adverse outcome pathway for sensitization of the respiratory tract by low-molecular-weight chemicals: building evidence to support the utility of

in vitro and in silico methods in a regulatory context," *Applied In Vitro Toxicology*, vol. 3, no. 3, pp. 213–226, 2017.

[62] A. Escamilla-Gutiérrez, R. M. Ribas-Aparicio, M. G. Córdova-Espinoza, and J. A. Castelán-Vega, "In silico strategies for modeling RNA aptamers and predicting binding sites of their molecular targets," *Nucleosides, Nucleotides and Nucleic Acids*, vol. 40, no. 8, pp. 798–807, 2021.

[63] A. C. Kaushik, A. Kumar, S. Bharadwaj, R. Chaudhary, and S. Sahi, "Ligand-based approach for in-silico drug designing," in *Bioinformatics Techniques for Drug Discovery*, pp. 11–19, Springer, Berlin, Germany, 2018.

[64] H. Zhang, J.-X. Ren, J.-X. Ma, and L. Ding, "Development of an in silico prediction model for chemical-induced urinary tract toxicity by using naïve Bayes classifier," *Molecular Diversity*, vol. 23, no. 2, pp. 381–392, 2019.

[65] R. C. Braga and C. H. Andrade, "Assessing the performance of 3D pharmacophore models in virtual screening: how good are they?" *Current Topics in Medicinal Chemistry*, vol. 13, no. 9, pp. 1127–1138, 2013.

[66] M. Muchtaridi, H. N. Syahidah, A. Subarnas, M. Yusuf, S. D. Bryant, and T. Langer, "Molecular docking and 3D-pharmacophore modeling to study the interactions of chalcone derivatives with estrogen receptor alpha," *Pharmaceuticals*, vol. 10, no. 4, p. 81, 2017.

[67] A. Kutlushina, A. Khakimova, T. Madzhidov, and P. Polishchuk, "Ligand-based pharmacophore modeling using novel 3D pharmacophore signatures," *Molecules*, vol. 23, no. 12, p. 3094, 2018.

[68] A. McGechan and K. Wellington, "Ramelteon," *CNS Drugs*, vol. 19, no. 12, pp. 1057–1065, 2005.

[69] P. K. Yadalam, T. M. Balaji, S. Varadarajan et al., "Assessing the therapeutic potential of agomelatine, ramelteon, and melatonin against SARS-CoV-2," *Saudi Journal of Biological Sciences*, vol. 29, no. 5, pp. 3140–3150, 2022.

[70] P. Krishnamoorthy, A. S. Raj, S. Roy, N. S. Kumar, and H. Kumar, "Comparative transcriptome analysis of SARS-CoV, MERS-CoV, and SARS-CoV-2 to identify potential pathways for drug repurposing," *Computers in Biology and Medicine*, vol. 128, Article ID 104123, 2021.

[71] Y. Chen, H. Tao, S. Shen et al., "A drug screening toolkit based on the−1 ribosomal frameshifting of SARS-CoV-2," *Heliyon*, vol. 6, no. 8, Article ID e04793, 2020.

[72] D. De Amici, F. Ramaioli, P. Ceriana, and E. Percivalle, "Antiviral activity of local anaesthetic agents," *Journal of Antimicrobial Chemotherapy*, vol. 37, no. 3, p. 635, 1996.

[73] M. Hosseini, W. Chen, D. Xiao, and C. Wang, "Computational molecular docking and virtual screening revealed promising SARS-CoV-2 drugs," *Precision clinical medicine*, vol. 4, no. 1, pp. 1–16, 2021.

[74] S. D. Black, "Molecular modeling and preliminary clinical data suggesting antiviral activity for chlorpheniramine (chlorphenamine) against COVID-19," *Cureus*, vol. 14, no. 1, Article ID e20980, 2022.

[75] S. A. Hollingsworth and R. O. Dror, "Molecular dynamics simulation for all," *Neuron*, vol. 99, no. 6, pp. 1129–1143, 2018.

[76] X. Liu, D. Shi, S. Zhou, H. Liu, H. Liu, and X. Yao, "Molecular dynamics simulations and novel drug discovery," *Expert Opinion on Drug Discovery*, vol. 13, no. 1, pp. 23–37, 2018.

[77] Y. X. Zhu, Y. J. Sheng, Y. Q. Ma, and H. M. Ding, "Assessing the performance of screening MM/PBSA in protein-ligand interactions," *Journal of Physical Chemistry*, vol. 126, no. 8, pp. 1700–1708, 2022.

[78] T. Fu, Z. Jin, Z. Xiu, and G. Li, "Binding free energy estimation for protein-ligand complex based on MM-PBSA with various partial charge models," *Current Pharmaceutical Design*, vol. 19, no. 12, pp. 2293–2307, 2013.

[79] G. Poli, C. Granchi, F. Rizzolio, and T. Tuccinardi, "Application of MM-PBSA methods in virtual screening," *Molecules*, vol. 25, no. 8, p. 1971, 2020.

[80] A. M. Metwaly, E. B. Elkaeed, B. A. Alsfouk, A. M. Saleh, A. E. Mostafa, and I. H. Eissa, "The computational preventive potential of the rare flavonoid, patuletin, isolated from Tagetes patula, against SARS-CoV-2," *Plants*, vol. 11, no. 14, p. 1886, 2022.

[81] M. S. Alesawy, E. B. Elkaeed, A. A. Alsfouk, A. M. Metwaly, and I. H. Eissa, "In silico screening of semi-synthesized compounds as potential inhibitors for SARS-CoV-2 papain-like protease: pharmacophoric features, molecular docking, ADMET, toxicity and DFT studies," *Molecules*, vol. 26, no. 21, p. 6593, 2021.

[82] P. D. bank, *R P D Bank*, PD Bank, Jalgaon, India, 2020.

[83] S. Jo, T. Kim, V. G. Iyer, and W. Im, "CHARMM-GUI: a web-based graphical user interface for CHARMM," *Journal of Computational Chemistry*, vol. 29, no. 11, pp. 1859–1865, 2008.

[84] B. R. Brooks, C. L. Brooks III, A. D. Mackerell Jr. et al., "CHARMM: the biomolecular simulation program," *Journal of Computational Chemistry*, vol. 30, no. 10, pp. 1545–1614, 2009.

[85] J. Lee, X. Cheng, J. M. Swails et al., "CHARMM-GUI input generator for NAMD, GROMACS, AMBER, OpenMM, and CHARMM/OpenMM simulations using the CHARMM36 additive force field," *Journal of Chemical Theory and Computation*, vol. 12, no. 1, pp. 405–413, 2016.

[86] R. B. Best, X. Zhu, J. Shim et al., "Optimization of the additive CHARMM all-atom protein force field targeting improved sampling of the backbone ϕ, ψ and side-chain χ_1 and χ_2 dihedral angles," *Journal of Chemical Theory and Computation*, vol. 8, no. 9, pp. 3257–3273, 2012.

[87] J. C. Phillips, R. Braun, W. Wang et al., "Scalable molecular dynamics with NAMD," *Journal of Computational Chemistry*, vol. 26, no. 16, pp. 1781–1802, 2005.

Research Article

Evaluation of 3,5-Diphenyl-2-Pyrazolines for Antimitotic Activity by Inhibition of Tubulin Polymerization

Soon Young Shin [ID],[1] Euitaek Jung [ID],[1] Young Han Lee [ID],[1] Yoongho Lim [ID],[2] Seunghyun Ahn [ID],[3] and Dongsoo Koh [ID][3]

[1]*Department of Biological Sciences, College of Biological Science and Biotechnology, Konkuk University, Seoul 05029, Republic of Korea*
[2]*Division of Bioscience and Biotechnology, BMIC, Konkuk University, Seoul 05029, Republic of Korea*
[3]*Department of Applied Chemistry, Dongduk Women's University, Seoul 02748, Republic of Korea*

Correspondence should be addressed to Dongsoo Koh; dskoh@dongduk.ac.kr

Chalcones have a skeleton of diphenyls connected *via* an α,β-unsaturated carbonyl group. Many chalcone derivatives have been shown to interact with tubulin. Based on previous reports, chalcones derived by substitution of a carbonyl group with 2-pyrazoline can be expected to inhibit tubulin polymerization. Therefore, 3,5-diphenyl-2-pyrazolines were prepared to investigate their ability to inhibit tubulin polymerization. The clonogenic long-term survival assay showed that derivative **4**, 5-(3,5-dimethoxyphenyl)-3-(2-methoxyphenyl)-4,5-dihydro-1H-pyrazole-1-carbothioamide, was the most effective at inhibiting the clonogenicity of HCT116 human colon cancer cells. Derivative **4** induced G2/M cell cycle arrest. In addition, derivative **4** caused dispersed microtubules, a disorganized spherical arrangement of chromosomes, and inhibition of mitotic spindle formation. The binding mode between tubulin and derivative **4** was elucidated by *in silico* molecular docking. Derivative **4** was superimposed with colchicine and entered the colchicine-binding site well. These results suggest that derivative **4** inhibits tubulin polymerization by binding to the colchicine binding site of tubulin, thus preventing mitotic spindle formation during mitosis in HCT116 colon cancer cells. We propose that derivative **4** could be used as a promising antimitotic chemotherapeutic agent.

1. Introduction

The clinical usefulness of chemotherapeutic drugs is based on the differential effect of the drugs on normal versus cancerous cells. One of the various targets of chemotherapy is alteration of microtubule dynamics. Molecules that bind to tubulin to alter its incorporation into microtubules can be used as chemotherapeutic agents [1]. Tubulin α,β heterodimers interact with ligands at different sites, such as colchicine, vinca domain, maytansine, and pironectin sites [2].

Colchicine was the first microtubule-destabilizing molecule to be discovered and it inhibits mitosis. As cancer cells generally proliferate at a much faster rate than normal cells, colchicine has been investigated as a potential chemotherapeutic agent, although it has not been used as such

[3]. Although colchicine is not used as an anticancer drug because of its low efficacy and high toxicity, including anemia and bone marrow damage, there have been extensive efforts to identify molecules that interact with the colchicine binding site. Although a chemotherapeutic agent that targets the colchicine binding site has yet to be developed, it is nonetheless still considered a potential target for anticancer drug development. Combretastatin isolated from *Combretum caffrum* have been shown to inhibit tubulin polymerization by interaction with the colchicine binding site [4]. These compounds are natural polyphenols that contain multiple phenol groups. Among these, chalcones have skeletons of diphenyls connected *via* an α,β-unsaturated carbonyl group, as shown in Figure S1. Many chalcone derivatives interact with tubulin. Chloro-substituted-2′-

hydroxychalcones have been studied as inhibitors of tubulin polymerization and cell proliferation [5]. As a natural chalcone with benzopyran, millepachine, exhibits anticancer activities, a derivative with a 4-diethylamino group as a substituent on the B ring was synthesized and shown to suppress tubulin polymerization in HepG2 cells and it was able to arrest HepG2 cells in G2/M phase [6].

Colorectal cancer is one of the most common cancers in both men and women worldwide and the second leading cause of cancer-related death in the United States [7]. HCT116 is a human colon carcinoma cell line that is commonly used in cancer biology research due to its characteristics, including aggressive oncogenic, invasive, undifferentiated, and growth factor-independent property. The authors designed and synthesized 2-hydroxy-2′,4′,6′-trimethoxy-5,6-benzochalcone, and they showed that it could disrupt the microtubule cytoskeleton of human colon cancer cells [8]. Another methoxylated benzochalcone synthesized by the authors, 2-hydroxy-4-methoxy-2′,3′-benzochalcone inhibited tubulin polymerization [9]. Naphthalene-chalcone derivatives interact with tubulin and lead to G_2/M cell cycle arrest and apoptosis [10, 11]. 3-(Naphthalen-2-yl)-N,5-diphenyl-pyrazoline-1-carbothioamide, prepared by substitution of the α,β-unsaturated carbonyl group of chalcone with 2-pyrazoline, has been shown to induce apoptosis and trigger cell death via a caspase-dependent mechanism [12].

Based on the previous results, chalcones derived by substitution of a carbonyl group with 2-pyrazoline can be expected to inhibit tubulin polymerization. Based on the pharmacophoric characteristics of colchicine, as shown in Figure 1, derivatives containing similar characteristics such as hydrogen bond acceptor, donor, and hydrophobic centers could be designed as colchicine-binding site inhibitors [13, 14]. 2,3′,5′-trimethoxy groups of 3,5-diphenyl-2-pyrazoline moiety contained in 19 derivatives satisfy hydrogen bond acceptor of the pharmacophoric characteristics shown in Figure 1. Benzene ring attached to thiazole (derivatives **6**–**12**) and benzylidene group attached to thiazolone (derivatives **13**–**19**) satisfy hydrophobic center of the pharmacophoric characteristics. Eighteen derivatives including 3,5-diphenyl-2-pyrazoline moiety (Figure S2) and a chalcone derivative, whose oxygen in the α,β-unsaturated carbonyl group was substituted with hydrazine were prepared and their inhibitory effects on tubulin polymerization were investigated. As mentioned above, disruption of microtubule dynamics is a property relevant to chemotherapeutic activity, the cytotoxicities of 3,5-diphenyl-2-pyrazoline derivatives toward cancer cells were determined using a clonogenic long-term survival assay. Among the 3,5-diphenyl-2-pyrazoline derivatives, derivative **4**, 5-(3,5-dimethoxyphenyl)-3-(2-methoxyphenyl)-4,5-dihydro-1H-pyrazole-1-carbothioamide, exhibited the greatest half-maximal cell growth inhibitory effect. It inhibited tubulin polymerization, similar to colchicine, and arrested the cell cycle in G_2/M phase. The molecular binding mode between tubulin and derivative **4** was elucidated by *in silico* docking, which demonstrated that it fits the colchicine binding site well.

2. Materials and Methods

2.1. Design and Synthesis of Derivatives. Eighteen 3,5-diphenyl-2-pyrazoline derivatives and a chalcone derivative, whose oxygen in the α,β-unsaturated carbonyl group was substituted with hydrazine, were synthesized, and their spectroscopic data obtained from NMR spectroscopy and mass spectrometry were previously reported by the authors [15]. In the current research, their activities against HCT116 human colon cancer cells were investigated. Their chemical structures are shown in Figure 2.

2.2. Cell Culture. Human colon cancer cells (HCT116) were obtained from the American Type Culture Collection (Rockville, MD, USA). The cells were cultured in Dulbecco's Modified Eagle's Medium (DMEM) supplemented with 10% (v/v) heat-inactivated fetal bovine serum (HyClone, Logan, UT, USA).

2.3. Clonogenic Long-Term Survival Assay. Clonogenic assays were performed as previously described [16] with a minor modification. In brief, HCT116 cells (4×10^3 cells per well) were treated with different concentrations of the compounds (0, 1, 5, 10, and 20 μM) for 7 days, followed by fixation with 6% glutaraldehyde and staining with 0.1% crystal violet.

2.4. Cell Cycle Analysis. The cell cycle was analyzed by flow cytometry as previously described [17]. In brief, HCT116 cells were treated with 100 ng/mL colchicine or 40 μM derivative **4** for 24 h, fixed in 70% ethanol, and stained with propidium iodide (50 μg/mL) in RNase buffer (50 μg/mL RNase A, 0.1% Triton X-100, and 0.1 mM EDTA). The cells were classified as G1, S, or G2/M phase depending on the diploid to tetraploid DNA contents. The percentage of the cell population in each cell cycle phase was determined using a NucleoCounter® NC-3000™ cytometer (ChemoMetec, Allerød, Denmark).

2.5. In silico Docking. Among the many 3D structures of tubulin deposited in the protein data bank, the 6xer.pdb was selected because it contains colchicine as its ligand [18]. *In silico* docking was performed using AutoDock Vina (The Scripps Research Institute, La Jolla, USA) as described previously [19]. The holoprotein was prepared using the UCSF Chimera visualization system [20]. The structure of derivative **4** was modified based on the 3D structure of 3,5-diphenyl-2-pyrazoline deposited in PubChem (PubChem CID 3683844) using the Sybyl 7.3/Sketch module. The modified derivative **4** was subjected to energy minimization using the molecular mechanics algorithms provided by Sybyl 7.3. Minimization ceased when the total energy was converged to 0.05 kcal/molÅ. Systematic conformational searches were performed using Sybyl 7.3/Molecular Dynamics module and the conformer with the lowest energy was selected as the three-dimensional (3D) structure of derivative 4 [21, 22]. To validate the docking process, the molecular dynamics (MD) simulation was performed using Sybyl 7.3/molecular dynamics module.
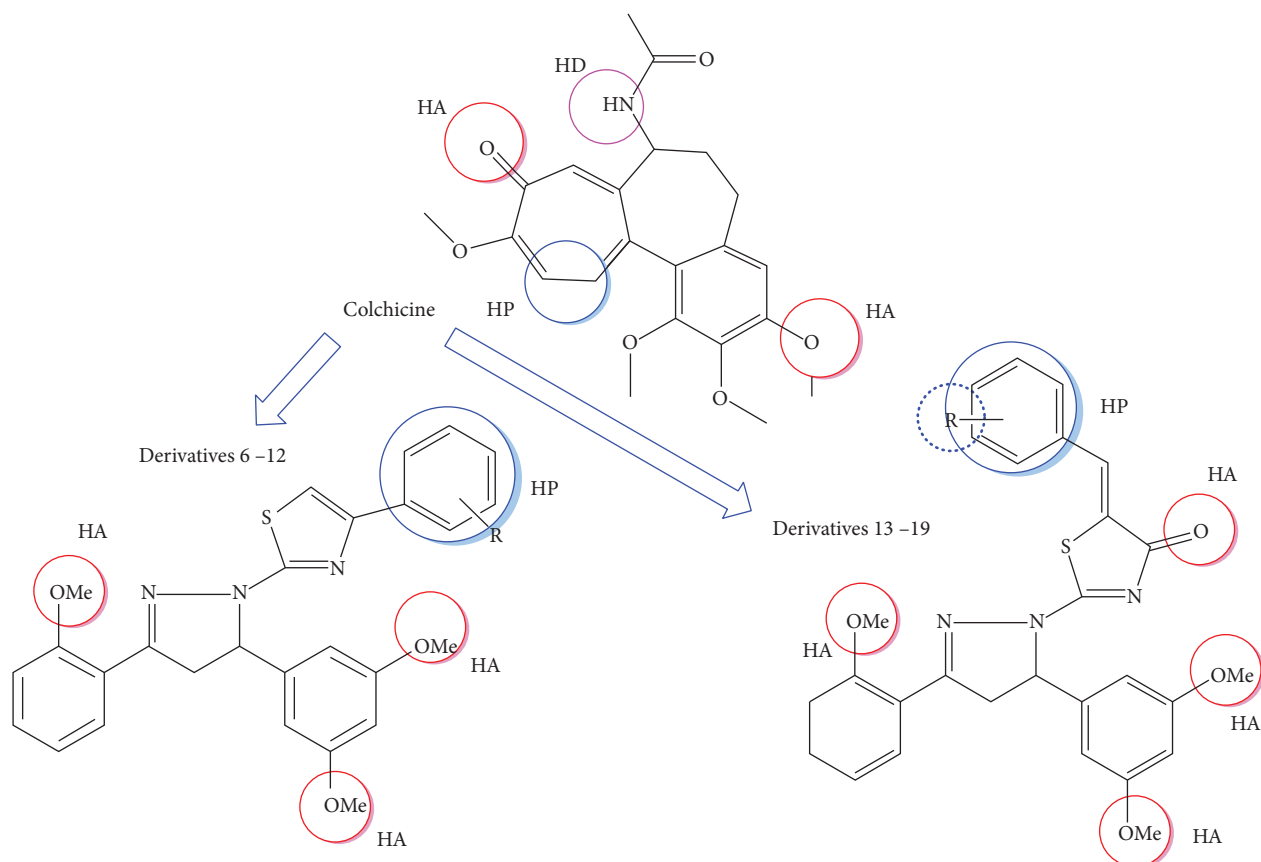
FIGURE 1: Schematic representation of the pharmacophoric characteristics of the derivatives where HA, HD, and HP denote hydrogen bond acceptor, donor, and hydrophobic centers, respectively.

2.6. Immunofluorescence Microscopy. HCT116 cells cultured on coverslips were treated with either vehicle (dimethyl sulfoxide) or 40 μM derivative **4**. After 24 h, the cells were fixed with 4% paraformaldehyde and permeabilized using 0.1% Triton X-100, as previously described [23]. The cells were then incubated with mouse anti-α,β-tubulin (1 : 500 dilution, Invitrogen) and rabbit antipericentrin (1 : 500 dilution, Invitrogen) antibodies for 2 h. After rinsing, the slides were double-labeled with red-fluorescent ALexa Fluor® 555-conjugated antimouse and green-fluorescent Alexa Fluor 488®-conjugated antirabbit antibodies (Invitrogen, Carlsbad, CA, USA) for 30 min. The nuclear DNA was stained with Hoechst 33258 (Sigma-Aldrich). Cells were imaged using an EVOSf1 fluorescence microscope (Advanced Microscopy Group, Bothell, WA, USA).

3. Results and Discussion

3.1. The Effect of 3,5-Diphenyl-2-Pyrazoline Derivatives on Clonogenicity of HCT116 Cells. To confirm whether 3,5-diphenyl-2-pyrazoline derivatives exhibit anticancer activities, their ability to inhibit the proliferation of cancer cell lines was evaluated using a clonogenic long-term survival assay. The inhibitory effects on the colony growth of HCT116 human colon cancer cells at different concentrations (0, 1, 5, 10, and 20 μM) of the derivatives were determined, as shown in Figure 3(a). Some derivatives,

including **4**, **6**, **9**, **10**, **11**, and **12** were tested at low concentrations (0, 0.1, 0.5, 1, and 5 μM) because they exhibited potent inhibitory effects (Figure 3(b)). The half-maximal cancer cell growth inhibitory concentrations (GI$_{50}$) were determined using densitometry and SigmaPlot software (SYSTAT, Chicago, IL, USA), as previously described [22]. The GI$_{50}$ values of the 3,5-diphenyl-2-pyrazoline derivatives are listed in Table 1, and the error bars are shown in Figure S3. The GI$_{50}$ values ranged between 0.09 and 14.82 μM. These data suggest that 3,5-diphenyl-2-pyrazoline derivatives differentially inhibited the growth of HCT116 colon cancer cells. The half-maximal cell growth inhibitory activities caused by substituents at 1-*N* of 5-(3,5-dimethoxyphenyl)-3-(2-methoxyphenyl)-4,5-dihydro-1*H*-pyrazole increase as follows: thiazol-4(5*H*)-one (derivative **5**) < methanethial (derivative **2**) < acetaldehyde (derivative **3**) < methanethioamide (derivative **4**). In the case of 2-(5-(3,5-dimethoxyphenyl)-3-(2-methoxyphenyl)-4,5-dihydro-1*H*-pyrazol-1-yl)-4-phenylthiazole moiety, the activities decrease as follows: *m*-F (derivative **10**) > *p*-OMe (derivative **7**) > *m*-OMe (derivative **6**) > *p*-Cl (derivative **12**) > *p*-F (derivative **11**) > *o*-F (derivative **9**) > *p*-CN (derivative **8**). In (*Z*)-5-benzylidene-2-(5-(3,5-dimethoxyphenyl)-3-(2-methoxyphenyl)-4,5-dihydro-1*H*-pyrazol-1-yl)thiazol-4(5*H*)-one moiety, the activities decrease as follows: *o*-OMe (derivative **13**) > *o*,*m*-di-OMe (derivative **16**) > *m*-OMe (derivative **14**) > *p*-OMe (derivative **15**) > *m*,*m*-di-OMe
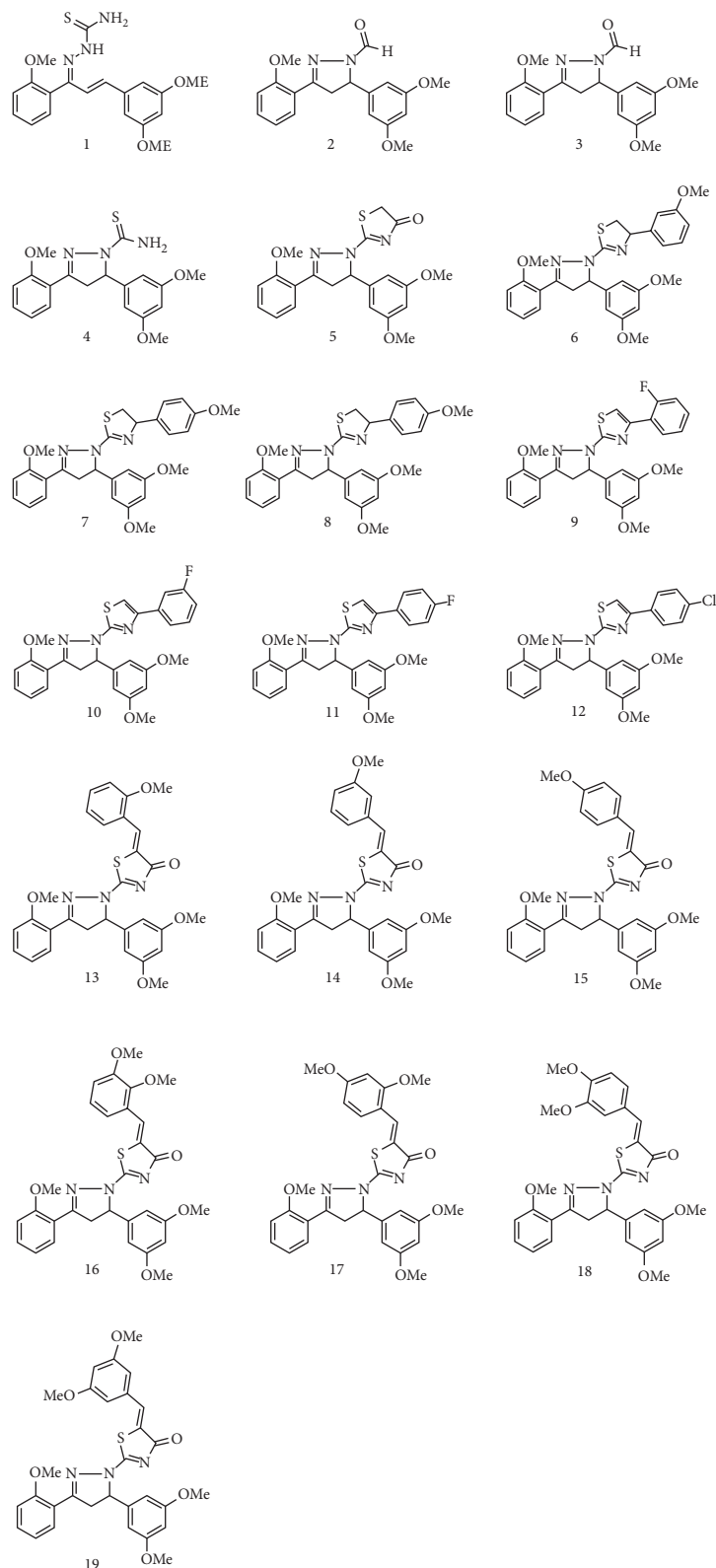
Figure 2: The chemical structures of 3,5-diphenyl-2-pyrazoline derivatives.

(derivative **19**) > *o,p*-di-OMe (derivative **17**) = *m,p*-di-OMe (derivative **18**). Structures of the 3,5-diphenyl-2-pyrazoline derivatives and their GI50 structure-activity relationships (SARs) are shown in Figure 4. While

derivative **1** consists of an open bridge between diphenyl rings, two phenyl rings of 18 derivatives are connected via 2-pyrazoline. As described in the introduction section, we focused on the activities of 3,5-diphenyl-2-pyrazoline

(a)

(b)
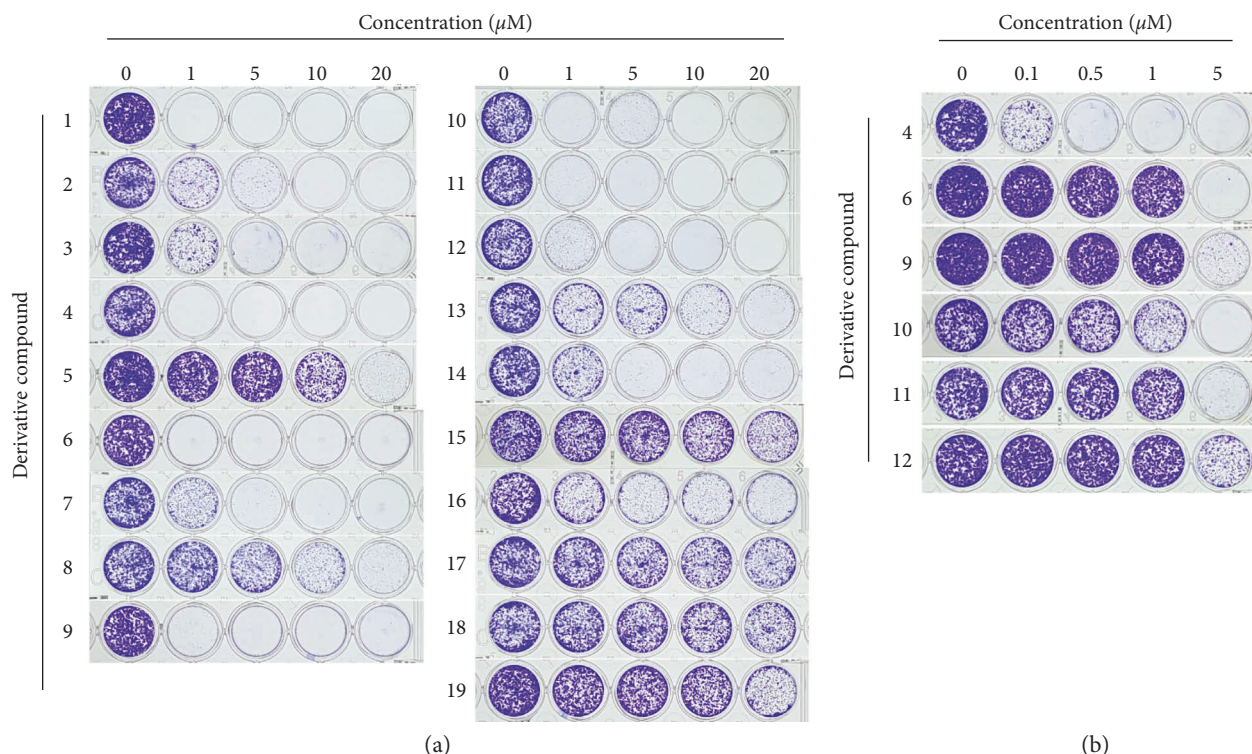
FIGURE 3: (a) Clonogenic long-term survival assay of 3,5-diphenyl-2-pyrazoline derivatives against HCT116 human colon cancer cells at different concentrations (0, 1, 5, 10, and 20 μM) and (b) of derivatives **4**, **6**, **9**, **10**, **11**, and **12** at lower concentrations (0, 0.1, 0.5, 1, and 5 μM).

TABLE 1: The half-maximal cell growth inhibitory concentrations (GI_{50}) of 3,5-diphenyl-2-pyrazolines obtained by the clonogenic long-term survival assay of HCT116 human colon cancer cells.

Derivatives	$GI_{50}/\mu M$	Standard deviation
1	0.09	0.00
2	0.94	0.00
3	0.93	0.00
4	0.09	0.00
5	9.74	0.06
6	1.47	0.03
7	0.97	0.00
8	6.07	0.12
9	2.11	0.04
10	0.80	0.00
11	2.01	0.06
12	1.84	0.01
13	0.95	0.00
14	0.98	0.00
15	11.94	0.24
16	0.98	0.00
17	Not detected	—
18	Not detected	—
19	14.82	0.23

derivatives. Therefore, we selected derivative **4** for further biological study even though derivatives **1** and **4** showed similar activities in the inhibition of clonogenicity of cancer cells.

3.2. The Effect of Derivative 4 on Cell Cycle Progression.
To investigate the mechanism of action of the colony growth inhibition of HCT116 cancer cells by 3,5-diphenyl-2-

pyrazoline derivatives, we tested the effect of derivative **4**, which exhibited the best GI_{50} value, on cell cycle progression. HCT116 cells were treated with 40 μM derivative **4** for 24 h, and changes in the distribution of the number of cells in the various cell cycle phases were examined by flow cytometry. As a reference compound, 100 ng/mL colchicine was used. Notably, derivative **4** treatment increased the cell population in the G_2/M phase from 25% to 63% after 24 h, with a concomitant decrease in the number of cells in the G_0/G_1 phase (Figure 5(a)). In addition, the percentage of sub-G_0/G_1 cells, representing apoptotic cells, increased slowly, but steadily, after exposure to derivative **4**. Cyclins are a family of proteins that control cell cycle progression by activating cyclin-dependent kinases (CDKs) at different stages of the cell cycle. Upon the addition of derivative **4**, cyclin E and cyclin A levels progressively decreased over 24 h after treatment (Figure 5(b)). In contrast, cyclin B1 levels increased by 12 h and declined at 24 h. As cyclin B levels begin to increase before entering mitosis and decline during metaphase and anaphase as cells reenter the next G1 phase [24], we suggest that derivative **4** triggers the cell cycle arrest at the G2/M phase, resulting in the growth of HCT116 cells.

3.3. The Effect of Derivative 4 on the Mitotic Spindle Network.
Inhibition of microtubule dynamics leads to disruption of the mitotic spindle in dividing cells and hence results in M phase cell cycle arrest [25]. We used antitubulin immuno-fluorescence microscopy to examine the effect of derivative **4** on the arrangement of the microtubule cytoskeleton. Vehicle-treated mitotic cells had mitotic spindles that were
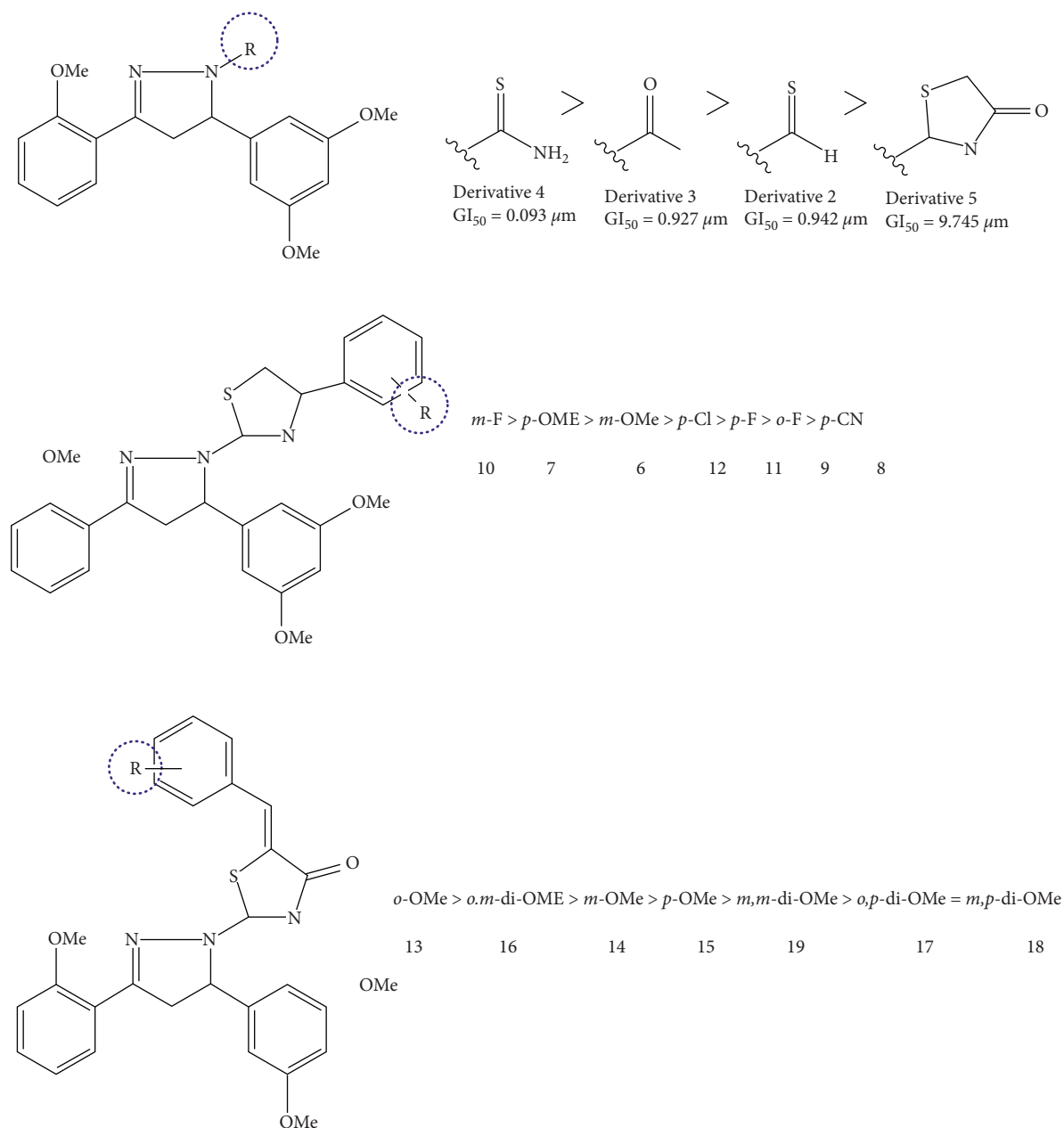
FIGURE 4: Structures of the 3,5-diphenyl-2-pyrazoline derivatives and their GI_{50} structure-activity relationships (SARs).

attached to chromosomes aligned at the metaphase equatorial plate. However, in the presence of derivative **4,** the mitotic cells exhibited densely dispersed microtubules and a disorganized spherical arrangement of chromosomes (Figure 6, top panel). The centrosome, composed of a pair of centrioles, is a cellular organelle that controls the cell cycle and regulates mitotic spindle formation and chromosome segregation [26]. At the G_2/M transition, the duplicated centrosomes separate and move to opposite poles of the cell by a process known as centrosome maturation. Pericentrin is a centrosome component involved in microtubule organization [27]. To address whether derivative **4** caused abnormal mitotic spindle formation, we stained the cells for pericentrin. In vehicle-treated cells, pericentrin was typically located at the edge of the bipolar spindles attached to

chromosomes. However, in the presence of derivative **4**, the distribution of pericentrin was abnormal, with singlet or doublet dots within spherically arranged chromosomes (Figure 6, third panel). These data suggest that derivative **4** inhibits mitotic spindle formation, leading to the incomplete microtubule networks during mitosis, which results in M phase cell cycle arrest.

3.4. Prediction of the α,β-Tubulin Binding Site of Derivative 4 through In Silico Docking Simulation.
To gain insight into the mechanism by which derivative **4** inhibits mitotic spindle formation, we tested whether derivative **4** binds to tubulin α,β-dimer. The binding mode between tubulin and derivative **4** was elucidated by *in silico* molecular docking. Since

(a)

(b)
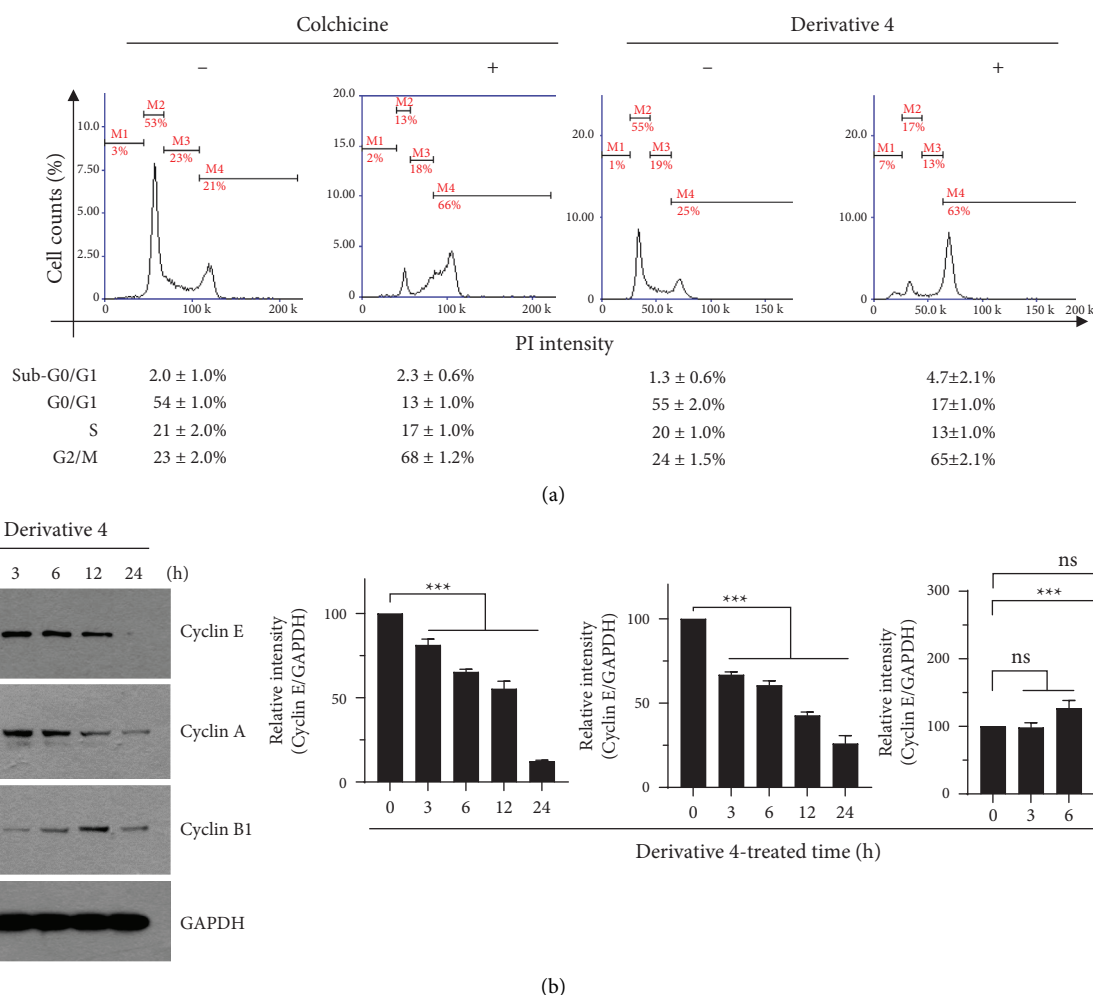
FIGURE 5: effect of derivative **4** on cell cycle progression. (a) HCT116 cells were either untreated or treated with 100 ng/mL colchicine or 40 μM derivative 4 for 24 h. The cellular DNA was stained with propidium iodide, and the DNA contents were determined by flow cytometry. M1, sub-G0/G1; M2, G0/G1; M3, S; and M4, G2/M. x-axis, DNA contents; y-axis, cell counts (%). Data represent mean ± S.D. ($n = 3$). (b) HCT116 cells were treated with 40 μM derivative **4** for different time periods. Total cell lysates were prepared and subjected to immunoblotting using antibodies against cyclin E cyclin A and cyclin B1. GAPDH was used as a loading control. For the quantification, the relative band intensity corresponding to each protein was normalized to the GAPDH level using ImageJ software. Data are expressed as mean ± S.D. ($n = 3$). ns, not significant; ***$P < 0.001$ ($n = 3$) by the Dunnett's multiple comparison test.

6xer.pdb contains colchicine as its ligand, its structure was used in *in silico* docking [18]. It consists of two α,β-tubulin heterodimers and stathmin-4. Since the colchicine site is located between the tubulin heterodimers, one α,β-tubulin heterodimer and stathmin-4 were deleted using the UCSF Chimera visualization system. To obtain the solution structure of the α, β-tubulin holo-protein without colchicine and stathmin-4 prepared by chimera, energy minimization was carried out using Sybyl 7.3/energy minimization module. This holoprotein was used in *in silico* docking. *In silico* docking experiments were performed using *AutoDock Vina* (The Scripps Research Institute, San Diego, CA, USA). The grid box was determined using AutoDock Tools (ADT; Scripps Research Institute). The grid box for the docking procedure was set as follows: the centers of x, y, and z were −7.639, −9.167, and 39.472, respectively, and the sizes of x, y, and z were 18, 20, and 18, respectively. To confirm whether

the current docking procedure was correct, colchicine was docked into the α,β-tubulin holoprotein. The binding energy between the α,β-tubulin holoprotein and colchicine was −10.4 kcal/mol, and the binding pose was superimposed on the crystal structure 6xer.pdb well (Figure S4*)*. Therefore, the docking procedure was considered to be effective. To validate the docking procedure, the MD simulation was carried out at the length of 100 nsec. The kinetic energy of colchicine was stable over the simulation time as shown in Figure S5A. Derivative **4** was docked into the α,β-tubulin holoprotein in the same manner, and its binding energy was −8.0∼−6.4 kcal/mol. As shown in Figure 7, its binding pose was similar to that of colchicine. For the validation of the docking process for derivative **4**, the MD simulation was performed, and its kinetic energy was stable at 100 nsec, as shown in Figure S5B. The residues participating in the binding site of colchicine were compared with those of
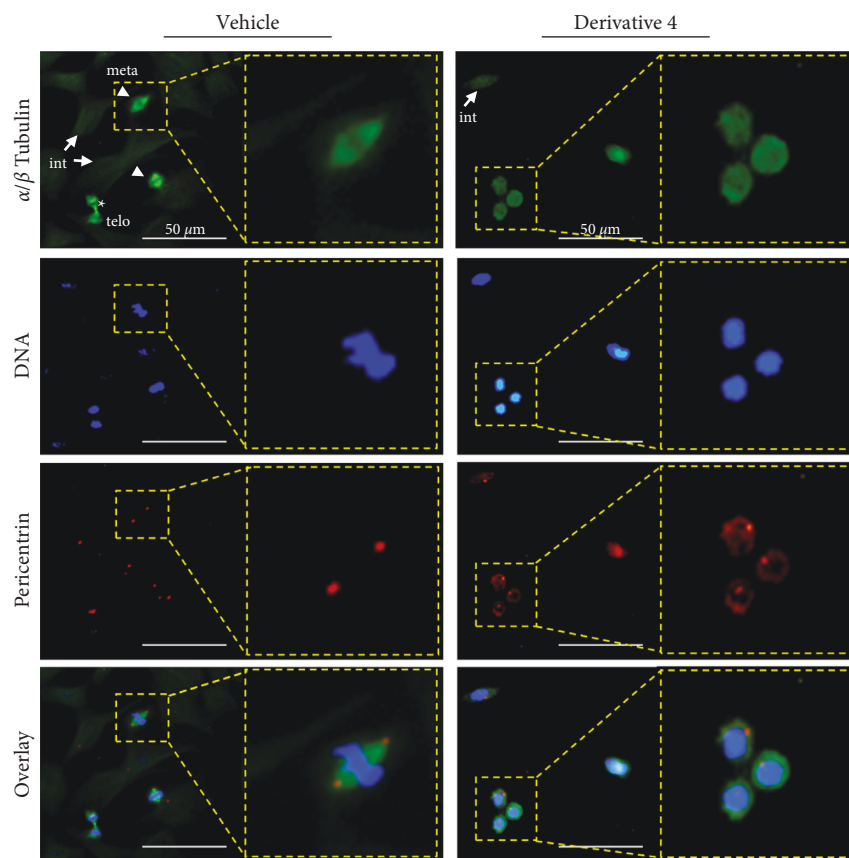
FIGURE 6: effect of derivative **4** on mitotic spindle formation. HCT116 cells cultured on coverslips were treated with 40 μM derivative **4** for 24 h The cells were fixed and incubated with antibodies against α,β-tubulin and pericentrin for 2 h followed by incubation with an AlexaFluor 488-conjugated (for α,β-tubulin, green signal) and AlexaFluor 555-conjugated (for pericentrin, red spot) secondary antibodies for 30 min. Nuclear DNA was stained with 1 μg/mL Hoechst 33258 for 10 min (blue signal). M phase cells were selected and analyzed for assembly of mitotic spindles. The fluorescent signals were imaged using an EVOSf1® fluorescence microscope. Arrows, interphase cells (int); arrowheads, metaphase spindle (meta); star-like, telophase spindle (telo). Scale bars, 50 μm.
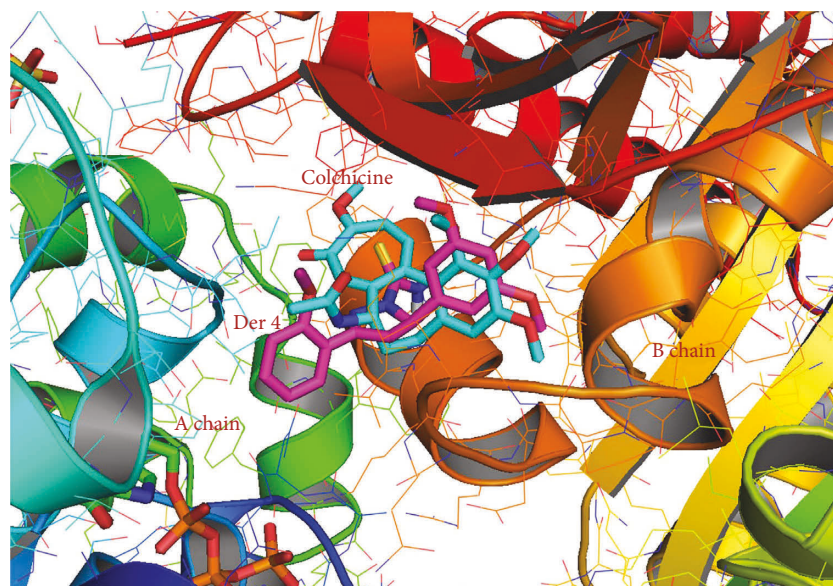
FIGURE 7: The 3D images of colchicine (cyan) and derivative **4** (magenta) contained in the binding pocket of 6xer.pdb generated using PyMol (the PyMOL Molecular Graphics System, Schrödinger, LLC).
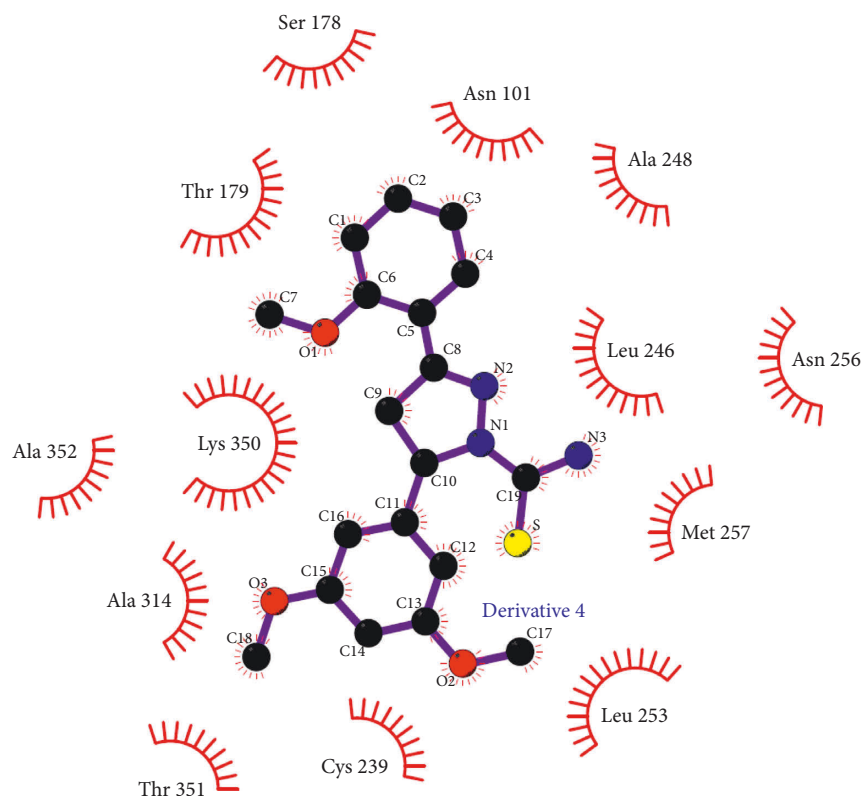
FIGURE 8: Interactions between derivative **4** and residues of the holoprotein of 6xer.pdb analyzed using LIGPLOT. All residues in the red half-circles denote hydrophobic interactions.

derivative **4** using the LigPlot program [28]. In the colchicine-α,β-tubulin holoprotein complex, hydrophobic interactions were formed by 19 residues, including S178(A), T179(A), A180(A), C239, L240, L246, A248, D249, K252, L253, N256, M257, T312, V313, A314, I316, N348, K350, and A352, and a hydrogen bond was observed between the nitrogen of V181(A) and the hydroxyl group of colchicine (2.88 Å), where (A) denotes residues of the A chain and the other residues belong to the B chain (Figure 1). In the derivative **4**, the α,β-tubulin holoprotein complex and hydrophobic interactionswere formed by 13 residues, including N101(A), S178(A), T179(A), C239, L246, A248, L253, N256, M257, A314, K350, T351, and A352 (Figure 8). Two residues, N101(A) and T351, were not detected for colchicine. As shown in Figure 7, the hydroxyl group of colchicine is close to V181, but derivative **4** is far away. As a result, there was no hydrogen bond to derivative **4**. It can be considered that a lesser number of residues participating in binding results in poor binding energy values. However, derivative **4** was superimposed with colchicine and readily entered the colchicine binding site.

Since there is a big problem in the solubility of the colchicine binding site inhibitors, the aqueous solubility of derivative **4** was assessed using SwissADME provided by the Swiss Institute of Bioinformatics (https://www.sib.swiss/). The lipophilicity of derivative **4** was determined based on iLogP of 3.44. Because the iLogP of colchicine is 3.28, derivative **4** is considered to show similar lipophilicity to

colchicine. Water solubility was determined using the decimal logarithm of the molar solubility in water (logS). While the logS values of colchicine obtained by three models namely ESOL, Ali, and SILICOS-IT were 0.502, 1.72, and 8.76×10^{-5} mg/mL, respectively, those of derivative **4**, 6.58×10^{-2}, 1.41×10^{-2}, and 3.67×10^{-3} mg/mL, respectively. This result demonstrated derivative **4** is moderately water soluble [29].

4. Conclusion

The GI$_{50}$ values showing the half-maximal cell growth inhibitory effects against HCT116 human colon cancer cells caused by nineteen 3,5-diphenyl-2-pyrazoline derivatives ranged between 0.09 and 14.82 μM. Because 5-(3,5-dimethoxyphenyl)-3-(2-methoxyphenyl)-4,5-dihydro-1H-pyrazole-1-carbothioamide (derivative **4**) showed the best effect (90 nM), further biological experiments were carried out using derivative **4** to investigate the mechanism of action by 3,5-diphenyl-2-pyrazoline derivatives. Derivative **4** inhibited tubulin polymerization by binding to the colchicine binding site on tubulin, thus disrupting mitotic spindle formation during mitosis in HCT116 colon cancer cells. As proper assembly of the mitotic spindle microtubules is essential for the segregation of chromosomes to the two daughter cells during cell division, derivative **4** was tested whether it binds two tubulin α,β-dimer through *in silico* docking simulation. Even the interactions between the residues surrounding the colchicine binding site of tubulin and derivative **4** were

slightly different with those of colchicine, the 3D image showing the docking pose of derivative **4** was superimposed with that of colchicine and it readily entered the colchicine binding site. As a result, we propose that derivative **4** could be a promising antimitotic chemotherapeutic agent.

Data Availability

The datasets used and analyzed to support this study are available from the corresponding author upon request.

Conflicts of Interest

The authors declare that there are no conflicts of interest regarding the publication of this paper.

Acknowledgments

Supplementary Materials

Figure S1: the chemical structure and numbering of chalcone. Figure S2: the chemical structure of 3,5-diphenyl-2-pyrazoline. Figure S3: graph of the half-maximal cell growth inhibitory concentrations (GI50) of 3,5-diphenyl-2-pyrazoline derivatives (with error bars). Figure S4: 3D images of colchicine obtained from the current docking (pink) and colchicine contained in the crystallographic structure of tubulin 6xer.pdb as its ligand (cyan) in the binding pocket of the 6xer.pdb generated using PyMol. Figure S5: plots of kinetic energy of the colchicine-tubulin complex (A) and derivative **4** (B) against the simulation time 100 nsec. Figure S6: interactions between colchicine and residues of the holoprotein of 6xer.pdb analyzed using LigPlot. Residues in the red half-circles denote hydrophobic interactions, and Val181 of the A chain forms a hydrogen bond with colchicine. Figure S7: 3D images of colchicine (cyan) and derivative **4** (magenta) contained in the binding pocket of 6xer.pdb generated using PyMol. The hydroxyl group of colchicine forms a hydrogen bond with the nitrogen of Val181 of the A chain (2.9 Å). (*Supplementary Materials*)

References

[1] Y. Lu, J. Chen, M. Xiao, W. Li, and D. D. Miller, "An overview of tubulin inhibitors that interact with the colchicine binding site," *Pharmaceutical Research*, vol. 29, no. 11, pp. 2943–2971, 2012.

[2] D. Alpízar-Pedraza, A. d. l. N. Veulens, E. C. Araujo, J. Piloto-Ferrer, and Á. Sánchez-Lamar, "Microtubules destabilizing agents binding sites in tubulin," *Journal of Molecular Structure*, vol. 1259, Article ID 132723, 2022.

[3] F. Naaz, M. R. Haider, S. Shafi, and M. S. Yar, "Anti-tubulin agents of natural origin: targeting taxol, vinca, and colchicine binding domains," *European Journal of Medicinal Chemistry*, vol. 171, pp. 310–331, 2019.

[4] S. N. A. Bukhari, G. B. Kumar, H. M. Revankar, and H. L. Qin, "Development of combretastatins as potent tubulin polymerization inhibitors," *Bioorganic Chemistry*, vol. 72, pp. 130–147, 2017.

[5] H. Aryapour, G. H. Riazi, A. Foroumadi et al., "Biological evaluation of synthetic analogues of curcumin: chloro-substituted-2′-hydroxychalcones as potential inhibitors of tubulin polymerization and cell proliferation," *Medicinal Chemistry Research*, vol. 20, no. 4, pp. 503–510, 2011.

[6] G. Wang, W. Wu, F. Peng et al., "Design, synthesis, and structure–activity relationship studies of novel millepachine derivatives as potent antiproliferative agents," *European Journal of Medicinal Chemistry*, vol. 54, pp. 793–803, 2012.

[7] A. Bhandari, M. Woodhouse, and S. Gupta, "Colorectal cancer is a leading cause of cancer incidence and mortality among adults younger than 50 years in the USA: a SEER-based analysis with comparison to other young-onset cancers," *Journal of Investigative Medicine*, vol. 65, no. 2, pp. 311–315, 2017.

[8] J. M. Lee, M. S. Lee, D. Koh, Y. H. Lee, Y. Lim, and S. Y. Shin, "A new synthetic 2′-hydroxy-2, 4, 6-trimethoxy-5′, 6′-naphthochalcone induces G2/M cell cycle arrest and apoptosis by disrupting the microtubular network of human colon cancer cells," *Cancer Letters*, vol. 354, no. 2, pp. 348–354, 2014.

[9] S. Y. Shin, J. H. Kim, H. Yoon et al., "Novel antimitotic activity of 2-hydroxy-4-methoxy-2′, 3′-benzochalcone (HymnPro) through the inhibition of tubulin polymerization," *Journal of Agricultural and Food Chemistry*, vol. 61, no. 51, pp. 12588–12597, 2013.

[10] G. Wang, W. Liu, Z. Gong, Y. Huang, Y. Li, and Z. Peng, "Synthesis, biological evaluation, and molecular modelling of new naphthalene-chalcone derivatives as potential anticancer agents on MCF-7 breast cancer cells by targeting tubulin colchicine binding site," *Journal of Enzyme Inhibition and Medicinal Chemistry*, vol. 35, no. 1, pp. 139–144, 2020.

[11] G. Wang, Z. Peng, J. Zhang, J. Qiu, Z. Xie, and Z. Gong, "Synthesis, biological evaluation and molecular docking studies of aminochalcone derivatives as potential anticancer agents by targeting tubulin colchicine binding site," *Bioorganic Chemistry*, vol. 78, pp. 332–340, 2018.

[12] Y. Lee, B. S. Kim, S. Ahn et al., "Anticancer and structure-activity relationship evaluation of 3-(naphthalen-2-yl)-N, 5-diphenyl-pyrazoline-1-carbothioamide analogs of chalcone," *Bioorganic Chemistry*, vol. 68, pp. 166–176, 2016.

[13] M. M. Hammouda, A. A. Elmaaty, M. S. Nafie et al., "Design and synthesis of novel benzoazoninone derivatives as potential CBSIs and apoptotic inducers: *in Vitro, in Vivo*, molecular docking, molecular dynamics, and SAR studies," *Bioorganic Chemistry*, vol. 127, Article ID 105995, 2022.

[14] I. H. Eissa, M. A. Dahab, M. K. Ibrahim et al., "Design and discovery of new antiproliferative 1, 2, 4-triazin-3(2H)-ones as tubulin polymerization inhibitors targeting colchicine binding site," *Bioorganic Chemistry*, vol. 112, Article ID 104965, 2021.

[15] B. Kim, S. Ahn, Y. Lee, D. Koh, and Y. Lim, "(1) H and (13) C NMR spectral assignments of nineteen 5-(3, 5-dimethoxyphenyl)-3-(2-methoxyphenyl)-2-pyrazoline derivatives," *Magnetic Resonance in Chemistry*, vol. 59, no. 4, pp. 478–488, 2021.

[16] N. A. P. Franken, H. M. Rodermond, J. Stap, J. Haveman, and C. van Bree, "Clonogenic assay of cells in vitro," *Nature Protocols*, vol. 1, no. 5, pp. 2315–2319, 2006.

[17] E. Jung, D. Koh, Y. Lim, S. Y. Shin, and Y. H. Lee, "Overcoming multidrug resistance by activating unfolded protein response of the endoplasmic reticulum in cisplatin-resistant A2780/CisR ovarian cancer cells," *BMB Reports*, vol. 53, no. 2, pp. 88–93, 2020.

[18] H. Chen, S. Deng, N. Albadari et al., "Design, synthesis, and biological evaluation of stable colchicine-binding site tubulin inhibitors 6-Aryl-2-benzoyl-pyridines as potential anticancer agents," *Journal of Medicinal Chemistry*, vol. 64, no. 16, pp. 12049–12074, 2021.

[19] O. Trott and A. J. Olson, "AutoDock Vina: improving the speed and accuracy of docking with a new scoring function, efficient optimization, and multithreading," *Journal of Computational Chemistry*, vol. 31, no. 2, pp. 455–461, 2010.

[20] E. F. Pettersen, T. D. Goddard, C. C. Huang et al., "UCSF Chimera—a visualization system for exploratory research and analysis," *Journal of Computational Chemistry*, vol. 25, no. 13, pp. 1605–1612, 2004.

[21] S. Y. Shin, H. Yoon, S. Ahn et al., "Chromenylchalcones showing cytotoxicity on human colon cancer cell lines and in silico docking with aurora kinases," *Bioorganic & Medicinal Chemistry*, vol. 21, no. 14, pp. 4250–4258, 2013.

[22] B. S. Kim, S. Y. Shin, S. Ahn, D. Koh, Y. H. Lee, and Y. Lim, "Biological evaluation of 2-pyrazolinyl-1-carbothioamide derivatives against HCT116 human colorectal cancer cell lines and elucidation on QSAR and molecular binding modes," *Bioorganic & Medicinal Chemistry*, vol. 25, no. 20, pp. 5423–5432, 2017.

[23] M. S. Lee, Y. Yong, J. M. Lee, D. Koh, S. Y. Shin, and Y. H. Lee, "A novel methoxyflavonol derivative, 2-hydroxy-3-(2-methoxyphenyl)-1H-Benzo[f]chromen-1-one (DK98), induces apoptosis in HCT116 human colon cancer cells," *Journal of the Korean Society for Applied Biological Chemistry*, vol. 57, no. 1, pp. 129–132, 2014.

[24] H. K. Matthews, C. Bertoli, and R. A. M. de Bruin, "Cell cycle control in cancer," *Nature Reviews Molecular Cell Biology*, vol. 23, no. 1, pp. 74–88, 2022.

[25] F. Mollinedo and C. Gajate, "Microtubules, microtubule-interfering agents and apoptosis," *Apoptosis*, vol. 8, no. 5, pp. 413–450, 2003.

[26] S. Doxsey, W. Zimmerman, and K. Mikule, "Centrosome control of the cell cycle," *Trends in Cell Biology*, vol. 15, no. 6, pp. 303–311, 2005.

[27] B. Delaval and S. J. Doxsey, "Pericentrin in cellular function and disease," *Journal of Cell Biology*, vol. 188, no. 2, pp. 181–190, 2010.

[28] A. C. Wallace, R. A. Laskowski, and J. M. Thornton, "LIGPLOT: a program to generate schematic diagrams of protein-ligand interactions," *Protein Engineering Design and Selection*, vol. 8, no. 2, pp. 127–134, 1995.

[29] S. Y. Shin, E. Jung, H. Yeo et al., "Design, synthesis, and biological activities of 3-((4, 6-diphenylpyrimidin-2-ylamino) methylene)-2, 3-dihydrochromen-4-ones," *Bioorganic Chemistry*, vol. 120, Article ID 105634, 2022.

Research Article

1,5-Dichloroethanoanthracene Derivatives As Antidepressant Maprotiline Analogs: Synthesis, DFT Computational Calculations, and Molecular Docking

Mujeeb A. Sultan ⬤,[1] **Renjith Raveendran Pillai** ⬤,[2] **Eman Alzahrani** ⬤,[3] **Ahmed A. Alsofi** ⬤,[1] **Sadam A. Al-Qadhi** ⬤,[1] **and Rami Adel Pashameah** ⬤[4]

[1]*Department of Pharmacy, Faculty of Medical Sciences, Aljanad University for Science and Technology, Taiz, Yemen*
[2]*Department of Physics, University College, Thiruvananthapuram, Kerala, India*
[3]*Department of Chemistry, College of Science, Taif University, P.O. Box 11099, Taif 21944, Saudi Arabia*
[4]*Department of Chemistry, Faculty of Applied Science, Umm Al-Qura University, Makkah 24230, Saudi Arabia*

Correspondence should be addressed to Mujeeb A. Sultan; mujeeb.aa@just.edu.ye

The chlorinated tetracyclic 1,5-dichloro-9,10-dihydro-9,10-ethanoanthracen-12-yl)-N-methylmethanamine **1**, a maprotiline analog, has been synthesized via reduction and the Diels–Alder reaction followed by reductive amination of aldehyde **2**.1D-NMR (DEPT) and 2D-NMR (HSQC, DQF-COSY) techniques were recruited for structural elucidation in addition to HRMS. Density functional theory calculations were performed to identify the possible isomers of the intermediate compound aldehyde **2**; these calculations were in good agreement with experimental results where aldehyde **2** could exist in three isomers with comparable energies. In addition, the side chain of this aldehyde **2** was extended via the Wittig reaction to obtain the unsaturated ester **5** that was subjected to selective olefinic catalytic hydrogenation to obtain the corresponding saturated ester **6**. Molecular docking simulation showed that all the compounds (**1, 2, 5,** and **6**) have high antidepressant activities and form stable complexes with LeuT by inhibiting the neurotransmitter reuptake at the synapse and hence are good candidates as antidepressant drugs.

1. Introduction

Anthracenes are simply and efficiently incorporated into several organic reactions and are proved to have a wide range of industrial applications such as in fluorescent sensors [1, 2], laser dyes [3], and supramolecular assemblies [4, 5]. Their application in pharmaceutical agents is another interesting field.

From the organic synthesis point of view, 1,5-dichloroanthracene was functionalized through the Kumada coupling to access a series of 1,5- functionalized anthracenes [6]. Based on 1,5-dichloroanthracene, many macrocyclic compounds have been synthesized and reported in the literature [7–9]. 1,5-dichloroanthracene was allowed to react with 3-chlorobenzene through the Diels–Alder (DA) reaction to access substituted triptycene derivatives [10, 11]. Starting from 1,5-dichloroanthracene and other anthracenes, a series of SiMe3-functionalized anthracene derivatives were synthesized via multistep cross-coupling reactions and NMR-qualitatively studied towards UV irradiation [12].

From a biological point of view, 1,5-dichloroanthracene itself shows antioxidant activities through proton transfer mechanisms [13]. A variety of 1,5-dichloroanthracene- and anthraquinone-related derivatives proved to possess an anti-inflammatory activity with no significant cytotoxicity in human neutrophils [14] and other anthracene analogs displayed potent anti-inflammatory activity against superoxide anion production and induced apoptosis, thus exerting antitumor activity [15].

1,5-dichloroethanoanthracene derivatives are related in structure to the antidepressant drug maprotiline 9,10-dihydro-N-methyl-9,10-ethanoanthracene-9-propanamine
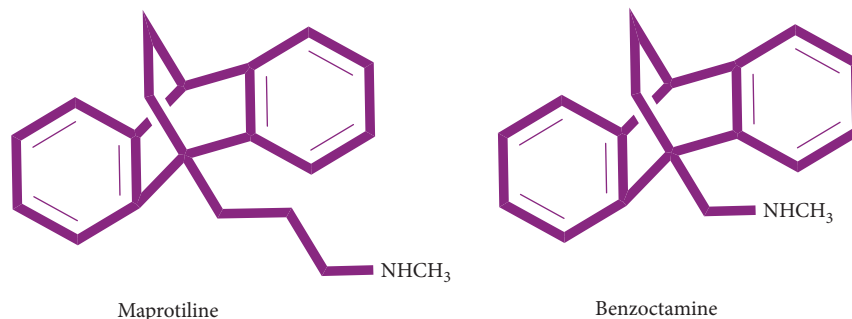
FIGURE 1: Structures of the ethanoanthracene pharmaceutical agents: maprotiline and benzoctamine.

(Figure 1), which exhibits *in vitro* antiproliferative activity against Burkitts's Lymphoma (BL) cell lines DG-75 [16] and induce anti-multidrug resistance (MDR) effect in the cancer cell lines, and plasmodium falciparum [17] as well the derivatives of 1,5-dichloroethanoanthracene are related in structure to benzoctamine 9,10-dihydro-9-(methyl-aminomethyl)-9,10-ethanoanthracene (Figure 1) that have been used to treat anxiety and tension [18]. Ethanoanthracene derivatives were described as therapeutically effective agents for treating neurodegenerative disorders and neurotoxic injury [19]. Another similar class of 9,10-dihydro- 9,10-ethanoanthracenes has been reported [20–22].

The serotonin transporter (SERT) has been considered to be the primary target for the treatment of major depressive and anxiety disorders [23, 24]. The most widely used antidepressants for the treatment of major depressive disorders are selective serotonin reuptake inhibitors, which inhibit serotonin uptake from the synaptic space into presynaptic neurons [25, 26]. It has been shown that serotonin reuptake inhibitors have contrasting chemical structures, which resulted in compounds with considerable pharmacological activities.

Designing and synthesizing new 1,5-dichloroethanoanthracene derivatives is not straightforward and is considered as imperative challenges that more than one isomer will be obtained in the first step of 1,5-dichloroanthracene functionalization. However, we were delighted to synthesize 1,5-dichloroethanoanthracenes (**1, 2, 5,** and 6) and discover their structures by using different spectroscopy techniques including 2D-NMR. In addition, computational calculations were performed in order to identify the possible isomers of the aldehyde 1,5-dichloroethanoanthracene **2**. Moreover, in the present study, molecular docking simulation was employed to investigate the binding mechanism of the compounds (**1, 2, 5,** and **6**) in the active binding site of a bacterial leucine transporter (LeuT) using the high-resolution structure of SERT (PDB : 2QJU) [27]. These compounds and standard antidepressant maprotiline were docked into the central active site of the SERT protein.

2. Results and Discussion

2.1. Retrosynthetic Analysis and Strategy for Chlorinated Maprotiline Analog 1. We began the synthesis with the intention of obtaining the products efficiently in high yields,

lowering the number of steps, high level of selectivity, high level of atom economy, making it environmentally friendly, and at a low cost. The retrosynthetic breakdown of our target chlorinated maprotiline analog **1** yields two fragments; the tetracyclic intermediate with its bridged dihydroethanoanthracene system **I** and anthracene precursor **3** (Scheme 1). The target compound **1** could be obtained by functional group interconversion (FGI) of the key intermediate **2**. The key intermediate **2** with its system [2.2.2] could be built in one step via a DA reaction between a suitable dienophile possessing a functional group and the 1,5-dichloroanthracene **3** center ring as a diene. Acrolein is a reactive dienophile in the DielsF02DAlder reaction and its reaction with 1,5-dichloroanthracene **3** could lead to the aldehyde functionality, which allows us to access other functional groups via FGI including the target amine **1**. Precursor **3** can be prepared from a commercially available 1,5-dichloroanthraquinone **4**, as described in the literature [6].

2.2. Synthesis of the Chlorinated Maprotiline Analog 1. The target compound **1** was obtained according to the synthetic pathway (Scheme 2). The intermediate 1,5-dichloro-9,10-dihydro-9,10-ethanoanthracene-12-carbaldehyde **2** was prepared by HCl-catalyzed reduction of 1,5-dichloroanthraquinone **4** followed by DA reaction of 1,5-dichloroanthracene **3** with acrolein. In fact, it attempts to react 1,5-dichloroanthracene **3** with acrolein to yield aldehyde **2** under a variety of conditions which were not successful. TLC monitoring of these attempts reactions showed that a substantial amount of starting materials remained unreacted; this may refer to the presence of chlorine atoms on anthracene that render it a poor electron-donating diene. Then, 1,5-dichloroanthracene **3** was allowed to react with acrolein using boron trifluoride etherate ($BF_3 \cdot OEt_2$) as a catalyst, at room temperature as well at F02D15F06F Celsius to yield compound **2** but as three isomers in a ratio of 1 : 1 : 1.75 were deduced from the ^{1}H-NMR spectrum (Figure. S1). The IR spectrum supported the structure of compound **2** and showed stretching vibration of the carbonyl group (CHO) as a strong peak at $1723 \, cm^{-1}$ (Figure. S2). Theoretically, compound **2** could exist in more than one isomer and conformer form, due to its three stereocenters as well due to the possible different spatial positions of the CHO group in relation to benzene

Scheme 1: The retrosynthetic analysis and strategy for compound **1**.

Scheme 2: Synthesis of 1,5-dichloroethanoanthracene derivatives.

Table 1: DEPT and HSQC results of the target amine **1**.

| Carbon NO. | Chemical shift δ | | | |
| | ^{1}H (M, J) | ^{13}C | | |
		δ	DEPT 90	DEPT 135
CH$_3$	2.32 (s)	33.39		($\uparrow$CH$_3$)
C1$'$, CH$_2$	2.25–2.29 (m), 2.43–2.47 (m)	54.31		($\downarrow$CH$_2$)
C9	4.47 (d, 1.64)	46.05	($\uparrow$CH)	($\uparrow$CH)
C10	4.29 (t, 2.12)	43.73	($\uparrow$CH)	($\uparrow$CH)
C11, CH$_2$	1.25–1.28 (m), 1.95–2.11 (m)	33.02		($\downarrow$CH$_2$)
C12	2.25–2.29 (m)	35.80	($\uparrow$CH)	($\uparrow$CH)

However, after several trials of normal column chromatography, the two isomers (called 2a) were initially eluted together (Figure S3(a) and Figure S4) while the third isomer (called 2b) was purely separated alone (Fig. S3(b), Figure S5, and Figure S6). The protons of the CHO group of the aldehyde 2a appeared separately as doublet signals at δ 952 and 9.56 ppm with coupling constant J 0.8 Hz for each, whereas the signals of bridgehead protons appeared collectively; and the signal of the protons integrated for carbon 10 (C10) appeared as pentet at δ 4.93 ppm with coupling constant $J = 2.74$ Hz and the signal of the protons integrated for carbon 9 (C9) appeared as a double doublet at δ 5.26 ppm with coupling constant $J = 7.2$ and 2.45 Hz (Figure. S3(c)).

The ^{1}H and ^{13}C spectra of the isomer **2b** can be divided into two regions: aromatic and aliphatic (Figure. S5, Figure. S6). In the aromatic region, multiple regions at δ 7.21–7.45 ppm were assigned for the protons integrated for anthracene rings and this region is exhibited in the ^{13}C spectrum as peaks at δ 123.45–144.06 ppm. In the aliphatic portion, there is a triplet signal at δ 4.44 ppm with a coupling constant J 0.8 Hz assigned for the protons integrated for carbon 10 (C10) and a doublet signal δ 4.72 ppm with a coupling constant J 0.8 Hz assigned for the protons integrated for carbon 9 (C9). These signals correspond to the peaks that appeared at δ 43.69 and 45.20 ppm in the ^{13}C spectrum, respectively; these signals are considered as one of the two markers indicating DA cycloaddition adduct **2b** (Figure. S5(b)). The multiplet signals that appeared at δ 1.99–2.06 and 2.11–2.18 ppm are assigned to the protons of

rings; in contrast, the C2 symmetry of the reactant 1,5-dichloroanthracene **3** could reduce the number of the product isomers. Computational calculations were in the same line, where three conformers were identified as presented in Table 1 and Figure 2. Different solvent systems were recruited to purify these isomers, among which the hexane: toluene (1:1) mixture was the best one. Unfortunately, the three isomers of aldehyde **2** could not be separated individually, so we have no chiral columns.

FIGURE 2: Conformational interconversion of the various minimum (C) and transition state (T) conformers of compound **2**.

carbon 11 (C11) that appeared at δ 28.76 ppm in the ^{13}C spectrum and the ^{1}H multiplet signal that appeared δ 2.77–2.84 ppm is assigned to the proton of carbon 12 (C12) that appeared at δ 51.22 ppm in ^{13}C spectrum. The aldehyde signal is considered as the second marker indicating DA cycloaddition adduct **2b,** and this signal represents the only aldehyde proton in the expected structure **2b** and appears as a doublet at δ 9.45 ppm with a coupling constant $J = 0.8$ Hz as well as ^{13}C NMR confirms the existence of aldehyde group (CHO) as a single peak at δ 202.73 ppm.

Reductive amination of the aldehyde **2** was achieved by using a combination of a commercially available solution of methylamine in methanol, molecular hydrogen, and Pd–C produced target amine 1. Generally, the two commonly used reductive amination protocols are based on either catalytic hydrogenation or hydride reducing agents; in contrast to hydride reducing agents, the use of molecular hydrogen is economically attractive [28–33]. The ^{1}H and ^{13}C NMR analysis of the target amine 1 is similar to its precursor 2 with slight differences but the signal of CHO disappeared in amine 1 and IR supported this finding (Figure 3), in addition to the appearance of singlet signal at δ 2.32 ppm that assigned to the methyl protons (-N-CH3) and correspond to the peak at δ 33.39 ppm in the ^{13}C NMR spectrum. For further structural elucidation of the target compound **1**, distortionless enhancement by polarization transfer (DEPT) and heteronuclear single quantum coherence spectroscopy (HSQC) were run and are presented in Table 2 and Figure S8, Figure S9, and Figure S10. It is well known that only CH groups appear as positive signals (↑CH) in the DEPT-90 spectrum, whereas in the DEPT-135 spectrum, CH$_3$ and CH groups appeared as positive signals (↑CH, ↑CH$_3$) but CH$_2$ groups appeared as negative signals (↓CH$_2$). The DEPT-90 spectrum of amine **1** shows three positive signals (↑CH) at δ

35.80, 43.73, and 46.05 ppm assigned to C12, C10, and C9, respectively (Figure. S8). The DEPT-135 spectrum shows four positive signals and two negative signals; among them, three positive signals were assigned to the three CH groups and the fourth positive one was assigned to the carbon of methyl group (CH$_3$) that appeared at δ 33.39 ppm, the two negative signals that appeared at δ 33.02 and 54.31 ppm were assigned to methylene groups (–CH$_2$–) of C11 and C1, respectively (Figure. S9).

HSQC experiments permit to obtain high-quality spectra of the protons attached to a specific carbon. According to the HSQC spectrum (Figure. S10), the structure of amine **1** is clearly elucidated and the H atoms that are attached to the carbon atoms are shown in Table 1. Interestingly, the two protons assigned to C11 have appeared in separate regions; one of them appeared at δ 1.25–1.28 ppm as multiple signals; although, it appeared as an overlapped triplet signal when enlarging this spectra region, and the other proton appeared at δ 1.95–2.11 ppm as multiple signals.

2.3. Extending the Side Chain of the Aldehyde **2** via the Wittig Reaction.

Aldehyde **2** was subjected to a Wittig olefination reaction employing two equivalents of the air-stable stabilized commercially available Wittig reagent (carbethoxymethylene) triphenylphosphorane (Scheme 2). The reaction was smoothly run at room temperature in dichloromethane (CH$_2$Cl$_2$) to give α,β-unsaturated ester 5 in 76% yield as a mixture of cis and trans isomers. The NMR J-coupling and chemical shift of the vinylic protons were recruited to differentiate between the cis and trans isomers. Based on the integration of the vinylic proton signals, the ratio of the cis and trans was approximately 1 : 3.5 (Figure. S11(a)–S11(c)). The ^{1}H-NMR spectrum of the trans isomer exhibited a
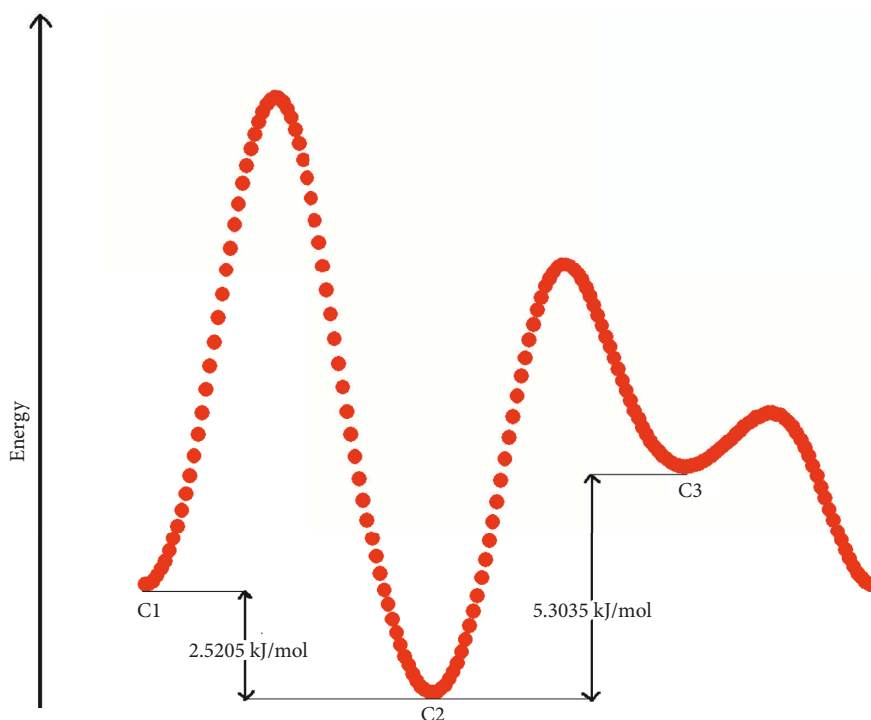
FIGURE 3: Binding modes of (a) the native ligand, desipramine, (b) standard drug, maprotiline, (c) compound 1, (d) compound **2**, (e) compound **5,** and (f) compound **6** and at the central binding site of LeuT.

TABLE 2: Energies (a.u.) of the predicted conformations of the compound **2**.

Parameter	2-C1	2-C2	2-C3
E_{Tot}	−1650.88155	−1650.88251	−1650.88049

doublet signal at δ 5.78 ppm with coupling constants $J = 25$ Hz assigned for olefinic proton attached to $C^{/}2$ (-C=**CH**–COOEt) and a double doublet signal at δ 6.45 ppm with coupling constant $J = 15, 5$ Hz assigned for an olefinic proton attached to $C^{/}1$ (-**CH**=C-) (Figure. S11(b)). The IR spectrum of the unsaturated ester **5** displayed characteristic absorption of the enone system at v 1650 cm^{-1} (C=C) together with the absorption peak of (C=O) at v 1709 cm^{-}1(Figure. S12). For further structural elucidation of compound **5**, HSQC were run and are presented in Figure. S13. α,β-unsaturated ester **5,** product of the Wittig reaction, was then subjected to selective hydrogenation to reduce (C=C) double bond using palladium on carbon (Pd/C) as catalyst under H$_2$ in ethanol at room temperature to obtain the saturated ester **6** in a yield of 42%. The NMR spectra of saturated ester **6** were clear where the signals of olefinic protons of the precursor **5** disappeared and instead, the triplet signal appeared at δ 2.33 ppm with coupling constant $J = 12$ Hz assigned for the protons attached to the $C^{/}2$ (-**CH$_2$**-COOEt) (Figure. S14). For further structural elucidation of saturated ester **6,** homonuclear correlation ^{1}H–^{1}H correlation, a double-quantum filtered correlation spectroscopy (DQF-COSY) technique was employed to assign proton chemical shifts (Figure. S15). HSQC experiments were performed to determine the protons attached to a specific

carbon (Figure. S16) and high-resolution mass spectroscopy (HRMS) was used to specify the molecular weight (Figure. S17). The NMR-based structural elucidations of these compounds were clear and valuable; however, the correlation study between experimental and theoretical NMR values will be more valuable than what is reported in the literature [34, 35].

2.4. DFT; Conformer Analysis. Conformational analysis of compound **2** revealed three minima and three transition states (Figure 2). The absence of imaginary frequencies on the calculated vibrational spectrum confirms the global minimum energy for all the conformers. Different conformers of compound **2** were found by carrying out a potential energy scan on the C–C bond connecting the aldehyde group (CHO) with the fused ring structure. The relative energies (kJ/mol) of different conformations are tabulated and are displayed in Table 2. The **2-C2** conformer was found to be the most stable, which is lower in energy than the other two conformers **2-C1** and **2-C3** by 2.5205 kJ/ mol and 5.3035 kJ/mol, respectively (Figure 4).

The low energy of the **2-C2** conformer may be the result of the electrostatic interaction between the electropositive region or σ hole of the chlorine atom, which serves as a Lewis acid, and the carbonyl oxygen, which serves as a Lewis base (Figure 4) and is analogous to a classical hydrogen bonding. This result is supported by the most "provisional recommendation" by IUPAC [36], which states that there is an interaction between the nucleophilic region of carbonyl oxygen and the electrophilic region of a halogen atom. More DFT confirmation and analysis of energy plane using TD-
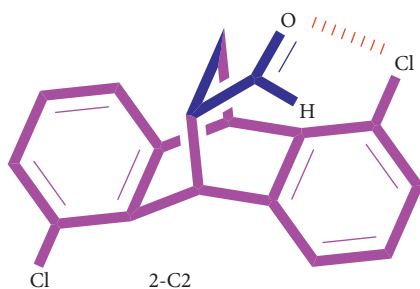
FIGURE 4: Plausible intramolecular interaction between chlorine (Cl) and oxygen (O) in **2-C2.**
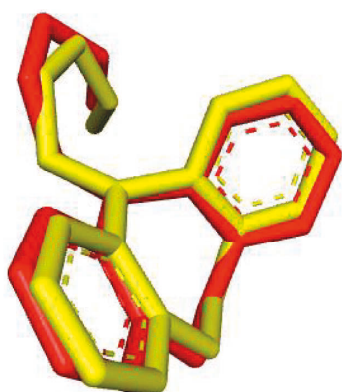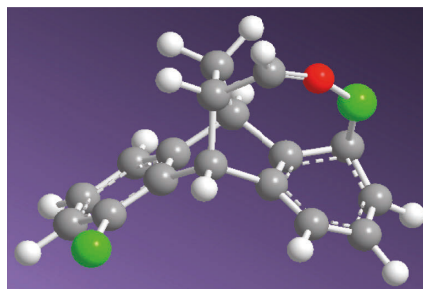
FIGURE 5: The docked pose (yellow) and the crystal structure conformation (red) of desipramine, the native ligand.
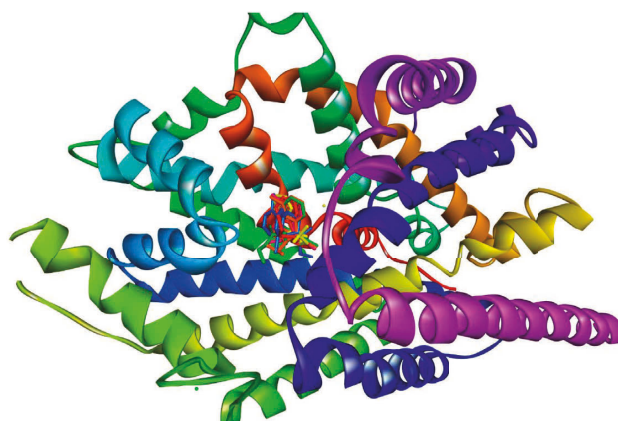
FIGURE 6: The docked structures of the co-crystallized ligand, desipramine (red), and standard drug maprotiline (yellow) along with the compounds **1** (orange), **2** (pink), **5** (green), and **6** (blue) in the binding site of LeuT.

DFT and UV-visible to know more about the conformer's differences are recommended [37, 38].

2.5. Molecular Docking. In order to verify the docking protocol, we have removed the co-crystallized ligand, desipramine, from the crystallized structure of LeuT and then redocked it at the same binding site. The root mean square deviation (RMSD) between the docked pose and the crystal structure conformation of desipramine was found to be less than 1 Å (Figure 5), which indicates the quality of the docking procedure [39]. All the compounds (**1, 2, 5,** and **6**) and the standard drug, maprotiline, were prepared for docking by minimizing their energies using the density function theory (DFT) at the B3LYP/6-311G(d, p) level of theory.

Among fifty docked confirmations obtained, one which has the lowest binding energies (−7.34 kcal/mol for compound **1**, −6.60 kcal/mol for compound **2**, −6.62 kcal/mol for compound **5**, −6.94 kcal/mol for compound **6** and 7.93 kcal/mol for the standard drug maprotiline) was selected for analyzing binding interactions within the active site of LeuT using Discovery Discover Studio Visualizer4.0 software [40] and Chimera [41]. The docked structure of the standard drug maprotiline, co-crystallized ligand, desipramine, and synthesized compounds (**1**, **2**, **5** and **6**) with LeuT crystal structure is shown in Figure 6. The binding poses and the interactions corresponding to the lowest energy conformations of the compounds at the central binding site of the LeuT protein are shown in Figure 7.

From Figures 7 and 8, it is clear that the amino acid residues responsible for the binding mechanism of all the derivatives in the active site are Arg30, Val33, Ile111, Ala319, and Phe320. As in the same manner by which the native ligand, desipramine and standard drug, maprotiline has the hydrogen bond interaction with Asp401, the amino group of compound **1** also forms a hydrogen bond with amino acid residue Asp401 in the binding site with a bond length of 1.97 Å. In the case of compounds **2**, **5,** and **6**, there are no observable hydrogen bonds with the amino acid residue ASP401. From the analysis of the binding mechanism, it is clear that all compounds **1**, **2**, **5**, and **6** show hydrophobic interactions with amino acid residues Arg30, Val33, Ile111, Ala319, and Phe320. The binding energy values and binding interactions show that all the compounds form stable complexes with the SERT protein by interacting with the important amino acids present in the central binding site similar to the native ligand, desipramine and the standard drug, maprotiline.

3. Experimental Methods

3.1. Chemistry Protocols. Most of the reagents and solvents were of analytical grade. Starting chemicals were purchased from Aldrich (Merck). A Perkin Elmer 240 elemental

(a)

(b)

(c)

(d)

(e)

(f)
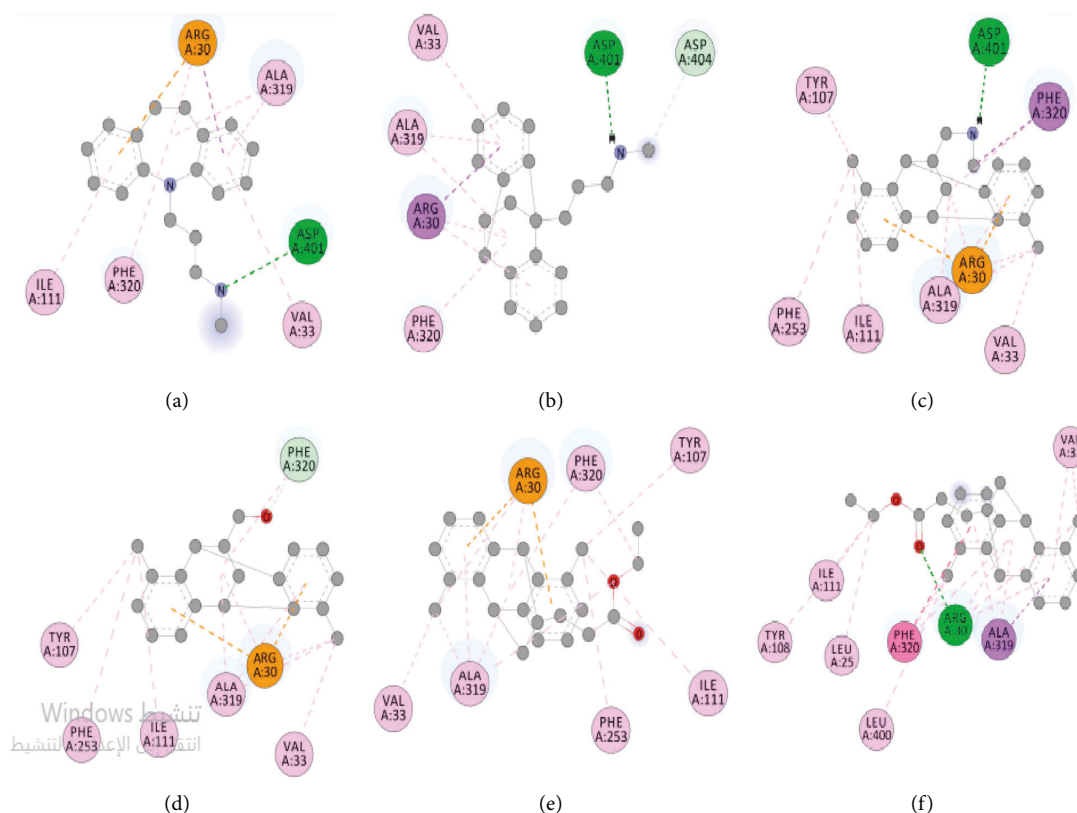
FIGURE 7: Potential energy scan profiles for the conformational interconversion of the conformers **2-C1**, **2-C2,** and **2-C3**.

analyzer was used to obtain the infrared (IR) spectrum. ^{1}H and ^{13}C-NMR spectra were recorded on either Joel 400 MHz or Bruker 500 MHz. Mass spectra (MS) and high-resolution mass spectra (HRMS) data were obtained on a Q-Tof Premier UPLC-MS. Reactions were monitored using thin-layer chromatography (TLC) plates (Merck, Germany), stained with valine and then spots were detected with a 254 nm UV lamp. Silica gel (35–70 mesh) was employed in column chromatography purification.

3.2. Synthesis

3.2.1. Synthesis of 1,5-Dichloroanthracene 3 [6, 42]. 1,5-Dichloroanthraquinone **4** (10.0 g, 36.1 mmol) and zinc dust (50.0 g, 765 mmol) were suspended in 200 mL of aqueous 28% NH_3 with stirring for 3 h at 100 degree Celsius. After cooling to r.t., the reaction mixture was separated by filtration and the filtrate was eluted and extracted several times with CH_2Cl_2. The CH_2Cl_2 organic phases were collected, dried over $MgSO_4$, filtered, and concentrated under a vacuum. To the residual crude, 500 mL isopropanol and 50 mL aqueous HC1 (12 M) were added. After refluxing the reaction mixture for 3 h, the mixture was cooled, concentrated in vacuo and then partitioned between CH_2Cl_2 and aqueous 5% $NaHC0_3$. The CH_2Cl_2 organic phase was collected, dried with $MgSO_4$, filtered, and concentrated to give crude 1,5-dichloroanthracene **3**. This crude was crystallized using a CH_2Cl_2-petroleum ether mixture. The product 1,5-

dichloroanthracene **3** was dried in the air for 24 h (7.5 g, 30.49 mmol) as yellow-orange needles in a 84.45% yield; mp 187–188 Celsius degree; IR (KBr): v = 681, 720, 736, 778, 849, 873, 903, 958, 996, 1145, 1162, 1212, 1300, 1449, 1530, and 1618 cm^{-1}; ^{1}H-NMR (CDCl$_3$, 400 MHz): δ = 7.40–7.61 (m, 4 H, ArH), 8.00 (dd; J = 2.92 Hz, 2 H, ArH), 8.42 (s, 1 H, ArH), 8.84 (s, 1 H, ArH) ppm. ^{13}C NMR (CDCl3, 100 MHz): δ = 124.37, 125.42, 125.58, 126.29, 128.24, 131.7, 132.8 ppm.

3.2.2. Synthesis of 1,5-Dichloro-9,10-dihydro-9,10-ethanoanthracene-12-carbaldehyde 2. Into a previously F02D15 Celsius degree cooled solution of 1,8-dichlorolanthracene **3** (500 mg, 2 mmol) in 70 mL CH_2Cl_2, acrolein (0.65 mL, 9.3 mmol) was added. Then, BF3·OEt2 (0.5 mL, 4.05 mmol) was added dropwise and the mixture was allowed to stir at -15 Celsius degree for 1 hour then at room temperature for 4 hours. The reaction was then quenched with sat. NaCl and extracted with CH_2Cl_2. The organic layers were collected, dried with Na_2SO_4, filtered and concentrated. The crude product was preliminary purified by column chromatography on silica gel using dichloromethane-petroleum ether (1 : 1) to obtain aldehyde **3** (450 mg, 1.49 mmol) as three isomeric adducts in a 74% yield; IR (KBr): v = 576, 706, 775, 1169, 1264, 1458, 1570, 1723, 2961, 3024,and 3047 cm^{-1}. A mixture of isomeric adducts (300 mg, 1 mmol) was separated by column chromatography on silica gel (1:1-hexane:toluene) to give the initially eluted two isomers of **2 (2a)** (160 mg, 0.53 mmol) as yellow viscous with the following

(a)

(b)

(c)

(d)

(e)

(f)
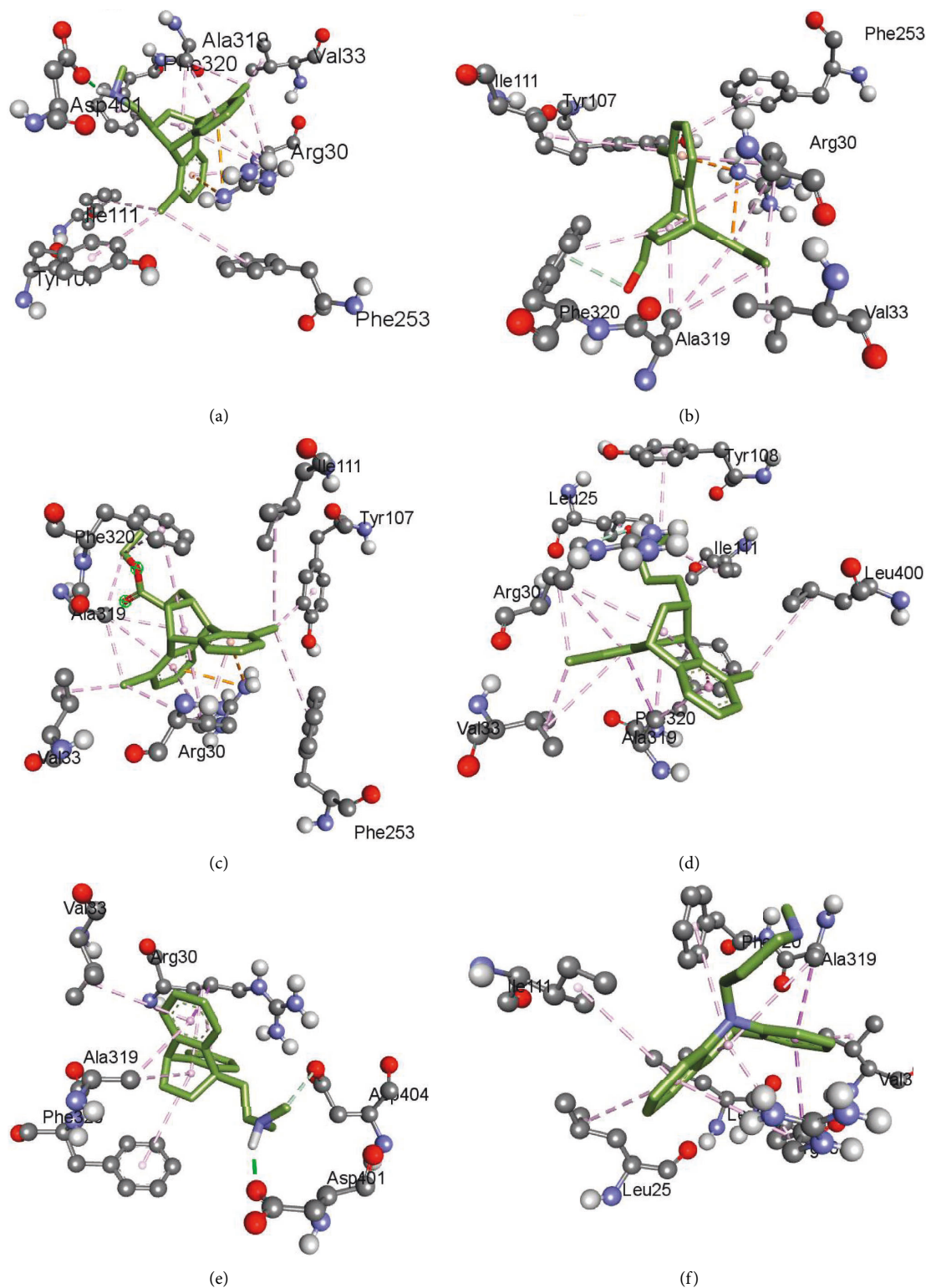
FIGURE 8: Binding modes of (a) compound **1**, (b) compound **2**, (c) compound **5,** (d) compound **6**, (e) standard drug maprotiline, and (f) the native ligand, desipramine at the central binding site of Leu T.

characteristics: ^{1}H-NMR (CDCl$_{3}$, 400 MHz): δ = 1.93–2.04 (m, 2H, H–C11), 2.14–2.22 (m, 2H, H–C11), 2.8–2.89 (m, 2H, H–C12), 4.93 (pent, J = 2.74 Hz, 2H H–C10), 5.26 (dd, J = 7.2, 2.45 Hz, 2H, H–C9), 7.1–7.47 (m, 12H, H–Ar), 9.52 (d, J = 0.8, ^{1}H, H–CHO), and 9.56 (d, J = 0.8, ^{1}H–CHO) ppm. ^{13}C NMR (CDCl3, 100 MHz): δ = 27.29, 27.32, 40.37, 41.50, 41.59, 49.87, 51.07, 122.45, 122.48, 122.56, 123.54, 123.77, 126.78, 127.11, 127.17, 127.24, 127.28, 127.50, 127.78, 129.35,

123.38, 129.57, 130.23, 136.58, 138.98, 140.61, 140.79, 140.94, 143.25, 145.08, 145.37, 200.91, 201.17 ppm, and a pure isomer of **2** (**2b**) (140 mg, 0.46 mmol) as a white solid with the following characteristics: ^{1}H-NMR (CDCl$_3$, 400 MHz): δ = 1.99–2.06 (m, ^{1}H, H–C11), 2.11–2.18 (m, ^{1}H, H–C11), 2.77–2.84 (m, ^{1}H, H–C12), 4.44 (t, J = 0.8 Hz, 1H, H–C10), 4.72 (d, J = 0.8 Hz, ^{1}H, H–C9), 7.21–7.45 (m, 6H, H–Ar), and 9.45 (d, J = 0.8, ^{1}H, H–CHO) ppm. ^{13}C NMR (CDCl3, 100 MHz): δ = 28.76, 43.69, 45.20, 51.22, 123.45, 123.51, 123.64, 124.53, 125.96, 125.99, 126.28, 126.55, 139.37, 142.12, 143.79, 144.06, and 202.73 ppm.

3.2.3. Synthesis of 1,5-Dichloro-9,10-dihydro-9,10-ethanoanthracen-12-yl)-N-methylmethanamine 1 [43].
To a 5° mL two-neck round-bottom flask connected to a condenser capped with a H$_2$ balloon and a rubber septum, a 100 mg Pd–C catalyst was added. The flask was evacuated and backfilled with H$_2$ two times. Then, a solution of aldehyde **2** (50 mg, 0.165 mmol) in methanol (3 mL) and (0.25 mL, 2 M) methylamine solution in methanol were added to the flask by syringe through a septum. After 1.5 h of the reaction time, the reaction mixture was filtered and washed with CH$_2$Cl$_2$, and the solvent was then removed to obtain amine **1** with the following characteristics: **IR (KBr):** v = 706, 740, 1266, 1422, 2987, 3055 cm^{-1}, ^{1}**H-NMR (CDCl$_3$, 500 MHz):** δ = 1.25–1.28 (m, ^{1}H, H–C11), 1.95–2.11 (m, ^{1}H, H–C11), 2.25–2.29 (m, 2H, H–C12, H–C1$^\prime$, CH$_2$), 2.32 (s, 3H, H–CH$_3$), 2.43–2.47 (m, ^{1}H, H–C1$^\prime$, CH$_2$), 4.29 (t, J = 2.12, ^{1}H, H–C10), 4.47 (d, J = 1.64, ^{1}H, H–C9), 7.07–7.17 (m, 3H, ArH), and 7.19–7.46 (m, 3H, ArH) ppm; **DEPT 90:** 35.80 ($\uparrow$CH), 43.73 (CH), and 46.05 ($\uparrow$CH); **DEPT 135:** 33.02 ($\downarrow$CH$_2$), 33.39 ($\uparrow$CH$_3$), 35.80 ($\uparrow$CH), 43.73 ($\uparrow$CH), 46.05 ($\uparrow$CH), and 54.31 ($\downarrow$CH$_2$) ppm; **MS (ES) *m/z* (%)** = 318 (100) [M$^+$], 284 (70), 250 (18), 184 (40), 117 (62), and 85 (40); **HRMS (ES)** Calcd for C$_{18}$H$_{18}$ NCl$_2$ [M$^+$] 318.0816, Found 318.0815.

3.2.4. Synthesis of Z/E-Ethyl 3-(1,5-dichloro-9,10-dihydro-9,10-ethanoanthracen-12-yl)-propenoate 5.
Into a 50-mL round-bottomed flask containing aldehyde **2** (755 mg, 2.5 mmol) predissolved in a 15 mL dichloromethane, a two equivalent Wittig reagent (carbethoxymethylene) triphenylphosphorane (174 mg, 5 mmol) was added. The reaction mixture was stirred overnight at room temperature; then, the solvent was removed to purify via silica gel column chromatography using the eluent system (ethyl acetate/petroleum ether, 1 : 20) obtaining unsaturated ester **5** as Z/E isomer (700 mg, 1.9 mmol, 76%) in ratio of 1 : 3.5, respectively, as a yellow oil with the following characteristics; **IR (KBr):** v = 650, 735, 909, 1036, 1097, 1170, 1240, 1271, 1305, 1369, 1461, 1650, 1709, 2254, 2875, 2971, and 3537 cm^{-1}; ^{1}**H-NMR (CDCl$_3$, 400 MHz):** δ = 1.15–1.35 (m, 6H, H–CH$_3$ (Z/E)), 1.45–1.52 (m, ^{1}H, H-11), 2.07–2.12 (m, ^{1}H, H-11), 2.73–2.80 (m, ^{1}H, H-12), 4.12–4.18 (q, J = 25, 2H), 4.22 (d, J = 5, 1H, H-9), 4.26 (q, J = 25, 2H), 4.34 (t, J = 3, ^{1}H, H-10), 4.35 (t, J = 2, ^{1}H, H-10), 5.78 (d, J = 25 Hz, ^{1}H), 6.45 (dd, J = 15, 5, ^{1}H), 7.1–7.19 (m, 6H, ArH), and 7.25–7.35 (m, 6H, ArH) ppm. For only (E) **HSQC** and ^{13}**C NMR (CDCl$_3$,**

100 MHz): δ = 14, 33.9 (CH$_3$), 43 (CH$_2$, C11), 40.09 (C12), 43 (C10), 48 (C9), 59.8 (-O–CH$_2$–), 120.7, 122.9, 123.2, 123.5, 125.03, 125.06, 125.08, 125.1, 134, 139.5, 143.4, 143.6, 143.9, 152, and 167 ppm; **HRMS (ES)** Calcd for C$_{21}$H$_{18}$ O$_2$Cl$_2$Na [*M*+] 395.0582, Found 395.0576.

3.2.5. Synthesis of Ethyl 3-(1,5-dichloro-9,10-dihydro-9,10-ethanoanthracen-12-yl)-propanoate 6.
A two-necked round-bottom flask containing Pd/C (70 mg, 10%) was wetted with ethanol. After evacuation and charging the flask with hydrogen (H$_2$, balloon) two times, a solution of unsaturated ester **5** (820 mg, 2.2 mmol) in 15 ml ethanol was added. The mixture was stirred overnight at room temperature under H$_2$, then filtered through celite with CH$_2$Cl$_2$. The solvent was removed in vacuo to obtain the saturated ester **6** (350 mg, 0.93 mmol, 42%) as yellow oil with the following characteristics; ^{1}**H-NMR (CDCl$_3$, 400 MHz):** δ = 1.15–1.2 (m, ^{1}H, H–C11), 1.21–1.30 (m, 4H; ^{1}H –C$^\prime$1, 3H, H–CH$_3$), 1.47–1.56 (m, ^{1}H, H–C$^\prime$1), 1.87–1.95 (m, ^{1}H, H–C12), 2–2.12 (m, ^{1}H, H–C11), 2.33 (t, J = 12, 2H, H–C$^\prime$2), 4.08 (q, J = 10 Hz, 2H, -O–CH$_2$–), 4.15 (d, J = 0.4 Hz, ^{1}H, H– C9), 4.26 (t, J = 2 Hz, ^{1}H, H–C10), 7.1–7.20 (m, 3H, ArH), and 7.25–7.35 (m, 3H, ArH) ppm; **HSQC (CDCl$_3$, 100 MHz):** δ = 14, 30.05 (CH$_3$), 30.05 (CH$_2$, C$^\prime$2), 31.15 (CH$_2$, C$^\prime$1), 34 (CH$_2$, C11), 38 (C10), 49 (C9), and 60 (CH$_2$, -O–CH$_2$–) ppm; **HRMS (ES)** Calcd for C$_{21}$H$_{20}$ O$_2$Cl$_2$Na [M$^+$] 397.0738, Found 397.0735.

3.3. Computational Details

3.3.1. DFT Calculations.
Density functional theory (DFT) calculations were performed using Gaussian 09 software [44] for identifying the possible conformers of compound **2**. A hybrid, nonlocal exchange, and correlation functional of Becke-Lee, Parr, and Yang (B3LYP) [45] has been used with the 6-311G (d, p) for DFT calculations. The lowest energy conformers have been obtained by detailed conformation search employing the potential energy scan method.

3.4. Molecular Docking.
The interactions of the ligands at the central binding site of LeuT were simulated using Autodock4.2 [46]. The crystal structure of the LeuT protein was downloaded from the Protein Databank [27] and was used as a target by removing all co-crystallized ligands. Discovery studio [25] and Chimera [41] were used to visualize and analyze the docked structures.

4. Conclusion

The synthesis of 1,5-dichloroethanoanthracenes (**2, 3, 5, 6**) has been successfully performed via multistep reactions involving the Diels–Alder and Wittig reactions. In order to identify the structures of the newly synthesized compounds clearly, the structural elucidation techniques, including COSY, HSQC, and HRMS, were extensively employed. The DFT calculations and the experimentally found isomers of aldehyde **2** were in good agreement. From the molecular docking, it can be concluded that all the synthesized

compounds have antidepressant activities and form stable complexes with LeuT by inhibiting the neurotransmitter reuptake at the synapse and hence are good candidates for use as antidepressant drugs. This study will pave way for the researchers to synthesize another 1,5-dichloroethanoanthracene and explore their biological activities as antidepressants, antimalarial agents, and antiproliferative agents.

5. Disclosure

An earlier version of this manuscript has been presented as preprint in Research Square according to the following link: https://www.researchsquare.com/article/rs-515953/v1 [47].

Data Availability

The data used to support the findings of this study are available from the corresponding author upon request.

Conflicts of Interest

The authors declare that they have no conflicts of interest.

Acknowledgments

Supplementary Materials

Supplementary Figure. S1. ^{1}H-NMR spectrum of the crude compound 2. Supplementary Figure. S2. IR spectrum of the crude compound 2. Supplementary Figure. S3 (a) ^{1}H-NMR spectrum of the 2a, (b) ^{1}H-NMR spectrum of the 2b, (c) Partial ^{1}H-NMR spectrum of the bridgehead protons (H–C9 and H–C10) of the 2a. Supplementary Figure. S4. ^{13}C NMR spectrum of the 2a. Supplementary Figure. S5 (a)) ^{1}H-NMR spectrum of the 2b, (b) Partial ^{1}H-NMR spectrum of the bridgehead protons (H–C9 and H–C10) of the 2b. Supplementary Figure. S6. ^{13}C NMR spectrum of the 2b. Supplementary Figure S7. IR Spectrum of the compound 1. Supplementary Figure S8. DEPT90 Spectrum of the compound 1. Supplementary Figure S9. DEPT135 Spectrum of the compound 1. Supplementary Figure. S10. HSQC spectrum of the compound 1. Supplementary Figure. S11 (a))^{1}H-NMR spectrum of the compound 5, (b) Partial ^{1}H-NMR of trans isomer 5 at vinylic protons (-CH=CH-), (c) Partial ^{1}H-NMR of trans isomer 5 at bridgehead protons (H–C9, H–C10) and methylene (-O–CH$_2$–CH$_3$) as quartet signals of both isomers 5 (cis/trans). Supplementary Figure. S12. IR spectrum of the compound 5. Supplementary Figure. S13. HSQC spectrum of the compound 5. Supplementary Figure. S14. ^{1}H-NMR spectrum of the compound 6. Supplementary Figure. S15. 1H–^{1}H COSY spectrum of the compound 6. Supplementary Figure. S16. HSQC spectrum of the compound 6. Supplementary Figure. S17. HRMS of the compound 6. (*Supplementary Materials*)

References

[1] O. Tosic and J. Mattay, *New Photochromic Dithienylethenes through a Click Chemistry Approach*, Wiley Online Library, Hoboken, USA, 2011.

[2] Q. P. B. Nguyen, J.-N. Kim, and T.-H. Kim, "Investigation of isomerism in anthracene-isothiouronium salts and application of these salts for anion sensing," *Bulletin of the Korean Chemical Society*, vol. 30, pp. 2093–2097, 2009.

[3] J. Langelaar, "Use of time-resolved excited state spectroscopy for selection of laser dyes," *Applied Physics*, vol. 6, no. 1, pp. 61–64, 1975.

[4] C. Schäfer, F. Strübe, S. Bringmann, and J. Mattay, "Photocyclizable resorcin [4] arene dimers," *Photochemical and Photobiological Sciences*, vol. 7, no. 12, pp. 1457–1462, 2008.

[5] J. J. Gassensmith, J. M. Baumes, J. Eberhard, and B. D. Smith, "Cycloaddition to an anthracene-derived macrocyclic receptor with supramolecular control of regioselectivity," *Chemical Communications*, no. 18, pp. 2517–2519, 2009.

[6] S. Bringmann, S. A. Ahmed, R. Hartmann, and J. Mattay, "Synthesis of 1, 5-Substituted Anthracenes by Means of Kumada Coupling and Their Derivatization," *Synthesis*, vol. 2011, pp. 2291–2296, 2011.

[7] I. P. Beletskaya, A. G. Bessmertnykh, A. D. Averin, F. Denat, and R. Guilard, "Palladium-catalysed amination of 1, 8-and 1, 5-dichloroanthracenes and 1, 8-and 1, 5-dichloroanthraquinones," *European Journal of Organic Chemistry*, vol. 2005, no. 2, pp. 281–305, 2005.

[8] E. R. Ranyuk, A. D. Averin, A. K. Buryak et al., "Palladium-catalyzed amination in the synthesis of macrocyclic compounds containing 1, 3-disubstituted adamantane fragments," *Russian Journal of Organic Chemistry*, vol. 45, no. 10, pp. 1555–1566, 2009.

[9] I. P. Beletskaya and A. D. Averin, "Palladium-catalyzed arylation of linear and cyclic polyamines," *Pure and Applied Chemistry*, vol. 76, no. 9, pp. 1605–1619, 2004.

[10] C. F. Chen, Y. X. Ma, and Z. Meng, "Synthesis of substituted iptycenes," *Synlett*, vol. 26, no. 1, pp. 6–30, 2014.

[11] I. Mori, T. Kadosaka, Y. Sakata, and S. Misumi, "Synthesis and spectral properties of chloro-substituted triptycenes," *Bulletin of the Chemical Society of Japan*, vol. 44, no. 6, pp. 1649–1652, 1971.

[12] J.-H. Lamm, J. Glatthor, J.-H. Weddeling et al., "Polyalkynylanthracenes–syntheses, structures and their behaviour towards UV irradiation," *Organic and Biomolecular Chemistry*, vol. 12, no. 37, pp. 7355–7365, 2014.

[13] H. Muhammad, M. Hanif, I. A. Tahiri et al., "Electrochemical behavior of superoxide anion radical towards quinones: a mechanistic approach," *Research on Chemical Intermediates*, vol. 44, no. 10, pp. 6387–6400, 2018.

[14] R. F. Chen, Y. C. Shen, H. S. Huang et al., "Evaluation of the anti-inflammatory and cytotoxic effects of anthraquinones and anthracenes derivatives in human leucocytes," *Journal of Pharmacy and Pharmacology*, vol. 56, no. 7, pp. 915–919, 2010.

[15] R.-F. Chen, C.-L. Chou, M.-R. Wang et al., "Small-molecule anthracene-induced cytotoxicity and induction of apoptosis through generation of reactive oxygen species," *Biological & Pharmaceutical Bulletin*, vol. 27, no. 6, pp. 838–845, 2004.

[16] S. M. Cloonan and D. C. Williams, "The antidepressants maprotiline and fluoxetine induce Type II autophagic cell death in drug-resistant Burkitt's lymphoma," *International Journal of Cancer*, vol. 128, no. 7, pp. 1712–1723, 2011.

[17] Y. McNamara, S. Bright, A. Byrne et al., "Synthesis and antiproliferative action of a novel series of maprotiline

analogs," *European Journal of Medicinal Chemistry*, vol. 71, pp. 333–353, 2014.

[18] M. Wilhelm and P. Schmidt, "Synthesis and properties of 1-aminoalkyl-dibenzo(b, e)bicyclo(2, 2, 2) octadienes," *Helvetica Chimica Acta*, vol. 52, no. 6, pp. 1385–1395, 1969.

[19] N. M. Gray and P. C. Contreras, "Use of bridged tricyclic amine derivatives as anti-ischemic agents," 1991, https://patents.google.com/patent/US5055468A/en.

[20] H. P. Schroeter and Daniel, "Verfahren zur Herstellung von 11-Aminoalkyl-9,10-dihydro-9,10-äthano-anthracenen," 1969, https://www.google.com/search?q=Verfahren+zur+Herstellung+von+11-Aminoalkyl-9%2C10-dihydro-9%2C10-%C3%A4thano-anthracenen&rlz=1C1GCEB_enIN993IN993&oq=Verfahren+zur+Herstellung+von+11-Aminoalkyl-9%2C10-dihydro-9%2C10-%C3%A4thano-anthracenen&aqs=chrome..69i57.339j0j4&sourceid=chrome&ie=UTF-8.

[21] H. Schroter and D. A. Prins, "10-dihydro-11-amino-alkylene-9, 10-ethanoanthracenes," 1969, https://pubchem.ncbi.nlm.nih.gov/compound/601095#section=3D-Conformer.

[22] W. Friebe, U. Tibes, and W. Scheuer, "9, 10-Dihydro-9, 10-ethanoanthracene derivatives as phospholipase inhibitors," 1999, https://patentscope.wipo.int/search/en/detail.jsf?docId=WO1999015493.

[23] K. Nagayasu, "Serotonin transporter: recent progress of in silico ligand prediction methods and structural biology towards structure-guided in silico design of therapeutic agents," *Journal of Pharmacological Sciences*, vol. 148, no. 3, pp. 295–299, 2022.

[24] M. Jarończyk and J. Walory, "Novel molecular targets of antidepressants," *Molecules*, vol. 27, no. 2, p. 533, 2022.

[25] J. A. Coleman and E. Gouaux, "Structural basis for recognition of diverse antidepressants by the human serotonin transporter," *Nature Structural & Molecular Biology*, vol. 25, no. 2, pp. 170–175, 2018.

[26] B. A. Davis, A. Nagarajan, L. R. Forrest, and S. K. Singh, "Mechanism of paroxetine (paxil) inhibition of the serotonin transporter," *Scientific Reports*, vol. 6, pp. 23789–23813, 2016.

[27] Z. Zhou, J. Zhen, N. K. Karpowich et al., "LeuT-desipramine structure reveals how antidepressants block neurotransmitter reuptake," *Science*, vol. 317, no. 5843, pp. 1390–1393, 2007.

[28] A. Robichaud and A. Nait Ajjou, "First example of direct reductive amination of aldehydes with primary and secondary amines catalyzed by water-soluble transition metal catalysts," *Tetrahedron Letters*, vol. 47, no. 22, pp. 3633–3636, 2006.

[29] A. F. Abdel-Magid, K. G. Carson, B. D. Harris, C. A. Maryanoff, and R. D. Shah, "Reductive amination of aldehydes and ketones with sodium triacetoxyborohydride. Studies on direct and indirect reductive amination procedures1," *Journal of Organic Chemistry*, vol. 61, no. 11, pp. 3849–3862, 1996.

[30] B. T. Cho and S. K. Kang, "Direct and indirect reductive amination of aldehydes and ketones with solid acid-activated sodium borohydride under solvent-free conditions," *Tetrahedron*, vol. 61, no. 24, pp. 5725–5734, 2005.

[31] C. Guyon, E. Da Silva, R. Lafon, E. Métay, and M. Lemaire, "Reductive amination using a combination of CaH 2 and noble metal," *RSC Advances*, vol. 5, no. 3, pp. 2292–2298, 2015.

[32] A. Heydari, A. Arefi, and M. Esfandyari, "Direct reductive amination of aldehydes and selective reduction of α, β-unsaturated carbonyl compounds by NaBH 4 in the presence of guanidine hydrochloride in water," *Journal of Molecular Catalysis A: Chemical*, vol. 274, pp. 169–172, 2007.

[33] S. Pisiewicz, T. Stemmler, A. E. Surkus, K. Junge, and M. Beller, "Synthesis of amines by reductive amination of aldehydes and ketones using Co_3O_4/NGr@ C catalyst," *ChemCatChem*, vol. 7, no. 1, pp. 62–64, 2015.

[34] A. I. Khodair, S. E. Kassab, N. A. Kheder, and A. M. Fahim, "Synthesis of novel d-α-galactopyranosyl-l-seryl/l-threonyl-l-alanyl-l-alanine as useful precursors of new glycopeptide antibiotics with computational calculations studies," *Carbohydrate Research*, vol. 514, Article ID 108546, 2022.

[35] A. M. Fahim, H. S. Magar, E. Nasar, F. M. Abdelrazek, and A. Aboelnaga, "Synthesis of Cu-porphyrazines by annulated diazepine rings with electrochemical, conductance activities and computational studies," *Journal of Inorganic and Organometallic Polymers and Materials*, vol. 32, no. 1, pp. 240–266, 2022.

[36] M. Kolář, P. Hobza, and A. K. Bronowska, "Plugging the explicit σ-holes in molecular docking," *Chemical Communications*, vol. 49, no. 10, pp. 981–983, 2013.

[37] A. M. Fahim, A. Mohamed, and M. A. Ibrahim, "Experimental and theoretical studies of some propiolate esters derivatives," *Journal of Molecular Structure*, vol. 1236, Article ID 130281, 2021.

[38] A. M. Fahim, M. A. Shalaby, and M. A. Ibrahim, "Microwave-assisted synthesis of novel 5-aminouracil-based compound with DFT calculations," *Journal of Molecular Structure*, vol. 1194, pp. 211–226, 2019.

[39] B. Kramer, M. Rarey, and T. Lengauer, "Evaluation of the FLEXX incremental construction algorithm for protein–ligand docking," *Proteins: Structure, Function, and Genetics*, vol. 37, no. 2, pp. 228–241, 1999.

[40] D. S. Biovia, *Discovery Studio Modeling Environment*, DassaultSystèmes, 2016.

[41] E. F. Pettersen, T. D. Goddard, C. C. Huang et al., "UCSF Chimera—a visualization system for exploratory research and analysis," *Journal of Computational Chemistry*, vol. 25, no. 13, pp. 1605–1612, 2004.

[42] A. Sanyal, "Chiral anthracenes as Diels-Alder/retro Diels-Alder templates in asymmetric synthesis," 2002, https://www.proquest.com/openview/97bbfcee7423d2a3258220ec70081a5c/1?pq-origsite=gscholar&cbl=18750&diss=y.

[43] U. Karama, M. A. Sultan, A. I. Almansour, and K. E. El-Taher, "Synthesis of chlorinated tetracyclic compounds and testing for their potential antidepressant effect in mice," *Molecules*, vol. 21, no. 1, p. 61, 2016.

[44] M. J. Frisch Gwt, H. B. Schlegel, G. E. Scuseria et al., *Gaussian 09W Reference*, Gaussian, Inc, Wallingford CT, 2009.

[45] A. D. Becke, "Density-functional thermochemistry. III. The role of exact exchange," *The Journal of Chemical Physics*, vol. 98, no. 7, pp. 5648–5652, 1993.

[46] G. M. Morris, R. Huey, W. Lindstrom et al., "AutoDock4 and AutoDockTools4: automated docking with selective receptor flexibility," *Journal of Computational Chemistry*, vol. 30, no. 16, pp. 2785–2791, 2009.

[47] *Mujeeb Sultan RRP EAea 1,5-Dichloroethanoanthracene Derivatives as Antidepressant Maprotiline Analogs: Synthesis and DFT Computational Calculations*, 2021.

Research Article

Phytochemical Investigation of Egyptian Riverhemp: A Potential Source of Antileukemic Metabolites

Shimaa M. Abdelgawad [1,2] **Mona H. Hetta**,[2] **Mohamed A. Ibrahim**,[1]
Premalatha Balachandran,[1] **Jin Zhang**,[1] **Mei Wang**,[3] **Wagdy M. Eldehna**,[4,5]
Ghada A. Fawzy,[6] **Hesham I. El-Askary**,[6] **and Samir A. Ross** [1,7]

[1]*National Center for Natural Products Research, Research Institute of Pharmaceutical Sciences, School of Pharmacy, University of Mississippi, Oxford, USA*
[2]*Pharmacognosy Department, Faculty of Pharmacy, Fayoum University, Fayoum 63514, Egypt*
[3]*National Center for Natural Products Research, Agricultural Research Service, United States Department of Agriculture, University of Mississippi, Oxford, USA*
[4]*School of Biotechnology, Badr University in Cairo, Badr 11829, Egypt*
[5]*Department of Pharmaceutical Chemistry, Faculty of Pharmacy, Kafrelsheikh University, Kafrelsheikh 33516, Egypt*
[6]*Pharmacognosy Department, Faculty of Pharmacy, Cairo University, Giza, Egypt*
[7]*Biomolecular Sciences, Division of Pharmacognosy, School of Pharmacy, University of Mississippi, Oxford, USA*

Correspondence should be addressed to Ghada A. Fawzy; ghada.ah.fawzy@pharma.cu.edu.eg and Samir A. Ross; sross@olemiss.edu

As part of our research group's continuous efforts to find alternative treatments for cancer, the aqueous ethanol extract of *Sesbania sesban* L. Merr. (*SS*, Egyptian riverhemp) demonstrated an antileukemic activity against K562 cell line. Bioguided fractionation of *SS* leaves hydroethanolic extract resulted in the isolation of one new compound (33) named as hederatriol 3-*O*-β-D-glucuronic acid methyl ester as well as 34 known compounds. Seven compounds ((34), (22), (20), (24), (21), (19), and (35)) showed high antiproliferative effects (IC$_{50}$ = 22.3, 30.8, 31.3, 33.7, 36.6, 37.5, and 41.5 μM, respectively), while four compounds ((32), (5), (29), and (1)) showed milder activities (IC$_{50}$ = 56.4, 67.6, 83.3, and 112.3 μM, respectively). A mechanistic study was further carried out on a molecular genetics level against several transcription factors signaling pathways that are incorporated in the incidence of cancer. The results showed that compounds (22) and (21) demonstrated a specific inhibition of Wnt pathway (IC$_{50}$ = 3.8 and 4.6 μM, respectively), while compound (22) showed a specific inhibition of Smad pathway (IC$_{50}$ = 3.8 μM). Compound (34) strongly altered the signaling of Smad and E2F pathways (IC$_{50}$ = 5 μM). The bioactive metabolites were further investigated *in silico* by docking against several targets related to K562 cell line. The results showed that compounds (22) and (34) exhibited a strong binding affinity towards topoisomerase (docking score = −7.81 and −9.30 Kcal/Mole, respectively). Compounds (22) and (34) demonstrated a strong binding affinity towards EGFR-tyrosine kinase (docking score = −7.12 and −7.35 Kcal/Mole, respectively). Moreover, compound (34) showed a strong binding affinity towards Abl kinase (docking score = −7.05 Kcal/Mole).

1. Introduction

In our previous study, the antileukemic activities of 56 medicinal plants grown in Upper Egypt were checked, where *Sesbania sesban* (*SS*) leaves extract demonstrated a promising antileukemic activity against the chronic myeloid leukemia cell line (K562) [1]. Considering the limited studies on the phytoconstituents of *SS* leaves, we carried out this research with the aim of bioguided isolation of the antileukemic metabolites from *SS* leaves.

Chronic myeloid leukemia (CML) is the third most regular mortality-causing neoplasm and the fourth predominant cancer among the Egyptian population [2, 3]. CML has a trademark and explicit chromosomal irregularity known as Philadelphia (Ph) chromosome (Bcr-Abl gene) that is produced from a reciprocal translocation between the Abl gene on chromosome 9 and the Bcr gene on chromosome 22 in the pluripotent hematopoietic stem cells [4].

The value of natural products in the arsenal of leukemia therapies is clearly correlated with several agents such as L-asparaginase, Daunorubicin, Anthracyclines, Vinca alkaloids (Vincristine and Vinblastine) [5, 6], Homoharringtonine, Indirubin, Flavopiridol, Maytansinoids, Meisoindigo [6], and the Podophyllotoxin derivatives (Etoposide and Teniposide) [7, 8].

S. sesban (Egyptian riverhemp or *Sesbania aegyptiaca* Pers.) is a perennial legume tree belonging to family Fabaceae (Figure 1). It has several names like *Aeschynomene aegyptiaca* (Pers.) Steud., *Aeschynomene sesban* L., *Sesbania confaloniana* Chiov., *Sesbania pubescens* sensu auct., *Sesbania punctata* DC., and *Emerus sesban* (L.) Kuntze [9].

Traditionally, *SS* leaves were used as a poultice for inflammatory conditions such as boils and abscesses as well as rheumatic swellings, and the juice of the fresh leaves was used as anthelmintic [10–12].

The methanolic extract of *SS* leaves exhibited several biological activities such as anti-inflammatory [13], antioxidant [14], molluscicidal [15, 16], antidiabetic [17], potent spermicidal [18], antimicrobial [16], and anthelmintic activities [10–12]. Phytochemical analyses of the leaves showed the presence of steroids such as β-sitosterol and campesterol [13], triterpenoids such as betulinic and oleanolic acids [13, 19, 20], saponins of oleanolic acid [15, 18], and flavonoids [21].

The aim of this study is to isolate the antileukemic metabolites of *SS* leaves through extensive biological and phytochemical investigations.

2. Materials and Methods

2.1. General Experimental Procedures. High-resolution electrospray ionization mass spectrometry (HRESIMS) data were acquired using a Bruker BioApex-FTMS with electrospray ionization (ESI). 1D (^{1}HNMR, DEPTQ) and 2D (HSQC, HMBC, and TOCSY) NMR spectra were recorded on a Bruker 400 and 500 MHz spectrometer. Optical activity was measured using AA-65 series automatic polarimeter (Cambridgeshire, PE26 1NF, England). HPLC analysis was conducted using an Agilent 1100 HPLC system (Supplementary Materials). GC-MS analysis was performed with an Agilent 7890B gas chromatograph (Supplementary Materials). Sephadex LH-20 (Mitsubishi Kagaku, Tokyo, Japan) and silica gel (60–120 μM·mesh, Merck, Darmstadt, Germany), reversed phase silica (40–63 μM, Sorbent Technologies, 5955 Peachtree Corners East, Suite A, Norcross, GA 30071 USA), and Diaion® HP-20 (250 μm, Supelco, Bellefonte, PA 16823-00048, USA) were used for column chromatography (CC). SPE cartridges silica gel and C18 (Supelco Inc., Bellefonte, PA, USA) were used in the fractionation

FIGURE 1: Entire *Sesbania sesban* branch.

work. Fractions from CC were monitored by TLC using precoated aluminum sheets (silica 60 F254, 0.25 mm (Merck, Darmstadt, Germany)). The fractions were dissolved in the appropriate solvents and spots were applied manually using the capillary micropipette, and the plates were then dried and developed in different mobile phase systems such as *n*-hexane: ethyl acetate (8 : 2), *n*-hexane: acetone (8 : 2), and DCM: methanol (9 : 1). The spots on the developed plates were detected using UV light (254 and 366 nm) and by spraying with 2% *p*-anisaldehyde-H_2SO_4 reagent followed by heating for 5–10 min (105°C). Number of spots, colors, and retardation factors (Rf values) for each of the spots were determined and recorded [22].

2.2. Plant Material. The leaves of *Sesbania sesban* were purchased from the medicinal, aromatic, and poisonous plants experimental station, Faculty of Pharmacy, Cairo University, Egypt, in April 2018. The plant material was authenticated by Professor Dr. Abdelhalim Mohamed, Flora and Phytotaxonomy Research Department, Horticulture Research Institute (HRI), Agricultural Research Center, Giza, Egypt. A voucher specimen (FUPD-45) was kept at the Herbarium of Pharmacognosy Department, Faculty of Pharmacy, Fayoum University, Egypt.

2.3. Extraction and Bioguided Isolation. The shade-dried leaves (1 kg) were grounded and extracted with 75% ethanol at room temperature three times 24 h each. The total extract was concentrated to afford a crude residue (177 g). 83 g of the 75% ethanolic extract was suspended in water and exposed to successive fractionation using *n*-hexane and EtOAc to afford 9 g and 12 g, respectively. The remaining aqueous fraction was lyophilized to afford 61 g. All fractions were phytochemically investigated and tested against K562 cell line. The bioactive fractions were subjected to bioguided isolation techniques as described in the consequent text.

The *n*-hexane fraction (6 g) of *SS* leaves was saponified according to the published procedure [23] and the fatty acid

methyl ester (FAME) and unsaponifiable matter (USM) were then subjected to GC/MS analysis. USM (78.8 mg) was chromatographed on silica gel column by gradient elution with n-hexane/EtOAc (2.5% gradient) to give 9 subfractions (A1–A9). **Fr-A-6** (eluted by 7.5% EtOAc) was one spot on TLC and afforded compound 1 (11 mg). **Fr-A-8** (eluted by 10% EtOAc) was one spot on TLC and afforded compound 2 (25 mg).

The EtOAc fraction (10 g) was chromatographed on a silica gel solid phase extraction (Si-SPE) column by gradient elution with n-hexane/EtOAc to give fractions (B1–B5). The subfraction **Fr-B-2** (520 mg) was first subjected to silica gel SPE column chromatography and eluted with n-hexane/EtOAc gradient (2% gradient) to afford 5 subfractions. Subfraction **Fr-B-2-2** was further purified using silica gel column and eluted with n-hexane/EtOAc (2.5% gradient) to afford compound (3) (5 mg) (eluted by 10% EtOAc). The subfraction **Fr-B-2-4** was further chromatographed on silica gel column and eluted with n-hexane/acetone (2.5% gradient) to afford compounds (4) (1 mg), (5) (15.6 mg), (6) (1 mg), and (7) (2.5 mg) (eluted by 7.5%, 10%, 12.5%, and 15% acetone, respectively). The subfraction **Fr-B-5** (4.5 g) was chromatographed on VLC silica gel column by gradient elution with DCM/MeOH (2.5% gradient) to afford 5 subfractions. **Fr-B-5-4** (614.8 mg) (eluted by 20% MeOH) was subjected to a column of Sephadex LH-20 and eluted with methanol to give 8 subfractions. **Fr-B-5-4-5** (164.2 mg) was chromatographed on a silica gel column and eluted with DCM/MeOH (2.5% gradient) to afford compound (8) (8 mg) (eluted by 25% MeOH). **Fr-B-5-4-6** (46 mg) was subjected to a column chromatography on Sephadex LH-20 and eluted with MeOH to give compound (9) (2 mg). **Fr-B-5-4-8** (34.3 mg) was subjected to column chromatography on a Sephadex LH-20 and eluted with MeOH to give compounds (10) (14.5 mg), (11) (11 mg), (12) (4 mg), and (13) (3 mg). **Fr-B-5-5** (2.35 g) was subjected to a column of Sephadex LH-20 and eluted with methanol to afford 8 subfractions. **Fr-B-5-5-4** (358 mg) was subjected to a column of Sephadex LH-20 and eluted with methanol to afford 5 subfractions. **Fr-B-5-5-4-3** (27 mg) was purified by HPLC RP column and eluted with water/methanol gradient to afford compounds (14) (20 mg) and (15) (2.36 mg) at retention times (RT) = 9.8 and 10.3 minutes, respectively (Fig. S1, Supplementary Materials). **Fr-B-5-5-4-5** (30 mg) was purified by HPLC RP column and eluted with water/methanol gradient to afford compounds (16) (15 mg) and (17) (3 mg) at RT = 8.0 and 8.29 minutes, respectively (Fig. S2, Supplementary Materials). **Fr-B-5-5-6** (80 mg) was chromatographed on a silica gel column by gradient elution with DCM/MeOH (2.5% gradient) to afford compound (18) (6 mg) (eluted by 25% MeOH).

The aqueous fraction (60.0 g) was subjected to a column chromatography using HP-20 ion exchange resin and eluted with MeOH/water (25% gradient) to afford five fractions (C1–C5). **Fr-C-5** (5 g) (eluted by 100% MeOH) was further chromatographed on a silica gel column by gradient elution with DCM/MeOH (2.5% gradient) to afford 9 subfractions. **Fr-C-5-2** (511 mg) (eluted by 2.5% MeOH) was further chromatographed on a silica gel column using gradient

elution with DCM/EtOAc (5% gradient) to afford compounds (19) (17.7 mg), (20) (33.3 mg), (21) (5 mg), (22) (8 mg), (23) (2 mg), (24) (52 mg), (25) (1.9 mg), and (26) (1.7 mg). **Fr-C-5-4** (511 mg) was chromatographed on RP-18-silica gel column by gradient elution with MeOH/water (5% gradient) to give four subfractions. **Fr-C-5-4-1** (7 mg) was purified by RP-18 preparative HPLC to give compounds (27) (20 mg) and (28) (6 mg) at retention times (RT) = 17.17 and 18.14 minutes, respectively (Fig. S3, Supplementary Materials). **Fr-C-5-4-3** (198 mg) was chromatographed on a silica gel column using DCM/MeOH (5% gradient) to afford compounds (29) (45 mg), (30) (2 mg), (31) (2 mg), (23) (3 mg), (33) (2 mg), and (34) (22.5 mg). **Fr-C-5-5** (672 mg) was chromatographed on reversed phase silica gel solid phase extraction (RP-SPE) column by gradient elution with MeOH/water (5% gradient) to give four subfractions. **Fr-C-5-5-2** (400 mg) was further chromatographed on a silica gel column by gradient elution with DCM/MeOH (5% gradient) to afford compound (35) (64.8 mg).

Compounds (1)–(35) were identified using ^{1}HNMR, DEPT-Q, HSQC, HMBC, and HRESIMS spectroscopic techniques as well as comparing these data with the literature.

2.4. Hederatriol 3-O-β-D-Glucuronic Acid Methyl Ester (33).
White powder (MeOH), $[\alpha]^{25°}_D$ = +34.5 (c = 0.15 in MeOH). ^{1}H and DEPT-Q data (Table 1); HRESIMS m/z 649.45082 $[M+H]^+$ (calcd. $C_{37}H_{61}O_9$ m/z 649.43156).

2.5. Cytotoxicity Assay.
K562 cells from the American Type Culture Collection (ATCC) were plated in clear 384-well plates at an initial density of 2500 cells/well in 40 μL of growth medium (DMEM with 10% FBS and 1% Pen/step). Next day, the test agents were added in quadruplicates at the specified concentration and the treatment continued for 48 h and the cell viability was finally assessed using WST-8 assay Cell Counting Kit from Bimake, according to manufacturer's instructions. The results were calculated by measuring the absorbance at 450 nm using SpectraMax M5 plate reader (Molecular Devices). Cell viability was calculated in comparison to DMSO as a negative control, as well as Taxol and Doxorubicin as positive controls [24]. The extract and fractions were screened primarily at concentrations of 50 and 75 μg/mL and the percentage inhibitions were calculated. Compounds (1)–(35) were tested at six concentrations (5, 10, 25, 50, 75, and 100 μg/mL), where compounds (1), (5), (19), (20), (21), (22), (24), (29), (32), (34), and (35) were shown to be bioactive and their IC_{50} values were calculated.

2.6. Transfection and Luciferase Assays.
Hela cells from ATCC were plated in white opaque 384-well plates at a density of 4300 cells/well in 30 μL of growth medium (DMEM with 10% FBS and 1% Pen/step). Next day, the medium was aspirated and replaced with DMEM containing 1% FBS. The cells were transfected with respective plasmids [25] using X-tremeGENE HP transfection reagent (Roche). After 24 h of transfection, the test agents were added in duplicates to the transfected cells, followed 30 min later by

TABLE 1: NMR data for compound (33) (500 MHz in DMSO-d_6).

Position	δ_C, type	δ_H (J in Hz)	HMBC	TOCSY
1	38.4, CH_2	0.82		2, 3
2	25.5, CH_2	1.59, 1.68		3
3	80.4, CH	3.50	$1'$	1
4	42.8, C			
5	46.4, CH	1.17	6	
6	17.6, CH_2	1.39		
7	32.7, CH_2	1.50		
8	39.2, C			
9	41.3, CH	2.77		
10	36.4, C			
11	23.3, CH_2	1.80, 1.88		12
12	121.7, CH	5.76		11, 18
13	144.6, C			
14	41.8, C			
15	27.7, CH_2	0.97, 1.61	27	
16	22.5, CH_2	1.41		15
17	45.9, C	-		
18	47.5, CH	1.51		
19	46.3, CH_2	1.59	12, 29, 30	28
20	30.9, C	-		
21	33.9, CH_2	1.41		28
22	32.4, CH_2	1.44		28
23	13.3, CH_3	0.59	3, 4, 5, 24	
24	62.8, CH_2	3.07, 3.44 (d, $J = 10.5$ Hz)	3	
25	16.0, CH_3	0.87	10, 11	9
26	17.4, CH_3	0.71	8, 14	
27	26.0, CH_3	1.09	8, 13, 14, 15	
28	70.2, CH_2	3.51 (S)	16, 18	18
29	23.9, CH_3	0.87	20, 30	
30	33.3, CH_3	0.86	18, 20	
$1'$	105.1, CH	4.33 (d, $J = 8$ Hz)	3	$2', 3', 4', 5'$
$2'$	74.1, CH	2.98 (t, $J = 8.5$ Hz)	$1', 5'$	$1', 4'$
$3'$	75.9, CH	3.16 (t, $J = 9$ Hz)	$4'$	$1', 2', 5'$
$4'$	72.1, CH	3.28 (t, $J = 9.5$ Hz)	$2'$	$1', 2', 5'$
$5'$	76.4, CH	3.65	$1'$	$1', 2', 3'$
$6'$	170.1, C			
$7'$	52.3, CH_3	3.67 (s)	$6'$	$2', 3', 4'$

an inducing agent (IL-6 for Stat 3, TGF-β for Smad, m-Wnt3a for Wnt, and PMA for AP-1, NFk-B, E2F, Myc, ETS, Notch, and Hedgehog). No inducer was added for pTK, FOXO, miR-2, K-Ras, and AhR. After 4 h or 6 h of induction, the cells were lysed by the addition of One-Glo luciferase assay system (Promega, Madison, WI, USA). The light output was detected in a GloMax-Multi+ Detection System with Instinct Software (Promega, Madison, WI, USA). This luciferase assay determines if the test agent was able to inhibit the activation of cancer-related signaling pathways. In the case of FOXO and mi-R21, the enhanced luciferase activity by the test agent was assessed [26].

2.7. *Molecular Docking.* All docking simulations were conducted using MOE 2019 software (https://www.chemcomp.com). The receptors and the ligands were prepared using the standard structure optimization protocol of the software. The receptors were obtained from the protein data bank, PDB IDs: 3QX3, 3QRJ, 1M17, and 2SRC for topoisomerase, Abl kinase, EGFR-tyrosine kinase, and SRC

kinase, respectively. Then they were energy-minimized under AMBER12:EHT force field. The active sites were set as where the cocrystalized ligand was bound. The docking was performed using a molecular structure of compounds isolated from *SS* leaves using the general protocol of MOE DOCKTITE Wizard. The validation of docking experiments was achieved through the redocking of the cocrystalized ligands into their corresponding active sites and then the root means square deviation (RMSD) was calculated. The docking results were visualized and analyzed by DS Visualizer available from BIOVIA Inc. and the affinity of binding (docking scores) was calculated in Kcal/Mole for each compound against the selected targets.

3. Results and Discussion

Through our ongoing efforts to discover antileukemic natural compounds from Egyptian plants, *SS* leaves showed a potential promising result against K562 cell line *in vitro* [1]. Accordingly, *SS* leaves were selected for further phytochemical and biological investigations with the aim of

isolating the bioactive metabolites. The total extract and the successive fractions were screened against K562 cell line at a concentration of 20 μg/mL and the percentage inhibitions were calculated. The extracts of 75% ethanol, *n*-hexane, ethyl acetate, and the aqueous fractions showed mild antileukemic activities with percent inhibitions of 13%, 16%, 23%, and 9%, respectively, at a concentration of 20 μg/mL. All the fractions were phytochemically investigated, and their columns subfractions were screened for their antileukemic activities as described in the biological study results.

3.1. Phytochemical Study

3.1.1. Bioguided Phytochemical Investigation of the n-Hexane Fraction. The study resulted in the identification of 16 compounds in the saponifiable matter (Table S1*, Supplementary Materials*) with five majors identified as methyl palmitate, methyl elaidate, methyl linoleate, methyl linolenate, and ethyl linolenate at retention times = 33.1, 37.5, 37.8, 38.4, and 39.6 minutes, respectively. Moreover, 12 compounds were identified in the unsaponifiable matter (Table S2, Supplementary Materials) with five majors identified as phytol, stigmasta-5,22-dien-3-ol acetate (3, beta, 22 Z), stigmastan-3,5,22-trien, stigmasta-3,5-diene, and stigmasterol at retention times = 37.2, 47, 47.2, 52.6, and 66.1 minutes, respectively. Additionally, the unsaponifiable matter was purified and resulted in the isolation of two compounds identified as phytol (1) [27] and stigmasterol (2) [28] (Fig. S4, Supplementary Materials).

3.1.2. Bioguided Phytochemical Investigation of the EtOAc Fraction. The result was the isolation of 16 known compounds identified as liquidambaric lactone (3) [29], maslinic lactone (4) [30], oleanolic acid (5) [31], 11α,12α-epoxy-oleanolic lactone (6) [32], oleanderolide (7) [33], stigmasterol glucoside (8) [34], *P*-aminophenol (9) [35], quercetin-3-*O*-α-L-rhamnopyranoside (10) [36], quercetin-3-*O*-β-D-glucopyranoside (11) [36], quercetin-3-*O*-α-L-arabinoside (12) [37], quercetin-3-*O*-β-D-xyloside (13) [37], mauritianin (14) [38], isorhamnetin 3-*O*-(2,6-di-*O*-α-rhamnosyl)-β-D-galactopyranoside (15) [39], clitorin (16) [40], 3-[(*O*-6-deoxy-α-L-mannopyranosyl-(1⟶2)-*O*-[6-deoxy-α-L-mannopyr-anosyl-(1⟶6)]-β-D-glucopyranosyl) oxy]-5,7-dihydroxy-2-(3-hydroxy-4-methoxyphenyl)-4H-1-benzopyran-4-one (17) [41], and kaempferol-3-*O*-α-L-rhamnopyranosyl-(1⟶2) [α-L-rhamnopyranosyl-(1⟶6)]-(4-*O*-E-*p*-coumaroyl-β-D-galactopyranoside) (18) [42] (Fig. S4 and Table S3, Supplementary Materials).

3.1.3. Bioguided Phytochemical Investigation of the Aqueous Fraction. The result was the isolation of one new compound (33) (Hederatriol 3-*O*-β-D-glucuronic acid methyl ester), as well as 16 known compounds identified as betulinic acid (19) [31,43], ursolic acid (20) [44], 3β-*O*-(*cis*-*p*-coumaroyl)-2α-hydroxyurs-12-en-28-oic acid (21) [45], 3β-*O*-(*trans*-*p*-coumaroyl)-2α-hydroxyurs-12-en-28-oic acid (known as jacoumaric acid) (22) [45], obtuslin (23) [44], corosolic acid

(24) [45], β-sitosterol glucoside (25) [46], hederagenin-3-*O*-β-D-glucuronopyranoside 6′-*O*-methyl ester (26) [47], kaempferol-3-*O*-rutinoside (27) [48], isorhamentin-3-*O*-rutinoside (28) [49], hederagenin-3-*O*-β-D-glucuronopyr-anoside (29) [47], 11-ketocorosolic acid (30) [50], hederagenin (31) [51], oleanolic acid 3-*O*-β-D-glucuronopyranoside 6′ methyl ester (32) [52], oleanolic acid 3-*O*-β-D-glucur-onopyranoside (34) [18], and chikusetsusaponin II (35) [53] Fig. S4 *and Table S3, (Supplementary Materials).*

Compounds (2), (5), (19), and (34) were previously reported in *SS* leaves [18,19], while this is the first report of compounds (1), (3)-(4), (6)–(18), (20)–(33), and (35) from this species.

3.2. Structure Elucidation of Compound (33).

Compound (33) was isolated as a white powder (2 mg, soluble in MeOH), $[\alpha]^{25°}_D = +34.5$ ($c = 0.15$ in MeOH). Its molecular formula, $C_{37}H_{60}O_9$, was derived from the ^{1}D NMR data (Table 1) and the supportive HRESIMS ion at m/*z* 649.45082 [M+H] $^+$ (calcd. for $C_{37}H_{61}O_9$, 649.43156). The molecular formula revealed the hydrogen deficiency index to be 29.6 ppm. From the ^{1}H NMR spectrum, the seven distinct methyls [δ_H 3.67 (3H, s), 1.09 (3H, s), 0.87 (6H, s), 0.86 (3H, s), 0.78 (3H, S), 0.71 (3H, s), and 0.59 (3H, s)] were observed alongside with the signal assignable to one olefinic proton [δ_H 5.76 (1H, t)]. Two oxygenated methylenes were detected (δ_H 3.51 (2H, S), 3.07 (1H, d, $J = 10.5$ Hz), and 3.44 (1H, d, $J = 11$ Hz)). Five oxygenated methines (δ_H 3.67 (1H), 3.50 (IH), 3.28 (1H, t), 3.16 (1H, t), 2.98 (1H, t)) alongside the one anomeric proton (δ_H 4.33 (d, $J = 8$ Hz)) were detected. The DEPTQ-135 spectra of (33) showed 37 carbon signals (Table 1) of which 30 signals were assigned to the aglycone moiety (hederatriol) and 7 to a glucuronic acid methyl ester moiety. The anomeric carbon resonances ($\delta_{C/H}$ 105.1/4.33) as well as four oxygenated methine signals at $\delta_{C/H}$ 74.1/2.98, 75.9/3.16, 72.1/3.28, and 76.4/3.67 alongside the carbonyl ester (δ_C 170.1) and the attached methoxy signal ($\delta_{C/H}$ 52.3/3.67) disclosed the presence of glucuronic acid 6′ methyl ester moiety. The anomeric configuration of the glucuronoid unit was determined to be based on the coupling constant ($J_{H1} = 8$ Hz). There were 30 carbons left for the skeleton, indicating a triterpenoid core of (33). The skeletal carbons, particularly the six methyl carbons (δ_C 33.3, 26.0, 23.9, 17.4, 16.0, and 13.3), alongside the two oxygenated methylenes [δ_C 62.8 (C-24) and 70.2 (C-28)] implied an olean-type triterpenes alcohol derivative (hederatriol) scaffold for (33) [54]. Free alcoholic methylene at position C28 was confirmed by 2D HMBC & TOCSY correlations between the OH-proton at C28 (δ_H 3.5) and C18 in HMBC spectrum. Moreover, protons H16, H19, and H21 showed TOCSY correlations to H28. Free alcohol OH signal (δ_H 3.79) showed TOCSY correlation with H28 methylene. All of the previous data supported the presence of hederatriol. The HMBC cross-peaks enabled the substituent groups to be positioned. The glucuronoid moiety was connected to C-3 as suggested by the HMBC correlation of H-1′ with δ_C 80.4 (C-3) and H-3 to the anomeric carbon at δ_C105.1 (C-1′) of the glucuronoid moiety (Figure 2). The structure of compound
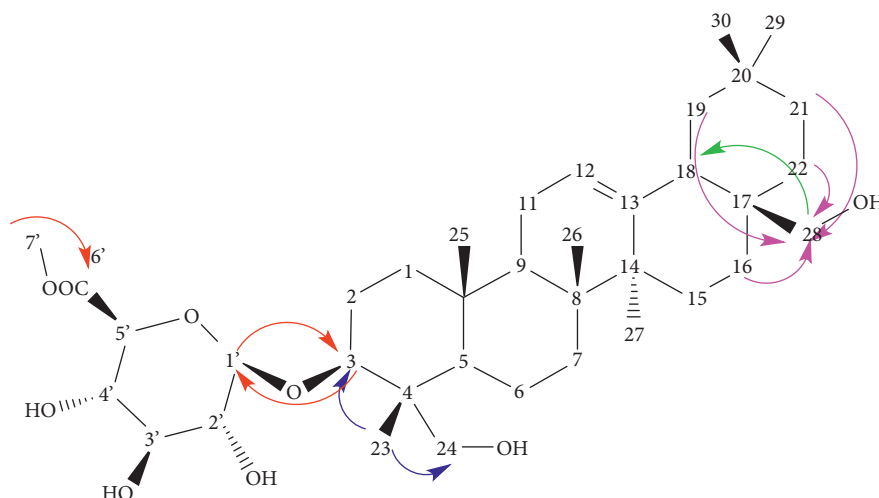
FIGURE 2: Structure and HMBC and TOCSY correlations of compound (33).

(33) is considered to be new due to the 3-*O*-glycosylation of hederatriol with glucuronic acid methyl ester. Thus, compound (33) was elucidated as hederatriol 3-*O*-β-D-glucuronic acid methyl ester (NMR data, Figures S5–*S11*, *Supplementary Materials*).

3.3. Biological Study

3.3.1. Cytotoxicity against Leukemia K562 Cell Line. The *n*-hexane fraction was fractionated by saponification with KOH, where the yielded saponifiable and unsaponifiable matters were tested against K562 cells and showed inhibitions of $IC_{50} = 75.7$ and $73.9 \, \mu g/mL$, respectively. Accordingly, the phytoconstituents in both fractions were investigated using GC-MS analysis.

The EtOAc fraction (Fr-B) was fractionated using Si-SPE column and the five resulted subfractions were tested against K562 cells at concentrations of 50 and $75 \, \mu g/mL$. The results showed that subfractions Fr-B-2 and Fr-B-5 were the bioactive fractions with percent inhibitions of 93.7% and 47.3%, respectively, at a concentration of $75 \, \mu g/mL$ (Figure S12, Supplementary Materials). The subfraction Fr-B-2 was chromatographed using silica gel SPE column and the resulting subfractions were tested against K562 cells. Subfractions Fr-B-2-2 and Fr-B-2-4 were the most cytotoxic with percent inhibitions of 45% and 47%, respectively, at a concentration of $75 \, \mu g/mL$ (Fig. S13, Supplementary Materials). The subfraction Fr-B-5 was chromatographed using VLC silica gel column and the resulting subfractions were tested against K562 cells. Subfractions Fr-B-5-4 and Fr-B-5-5 were the most cytotoxic with percent inhibitions of 28% and 85%, respectively, at a concentration of $75 \, \mu g/mL$ (Fig. S13, Supplementary Materials).

The aqueous fraction (Fr-C) was chromatographed using HP-20 ion exchange resin and the five resulting subfractions that were screened for their activity against K562 cells at concentrations of 50 and $75 \, \mu g/mL$. The results showed that subfraction Fr-C-5 was the bioactive fraction with 94.4% percent of inhibition at concentrations of 50 and $75 \, \mu g/mL$

(Fig. S14, Supplementary Materials). Subfraction Fr-C-5 was chromatographed on silica gel column and the eight produced subfractions that were screened for their activity against K562 cells at concentrations of 50 and $75 \, \mu g/mL$. The results showed that subfractions Fr-C-5-2 and Fr-C-5-4 were the most active ones with 65% and 63% percent of inhibitions, respectively, at a concentration of $75 \, \mu g/mL$ (Fig. S15, Supplementary Materials).

All the detected bioactive subfractions were subjected to several chromatographic techniques as mentioned in the Materials and Methods section with the aim of isolating and elucidating the structures of the bioactive constituents.

Compounds (1)–(35) were screened against K562 cell line at concentrations of 50 and $75 \, \mu g/mL$ and IC_{50} values were calculated. Oleanolic acid 3-*O*-β-D-glucuronopyranoside (34) was identified as the most antiproliferative compound isolated from *SS* extract with IC_{50} value of $22.3 \, \mu M$ compared to Taxol (~$2 \, \mu M$) and Doxorubicin (~$4 \, \mu M$). Other active triterpenes were betulinic acid (19), ursolic acid (20), 3β-*O*-(*cis-p*-coumaroyl)-2α-hydroxyurs-12-en-28-oic acid (21), jacoumaric acid (22), corosolic acid (24), and chikusetsusaponin II (35) with IC_{50} values of 37.5, 31.3, 36.6, 30.8, 33.7, and $41.5 \, \mu M$, respectively. Phytol (1), oleanolic acid (5), hederagenin 3-*O*-β-D-glucuronopyranoside (29), and oleanolic acid 3-*O*-β-D-glucuronopyranoside methyl ester (32) showed mild activity against K562 cell line with IC_{50} values of 112.3, 67.6, 83.3, and $56.4 \, \mu M$, respectively (Figure 3). Out of the 35 isolated compounds, the triterpene glycosides were shown to be the most active antileukemic compounds in this plant. Antileukemic activities of betulinic acid (19) [55], ursolic acid (20) [56], oleanolic acid (5) [57], and phytol (1) [58] were previously reported in literature but this is the first report of antileukemic activities of compounds (21), (22), (24), (29), (32), (34), and (35). Moreover, methyl linolenate, the major constituent of the saponifiable matter of the *n*-hexane fraction of *SS* leaves, was

IC50 [μM] of active isolated compounds against leukemia K562 cell line
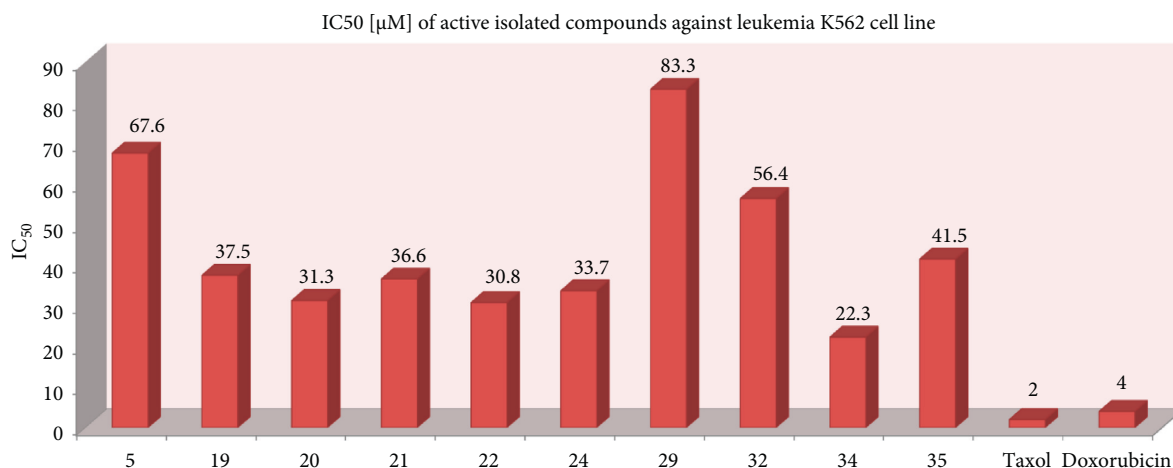
FIGURE 3: IC$_{50}$ [μM] of the active isolated compounds against leukemia K562 cell line.

TABLE 2: IC$_{50}$ [μM] of active isolated compounds against selected transcription factor signaling pathways in HeLa cells

Compound no.	Stat 3/IL-6	Smad/ TGF-β	AP-1/ PMA	NF-kB/ PMA	E2F/ PMA	Myc/ PMA	ETS/ PMA	Notch/ PMA	FOXO	Wnt/ m-Wnt-3a	Hedgehog /PMA	pTK	miR-21	K-Ras	AhR
21	13.9	9.5	20.9	21.3	10.5	15.2	11.4	11.3	ND	4.6	14.4	ND	21.4	23.1	ND
22	17.5	3.8	22.2	32.3	ND	18.3	18.9	21.0	ND	3.8	20.1	ND	25.8	26.3	ND
24	15.9	13.9	16.3	18.8	ND	14.4	16.5	17.9	ND	13.5	16.9	ND	18.2	15.5	17.5
34	6.9	5.8	7.0	6.3	5.3	5.9	6.8	6.5	ND	6.70	7.40	7.30	8.00	NA	ND

- Smad/TGF-β
- E2F/PMA
- Wnt/m-wnt 3a
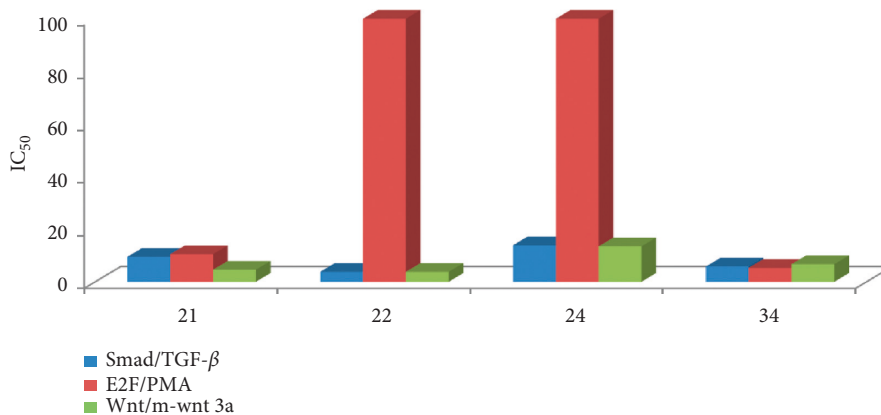
FIGURE 4: IC$_{50}$ [μM] of active isolated compounds against selected transcription factor signaling pathways.

previously reported for its cytotoxicity against K562 cell line [59]. Other isolated compounds showed no cytotoxicity against K562 cell line.

3.3.2. Triterpenes Selectively Target Cancer Signaling Pathways.

The most active isolated compounds (21), (22), (24), and (34) against K562 cell line were further evaluated for targeting the cancer signaling pathways. These compounds were tested for their influence on the battery of 15-plex transcription factor assay. The results (Table 2 and Figure 4) showed that compounds (22) and (21) showed

specific inhibition of Wnt pathway (IC$_{50}$ = 3.8 and 4.6 μM, respectively) while compound (22) showed specific inhibition of Smad (IC$_{50}$ = 3.8 μM). Compound (34) can strongly alter the signaling pathways of Smad and E2F (IC$_{50}$ = 5 μM). From these results, we can conclude the correlation between the inhibition of Smad, E2F, and Wnt signaling pathways and the leukemia K562 cell line growth inhibition (Figure 5).

As cancer signaling plays a complex role in CML, the observed results from this study could be helpful in finding new therapeutic agents and molecular genetics-based treatment targeting these metabolic pathways. Despite the fortune
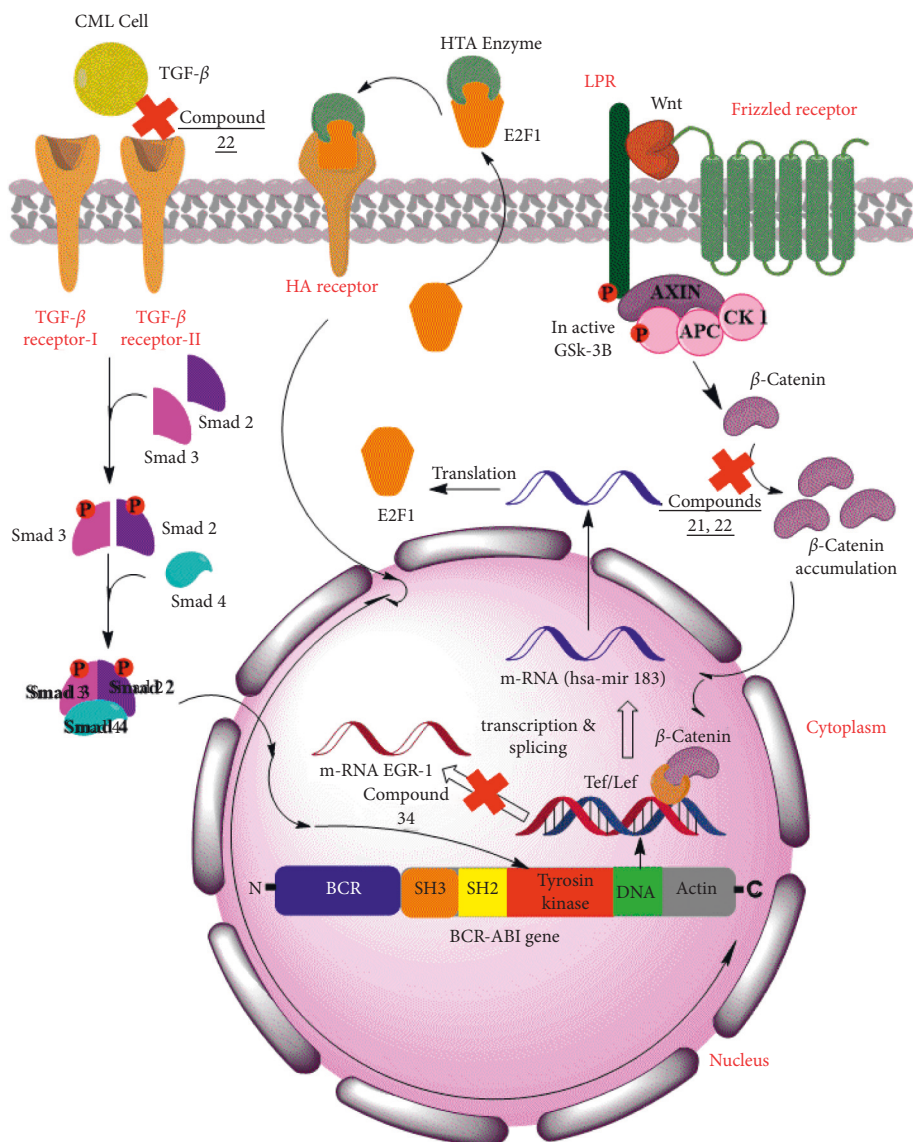
FIGURE 5: Mode of action of active isolated compounds against Smad, Wnt, and E2F signaling pathways.

available research on the molecular details of TGF-β signaling, little is known regarding how TGF-β and Smad influence CML [60]. One of these realized relationships is that the constitutively active tyrosine kinase produced by the specific Bcr-Abl fusion gene on the Philadelphia chromosome can enhance the resistance of malignant cells to TGF-β1-induced growth inhibition and apoptosis [61]. Previous studies reported ursolic acid and oleanolic acid as antagonists of TGF-β1 binding to its receptor in Balb/c 3T3 cells [62]. A recent study revealed that inhibition of E2F1 reduced CML cell proliferation, leading to p53-mediated apoptosis [63]. The BCR-ABL1 protein kinase-dependent pathway intervened by the upregulation of *hsa-mir183*, the downregulation of its direct target early growth response 1 (EGR1), and, as a consequence, upregulation of E2F1 [58]. Wnt signaling assumes a significant part in the malignancies of the hematopoietic system [64]. Several compounds that are natural in origin were reported in literature for targeting Wnt pathway as

a mechanism for anticancer activity such as ursolic acid and corosolic acid that were reported as antagonists of the Wnt/β-catenin pathway [65–67]. Correlating the previous literature to the results, a mechanism of action of the active compounds could be supposed. The active compounds were mainly oleanolic acid and ursolic acid derivatives which exhibited their antileukemic activities by targeting Smad, E2F, and Wnt signaling pathways (Figure 5).

3.3.3. Molecular Docking. Multitarget therapies are crucial in the field of complex diseases such as cancers due to activation of compensatory mechanisms and consecutive cellular pathways [68]. The recent research showed a correlation between CML cell line K562 and several proteins which are considered as targets whose inhibition leads to antiproliferative effect in this cell line. Four target proteins, human topoisomerase II beta in complex with DNA and

TABLE 3: Affinity binding docking scores (Kcal/Mole) of bioactive isolated compounds.

Compound no.	Topoisomerase (3QX3)	SRC kinase (2SRC)	Abl kinase (3QRJ)	EGFR-tyrosine kinase (1M17)
22	−7.81	−5.75	−5.70	−7.12
34	−9.30	−2.63	−7.05	−7.35
Etoposide	−7.10			
Adenylyl-imidodiphosphate		−5.78		
Rebastinib			−7.86	
Erlotinib				−6.99

22

(a)

34

(b)

Etposide

(c)

FIGURE 6: Docking of compounds **(22)** and **(34)** with topoisomerase.

Lupane triterpenoid

Betulinic acid

Oleane triterpenoid

Oleanolic acid

Ursane triterpenoid

Ursolic acid

IC$_{50}$ = 37.5 μm · · · **IC$_{50}$ = 67.6 μm** · · · **IC$_{50}$ = 31.3 μm**

FIGURE 7: Antileukemic activities of different types of triterpenes isolated from *SS* leaves against K562 cell line.

etoposide (PDB ID: 3QX3), epidermal growth factor receptor complexed with erlotinib (PDB ID: 1M17), human Abl-1 kinase (PDB ID: 3QRJ), and SRC Kinase (PDB ID: 2SRC), were reported as docking targets in the K562 cell line [69, 70].

Based on the previous biological results, compounds (22) and (34) were selected and screened against the selected targets and the affinity of binding was calculated (Table 3). Compounds (22) and (34) showed a strong binding affinity towards topoisomerase (docking score = −7.81 and −9.30 Kcal/Mole,

R_1	R_2	Compound name	K562 IC$_{50}$ μM	Smad/ TGF-β	E2F /PMA	Wnt/m-wnt 3a
H	H	Ursolic acid (20)	31.3			
OH	H	Corosolic acid (24)	33.7	13.9	NA	13.5
OH	Z-p-coumaric acid	3β-O-(cis-p-Coumaroyl)-2α-hydroxyurs-12-en-28-oic acid (21)	36.6	9.5	10.5	4.6
OH	E-p-coumaric acid	Jacoumaric acid (22)	30.8	3.8	NA	3.8

FIGURE 8: Antileukemic activities of different types of ursane triterpenes isolated from SS leaves.
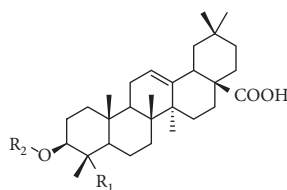
R_1	R_2	Compound name	K562 IC$_{50}$ μM
CH$_3$	H	Oleanolic acid (5)	67.6
CH$_3$	Glucuronic acid	Oleanolic acid 3-O-β-D-glucuronopyranoside (34)	22.3
CH$_3$	Glucuronic acid methyl ester	Oleanolic acid 3-O-β-D-glucuronopyranoside methyl ester (32)	56.4
CH$_3$	β-D-glucuronopyranoside (6→1) -β-D-glucopyranoside	Chikusetsusaponin II (35)	41.5
CH$_2$OH	Glucuronic acid	Hederagenin 3-O-β-D-glucuronopyranoside (21)	83.3

FIGURE 9: Antileukemic activities of different types of oleane triterpenes isolated from SS leaves.

respectively) compared to etoposide (docking score = −7.10 Kcal/Mole). Compounds (22) and (34) demonstrated a strong binding affinity towards EGFR-tyrosine kinase (docking score = −7.12 and −7.35 Kcal/Mole, respectively) compared to erlotinib (docking score = −6.99 Kcal/Mole). Moreover, compound (34) showed a strong binding affinity towards Abl kinase (docking score = −7.05 Kcal/Mole) compared to rebastinib (docking score = −7.86 Kcal/Mole) (Table 3 and Figure 6).

3.3.4. Structure Activity Relationship (SAR) Study. The structures of the isolated compounds could be classified as oleane triterpenoids, oleane lactones triterpenoids, ursane

triterpenoids, lupane triterpenes, steroids, and flavonoid glycosides (Fig. S3 and Table S4, Supplementary Materials).

Among the different classes of isolated compounds, triterpenes were shown as the bioactive antileukemic molecules present in the *SS* leaves. The potency of the isolated triterpenoids prompted us to investigate the structure activity relationships underlying their antileukemic activities.

In this study, three types of triterpenoids aglycones were isolated and identified: lupane triterpenoids represented by betulinic acid, oleane type represented by oleanolic acid, and ursane type represented by ursolic acid. The results showed that the most active antileukemic triterpenoid is ursane type followed by lupane and the least active type is oleane triterpenoids (Figure 7).

From ursane type triterpenoids, six compounds (20)–(24) and (30) were isolated. Comparing their structures and antileukemic activities, two positions, C-2 and C-3, were believed to affect the activity. Hydroxylation at C-2 position slightly decreases the antileukemic activity. Also, the esterification at C-3 position by coumaric acid can increase or decrease the activity depending on the configuration of coumaric acid moiety. The *trans* coumaroyl derivative, jacoumaric acid (22), showed higher antileukemic activity than corosolic acid (24), while *cis* derivative, 3β-O-(*cis-p*-coumaroyl)-2α-hydroxyurs-12-en-28-oic acid (21), showed lower activity and these results support the idea of the higher activity of *trans* conformers than the *cis* one (Figure 8).

The SAR study showed that the activity of oleanolic acid can be greatly increased when esterified at C-3 position by glucuronic acid. Compound (34) showed strong antileukemic activity compared to compound (5) due to the presence of glucuronic acid moiety attached at C-3. In addition, the free OH group in glucuronic acid is crucial for the activity and, as the results show, when it is methylated as in compound (32) or glycosylated as in compound (35), the activity decreased. Meanwhile, for oleane triterpenes, the methylation at C-23 as in compounds (5), (32), and (34) increases the activity compared to compound (29) (Figure 9).

4. Conclusion

One new compound (33) and 34 known compounds were isolated from the leaves of *Sesbania sesban* encompassing 19 triterpenoids ((3)–(7), (19)–(24), (26), and (29)–(35)), three steroids ((2), (8), and (25)), 11 flavonoid glycosides ((10)–(18) and (27)-(28)), one fatty alcohol (1), and one phenolic compound (9). The antileukemic activity of the isolated compounds was evaluated against leukemia K562 cell line *in vitro* and 11 triterpenoids exhibited remarkable antileukemic activities against this cell line. Compounds (34) (oleanolic acid 3-O-β-D-glucuronopyranoside) and (22) (jacoumaric acid) exhibited the strongest activities with IC$_{50}$ values of 22.3 and 30.8 μM, respectively. The mechanism of the antileukemic activity of these compounds could be attributed to the attenuation of Smad, Wnt, and E2F signaling pathways. Compound (22) demonstrated a specific inhibition of Wnt and Smad signaling with an IC$_{50}$ value of 3.8 μM for both pathways. Meanwhile compound (34) showed an inhibition of E2F with an IC$_{50}$ value of 5 μM.

Moreover, the binding patterns of the bioactive molecules against leukemia cell related targets were explored by docking them against topoisomerase, EGFR-tyrosine kinase, and Abl kinase. Compounds (22) and (34) exhibited a strong binding affinity towards topoisomerase (docking score- $= -7.81$ and -9.30 Kcal/Mole, respectively). Furthermore, SAR study reveals that the presence of a carboxyl group either in the triterpene or in the sugar moiety was identified as contributing to the cytotoxic activity.

Data Availability

Data are available in the Supplementary Materials.

Conflicts of Interest

The authors declare no conflicts of interest.

Supplementary Materials

Table S1: results of GC/MS analysis of fatty acid methyl ester (FAME) of the n-hexane fraction of SS leaves. Table S2: results of GC/MS analysis of unsaponifiable matter of the n-hexane fraction of SS leaves. Table S3: list of compounds isolated from *Sesbania sesban* L. leaves. Figure S1: HPLC (RP column) purification of compounds (14) and (15) using MeOH/water gradient. Figure S2: HPLC (RP column) purification of compounds (16) and (17) using MeOH/water gradient. Figure S3: HPLC (RP column) purification of compounds (27) and (28) using MeOH/water gradient. Figure S4: chemical structures of compounds isolated from SS leaves. Figure S5: ^{1}H NMR spectrum of compound (33). Figure S6: deptq135 spectrum of compound (33). Figure S7: dept spectrum of compound (33). Figure S8: HSQC spectrum of compound (33). Figure S9: TOCSY spectrum of compound (33). Figure S10: TOCSY spectrum of compound (33). Figure S11: ESI(-) MS spectrum of compound (33). Figure S12: bioguided screening of EtOAc (Fr-B) column subfractions against leukemia K562 cell line. Figure S13: bioguided screening of Fr-B-2 column subfractions and Fr-B-5 column subfractions against leukemia K562 cell line. Figure S14: bioguided screening of aqueous (Fr-C) column subfractions against leukemia K562 cell line. Figure S15: bioguided screening of Fr-C-5 column subfractions against leukemia K562 cell line. (*Supplementary Materials*)

References

[1] M. H. H. Shimaa Mohammed Abdelgawad, G. Ahmed Fawzy, and H. I. El-Askary, "In vitro antileukemic activity of extracts of some medicinal plants from upper Egypt in human chronic leukemia K562 cell line," *Tropical Journal of Natural Products Research*, vol. 5, no. 12, pp. 2115–2122, 2021.

[2] M. A. Aboul-Soud, H. A. El-Shemy, K. M. Aboul-Enein, A. M. Mahmoud, A. M. Al-Abd, and D. A. Lightfoot, "Effects of plant-derived anti-leukemic drugs on individualized leukemic cell population profiles in Egyptian patients," *Oncology letters*, vol. 11, no. 1, pp. 642–648, 2016.

[3] A. S. Ibrahim, H. M. Khaled, N. N. Mikhail, H. Baraka, and H. Kamel, "Cancer incidence in Egypt: results of the national population-based cancer registry program," *Journal of cancer epidemiology*, vol. 2014, Article ID 437971, 18 pages, 2014.

[4] S. Eskandari and R. Yazdanparast, "Bcl6 gene-silencing facilitates PMA-induced megakaryocyte differentiation in K562 cells," *Journal of Cell Communication and Signaling*, vol. 11, no. 4, pp. 357–367, 2017.

[5] M. Karon, E. J. Freireich, E. Frei et al., "The role of vincristine in the treatment of childhood acute leukemia," *Clinical Pharmacology & Therapeutics*, vol. 7, no. 3, pp. 332–339, 1966.

[6] D. M. Lucas, P. C. Still, L. Bueno Perez, M. R. Grever, and A. Douglas Kinghorn, "Potential of plant-derived natural products in the treatment of leukemia and lymphoma," *Current Drug Targets*, vol. 11, no. 7, pp. 812–822, 2010.

[7] J. M. S. van Maanen, J. Retel, J. De Vries, and H. M. Pinedo, "Mechanism of action of antitumor drug etoposide: a review," *JNCI Journal of the National Cancer Institute*, vol. 80, no. 19, pp. 1526–1533, 1988.

[8] K. Hande, "Etoposide: four decades of development of a topoisomerase II inhibitor," *European Journal of Cancer*, vol. 34, no. 10, pp. 1514–1521, 1998.

[9] T. G. Heuzé, D. Bastianelli, and F. Lebas, "Sesban (Sesbania sesban)," 2015, https://www.feedipedia.org/node/253.

[10] E. Debela, A. Tolera, L. O. Eik, and R. Salte, "Condensed tannins from Sesbania sesban and Desmodium intortum as a means of *Haemonchus contortus* control in goats," *Tropical Animal Health and Production*, vol. 44, no. 8, 2012.

[11] E. G. Kamel, M. A. El-Emam, S. S. Mahmoud, F. M. Fouda, and F. E. Bayaumy, "Parasitological and biochemical parameters in Schistosoma mansoni-infected mice treated with methanol extract from the plants Chenopodium ambrosioides, Conyza dioscorides and Sesbania sesban," *Parasitology International*, vol. 60, no. 4, pp. 388–392, 2011.

[12] A. D. Soren, R. P. Chen, and A. K. Yadav, "In vitro and in vivo anthelmintic study of Sesbania sesban var. bicolor, a traditionally used medicinal plant of Santhal tribe in Assam, India," *Journal of Parasitic Diseases*, vol. 45, no. 1, pp. 1–9, 2021.

[13] A. U. Tatiya, P. R. Dande, R. E. Mutha, and S. J. Surana, "Effect of saponins from of Sesbania sesban L.(Merr) on acute and chronic inflammation in experimental induced animals," *Journal of Biological Sciences*, vol. 13, no. 3, pp. 123–130, 2013.

[14] S. N. Fitriansyah, I. Fidrianny, and K. Ruslan, "Correlation of total phenolic, flavonoid and carotenoid content of Sesbania sesban (L. Merr) leaves extract with DPPH scavenging activities," *International Journal of Pharmacognosy and Phytochemical Research*, vol. 9, no. 1, pp. 89–94, 2017.

[15] A.-C. Dorsaz, M. Hostettmann, and K. Hostettmann, "Molluscicidal saponins from Sesbania sesban," *Planta Medica*, vol. 54, no. 03, pp. 225–227, 1988.

[16] M. N. Walekhwa, T. K. Ogeto, M. K. Murithi, and Z. L. Malago, "Pharmacological effects of Sesbania sesban: a systematic review," *International Journal of Research in Medical Sciences*, vol. 8, no. 3, p. 1185, 2020.

[17] R. B. Pandhare, B. Sangameswaran, P. B. Mohite, and S. G. Khanage, "Antidiabetic activity of aqueous leaves extract of Sesbania sesban (L) Merr. in streptozotocin induced diabetic rats," *Avicenna Journal of Medical Biotechnology*, vol. 3, no. 1, pp. 37–43, 2011.

[18] N. Das, P. Chandran, and S. Chakraborty, "Potent spermicidal effect of oleanolic acid 3-beta-D-glucuronide, an active principle isolated from the plant Sesbania sesban Merrill," *Contraception*, vol. 83, no. 2, pp. 167–175, 2011.

[19] M. Farooq, I. Varshney, and M. S. Khan, "Saponins and sapogenins IV," *Journal of the American Pharmaceutical Association*, vol. 48, no. 8, pp. 466–468, 1959.

[20] S. Manoharan and J. Kaur, "Anticancer, antiviral, antidiabetic, antifungal and phytochemical constituents of medicinal plants," *American Journal of PharmTech Research*, vol. 3, pp. 149–169, 2013.

[21] H. Dianhar, Y. M. Syah, D. Mujahidin, E. H. Hakim, and L. D. Juliawaty, "A flavone derivative from Sesbania sesban leaves and its cytotoxicity against murine leukemia P-388 cells," *AIP Conference Proceedings*, vol. 1589, no. 1, pp. 411–413, 2014.

[22] M. Namadina, S. Yahuza, H. Haruna et al., "Pharmacognostic and antioxidant activity of bryophyllum pinnatum leaves," *International Journal Of Science for Global Sustainability*, vol. 6, no. 2, 2020.

[23] I. Finar, *Organic Chemistry*, ELBS, Ghitorni, India, 6 edition, 1973.

[24] M. Kageyama, K. Li, S. Sun et al., "Anti-tumor and anti-metastasis activities of honey bee larvae powder by suppressing the expression of EZH2," *Biomedicine & Pharmacotherapy*, vol. 105, pp. 690–696, 2018.

[25] P. Balachandran, M. A. Ibrahim, J. Zhang, M. Wang, D. S. Pasco, and I. Muhammad, "Crosstalk of cancer signaling pathways by cyclic hexapeptides and anthraquinones from rubia cordifolia," *Molecules*, vol. 26, no. 3, p. 735, 2021.

[26] M. A. Zaki, P. Balachandran, S. Khan et al., "Cytotoxicity and modulation of cancer-related signaling by (Z)-and (E)-3, 4, 3′, 5′-tetramethoxystilbene isolated from Eugenia rigida," *Journal of Natural Products*, vol. 76, no. 4, pp. 679–684, 2013.

[27] D. Arigoni, W. Eisenreich, C. Latzel et al., "Dimethylallyl pyrophosphate is not the committed precursor of isopentenyl pyrophosphate during terpenoid biosynthesis from 1-deoxyxylulose in higher plants," *Proceedings of the National Academy of Sciences*, vol. 96, no. 4, pp. 1309–1314, 1999.

[28] P. Jain, S. Bari, and S. Surana, "Isolation of stigmasterol and γ-sitosterol from petroleum ether extract of woody stem of Abelmoschus manihot," *Asian journal of biological sciences*, vol. 2, no. 4, pp. 112–117, 2009.

[29] Y. Zhu, Y. J. Guan, Q. Z. Chen et al., "Pentacyclic Triterpenes from the resin of Liquidambar formosana have anti-angiogenic properties," *Phytochemistry*, vol. 184, Article ID 112676, 2021.

[30] G. R. Mallavarapu and E. Muralikrishna, "Maslinic lactone from the heartwood of Terminalia alata," *Journal of Natural Products*, vol. 46, no. 6, pp. 930-931, 1983.

[31] M. A. Hossain and Z. Ismail, "Isolation and characterization of triterpenes from the leaves of Orthosiphon stamineus," *Arabian Journal of Chemistry*, vol. 6, no. 3, pp. 295–298, 2013.

[32] Q. Fu, L. Qiu, H.-M. Yuan, T. Yu, L. Zou, and D. and E. Paeonenoides, "Two new nortriterpenoids from-Paeonia lactiflora and their inhibitory activities on NO production," *Helvetica Chimica Acta*, vol. 99, no. 1, pp. 46–49, 2016.

[33] L. Fu, S. Zhang, N. Li et al., "Three new triterpenes from nerium oleander and biological activity of the isolated compounds," *Journal of Natural Products*, vol. 68, no. 2, pp. 198–206, 2005.

[34] S. K. Nigam, G. Misra, and C. R. Mitra, "Stigmasterol glucoside a constituent of *Adenanthera pavonina* seed and leaf," *Planta Medica*, vol. 23, no. 2, pp. 145–148, 1973.

[35] R. Eyanagi, Y. Hisanari, and H. Shigematsu, "Studies of paracetamol/phenacetin toxicity: isolation and characterization of p-aminophenol-glutathione conjugate," *Xenobiotica*, vol. 21, no. 6, pp. 793–803, Jun 1991.

[36] K. R. Markham and B. Ternai, "13C NMR of flavonoids—II," *Tetrahedron*, vol. 32, no. 21, pp. 2607–2612, 1976.

[37] M. Kalegari, M. D. Miguel, JdF. G. Dias et al., "Phytochemical constituents and preliminary toxicity evaluation of leaves from Rourea induta Planch.(Connaraceae)," *Brazilian Journal of Pharmaceutical Sciences*, vol. 47, no. 3, pp. 635–642, 2011.

[38] I. Dini, G. Carlo Tenore, and A. Dini, "Phenolic constituents of Kancolla seeds," *Food Chemistry*, vol. 84, no. 2, pp. 163–168, 2004/02/01/2004.

[39] F. Ferreres, D. M. Pereira, P. Valentão, P. B. Andrade, R. M. Seabra, and M. Sottomayor, "New phenolic compounds and antioxidant potential of catharanthus roseus," *Journal of Agricultural and Food Chemistry*, vol. 56, no. 21, pp. 9967–9974, 2008/11/12 2008.

[40] N. Morita, M. Arisawa, M. Nagase, H. Hsu, and Y. Chen, "Studies on the constituents of formosan leguminosae. I. The constituents in the leaves of Clitoria ternatea L," *Yakugaku zasshi: Journal of the Pharmaceutical Society of Japan*, 1977.

[41] R. S. Mohammed, A. H. Abou Zeid, E. A. El-Kashoury, A. A. Sleem, and D. A. Waly, "A new flavonol glycoside and biological activities of *Adenanthera pavonina* L. leaves," *Natural Product Research*, vol. 28, no. 5, pp. 282–289, 2014.

[42] G. C. Kite, E. R. Rowe, G. P. Lewis, and N. C. Veitch, "Acylated flavonol tri- and tetraglycosides in the flavonoid metabolome of Cladrastis kentukea (Leguminosae)," *Phytochemistry*, vol. 72, no. 4-5, pp. 372–384, 2011/04/01/2011.

[43] H. H. F. Koolen, E. R. Soares, F. M. A. da. Silva, A. Q. L. de. Souza, E. Rodrigues Filho, and A. D. L. de. Souza, "Triterpenes and flavonoids from the roots of Mauritia flexuosa," *Revista Brasileira de Farmacognosia*, vol. 22, no. 1, pp. 189–192, 2012.

[44] W. Seebacher, N. Simic, R. Weis, R. Saf, and O. Kunert, "Complete assignments of 1H and 13C NMR resonances of oleanolic acid, 18α-oleanolic acid, ursolic acid and their 11-oxo derivatives," *Magnetic Resonance in Chemistry*, vol. 41, no. 8, pp. 636–638, 2003.

[45] C.-K. Lee, "Ursane triterpenoids from leaves of Melaleuca leucadendron," *Phytochemistry*, vol. 49, no. 4, pp. 1119–1122, 1998.

[46] A. Hamed, M. Ismail, M. M. El-Metwally et al., "Diverse polyketides and alkaloids from Penicillium sp. KHMM: structural elucidation, biological and molecular docking studies," *Zeitschrift fuer Naturforschung, C: Journal of Biosciences*, vol. 74, no. 5-6, pp. 131–137, 2019.

[47] S. Srivastava and D. Jain, "Triterpenoid saponins from plants of Araliaceae," *Phytochemistry*, vol. 28, no. 2, pp. 644–647, 1989.

[48] R. González-Laredo, M. Flores De La Hoya, M. Quintero-Ramos, and J. Karchesy, "Flavonoid and cyanogenic contents of chaya (spinach tree)," *Plant Foods for Human Nutrition*, vol. 58, no. 3, pp. 1–8, 2003.

[49] A. M. El-Hawiet, S. M. Toaima, A. M. Asaad, M. M. Radwan, and N. A. El-Sebakhy, "Chemical constituents from *Astragalus annularis* forssk. and A. Trimestris L., Fabaceae," *Revista Brasileira de Farmacognosia*, vol. 20, no. 6, pp. 860–865, 2010.

[50] A. Ikuta, H. Tomiyasu, Y. Morita, and K. Yoshimura, "Ursane-and oleanane-type triterpenes from ternstroemia g

[51] ymnanthera callus tissues," *Journal of Natural Products*, vol. 66, no. 8, pp. 1051–1054, 2003.

[51] B. S. Joshi, K. L. Singh, and R. Roy, "Complete assignments of 1H and 13C NMR spectra of the pentacyclic triterpene hederagenin from Nigella sativa Linn," *Magnetic Resonance in Chemistry*, vol. 37, no. 4, pp. 295–298, 1999.

[52] D. Zhang, Y. Fu, J. Yang et al., "Triterpenoids and their glycosides from Glinus oppositifolius with antifungal activities against Microsporum gypseum and Trichophyton rubrum," *Molecules*, vol. 24, no. 12, p. 2206, 2019.

[53] T.-D. Lin and J. Shoji, "Constituents of*Panacis Japonici*Rhizoma. VI the structure of chikusetsu-saponin II, IVC," *Journal of the Chinese Chemical Society*, vol. 26, no. 1, pp. 29–35, 1979.

[54] K. Tori, S. Seo, A. Shimaoka, and Y. Tomita, "Carbon-13 NMR spectra of olean-12-enes. Full signal assignments including quaternary carbon signals assigned by use of indirect 13C, 1H spin couplings," *Tetrahedron Letters*, vol. 15, no. 48, pp. 4227–4230, 1974.

[55] W. Qiuling, H. Jing, F. Jun, and H. Mei, "Antitumor effect of betulinic acid on human acute leukemia K562 cells in vitro," *Journal of Huazhong University of Science and Technology - Medical sciences*, vol. 30, no. 4, pp. 453–457, 2010.

[56] B. Wu, X. Wang, Zf Chi et al., "Ursolic acid-induced apoptosis in K562 cells involving upregulation of PTEN gene expression and inactivation of the PI3K/Akt pathway," *Archives of Pharmacal Research*, vol. 35, no. 3, pp. 543–548, 2012.

[57] S. Pan, J. Hu, T. Zheng, X. Liu, Y. Ju, and C. J. C. Xu, "Oleanolic acid derivatives induce apoptosis in human leukemia K562 cell involved in inhibition of both Akt1 translocation and pAkt1 expression," *Cytotechnology*, vol. 67, no. 5, pp. 821–829, 2015.

[58] S. Anuchapreeda et al., "Antileukemic cell proliferation of active compounds from kaffir lime (citrus hystrix) leaves," in *Molecules*, eng, Ed., vol. 25, no. 6, p. 1300, 2020.

[59] H. Ge, X. Kong, L. Shi, L. Hou, Z. Liu, and P. Li, "Gamma-linolenic acid induces apoptosis and lipid peroxidation in human chronic myelogenous leukemia K562 cells," *Cell Biology International*, vol. 33, no. 3, pp. 402–410, 2009.

[60] G. M. Møller, V. Frost, J. V. Melo, and A. Chantry, "Upregulation of the TGFβ signalling pathway by Bcr-Abl: implications for haemopoietic cell growth and chronic myeloid leukaemia," *FEBS Letters*, vol. 581, no. 7, pp. 1329–1334, 2007.

[61] S. Mohan, A. B. Abdul, S. I. Abdelwahab et al., "Typhonium flagelliforme inhibits the proliferation of murine leukemia WEHI-3 cells in vitro and induces apoptosis in vivo," *Leukemia Research*, vol. 34, no. 11, pp. 1483–1492, 2010.

[62] S. Murakami, H. Takashima, M. Sato-Watanabe et al., "Ursolic acid, an antagonist for transforming growth factor (TGF)-β1," *FEBS Letters*, vol. 566, no. 1-3, pp. 55–59, 2004.

[63] F. Pellicano, L. Park, L. E. M. Hopcroft et al., "hsa-mir183/EGR1−mediated regulation of E2F1 is required for CML stem/progenitor cell survival," *Blood*, vol. 131, no. 14, pp. 1532–1544, 2018.

[64] F. J. Staal, F. Famili, L. Garcia Perez, and K. Pike-Overzet, "Aberrant Wnt signaling in leukemia," *Cancers*, vol. 8, no. 9, p. 78, 2016.

[65] D. Liu, L. Chen, H. Zhao, N. D. Vaziri, S.-C. Ma, and Y.-Y. Zhao, "Small molecules from natural products targeting the Wnt/β-catenin pathway as a therapeutic strategy," *Biomedicine & Pharmacotherapy*, vol. 117, Article ID 108990, 2019.

[66] M. Sheremet, S. Kapoor, P. Schröder, K. Kumar, S. Ziegler, and H. Waldmann, "Small molecules inspired by the natural

product withanolides as potent inhibitors of wnt signaling," *ChemBioChem*, vol. 18, no. 18, pp. 1797–1806, 2017.

[67] M. Ishibashi, "Screening for natural products that affect Wnt signaling activity," *Journal of Natural Medicines*, vol. 73, no. 4, pp. 697–705, 2019.

[68] Z. i. Skok, N. Zidar, D. Kikelj, and J. Ilaš, "Dual inhibitors of human DNA topoisomerase II and other cancer-related targets," *Journal of Medicinal Chemistry*, vol. 63, no. 3, pp. 884–904, 2019.

[69] A. R. James, B. Unnikrishnan, R. Priya et al., "Computational and mechanistic studies on the effect of galactoxyloglucan: imatinib nanoconjugate in imatinib resistant K562 cells," *Tumor Biology*, vol. 39, no. 3, Article ID 101042831769594, 2017.

[70] N. H. Zamakshshari, G. C. L. Ee, I. S. Ismail, Z. Ibrahim, and S. H. Mah, "Cytotoxic xanthones isolated from Calophyllum depressinervosum and Calophyllum buxifolium with antioxidant and cytotoxic activities," *Food and Chemical Toxicology*, vol. 133, Article ID 110800, 2019.

Research Article

Structure-Based Virtual Screening, Docking, ADMET, Molecular Dynamics, and MM-PBSA Calculations for the Discovery of Potential Natural SARS-CoV-2 Helicase Inhibitors from the Traditional Chinese Medicine

Ahmed M. Metwaly [1,2] **Alaa Elwan,**[3] **Abdul-Aziz M. M. El-Attar,**[4] **Sara T. Al-Rashood,**[5] **and Ibrahim H. Eissa** [3]

[1]*Pharmacognosy and Medicinal Plants Department, Faculty of Pharmacy (Boys), Al-Azhar University, Cairo 11884, Egypt*
[2]*Biopharmaceutical Products Research Department, Genetic Engineering and Biotechnology Research Institute, City of Scientific Research and Technological Applications (SRTA-City), Alexandria 21934, Egypt*
[3]*Pharmaceutical Medicinal Chemistry & Drug Design Department, Faculty of Pharmacy (Boys), Al-Azhar University, Cairo 11884, Egypt*
[4]*Pharmaceutical Analytical Chemistry Department, Faculty of Pharmacy, Al-Azhar University, Nasr City 11884, Cairo, Egypt*
[5]*Department of Pharmaceutical Chemistry, College of Pharmacy, King Saud University, P.O. Box 2457, Riyadh 11451, Saudi Arabia*

Correspondence should be addressed to Ahmed M. Metwaly; ametwaly@azhar.edu.eg and Ibrahim H. Eissa; ibrahimeissa@azhar.edu.eg

Continuing our antecedent work against COVID-19, a set of 5956 compounds of traditional Chinese medicine have been virtually screened for their potential against SARS-CoV-2 helicase (PDB ID: 5RMM). Initially, a fingerprint study with **VXG**, the ligand of the target enzyme, disclosed the similarity of 187 compounds. Then, a molecular similarity study declared the most similar 40 compounds. Subsequently, molecular docking studies were carried out to examine the binding modes and energies. Then, the most appropriate 26 compounds were subjected to *in silico* ADMET and toxicity studies to select the most convenient inhibitors to be: (1*R*,2*S*)-ephedrine (**57**), (1*R*,2*S*)-norephedrine (**59**), 2-(4-(pyrrolidin-1-yl)phenyl)acetic acid (**84**), 1-phenylpropane-1,2-dione (**195**), 2-methoxycinnamic acid (**246**), 2-methoxybenzoic acid (**364**), (*R*)-2-((*R*)-5-oxopyrrolidin-3-yl)-2-phenylacetic acid (**405**), (*Z*)-6-(3-hydroxy-4-methoxystyryl)-4-methoxy-2*H*-pyran-2-one (**533**), 8-chloro-2-(2-phenylethyl)-5,6,7-trihydroxy-5,6,7,8-tetrahydrochromone (**637**), 3-((1*R*,2*S*)-2-(dimethylamino)-1-hydroxypropyl)phenol (**818**), (*R*)-2-ethyl-4-(1-hydroxy-2-(methylamino)ethyl)phenol (**5159**), and (*R*)-2-((1*S*,2*S*,5*S*)-2-benzyl-5-hydroxy-4-methylcyclohex-3-en-1-yl)propane-1,2-diol (**5168**). Among the selected 12 compounds, the metabolites, compound **533** showed the best docking scores. Interestingly, the MD simulation studies for compound **533**, the one with the highest docking score, over 100 ns showed its correct binding to SARS-CoV-2 helicase with low energy and optimum dynamics. Finally, MM-PBSA studies showed that **533** bonded favorably to SARS-CoV-2 helicase with a free energy value of −83 kJ/mol. Further, the free energy decomposition study determined the essential amino acid residues that contributed favorably to the binding process. The obtained results give a huge hope to find a cure for COVID-19 through further *in vitro* and *in vivo* studies for the selected compounds.

1. Introduction

The WHO disclosed on December 25, 2021 that the confirmed COVID-19 infections globally became over 276 million including more than 5 million dead persons [1]. These massive numbers demand enormous work from scientists all over the world to find a cure.

The utilization of natural products for the treatment has been mentioned since the oldest historical points [2]; the traditional medicines were unlimited sources for bioactive natural compounds such as flavonoids [3–5], alkaloids [6], saponins [7–9], isochromenes [10], α-pyrones [11, 12], diterpenoids [13], sesquiterpenoids [14, 15], and steroids [16].

Traditional Chinese medicine (TCM) is an ethnomedicine that authenticates the experience of ancient Chinese people in the treatment of different illnesses [17]. TCM is a reflection of a great experience of clinical practice that extended for thousands of years [18]. To date, the TCM remedies are still utilized effectively in China as well as several places of the world [19, 20].

Computer-aided drug design methodologies play an ever-increasing essential role in the discovery of new drugs [21, 22]. These methodologies have been very effective in the identification of new promising drug candidates with a noticeable limitation in time, cost, effort, and use of animal models [13–15]. The application of *in silico* methodologies included molecular docking [16–23], molecular design [24, 25], rational drug design [26–31], computational chemistry [32, 33], toxicity [34–36], ADMET [37–39], and DFT [40] assessments.

Our teamwork utilized computer-based methodologies to determine potential inhibitors against COVID-19 in various reports. For example, metabolites of *Artemisia sublessingiana* [41]þ and *Monanchora* species [42] were examined *in silico* against COVID-19. We suggested four isoflavonoids between a set of 59 as the most promising inhibitors against hACE2 and M^{pro} [43]. Recently, our team adjusted a multistep *in silico* filtration technique to select the most promising compound through a huge group of compounds against a certain COVID-19 protein. For instance, vidarabine was selected to be the most promising inhibitor against SARS-CoV-2 nsp10 [44]. Complementarily, the most convenient semisynthetic molecule against PLpro has been determined via a set of 69 compounds [45].

Helicases are pivotal enzymes in the viral lifecycle because of their responsibility to separate the dsDNA or RNA strands as well as their essential role in the process of RNA replication and repair [46]. Helicases can translocate molecules along the double-stranded (ds) DNA as well as RNA in a certain direction. Additionally, it can unwind (separate) the complementary strand of the DNA duplex through the dissociation of the hydrogen bonds between the nucleotide bases [47].

In this work, a collection of 5956 natural compounds, that were derived from traditional Chinese medicine and available at http://tcm.cmu.edu.tw/, has been subjected to structure and ligand-based *in silico* approaches (Figure 1) to determine the most convenient SARS-CoV-2 helicase inhibitors. The starting step in our research was (3*S*,4*R*)-1-acetyl-4-phenylpyrrolidine-3-carboxylic acid (**VXG**), the co-crystallized ligand of the SARS-CoV-2 helicase (PDB ID: 5RMM). **VXG** showed a high binding affinity against the target enzyme. Accordingly, it is expected according to the SAR principles that any compound with a similar structure could have a high binding affinity too. The utilized *in silico* methods included molecular structure similarity and fingerprint study against the **VXG**. Then, molecular docking against SARS-CoV-2 helicase (PDB ID: 5RMM) was conducted to examine the binding. ADMET and toxicity were utilized to make sure about the likeness of the selected compounds. Finally, molecular dynamics (MD) simulation experiments (RMSD, RMSF, R_g, SASA, and H-bonding) over 100 ns for the compound of the highest docking score, as well as MM-PBSA studies, were preceded to confirm the correct binding mode.

2. Results and Discussion

2.1. Molecular Filtration Using Fingerprint Method. The ligand-based *in silico* approach depends on the computation of chemical and physical properties of a molecule (ligand) and comparison of these properties with some biologically active compounds [48]. The fingerprint study is one of the ligand-based *in silico* methods that is vastly employed to predict the chemical structure's similarity or dissimilarity of two compounds or more [49, 50]. During the fingerprint study, the computer converts the chemical descriptors of a molecule to mathematical symbols. The obtained data are presented as bit strings. These strings describe the presence (1) or absence (0) of a certain 2D fragment or atomic descriptor (property) in the test and reference molecules [51, 52]. The co-crystallized ligand is a molecule that has a very high affinity to bind to a specific protein forming a ligand-protein complex in a crystallized form [53]. In consequence, the chemical structure of the co-crystallized ligand could be utilized effectively as a starting point to design and discover a potential inhibitor against the target protein.

Discovery studio 4.0 software was employed to examine the fingerprint similarity of 5956 natural compounds, which were derived from traditional Chinese medicine, against **VXG**, the co-crystallized ligand of SARS-CoV-2 helicase (PDB ID: 5RMM). The experiment determined 187 compounds to be the most similar candidates to **VXG** (Table 1). The study compared the following descriptors (properties) in the chemical structures of the experiment set and **VXG**: H-bond acceptor [54], H-bond donor [55], charge [56], hybridization [57], positive ionizable atoms [58], negative ionizable atoms [59], halogens [60], aromatic groups [61], and aligning with the ALog$P$ [62] of fragments as well as atoms.

2.2. Molecular Similarity. The difference between molecular similarity and fingerprint studies is that the fingerprint study computes the presence and/or absence of specific 2D atom
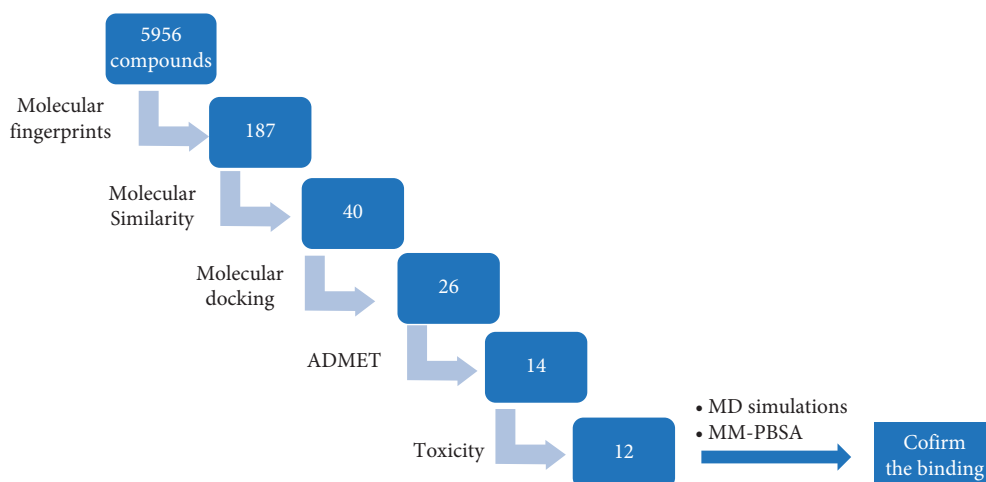
Figure 1: The employed computational techniques.

Table 1: Fingerprint similarity between 187 natural compounds and **VXG**.

Comp.	Similarity	SA	SB	SC	Comp.	Similarity	SA	SB	SC
VXG	1	166	0	0	**5412**	0.582205	602	580	−148
138	1	160	100	6	**1585**	0.581927	586	553	−132
167	1	169	118	−3	**1566**	0.581457	439	301	15
215	1	180	166	−14	**810**	0.581121	197	173	−31
258	1	153	128	13	**5449**	0.580863	431	288	23
347	1	143	101	23	**2379**	0.580247	329	113	125
364	1	90	−7	76	**5154**	0.579775	258	−9	196
379	1	143	101	23	**3239**	0.579154	589	563	−135
380	1	143	101	23	**2356**	0.57854	523	450	−69
411	1	112	42	54	**3258**	0.578205	451	326	3
445	1	186	146	−20	**3589**	0.578089	496	404	−42
496	1	196	201	−30	**362**	0.577495	272	17	182
501	1	163	145	3	**5439**	0.577398	608	599	−154
507	1	158	136	8	**3255**	0.577267	452	329	2
526	1	143	101	23	**1584**	0.576874	454	333	0
533	1	133	70	33	**71**	0.576792	169	127	−3
552	1	173	123	−7	**623**	0.576792	169	127	−3
554	1	173	121	−7	**38**	0.576087	265	6	189
555	1	173	121	−7	**5441**	0.576077	602	591	−148
577	1	154	90	12	**1982**	0.575087	494	405	−40
610	1	116	39	50	**398**	0.57485	96	1	70
619	1	156	131	10	**114**	0.561111	101	14	65
637	1	162	108	4	**816**	0.56	112	34	54
733	1	169	157	−3	**92**	0.556886	93	1	73
756	1	206	193	−40	**169**	0.556886	93	1	73
782	1	220	219	−54	**5157**	0.556701	108	28	58
792	1	207	178	−41	**451**	0.554878	182	162	−16
794	1	196	177	−30	**5154**	0.554307	148	101	18
803	1	169	147	−3	**768**	0.55418	179	157	−13
806	1	210	206	−44	**190**	0.553299	109	31	57
807	1	183	144	−17	**557**	0.55298	167	136	−1
818	1	99	9	67	**629**	0.55	176	154	−10
2379	1	213	229	−47	**495**	0.543333	163	134	3
405	0.777	136	9	30	**433**	0.538462	91	3	75
442	0.738	127	6	39	**754**	0.537764	178	165	−12
85	0.731	125	5	41	**566**	0.534743	177	165	−11
260	0.722	117	−4	49	**354**	0.534535	178	167	−12
208	0.697	124	12	42	**597**	0.53271	171	155	−5
91	0.689	122	11	44	**596**	0.531148	162	139	4

TABLE 1: Continued.

Comp.	Similarity	SA	SB	SC	Comp.	Similarity	SA	SB	SC
102	0.689	122	11	44	**601**	0.528302	168	152	−2
195	0.681	109	−6	57	**752**	0.527473	192	198	−26
280	0.674	116	6	50	**568**	0.526946	176	168	−10
344	0.658	121	18	45	**790**	0.526012	182	180	−16
370	0.658	121	18	45	**2368**	0.523041	227	268	−61
672	0.652	167	90	−1	**439**	0.522222	188	194	−22
48	0.649	113	8	53	**158**	0.521978	95	16	71
58	0.649	113	8	53	**5152**	0.521898	143	108	23
100	0.646	104	−5	62	**250**	0.520408	153	128	13
246	0.644	105	−3	61	**591**	0.519737	158	138	8
84	0.638	118	19	48	**5153**	0.517699	117	60	49
5169	0.636	159	84	7	**150**	0.517241	90	8	76
817	0.633	126	33	40	**297**	0.515789	147	119	19
396	0.624	106	4	60	**2370**	0.515738	213	247	−47
245	0.622	102	−2	64	**5167**	0.51567	181	185	−15
57	0.62	106	5	60	**413**	0.513986	147	120	19
65	0.62	106	5	60	**491**	0.513699	150	126	16
1942	0.614339	497	355	−43	**5177**	0.512195	189	203	−23
5415	0.614108	592	510	−138	**415**	0.511945	150	127	16
5434	0.614017	587	502	−133	**5151**	0.511696	175	176	−9
3941	0.613833	426	240	28	**2367**	0.511364	225	274	−59
4050	0.613551	489	343	−35	**544**	0.511299	181	188	−15
5441	0.613124	626	567	−172	**5159**	0.511111	92	14	74
5039	0.613119	458	293	−4	**266**	0.510903	164	155	2
4055	0.612984	491	347	−37	**374**	0.510563	145	118	21
3591	0.612751	519	393	−65	**418**	0.510417	147	122	19
2348	0.612622	563	465	−109	**5155**	0.510288	124	77	42
3912	0.612319	507	374	−53	**207**	0.510274	149	126	17
3579	0.612128	535	420	−81	**5149**	0.51005	203	232	−37
3919	0.611429	428	246	26	**5180**	0.508197	186	200	−20
5055	0.611111	440	266	14	**299**	0.507042	144	118	22
5168	0.61	158	93	8	**5158**	0.506329	120	71	46
539	0.609	162	100	4	**5176**	0.505208	194	218	−28
342	0.608	110	15	56	**397**	0.505051	150	131	16
511	0.608	178	127	−12	**614**	0.505017	151	133	15
784	0.607	193	152	−27	**622**	0.504983	152	135	14
564	0.605	182	135	−16	**512**	0.504615	164	159	2
201	0.604	186	142	−20	**5173**	0.50358	211	253	−45
542	0.589905	187	151	−21	**639**	0.503356	150	132	16
492	0.58885	169	121	−3	**50**	0.503165	159	150	7
228	0.586319	180	141	−14	**116**	0.502982	253	337	−87
2365	0.584081	521	438	−67	**80**	0.502092	120	73	46
3254	0.58408	587	551	−133	**3288**	0.502092	240	312	−74
206	0.583178	624	616	−170	**454**	0.502075	121	75	45
1571	0.582915	464	342	−10	**419**	0.501742	144	121	22
3591	0.582851	503	409	−49	**621**	0.50165	152	137	14
1593	0.582512	473	358	−19	**203**	0.501449	173	179	−7
59	0.582353	99	4	67	**3291**	0.501006	249	331	−83
64	0.582353	99	4	67	**86**	0.5	154	142	12
86	0.582278	276	20	178	**118**	0.5	100	34	66

SA, bits number in both similar natural compounds and **VXG**; SB, bits number in the similar natural compounds but not in **VXG**; SC, bits number in **VXG** but not in the similar natural compounds.

paths and descriptors regarding fragments or substructures in the examined compounds [63]. Contrastingly, the molecular similarity calculates specific molecular descriptors considering the whole chemical structure of compounds. These descriptors are steric, topological, electronic, and/or physical [64]. Utilizing Discovery studio 4.0 software, a molecular similarity study was

done on the most similar 187 compounds against **VXG.** The applied descriptors in this study (Figure 2 and Table 2) were partition coefficient ($A\text{Log } p$) [65], molecular weight (M. W) [66], H-bond donors (HBA) [67], H-bond acceptors (HBD) [68], rotatable bond numbers [69], number of rings as well as aromatic rings [70], and minimum distance [71] together with the molecular
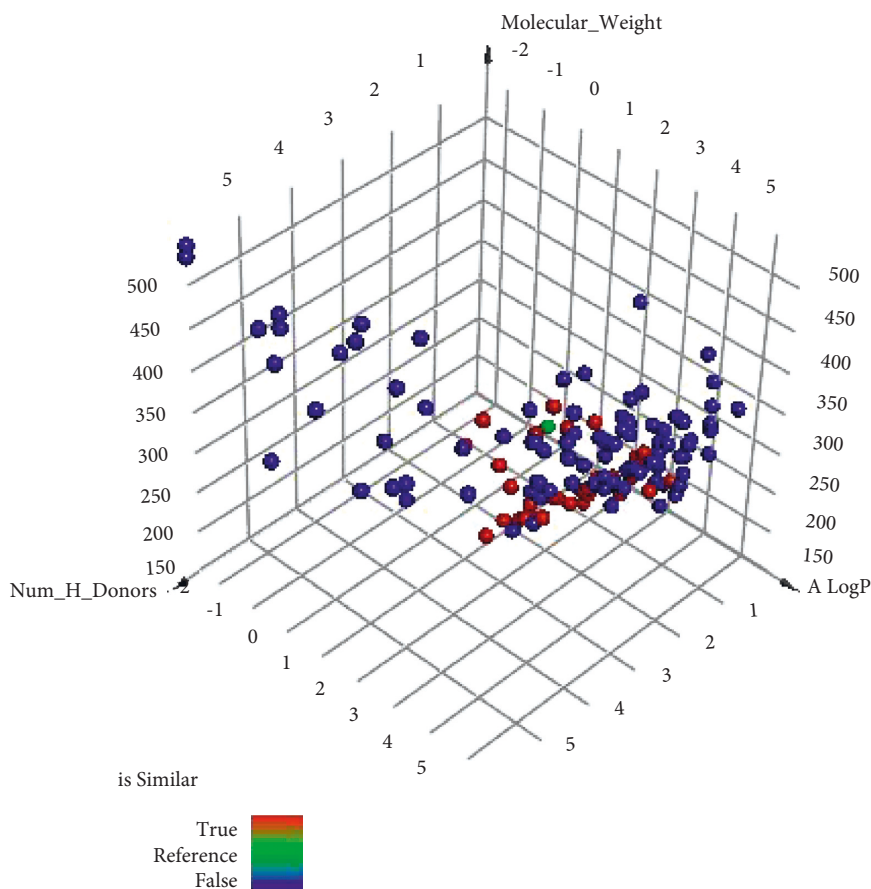
Figure 2: Molecular similarity of the examined compounds and **VXG**.

fractional polar surface area (MFPSA) [72]. The study was adapted to select the most similar 40 metabolites (Figure 3).

2.3. Docking Studies. Computer-aided drug design applies various techniques to optimize natural products into potentially active against certain biological targets [44, 45]. A molecular docking technique was applied for 40 **VXG** similar compounds against SARS-CoV-2 helicase (PDB ID: 5RMM). The binding modes and affinities of these compounds were examined.

The target protein was downloaded from Protein Data Bank (http://www.pdb.org), and Molecular Operating Environment (MOE .14) was used for the docking analysis. The docking process was validated by the re-docking of **VXG** inside the active pocket of the helicase protein. The root mean square deviation (RMSD) between the re-docked and the co-crystallized conformers was 0.74 A, which confirms the validity of the docking protocol (Figure 4).

Out of the examined 40 compounds, 26 displayed correct binding modes as well as good free energies. The promising compounds are as follows: (+)-methyl-pseudoephedrine (**48**), (1*R*,2*S*)-ephedrine (**57**), (1*R*,2*S*)-N-methylephedrine (**58**), (1*R*,2*S*)-norephedrine (**59**), (3*S*)-2,2-

dimethyl-3,5-dihydroxy-8-hydroxymethyl-3,4-dihydro-2*H*,6*H*-benzo[1,2-*b*5,4-*b′*]dipyran-6-one (**80**), 2-(4-(pyrrolidin-1-yl)phenyl)acetic acid (**84**), (4*S*,5*R*)-ephedroxane (**85**), 1-phenylpropane-1,2-dione (**195**), 2-methoxycinnamaldehyde (**245**), 2-methoxycinnamic acid (**246**), 2-methoxybenzoic acid (**364**), 3′-*o*-acetylhamaudol (**374**), 3′-*o*-propionylhamaudol (**388**), (*R*)-2-((*R*)-5-oxopyrrolidin-3-yl)-2-phenylacetic acid (**405**), (*Z*)-6-(3-hydroxy-4-methoxystyryl)-4-methoxy-2*H*-pyran-2-one (**533**), 6,7-dihydroxy-2-(2-phenylethyl)-5,6,7,8-tetrahydrochromone (**539**), 7-demethylsuberosin (**610**), 8-chloro-2-(2-phenylethyl)-5,6,7-trihydroxy-5,6,7,8-tetrahydrochromone (**637**), 3-((*R*)-hydroxy ((*S*)-1-methylpiperidin-2-yl)methyl)phenol (**816**), (*R*)-((*S*)-1-methylpiperidin-2-yl)(phenyl)methanol (**817**), 3-((1*R*,2*S*)-2-(dimethylamino)-1-hydroxypropyl)phenol (**818**), (*R*)-4-(1-Hydroxy-2-(methyl-amino)ethyl)-7,7-dimethyl-5,6,7,8-tetrahydronaphthalen-1-ol (**5153**),(*R*)-4-(1-hydroxy-2-(methylamino)ethyl)-8,8-dimethyl-6,7,8,9-tetrahydro-5*H*-benzo [7]annulen-1-ol (**5155**), (*R*)-2-ethyl-4-(1-hydroxy-2-(methylamino)ethyl)phenol (**5159**), (*R*)-2-((1*S*,2*S*,5*S*)-2-benzyl-5-hydroxy-4-methyl-cyclohex-3-en-1-yl)propane-1,2-diol (**5168**), and (1*S*,4*R*,5*S*)-4-benzyl-5-(2-hydroxypropan-2-yl)-2-methylcyclohex-2-en-1-ol (**5169**).

The docking scores of the experienced ligands are predicted and summarized in Table 3. The binding modes of the

Table 2: Molecular descriptors of the examined 40 compounds and **VXG**.

Comp.	ALog p	M. Wt	HBA	HBD	Rotatable bonds	Rings	Aromatic rings	MFPSA	Minimum distance
VXG	0.71	233.26	3	1	2	2	1	0.237	
405	0.62	219.24	3	2	3	2	1	0.307	0.357
84	2.12	205.25	3	1	3	2	1	0.187	0.446
816	2.1	221.3	3	2	2	2	1	0.181	0.454
433	1.69	178.19	3	1	3	1	1	0.239	0.529
100	1.09	149.19	2	1	2	1	1	0.252	0.531
342	2.76	204.22	3	1	2	2	1	0.224	0.541
533	1.97	274.27	5	1	4	2	1	0.229	0.552
818	1.53	195.26	3	2	3	1	1	0.187	0.553
364	1.44	152.15	3	1	2	1	1	0.285	0.555
246	1.91	178.19	3	1	3	1	1	0.24	0.559
59	0.8	151.21	2	2	2	1	1	0.264	0.56
64	0.8	151.21	2	2	2	1	1	0.264	0.56
539	1.57	286.32	4	2	3	3	1	0.239	0.564
150	1.54	178.19	3	2	2	1	1	0.3	0.568
85	2.03	191.23	2	0	1	2	1	0.143	0.575
398	1.81	164.2	2	1	3	1	1	0.202	0.596
195	1.45	148.16	2	0	2	1	1	0.21	0.597
57	1.23	165.23	2	2	3	1	1	0.165	0.614
65	1.23	165.23	2	2	3	1	1	0.165	0.614
817	2.34	205.3	2	1	2	2	1	0.102	0.648
5168	2.17	276.37	3	3	4	2	1	0.198	0.672
5153	2.59	249.35	3	3	3	2	1	0.181	0.678
5159	1.56	195.26	3	3	4	1	1	0.231	0.691
118	2.22	203.28	2	0	0	2	1	0.122	0.695
374	2.4	317.36	4	2	2	3	1	0.244	0.706
245	1.93	162.19	2	0	3	1	1	0.143	0.713
48	1.77	179.26	2	1	3	1	1	0.105	0.715
58	1.77	179.26	2	1	3	1	1	0.105	0.715
114	2.2	194.23	3	0	4	1	1	0.157	0.731
610	3.51	230.26	3	1	2	2	1	0.192	0.738
388	2.01	333.36	5	2	3	3	1	0.264	0.743
5169	3.05	260.37	2	2	3	2	1	0.136	0.76
260	1.93	164.2	2	0	4	1	1	0.141	0.765
91	2.99	188.22	2	0	1	2	1	0.131	0.769
102	2.99	188.22	2	0	1	2	1	0.131	0.769
280	1.98	177.24	2	0	1	2	1	0.062	0.775
5155	3.04	263.38	3	3	3	2	1	0.171	0.782
637	1.37	336.77	5	3	3	3	1	0.282	0.784
208	2.16	191.27	2	0	1	2	1	0.057	0.795
80	0.9	292.28	6	3	1	3	1	0.337	0.81

tested ligands inside the active site of the target protein were depicted. The binding poses of the top five compounds with the highest energy scores as well as the most perfect modes were selected for detailed discussion as representative examples.

Starting with the binding interactions and orientation of the co-crystallized ligand (**VXG**) inside the active SARS-CoV-2 helicase (PDB ID: 5RMM), it revealed a binding affinity value of −19.37 kcal/mol. It showed a characteristic four hydrogen bonding interactions through carboxylate moiety of pyrrolidine ring with the essential amino acids SER486, ASN516, and ASN177. In addition, two hydrophobic interactions were formed between pyrrolidine ring and amino acid residues HIS554 and TYR515 (Figure 5).

The results of docking studies showed that the tested ligands have orientations and binding interactions similar

to that of **VXG** against SARS-CoV-2 helicase. Three- and two-dimensional representations of binding modes of the most potent derivatives **533**, **637**, **84**, **195**, and **364** inside the active site of the target protein are depicted in Figures 6–10.

Compound **533** exhibited an interesting binding mode similar to that of the co-crystallized ligand against SARS-CoV-2 helicase with a docking score of −17.10 kcal/mol. It keeps the hydrogen bonding interactions with the essential amino acids SER486, ASN516, and ASN177. Also, it formed two additional hydrogen bonds with ASN179 and SER485 residues. Furthermore, compound **533** was incorporated in two hydrophobic interactions with amino acid residues HIS554 and TYR515 (Figure 6).

For compound **637**, the binding affinity was −18.85 kcal/mol. Such compound exhibited the best binding mode into
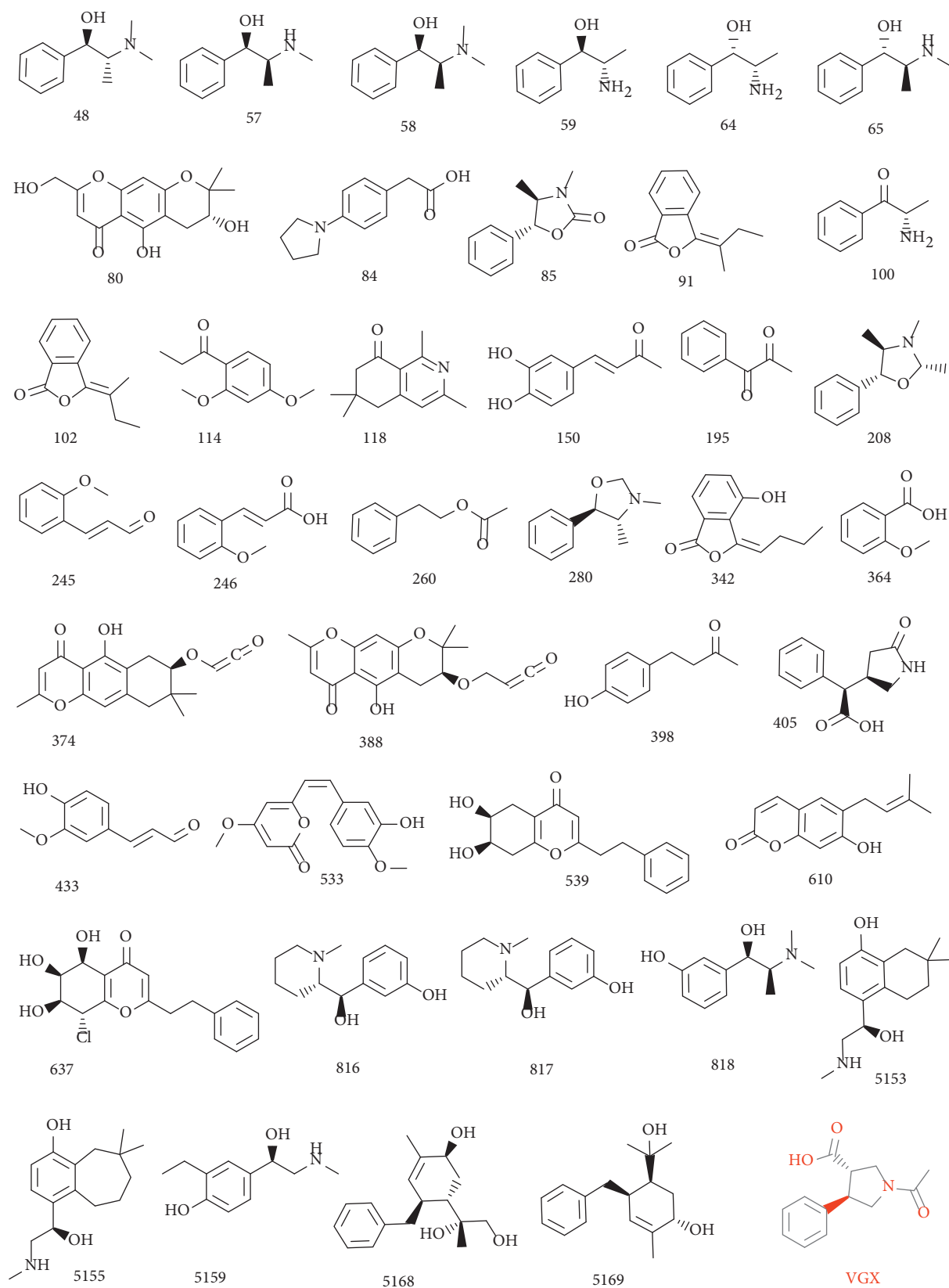
FIGURE 3: The most similar compounds to **VXG**.

(a)

(b)
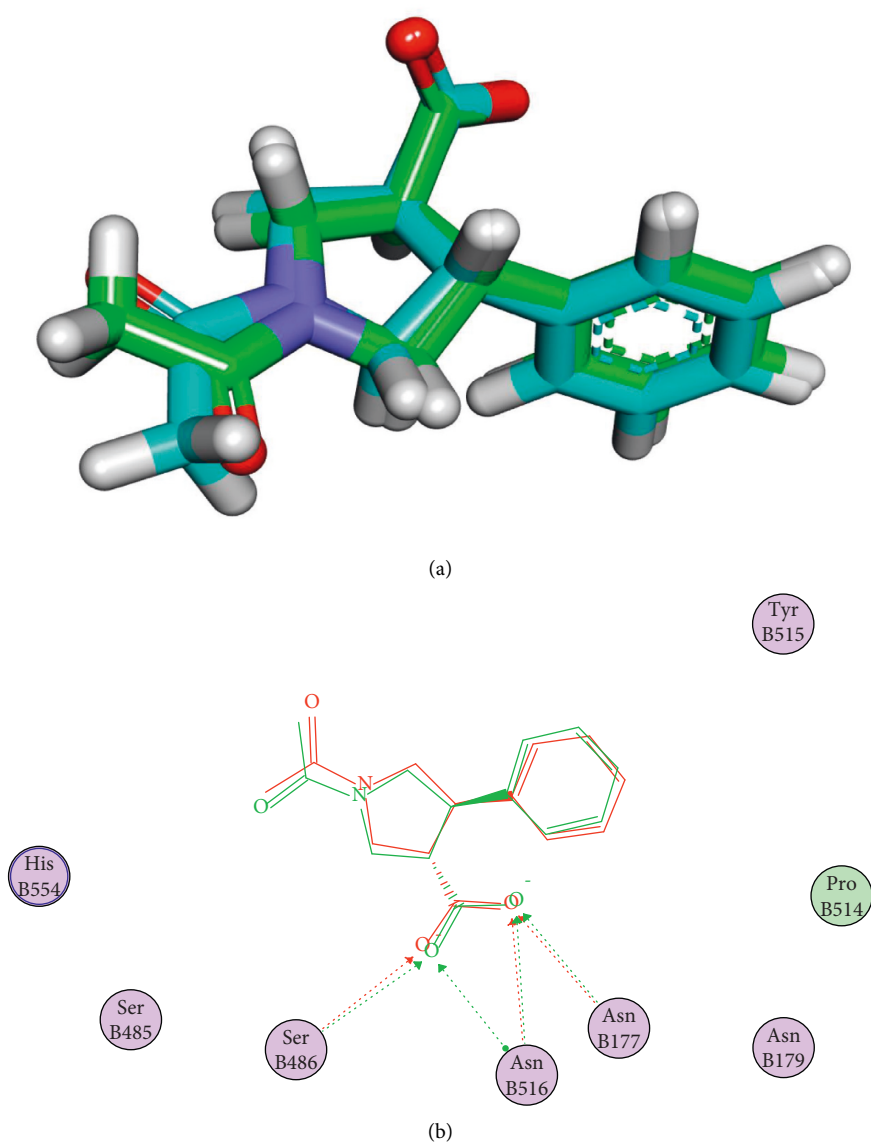
FIGURE 4: (a) 3D and (b) 2D superimposition of the re-docked conformer of **VXG** over the co-crystallized one with an RMSD value of 0.74 Å.

TABLE 3: ΔG (in kcal/mole) of the most similar 40 compounds to **VXG**.

Compound	Name	ΔG (kcal/mole)
48	(+)-Methylpseudoephedrine	−15.92
57	(1*R*,2*S*)-Ephedrine	−15.64
58	(1*R*,2*S*)-*N*-methylephedrine	−15.24
59	(1*R*,2*S*)-Norephedrine	−14.29
64	(1*S*,2*S*)-Norpseudoephedrine	−13.65
65	(1*S*,2*S*)-Pseudoephedrine	−11.66
80	(3S)-2,2-Dimethyl-3,5-dihydroxy-8-hydroxymethyl-3,4-dihydro-2*H*,6*H*-benzo[1,2-*b*5,4-*b′*]dipyran-6-one	−14.27
84	2-(4-(Pyrrolidin-1-yl) phenyl) acetic acid	−15.46
85	(4*S*,5*R*)-Ephedroxane	−14.01
91	(*E*)-3-Butylidene phthalide	−13.31
100	(*S*)-Cathinone	−12.6
102	(*Z*)-3-Butylidene phthalide	−13.9
114	1-(2,4-Dimethoxyphenyl)-1-propanone	−13.53

TABLE 3: Continued.

Compound	Name	ΔG (kcal/mole)
118	1,3,6,6-Tetramethyl-6,7-dihydroisoquinolin-8(5*H*)-one	−12.41
150	(4*S*,5*R*)-Ephedroxane	−13.02
195	1-Phenylpropane-1,2-dione	−11.07
208	2,3,4-Trimethyl-5-phenyloxazolidine	−13.76
245	2-Methoxycinnamaldehyde	−14.92
246	2-Methoxycinnamic acid	−14.22
260	2-Phenylethyl acetate	−13.29
280	3,4-Dimethyl-5-phenyloxazolidine	−13.21
342	3-Butylidene-4-hydro-phthalide	−13.24
364	2-Methoxybenzoic acid	−12.16
374	3′-*o*-Acetylhamaudol	−18.21
388	3′-*o*-Propionylhamaudol	−18.13
398	4-(4-Hydroxyphenyl)-2-butanone	−12.88
405	(*R*)-2-((*R*)-5-Oxopyrrolidin-3-yl)-2-phenylacetic acid	−15.74
433	4-Hydroxy-3-methoxycinnamaldehyde	−13.11
533	(*Z*)-6-(3-Hydroxy-4-methoxystyryl)-4-methoxy-2*H*-pyran-2-one	−17.1
539	6,7-Dihydroxy-2-(2-phenylethyl)-5,6,7,8-tetrahydrochromone	−18.36
610	7-Demethylsuberosin	−15.48
637	8-Chloro-2-(2-phenylethyl)-5,6,7-trihydroxy-5,6,7,8-tetrahydrochromone	−18.85
816	3-((*R*)-Hydroxy ((*S*)-1-methylpiperidin-2-yl)methyl)phenol	−17.09
817	(*R*)-((*S*)-1-Methylpiperidin-2-yl) (phenyl)methanol	−15.95
818	3-((1*R*,2*S*)-2-(Dimethylamino)-1-hydroxypropyl)phenol	−15.79
5153	(*R*)-4-(1-Hydroxy-2-(methylamino)ethyl)-7,7-dimethyl-5,6,7,8-tetrahydronaphthalen-1-ol	−17.84
5155	(*R*)-4-(1-Hydroxy-2-(methylamino)ethyl)-8,8-dimethyl-6,7,8,9-tetrahydro-5*H*-benzo[7]annulen-1-ol	−16.59
5159	(*R*)-2-Ethyl-4-(1-hydroxy-2-(methylamino)ethyl)phenol	−17.89
5168	(*R*)-2-((1*S*,2*S*,5*S*)-2-Benzyl-5-hydroxy-4-methylcyclohex-3-en-1-yl)propane-1,2-diol	−18.4
5169	(1*S*,4*R*,5*S*)-4-Benzyl-5-(2-hydroxypropan-2-yl)-2-methylcyclohex-2-en-1-ol	−17.42
VXG	(3*S*,4*R*)-1-Acetyl-4-phenylpyrrolidine-3-carboxylic acid	−19.37
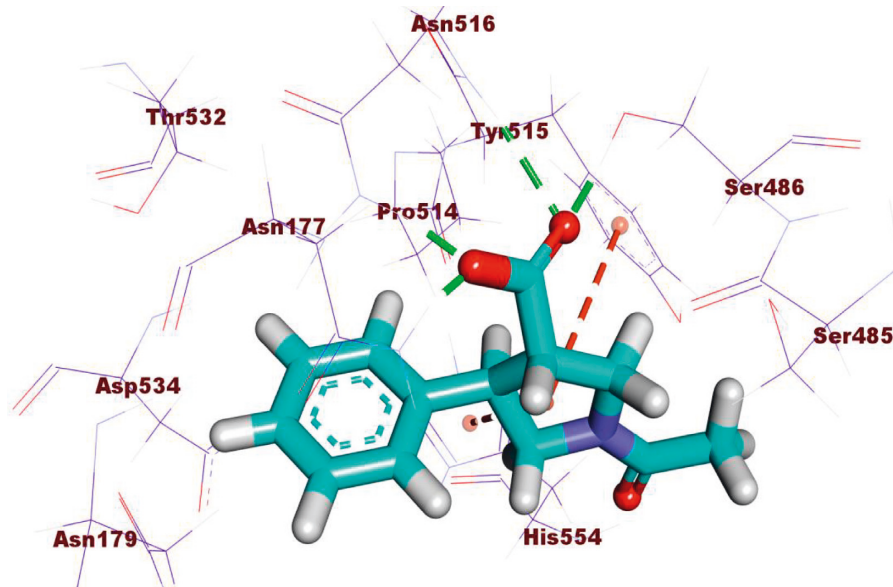
(a)

FIGURE 5: Continued.

(b)
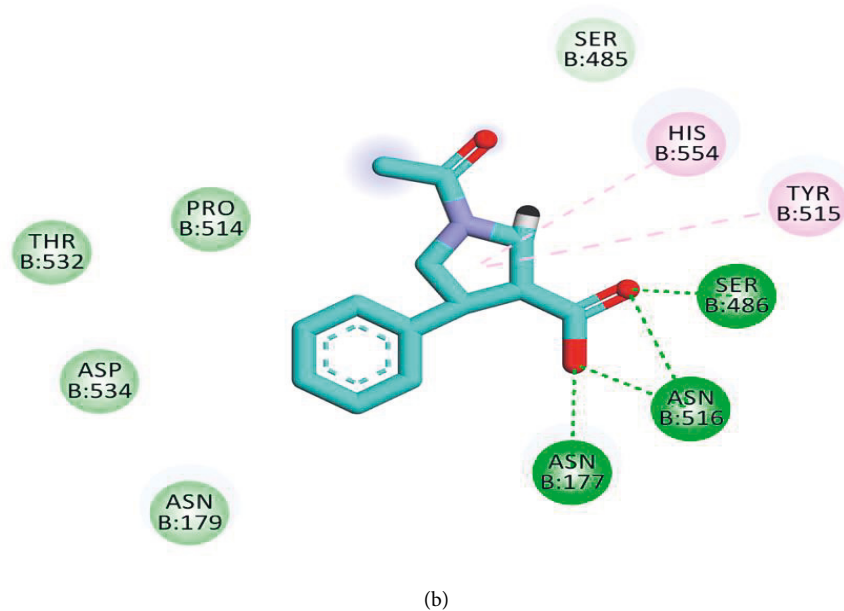
FIGURE 5: (a) 3D and (b) 2D of **VXG** docked into the active site of SARS-CoV-2 helicase.

(a)
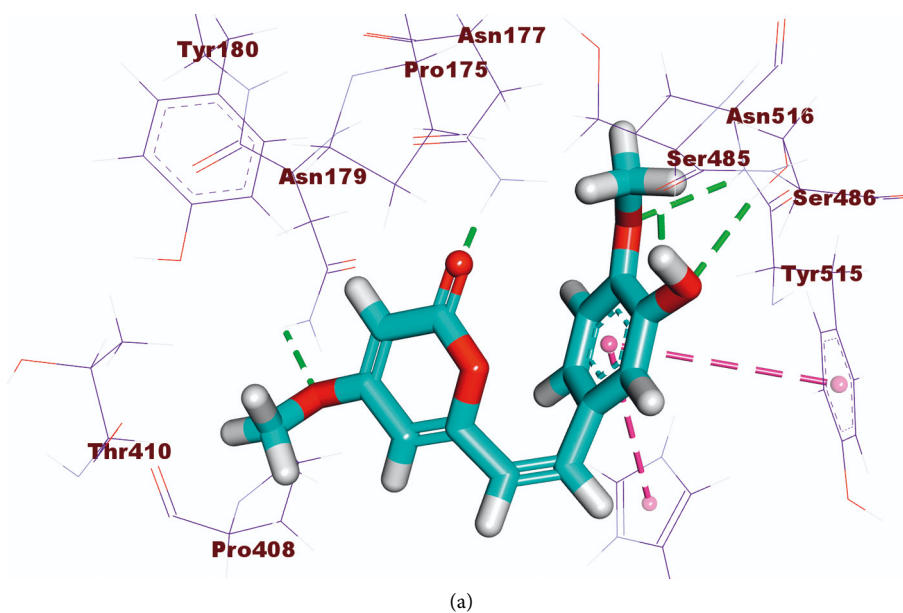
FIGURE 6: Continued.

(b)
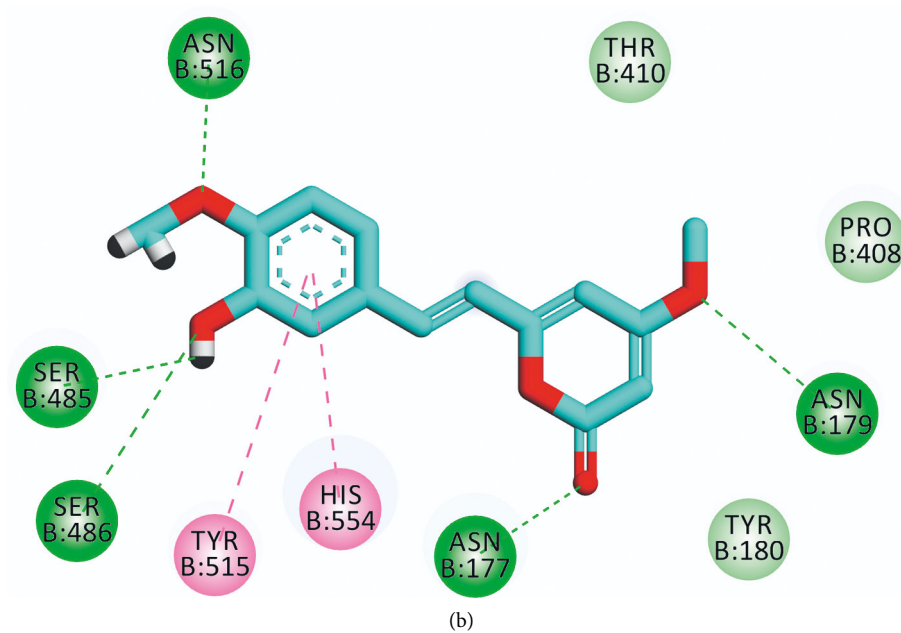
FIGURE 6: (a) 3D and (b) 2D images of the docked compound **533** into the active site of SARS-CoV-2 helicase.

(a)
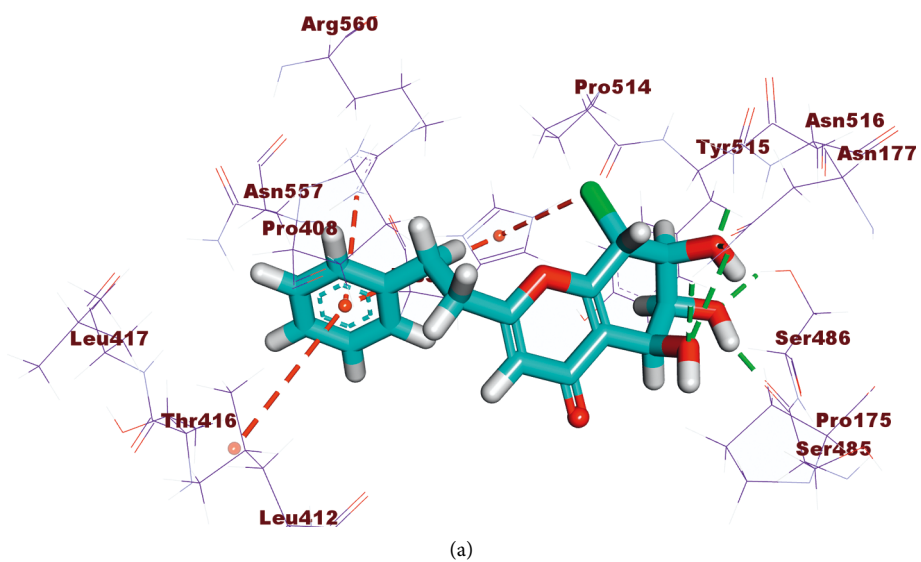
FIGURE 7: Continued.

(b)
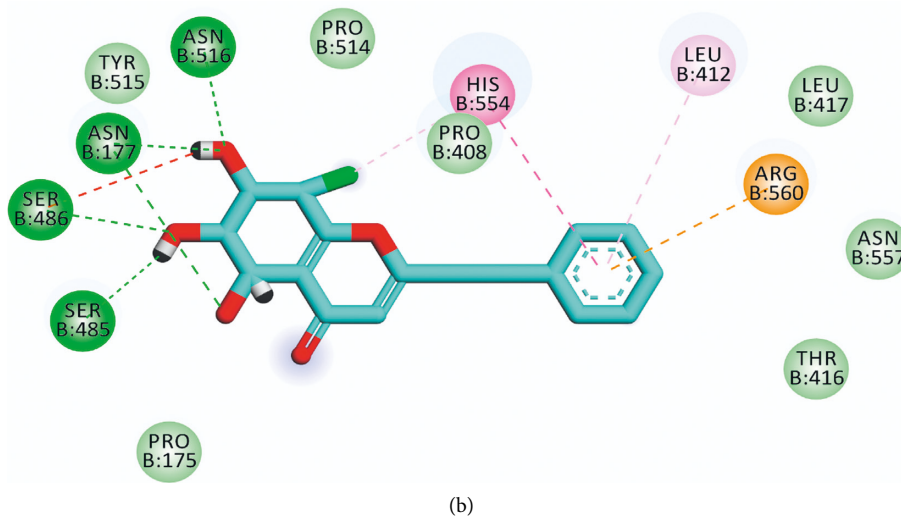
FIGURE 7: (a) 3D and (b) 2D images of the docked compound **637** into the active site of SARS-CoV-2 helicase.

(a)

(b)
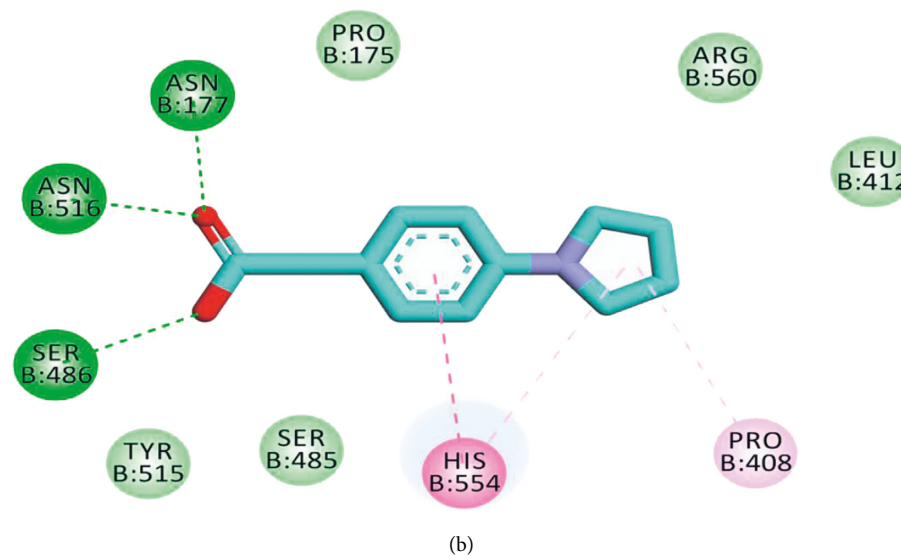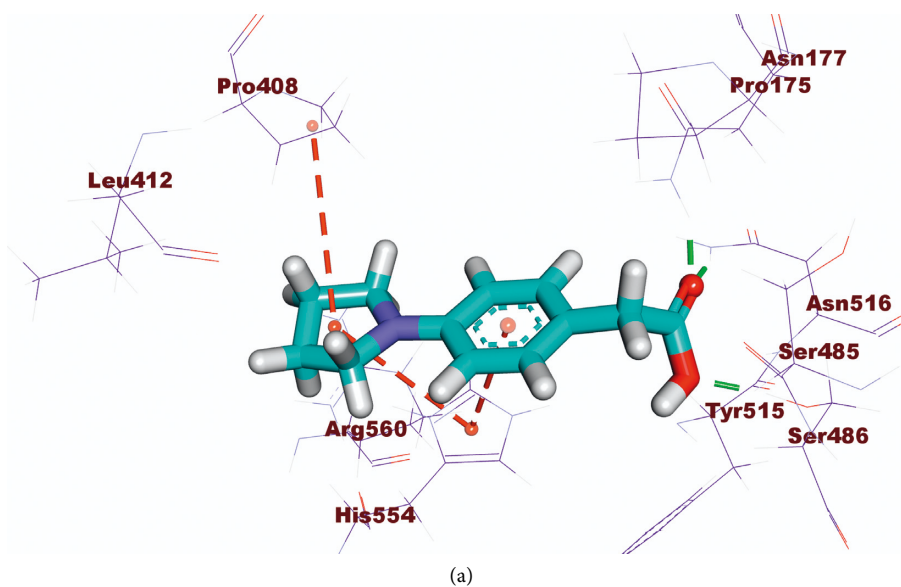
FIGURE 8: (a) 3D and (b) 2D images of the docked compound **84** into the active site of SARS-CoV-2 helicase.

(a)

(b)
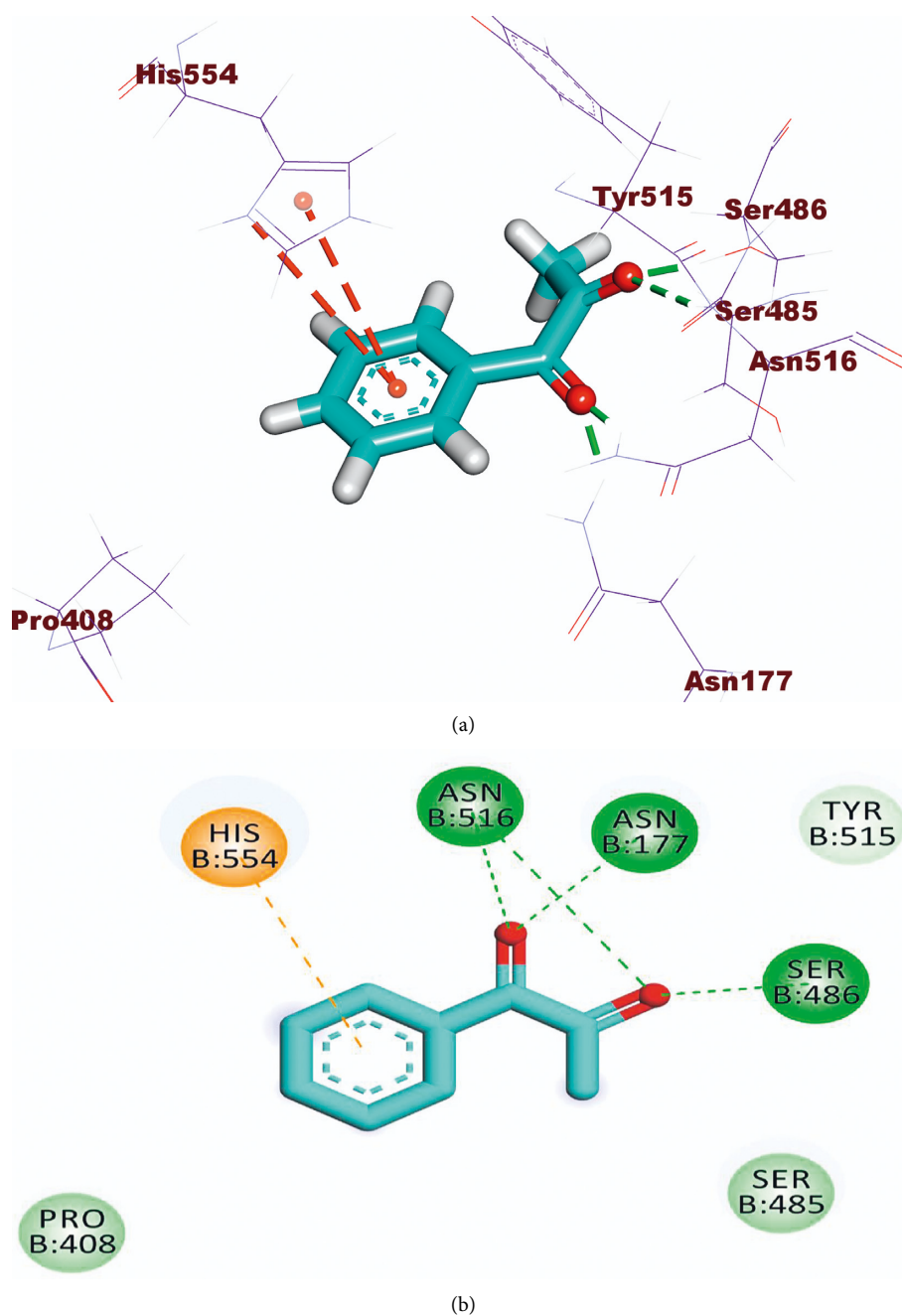
Figure 9: (a) 3D and (b) 2D images of the docked compound **195** into the active site of SARS-CoV-2 helicase.

the target protein, where it completely occupied the protein through seven hydrogen bonding interactions with SER486, ASN516, ASN177, SER485, and HIS554 residues. In addition, the terminal phenyl ring formed three hydrophobic interactions with HIS554, LEU412, and ARG560 residues (Figure 7).

Concerning the binding mode of compound **84** against SARS-CoV-2 helicase, the binding energy was −15.46 kcal/mol. The structural similarity of that compound with the co-crystallized ligand revealed the same binding mode against the receptor, where three hydrogen bonds were formed with SER486, ASN516, and ASN177 and three hydrophobic interactions were molded with HIS554 and PRO408 (Figure 8).

The binding affinity of compound **195** was −11.07 kcal/mol. Such affinity was represented by four hydrogen bonds with the key amino acids SER486, ASN516, and ASN177 and one hydrophobic interaction with HIS554 (Figure 9).

Finally, analyzing the binding interactions of compound **364** indicated a binding score of −12.16 kcal/mol. The carboxylate moiety formed three hydrogen bonding interactions with the key amino acids SER486, ASN516, and ASN177

(a)

(b)
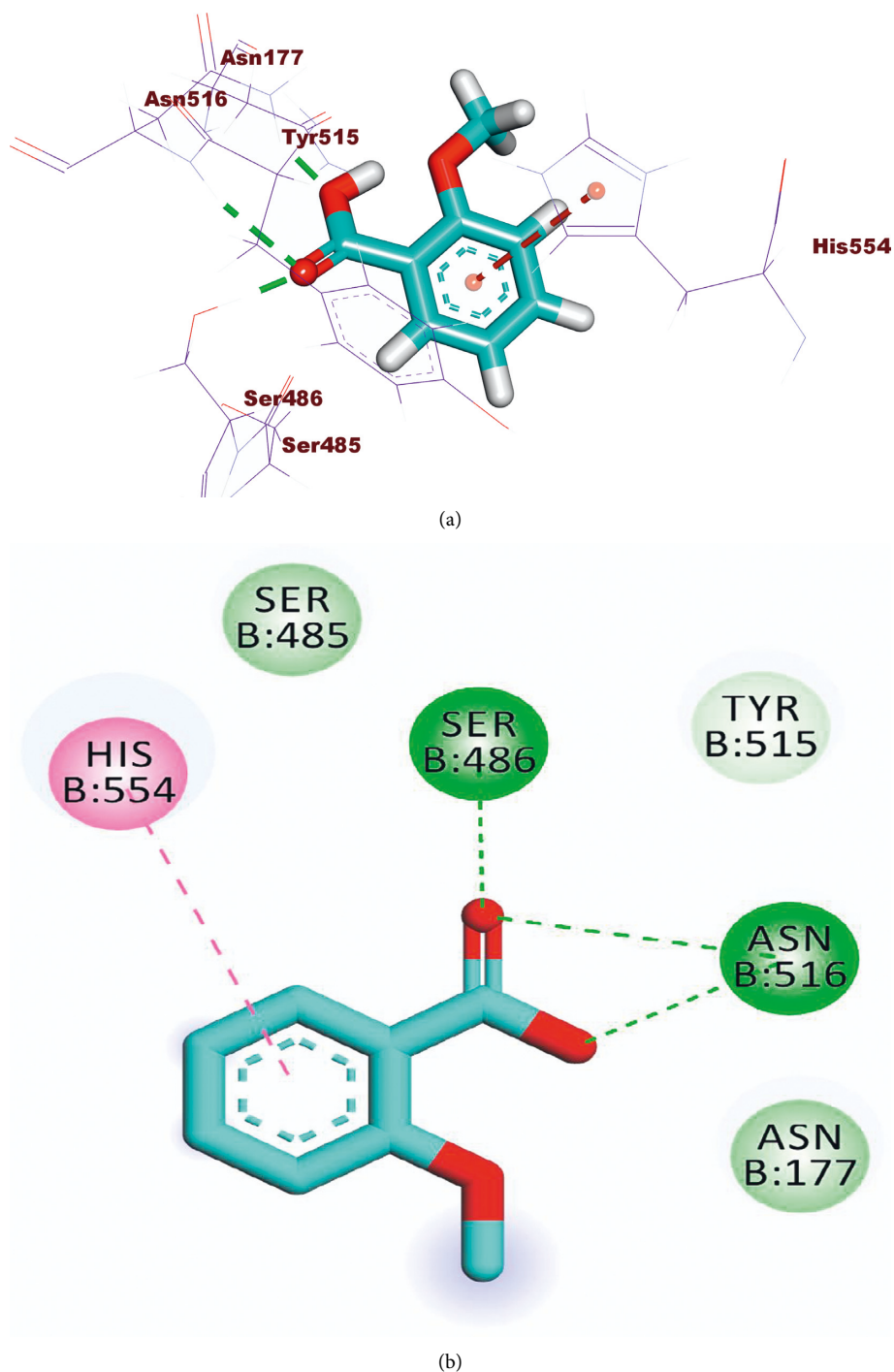
Figure 10: (a) 3D and (b) 2D images of docked compound **364** into the active site of SARS-CoV-2 helicase.

while the phenyl ring was incorporated in hydrophobic interaction with HIS55 (Figure 10).

2.4. ADMET Studies. The likeness of any molecule to be approved as a drug depends greatly on its pharmacokinetic properties as well as its activity. Subsequently, the investigation of the ADMET profile of a molecule should be considered in the early stages of drug design and discovery to avoid the withdrawal possibility of the drug from the pharmaceutical market [73]. These descriptors identify the absorption, distribution, metabolism, excretion, as well as the toxicity of the examined compound. Although, there are different *in vitro* experiments that can determine the ADMET profile, *in silico* determination is an available and reliable tool with the profit of being faster, cheaper, as well as and lifesaver of the experimental animals [74].

Table 4: ADMET profile of the 26 compounds with the best docking scores.

Comp.	BBB level[a]	HIA[b]	Aq[c]	CYP2D6[d]	PPB[e]
48	1	0	4	T	F
57	2	0	4	F	F
58	1	0	4	T	F
59	3	0	4	F	F
80	3	0	3	F	F
84	2	0	3	F	T
85	1	0	3	F	F
195	2	0	3	F	T
245	1	0	3	F	T
246	2	0	3	F	T
364	2	0	4	F	T
374	2	0	3	F	F
388	3	0	3	F	F
405	3	0	4	F	F
533	3	0	3	F	T
539	3	0	3	F	T
610	1	0	3	F	T
637	3	0	3	F	T
816	2	0	3	T	F
817	1	0	3	T	F
818	2	0	4	F	F
5153	2	0	3	T	T
5155	2	0	3	T	T
5159	3	0	4	F	F
5168	2	0	4	F	T
5169	1	0	3	F	T
Simeprevir	4	3	2	F	T

[a]BBB, ability to pass the blood-brain barrier, 1 is high, 2 is medium, 3 is low, and 4 is very low; [b]HIA, human intestinal absorption level, 0 is good, 1 is moderate, 2 is poor, and 3 is very poor; [c]Aq, aqueous solubility level, 0 is extremely low, 1 is very low, 2 is low, 3 is good, and 4 is optimal; [d]CYP2D6, inhibition of CYP2D6 enzyme, T is an inhibitor and F is a noninhibitor; [e]PPB, F means less than 90% and T means more than 90%.

The predicted ADMET profiles of the 26 compounds that showed correct modes of binding besides Remdesivir, the reference drug, are shown in Table 4 and Figure 11. Compounds **48**, **58**, **85**, **245**, **610**, **816**, **817**, **5153**, **5155**, and **5169** were excluded because of their predicted strong ability to pass the blood-brain barriers which may be combined with a CNS toxicity. Among the excluded compounds, compounds **48**, **58**, **816**, **817**, **5153**, and **5155** were predicted to be inhibitors against the CYP2D6 enzyme which would cause hepatotoxicity. The predicted intestinal absorption and aqueous solubility of all compounds were good to optimal.

2.5. Toxicity Studies. The early prediction of toxicity is a crucial step that minimizes drug failure because of toxicity in the development stage or the clinical trials [75]. *In silico* prediction of toxicity is a credible approach that plays an essential role in drug design and discovery of lead compounds because *in vitro* and *in vivo* approaches are usually controlled by strict ethical regulations, time, and availability of resources [76], whereas the *in silico* prediction is based on a structure-activity relationship toxicology. The software compares the essential structural descriptors of the examined compounds with a huge library of hundreds of thousands of reported safe and toxic compounds [77] (Supporting data (available here)). Discovery studio 4.0 software was employed to predict the toxicity profile of the selected compounds after the ADMET study against 7 models. The applied models are FDA rat carcinogenicity [78, 79], mouse carcinogenic potency (TD_{50}) [80], rat maximum tolerated dose (MTD) [81, 82], rat oral LD_{50} [83], rat chronic LOAEL [84, 85], ocular irritancy, and skin irritancy [86]. According to the obtained results (Table 5), compounds **80**, **388**, and **539** were eliminated due to the predicted high carcinogenic potency.

2.6. Molecular Dynamics (MD) Simulations. Despite the ability of molecular docking studies to expect the mode of binding of a compound inside a specific protein correctly, it has a serious defect that it deals with the protein as a rigid unit. Resultantly, it does not compute the conformational changes that happen in the protein because of ligand binding [87]. On the contrary, the MD simulations can adequately describe the behavior of a protein at the atomic level in full detail and at very accurate temporal resolution [88]. In accordance, the MD simulations have the advantage of being able to predict the conformational changes that occurred in the protein after ligand binding [89]. Furthermore, MD simulation studies can effectively compute various factors related to the energy of the protein-ligand complex for a determined time. Subsequently, it accurately describes the binding mode, stability, and flexibility of the ligand inside the target protein [90].

The first successful MD simulation experiment of a protein (bovine pancreatic trypsin inhibitor) was published in Nature in 1977 [91]. Fortunately, because of the recently introduced supercomputer hardware, especially the advanced graphics processing units, MD simulation experiments became much more accessible, powerful, and accurate [92].

In the MD simulation study, the forces on every atom of the examined ligand-protein complex are computed at every ultra-short time interval according to the basics of the "force field" [93]. The computed force field can be utilized to describe the position and velocity of atoms at each time interval. The force field is a physical expression that describes the functional potential energy of atoms. The force field is calculated based on Newton's laws of motion considering bonded interactions (bonds, angles, and dihedrals) in addition to nonbonded interactions (van der Waals potentials and Coulomb potentials) between all atoms of the complex. This step is repeated billions of times to produce the atomic trajectories for a specific time interval [94].

Several MD simulation studies were employed to investigate the stability and mimic the dynamic of compound **533**, (Z)-6-(3-hydroxy-4-methoxystyryl)-4-methoxy-2*H*-pyran-2-one, that exhibited the best docking score inside SARS-CoV-2 helicase for 100 ns.

First, the interaction of a ligand inside the active site of a protein leads to some changes in the structure of that protein [95]. In consequence, the dynamics and the conformational
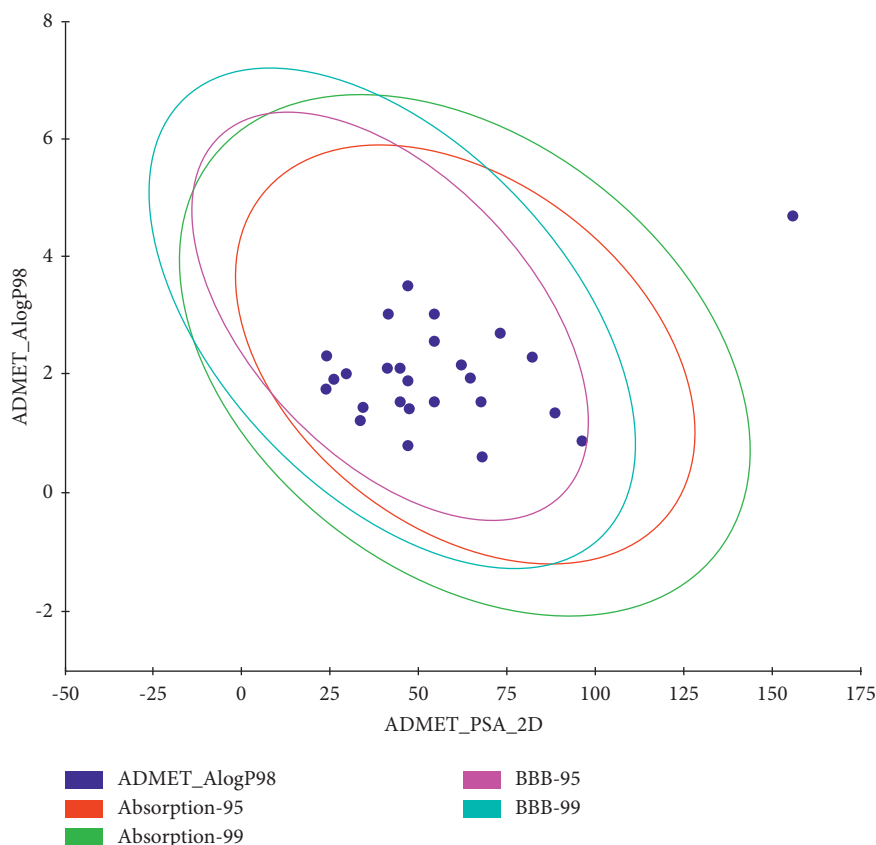
FIGURE 11: Results of the ADMET study.

TABLE 5: *In silico* toxicity profile of 15 compounds with good ADMET profile.

Comp.	FDA rat carcinogenicity (mouse-female)	TD_{50} ($mg \cdot kg^{-1} \cdot day^{-1}$)	MTD ($g \cdot kg^{-1}$)	Rat oral LD_{50} ($g \cdot kg^{-1}$)	LOAEL ($g \cdot kg^{-1}$)	Ocular irritancy	Skin irritancy
Simeprevir	Not a carcinogen	2.0138	0.002967	0.208835	0.0021057	Mild	None
57	Not a carcinogen	306.685	0.126925	0.678557	0.1091	Severe	None
59	Not a carcinogen	209.013	0.130669	1.17822	0.153373	Severe	None
80	Multicarcinogen	30.9654	0.320563	0.112645	0.0104398	Moderate	None
84	Not a carcinogen	86.2745	0.432043	0.651537	0.0466934	Severe	None
195	Not a carcinogen	734.376	0.0920234	0.80394	0.58711	Mild	None
246	Not a carcinogen	896.437	0.185908	0.975783	0.0690491	Mild	Mild
364	Not a carcinogen	1,152.33	0.178125	1.10017	0.269177	Mild	None
388	Multicarcinogen	77.4401	0.158212	0.128576	0.0111578	Severe	Mild
405	Not a carcinogen	1,019.87	0.355843	0.565566	0.0958513	Moderate	None
533	Not a carcinogen	587.516	0.109002	0.765306	0.026065	Mild	Mild
539	Multicarcinogen	71.1582	0.12354	0.366215	0.0229232	Severe	None
637	Not a carcinogen	30.3365	0.136595	0.428434	0.0201137	Severe	Mild
818	Not a carcinogen	145.39	0.355736	0.71245	0.0937066	Severe	None
5159	Not a carcinogen	227.599	0.559977	0.526787	0.0808567	Severe	None
5168	Not a carcinogen	128.911	0.242854	2.09646	0.0494677	Moderate	Mild

changes of the SARS-CoV-2 helicase-**533** complex were computed as root mean square deviation (RMSD) to detect the stability due to binding. It is observed that the SARS-CoV-2 helicase and **533** exhibited lower RMSD with no major fluctuations indicating their greater stability (Figure 12(a)). Interestingly, the SARS-CoV-2 helicase-**533**

complex was stable till 90 ns~. Although the SARS-CoV-2 helicase-**533** complex showed a minor fluctuation later, it reached equilibrium again.

Second, the flexibility of SARS-CoV-2 helicase was calculated in terms of root mean square fluctuation (RMSF) to calculate the differences in flexibility in the SARS-CoV-2

(a)

(b)

(c)

(d)

(e)
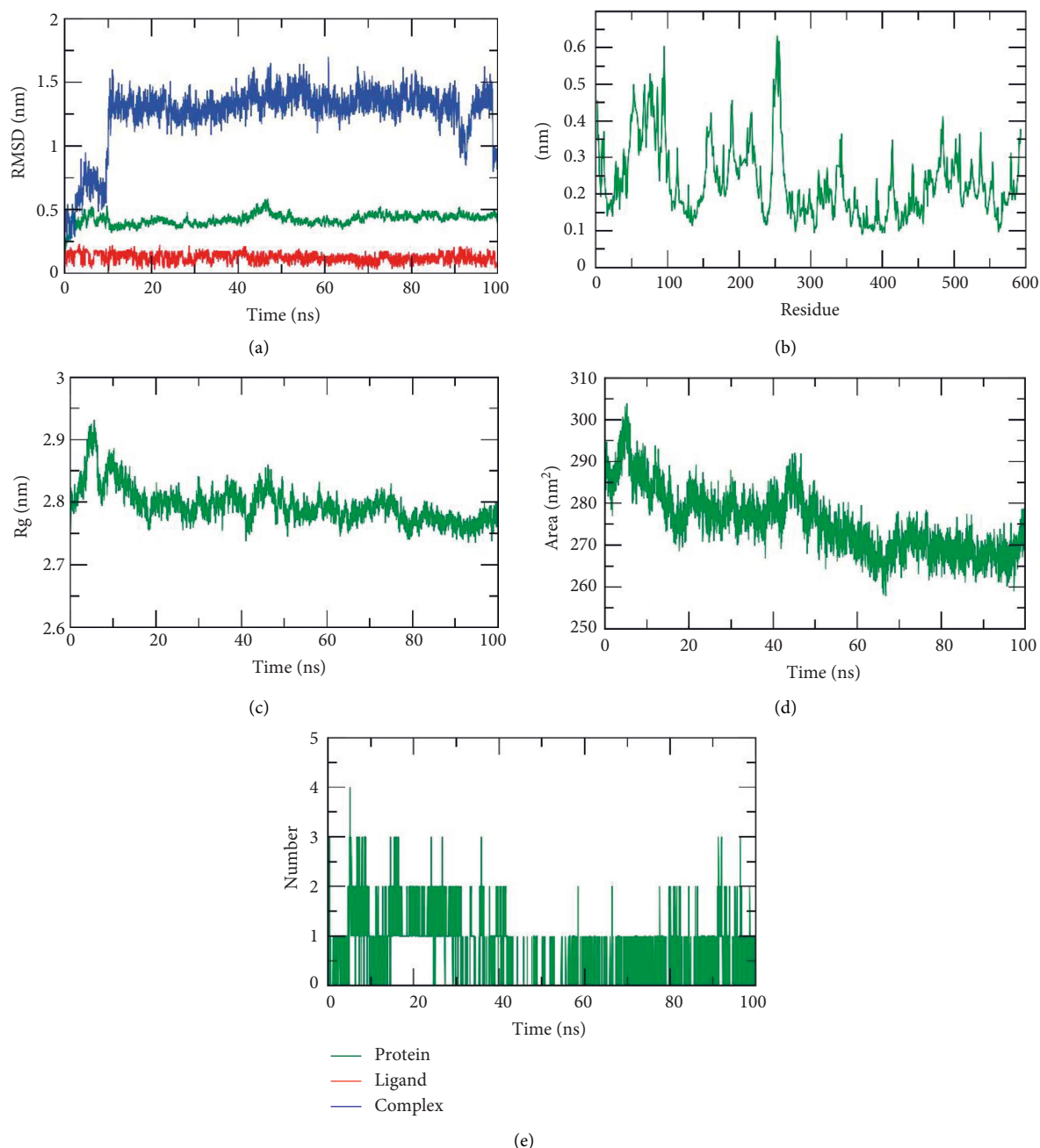
FIGURE 12: M D simulation results: (a) RMSD values of SARS-CoV-2 helicase, **533,** and SARS-CoV-2 helicase-**533** complex; (b) RMSF for SARS-CoV-2 helicase; (c) R_g of SARS-CoV-2 helicase; (d) SASA of SARS-CoV-2 helicase; and (e) H-bonding between SARS-CoV-2 helicase-**533** complex in the MD run.

helicase-**533** complex during the 100 ns of the MD simulations. The decrease of RMSF values during the MD simulation in 50–100 residue areas (Figure 12(b)) denotes that SARS-CoV-2 residues were more rigid and stabilized after binding to **533**.

Third, the radius of gyration (R_g) is a crucial parameter that is linked to the protein stability according to the change in its volume. R_g is defined as the root mean square distance (RMSD) of a weighted mass group of atoms from their mass center [96, 97]. Thus, the calculation of R_g identifies the dimensions as well as the compactness of the SARS-CoV-2

helicase-**533** complex. The lower degree of fluctuation throughout the simulation period indicates the greater compactness of a system. The R_g of the SARS-CoV-2 helicase-**533** complex was found to be lower than the starting period (Figure 12(c)) displaying compactness and stability**.**

Fourth, the interaction between protein-ligand complexes and solvents was measured by solvent accessible surface area (SASA) over the simulation period. So, the SASA of the SARS-CoV-2 helicase-**533** complex was calculated to provide the extent of the conformational changes that occurred during binding. Interestingly, SARS-CoV-2

(a)

(b)
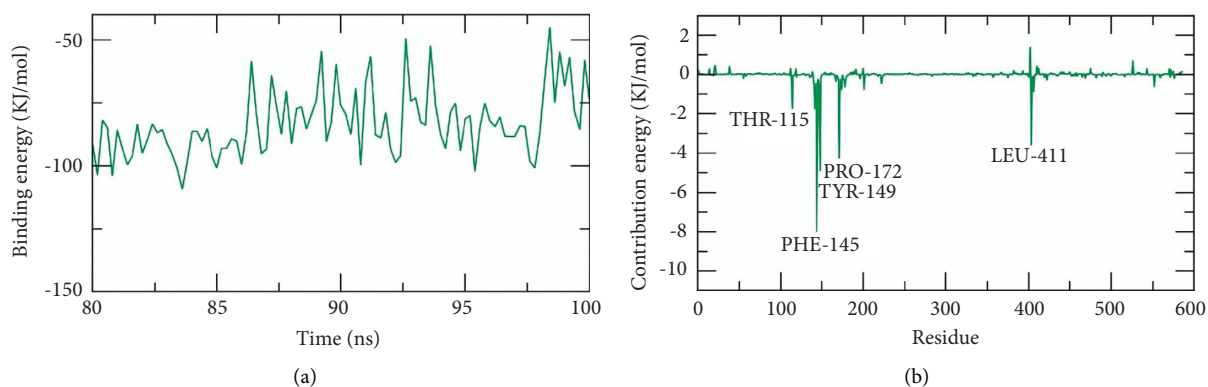
FIGURE 13: MM-PBSA results of SARS-CoV-2 helicase-**1552** complex.

helicase featured a reduction of the surface area showing a relatively lower SASA value than the starting period (Figure 12(d)).

Finally, hydrogen bonding between a SARS-CoV-2 helicase-**533** complex is essential to stabilize the structure. MD simulation studies showed that the highest number of conformations of the SARS-CoV-2 helicase formed up to three hydrogen bonds with **533** (Figure 12(e)).

2.7. Molecular Mechanics Poisson–Boltzmann Surface Area (MM-PBSA).
In this experiment, the molecular mechanics Poisson–Boltzmann surface area (MM-PBSA) method was the utilized method to calculate the free binding energy of the SARS-CoV-2 helicase-**533** complex. The MM-PBSA can evaluate the binding between a specific receptor and a ligand through the accurate calculation of the binding free energy of the ligand-protein complex. The MM-PBSA method utilizes both thermodynamic cycle and molecular dynamics (MD) methods to compute the binding free energy. The MM-PBSA calculates the binding free energies according to the following equation: $\Delta G_{bind.} = G_{comp.} - (G_{prot.} + G_{lig.})$.

$\Delta G_{bind.}$ refers to the total energy difference that was calculated as the difference between the energy at the bound-state ($G_{comp.}$) and the sum of energy of both protein ($G_{prot.}$) and ligand ($G_{lig.}$) before binding [98]. To compute the biding energy accurately, two main types of energies should be considered: first, the gas-phase interaction energy, which consists of van der Waals and electrostatic interactions; and, second, the solvation energy, which includes both polar and nonpolar components [99].

The MM-PBSA, as a tool to calculate the free binding energies, has several advantages over other methods such as free energy perturbation and thermodynamic integration such as being faster, simpler, and producing consistent results with the experimental [100].

The binding free energy of the SARS-CoV-2 helicase-**533** complex was computed at the last stable 20 ns of the MD production run at a time interval of 100 ps from MD trajectories. The MM/PBSA method was utilized. Also, the MmPbSaStat.py script was employed to calculate the average free binding energy and its standard deviation/error from the output files that were obtained from g_mmpbsa. Compound **533**, (Z)-6-(3-hydroxy-

4-methoxystyryl)-4-methoxy-2H-pyran-2-one, showed a low binding free energy of −83 kJ/mol with the SARS-CoV-2 helicase (Figure 13(a)). The binding energy was stable during all the time of examination indicating the correct binding of the SARS-CoV-2 helicase-**533** complex.

2.7.1. Free Energy Decomposition.
The total binding free energy of the SARS-CoV-2 helicase-**533** complex was decomposed to analyze and understand the different components of that obtained binding energy as well as to disclose the contribution of each amino acid residue of the SARS-CoV-2 helicase in the binding with **533**. The total binding free energy was decomposed into per amino acid residue contribution energy. This experiment gives a clearer idea about the essential amino acid residues that have favorable contributions to the binding process. It was found that THR-115, PHE-145, PRO-172, TYR-149, and LEU-411 residues of the protein contributed higher than −2 kJ/mol binding energy and thus they are crucial residues in the binding with **533** (Figure 13(b)).

3. Methods

3.1. Molecular Similarity.
Discovery studio 4.0 software was used [101, 102] (see Section 3 in Supplementary data).

3.2. Fingerprints Studies.
Discovery studio 4.0 software was used [103, 104] (see Section 3 in Supplementary data).

3.3. Docking Studies.
Docking studies were done against the target enzyme using Discovery studio 4.0 software [105, 106] (see Section 3 in Supplementary data).

3.4. ADMET Analysis.
Discovery studio 4.0 was used [40, 107] (see Section 3 in Supplementary data).

3.5. Toxicity Studies.
Discovery studio 4.0 software was used [108–110] (see Section 3 in Supplementary data).

3.6. Molecular Dynamics Simulation. The system was prepared using the web-based CHARMM-GUI [111–113] utilizing CHARMM36 force field [114] and NAMD 2.13 [115] package. The TIP3P explicit solvation model was used (see supporting data (available here)).

3.7. MM-PBSA Studies. The g_mmpbsa package of GROMACS was utilized to calculate the MM/PBSA (see supporting data (available here)).

4. Conclusion

Twelve of 5956 TCM compounds were suggested to be the potential inhibitors against SARS-CoV-2 helicase (PDB ID: 5RMM). The compounds were selected according to structural similarity and fingerprint studies with **VXG,** the co-crystallized ligand of the target protein. Then, molecular docking studies were carried out. Then, ADMET and toxicity studies were preceded to select the following metabolites: (1*R*,2*S*)-ephedrine (**57**), (1*R*,2*S*)-norephedrine (**59**), 2-(4-(pyrrolidin-1-yl)phenyl)acetic acid (**84**), 1-phenylpropane-1,2-dione (**195**), 2-methoxycinnamic acid (**246**), 2-methoxybenzoic acid (**364**), (*R*)-2-((*R*)-5-oxopyrrolidin-3-yl)-2-phenylacetic acid (**405**), (*Z*)-6-(3-hydroxy-4-methoxystyryl)-4-methoxy-2*H*-pyran-2-one (**533**), 8-chloro-2-(2-phenylethyl)-5,6,7-trihydroxy-5,6,7,8-tetrahydrochromone (**637**), 3-((1*R*,2*S*)-2-(dimethylamino)-1-hydroxypropyl) phenol (**818**), (*R*)-2-ethyl-4-(1-hydroxy-2-(methylamino) ethyl)phenol (**5159**), and (*R*)-2-((1*S*,2*S*,5*S*)-2-benzyl-5-hydroxy-4-methylcyclohex-3-en-1-yl)propane-1,2-diol (**5168**). Among them, compounds **84, 195, 364, 533,** and **637** showed the best docking scores. Interestingly, compound **533**, the one with the highest docking score, bonded favorably to the target protein with low energy and optimum dynamics according to advanced MD simulation studies over 100 ns.

Data Availability

The data that support the findings of this study are included within this article.

Conflicts of Interest

The authors declare that they have no conflicts of interest.

Acknowledgments

Supplementary Materials

Supplementary data contain the detailed methodology and the toxicity reports. (*Supplementary Materials*)

References

[1] WHO, WHO coronavirus (COVID-19) dashboard, https://covid19.who.int/.

[2] A. M. Metwaly, M. M. Ghoneim, I. H. Eissa et al., "Traditional ancient Egyptian medicine: a review," *Saudi Journal of Biological Sciences*, vol. 28, no. 10, pp. 5823–5832, 2021.

[3] A. Metwaly, M. Ghoneim, W. Afifi et al., "Biological evaluation and molecular docking study of metabolites from salvadora persica L. growing in Egypt," *Pharmacognosy Magazine*, vol. 15, no. 61, p. 232, 2019.

[4] L. Liu, S. Luo, M. Yu et al., "Chemical constituents of *Tagetes patula* and their neuroprotecting action," *Natural Product Communications*, vol. 15, no. 11, 2020.

[5] Y.-M. Wang, X.-K. Ran, M. Riaz et al., "Chemical constituents of stems and leaves of *Ttagetes patula* L. and its fingerprint," *Molecules*, vol. 24, no. 21, p. 3911, 2019.

[6] A. M. Metwaly, M. M. Ghoneim, and A. Musa, "Two new antileishmanial diketopiperazine alkaloids from the endophytic fungus Trichosporum sp," *Derpharmachemica*, vol. 7, pp. 322–327, 2015.

[7] A. M. Yassin, N. M. El-Deeb, A. M. Metwaly, G. F. El Fawal, M. M. Radwan, and E. E. Hafez, "Induction of apoptosis in human cancer cells through extrinsic and intrinsic pathways by *Balanites aegyptiaca* furostanol saponins and saponin-coated silver nanoparticles," *Applied Biochemistry and Biotechnology*, vol. 182, no. 4, pp. 1675–1693, 2017.

[8] M. H. Sharaf, G. M. El-Sherbiny, S. A. Moghannem et al., "New combination approaches to combat methicillin-resistant *Staphylococcus aureus* (MRSA)," *Scientific Reports*, vol. 11, pp. 4240–4316, 2021.

[9] A. M. Metwaly, Z. Lianlian, H. Luqi, and D. Deqiang, "Black ginseng and its saponins: preparation, phytochemistry and pharmacological effects," *Molecules*, vol. 24, no. 10, p. 1856, 2019.

[10] A. M. Metwaly, H. A. Kadry, A. A. El-Hela et al., "Nigrosphaerin a new isochromene derivative from the endophytic fungus *Nigrospora sphaerica*," *Phytochemistry Letters*, vol. 7, pp. 1–5, 2014.

[11] A. M. Metwaly, F. R. Fronczek, G. Ma et al., "Antileukemic *α*-pyrone derivatives from the endophytic fungus *Alternaria phragmospora*," *Tetrahedron Letters*, vol. 55, no. 24, pp. 3478–3481, 2014.

[12] A. M. Metwaly, A. S. Wanas, M. M. Radwan, S. A. Ross, and M. A. ElSohly, "New *α*-pyrone derivatives from the endophytic fungus *Embellisia* sp," *Medicinal Chemistry Research*, vol. 26, no. 8, pp. 1796–1800, 2017.

[13] A. Zhanzhaxina, Y. Suleimen, A. M. Metwaly et al., "In vitro and in silico cytotoxic and antibacterial activities of a diterpene from *Cousinia alata* Schrenk," *Journal of Chemistry*, vol. 2021, pp. 2021–2111.

[14] V. O. Imieje, A. A. Zaki, A. M. Metwaly et al., *Antileishmanial Derivatives of Humulene from Asteriscus hierochunticus with in silico Tubulin Inhibition Potential*, ACG Publications, Kocaeli, Turkey, 2021.

[15] R. I. Jalmakhanbetova, E. B. Elkaeed, I. H. Eissa, A. M. Metwaly, and Y. M. Suleimen, "Synthesis and molecular docking of some Grossgemin amino derivatives as tubulin inhibitors targeting colchicine binding site," *Journal of Chemistry*, vol. 2021, Article ID 5586515, 10 pages, 2021.

[16] Y. M. Suleimen, A. M. Metwaly, A. E. Mostafa et al., "Isolation, crystal structure, and in silico aromatase inhibition activity of ergosta-5, 22-dien-3*β*-ol from the fungus

Gyromitra esculenta," *Journal of Chemistry*, vol. 2021, Article ID 5529786, 10 pages, 2021.

[17] L.-J. Xiao and R. Tao, "Traditional Chinese medicine (TCM) therapy," *Advances in Experimental Medicine and Biology*, vol. 2017, no. 1010, pp. 261–280, 2017.

[18] J.-L. Tang, B.-Y. Liu, and K.-W. Ma, "Traditional Chinese medicine," *The Lancet*, vol. 372, no. 9654, pp. 1938–1940, 2008.

[19] X. Han, Y. Yang, A. M. Metwaly, Y. Xue, Y. Shi, and D. Dou, "The Chinese herbal formulae (Yitangkang) exerts an anti-diabetic effect through the regulation of substance metabolism and energy metabolism in type 2 diabetic rats," *Journal of Ethnopharmacology*, vol. 239, Article ID 111942, 2019.

[20] Y. Lao, X. Wang, N. Xu, H. Zhang, and H. Xu, "Application of proteomics to determine the mechanism of action of traditional Chinese medicine remedies," *Journal of Ethnopharmacology*, vol. 155, pp. 1–8, 2014.

[21] J. Xu and A. Hagler, "Chemoinformatics and drug discovery," *Molecules*, vol. 7, no. 8, pp. 566–600, 2002.

[22] T. Engel, "Basic overview of chemoinformatics," *Journal of Chemical Information and Modeling*, vol. 46, no. 6, pp. 2267–2277, 2006.

[23] E. March-Vila, L. Pinzi, N. Sturm et al., "On the integration of in silico drug design methods for drug repurposing," *Frontiers in Pharmacology*, vol. 8, p. 298, 2017.

[24] W. Zhang, J. Pei, and L. Lai, "Computational multitarget drug design," *Journal of Chemical Information and Modeling*, vol. 57, no. 3, pp. 403–412, 2017.

[25] M. I. Youssef, Y. Zhou, I. H. Eissa et al., "Tetradecyl 2, 3-dihydroxybenzoate alleviates oligodendrocyte damage following chronic cerebral hypoperfusion through IGF-1 receptor," *Neurochemistry International*, vol. 138, Article ID 104749, 2020.

[26] F. Zhong, J. Xing, X. Li et al., "Artificial intelligence in drug design," *Science China Life Sciences*, vol. 61, no. 10, pp. 1191–1204, 2018.

[27] M. Hagras, M. A. El Deeb, H. S. A. Elzahabi, E. B. Elkaeed, A. B. M. Mehany, and I. H. Eissa, "Discovery of new quinolines as potent colchicine binding site inhibitors: design, synthesis, docking studies, and anti-proliferative evaluation," *Journal of Enzyme Inhibition and Medicinal Chemistry*, vol. 36, no. 1, pp. 640–658, 2021.

[28] I. H. Eissa, M. A. Dahab, M. K. Ibrahim et al., "Design and discovery of new antiproliferative 1, 2, 4-triazin-3 (2H)-ones as tubulin polymerization inhibitors targeting colchicine binding site," *Bioorganic Chemistry*, vol. 112, Article ID 104965, 2021.

[29] I. H. Eissa, A.-G. A. El-Helby, H. A. Mahdy et al., "Discovery of new quinazolin-4 (3H)-ones as VEGFR-2 inhibitors: design, synthesis, and anti-proliferative evaluation," *Bioorganic Chemistry*, vol. 105, Article ID 104380, 2020.

[30] K. El-Adl, A.-G. A. El-Helby, R. R. Ayyad et al., "Design, synthesis, and anti-proliferative evaluation of new quinazolin-4 (3H)-ones as potential VEGFR-2 inhibitors," *Bioorganic & Medicinal Chemistry*, vol. 29, Article ID 115872, 2021.

[31] A.-G. A. El-Helby, R. R. A. Ayyad, K. El-Adl et al., "Design, molecular docking and synthesis of some novel 4-acetyl-1-substituted-3, 4-dihydroquinoxalin-2 (1 H)-one derivatives for anticonvulsant evaluation as AMPA-receptor antagonists," *Medicinal Chemistry Research*, vol. 25, no. 12, pp. 3030–3046, 2016.

[32] V. Kairys, L. Baranauskiene, M. Kazlauskiene, D. Matulis, and E. Kazlauskas, "Binding affinity in drug design: experimental and computational techniques," *Expert Opinion on Drug Discovery*, vol. 14, no. 8, pp. 755–768, 2019.

[33] T. Al-Warhi, A. M. El Kerdawy, N. Aljaeed et al., "Synthesis, biological evaluation and in silico studies of certain oxindole–indole conjugates as anticancer CDK inhibitors," *Molecules*, vol. 25, no. 9, p. 2031, 2020.

[34] S. A. El-Metwally, M. M. Abou-El-Regal, I. H. Eissa et al., "Discovery of thieno [2, 3-d] pyrimidine-based derivatives as potent VEGFR-2 kinase inhibitors and anti-cancer agents," *Bioorganic Chemistry*, vol. 112, Article ID 104947, 2021.

[35] M. M. Alanazi, I. H. Eissa, N. A. Alsaif et al., "Design, synthesis, docking, ADMET studies, and anticancer evaluation of new 3-methylquinoxaline derivatives as VEGFR-2 inhibitors and apoptosis inducers," *Journal of Enzyme Inhibition and Medicinal Chemistry*, vol. 36, no. 1, pp. 1760–1782, 2021.

[36] M. M. Alanazi, A. Elwan, N. A. Alsaif et al., "Discovery of new 3-methylquinoxalines as potential anti-cancer agents and apoptosis inducers targeting VEGFR-2: design, synthesis, and in silico studies," *Journal of Enzyme Inhibition and Medicinal Chemistry*, vol. 36, no. 1, pp. 1732–1750, 2021.

[37] N. A. Alsaif, M. S. Taghour, M. M. Alanazi et al., "Discovery of new VEGFR-2 inhibitors based on bis ([1, 2, 4] triazolo) [4, 3-a: 3′, 4′-c] quinoxaline derivatives as anticancer agents and apoptosis inducers," *Journal of Enzyme Inhibition and Medicinal Chemistry*, vol. 36, no. 1, pp. 1093–1114, 2021.

[38] N. A. Alsaif, M. A. Dahab, M. M. Alanazi et al., "New quinoxaline derivatives as VEGFR-2 inhibitors with anti-cancer and apoptotic activity: design, molecular modeling, and synthesis," *Bioorganic Chemistry*, vol. 110, Article ID 104807, 2021.

[39] K. El-Adl, M.-K. Ibrahim, M. S. Alesawy, and I. H. Eissa, "[1, 2, 4] Triazolo [4, 3-c] quinazoline and bis ([1, 2, 4] triazolo) [4, 3-a: 4′, 3′-c] quinazoline derived DNA intercalators: design, synthesis, in silico ADMET profile, molecular docking and anti-proliferative evaluation studies," *Bioorganic & Medicinal Chemistry*, vol. 30, Article ID 115958, 2021.

[40] D. R. Parmar, J. Y. Soni, R. Guduru et al., "Discovery of new anticancer thiourea-azetidine hybrids: design, synthesis, in vitro antiproliferative, SAR, in silico molecular docking against VEGFR-2, ADMET, toxicity, and DFT studies," *Bioorganic Chemistry*, vol. 115, Article ID 105206, 2021.

[41] R. I. Jalmakhanbetova, Y. M. Suleimen, M. Oyama et al., "Isolation and in silico anti-COVID-19 main protease (Mpro) activities of flavonoids and a sesquiterpene lactone from *Artemisia sublessingiana*," *Journal of Chemistry*, vol. 2021, Article ID 5547013, 8 pages, 2021.

[42] A. El-Demerdash, A. M. Metwaly, A. Hassan et al., "Comprehensive virtual screening of the antiviral potentialities of marine polycyclic guanidine alkaloids against SARS-CoV-2 (COVID-19)," *Biomolecules*, vol. 11, no. 3, p. 460, 2021.

[43] M. S. Alesawy, A. E. Abdallah, M. S. Taghour, E. B. Elkaeed, I. H Eissa, and A. M. Metwaly, "In silico studies of some isoflavonoids as potential candidates against COVID-19 targeting human ACE2 (hACE2) and viral main protease (Mpro)," *Molecules*, vol. 26, no. 9, p. 2806, 2021.

[44] I. H. Eissa, M. M. Khalifa, E. B. Elkaeed, E. E. Hafez, A. A. Alsfouk, and A. M. Metwaly, "In silico exploration of potential natural inhibitors against SARS-cov-2 nsp10," *Molecules*, vol. 26, no. 20, p. 6151, 2021.

[45] M. S. Alesawy, E. B. Elkaeed, A. A. Alsfouk, A. M. Metwaly, and I. H. Eissa, "In silico screening of semi-synthesized compounds as potential inhibitors for SARS-CoV-2 papain-like protease: pharmacophoric features, molecular docking, ADMET, toxicity and DFT studies," *Molecules*, vol. 26, no. 21, p. 6593, 2021.

[46] K. A. Ivanov, V. Thiel, J. C. Dobbe, Y. Van Der Meer, E. J. Snijder, and J. Ziebuhr, "Multiple enzymatic activities associated with severe acute respiratory syndrome corona-virus helicase," *Journal of Virology*, vol. 78, no. 11, pp. 5619–5632, 2004.

[47] D. Huttner and I. D. Hickson, "Helicases," in *Brenner's Encyclopedia of Genetics*, S. Maloy and K. Hughes, Eds., , Academic Press, San Diego, CA, USA, 2nd edition, 2013.

[48] P. Ripphausen, B. Nisius, and J. Bajorath, "State-of-the-art in ligand-based virtual screening," *Drug Discovery Today*, vol. 16, no. 9-10, pp. 372–376, 2011.

[49] B. J. Burke, *Developments in Molecular Shape Analysis to Establish Spatial Similarity Among Flexible Molecules*, University of Illinois at Chicago, Health Sciences Center, Chicago, IL, USA, 1993.

[50] P. Willett, "Similarity-based virtual screening using 2D fingerprints," *Drug Discovery Today*, vol. 11, no. 23-24, pp. 1046–1053, 2006.

[51] H. Briem and I. D. Kuntz, "Molecular similarity based on DOCK-generated fingerprints," *Journal of Medicinal Chemistry*, vol. 39, no. 17, pp. 3401–3408, 1996.

[52] P. Willett, "Similarity searching using 2D structural fingerprints," *Methods in Molecular Biology*, vol. 672, pp. 133–158, 2011.

[53] A. M. Hassell, G. An, R. K. Bledsoe et al., "Crystallization of protein–ligand complexes," *Acta Crystallographica Section D Biological Crystallography*, vol. 63, no. 1, pp. 72–79, 2007.

[54] M. A. Spackman and J. J. McKinnon, "Fingerprinting intermolecular interactions in molecular crystals," *CrystEngComm*, vol. 4, no. 66, pp. 378–392, 2002.

[55] H. Chu, Q.-x. He, J. Wang, Y. Hu, Y.-q. Wang, and Z.-h. Lin, "In silico design of novel benzohydroxamate-based compounds as inhibitors of histone deacetylase 6 based on 3D-QSAR, molecular docking, and molecular dynamics simulations," *New Journal of Chemistry*, vol. 44, no. 48, pp. 21201–21210, 2020.

[56] C. Ieritano, J. L. Campbell, and W. S. Hopkins, "Predicting differential ion mobility behaviour in silico using machine learning," *Analyst*, vol. 146, no. 15, pp. 4737–4743, 2021.

[57] M. Taha, N. H. Ismail, M. Ali et al., "Molecular hybridization conceded exceptionally potent quinolinyl-oxadiazole hybrids through phenyl linked thiosemicarbazide anti-leishmanial scaffolds: in silico validation and SAR studies," *Bioorganic Chemistry*, vol. 71, pp. 192–200, 2017.

[58] K. Heikamp and J. R. Bajorath, "How do 2D fingerprints detect structurally diverse active compounds? Revealing compound subset-specific fingerprint features through systematic selection," *Journal of Chemical Information and Modeling*, vol. 51, no. 9, pp. 2254–2265, 2011.

[59] F. A. D. M. Opo, M. M. Rahman, F. Ahammad, I. Ahmed, M. A. Bhuiyan, and A. M. Asiri, "Structure based pharmacophore modeling, virtual screening, molecular docking and ADMET approaches for identification of natural anticancer agents targeting XIAP protein," *Scientific Reports*, vol. 11, pp. 4049–4117, 2021.

[60] J. Duan, M. Sastry, S. Dixon, J. Lowrie, and W. Sherman, "Analysis and comparison of 2D fingerprints: insights into database screening performance using eight fingerprint methods," *Journal of Cheminformatics*, vol. 3, no. S1, pp. 157–170, 2011.

[61] M. Sastry, J. F. Lowrie, S. L. Dixon, and W. Sherman, "Large-scale systematic analysis of 2D fingerprint methods and parameters to improve virtual screening enrichments," *Journal of Chemical Information and Modeling*, vol. 50, no. 5, pp. 771–784, 2010.

[62] T. Kogej, O. Engkvist, N. Blomberg, and S. Muresan, "Multifingerprint based similarity searches for targeted class compound selection," *Journal of Chemical Information and Modeling*, vol. 46, no. 3, pp. 1201–1213, 2006.

[63] I. Muegge and P. Mukherjee, "An overview of molecular fingerprint similarity search in virtual screening," *Expert Opinion on Drug Discovery*, vol. 11, no. 2, pp. 137–148, 2016.

[64] G. Maggiora, M. Vogt, D. Stumpfe, and J. Bajorath, "Molecular similarity in medicinal chemistry: miniperspective," *Journal of Medicinal Chemistry*, vol. 57, no. 8, pp. 3186–3204, 2014.

[65] M. Turchi, Q. Cai, and G. Lian, "An evaluation of in-silico methods for predicting solute partition in multiphase complex fluids–a case study of octanol/water partition coefficient," *Chemical Engineering Science*, vol. 197, pp. 150–158, 2019.

[66] K. M. Sullivan, S. J. Enoch, J. Ezendam, K. Sewald, E. L. Roggen, and S. Cochrane, "An adverse outcome pathway for sensitization of the respiratory tract by low-molecular-weight chemicals: building evidence to support the utility of in vitro and in silico methods in a regulatory context," *Applied In Vitro Toxicology*, vol. 3, pp. 213–226, 2017.

[67] T. Altamash, A. Amhamed, S. Aparicio, and M. Atilhan, "Effect of hydrogen bond donors and acceptors on CO_2 absorption by deep eutectic solvents," *Processes*, vol. 8, no. 12, p. 1533, 2020.

[68] Y. Wan, Y. Tian, W. Wang, S. Gu, X. Ju, and G. Liu, "In silico studies of diarylpyridine derivatives as novel HIV-1 NNRTIs using docking-based 3D-QSAR, molecular dynamics, and pharmacophore modeling approaches," *RSC Advances*, vol. 8, no. 71, pp. 40529–40543, 2018.

[69] A. Escamilla-Gutiérrez, R. M. Ribas-Aparicio, M. G. Córdova-Espinoza, and J. A. Castelán-Vega, "In silico strategies for modeling RNA aptamers and predicting binding sites of their molecular targets," *Nucleosides, Nucleotides & Nucleic Acids*, vol. 40, no. 8, pp. 798–807, 2021.

[70] A. C. Kaushik, A. Kumar, S. Bharadwaj, R. Chaudhary, and S. Sahi, "Ligand-based approach for in-silico drug designing," in *Bioinformatics Techniques for Drug Discovery*, pp. 11–19, Springer, Berlin, Germany, 2018.

[71] A. N. Jain, "Morphological similarity: a 3D molecular similarity method correlated with protein-ligand recognition," *Journal of Computer-Aided Molecular Design*, vol. 14, no. 2, pp. 199–213, 2000.

[72] H. Zhang, J.-X. Ren, J.-X. Ma, and L. Ding, "Development of an in silico prediction model for chemical-induced urinary tract toxicity by using naïve Bayes classifier," *Molecular Diversity*, vol. 23, no. 2, pp. 381–392, 2019.

[73] L. L. Ferreira and A. D. Andricopulo, "ADMET modeling approaches in drug discovery," *Drug Discovery Today*, vol. 24, no. 5, pp. 1157–1165, 2019.

[74] U. Norinder and C. A. Bergström, "Prediction of ADMET properties," *ChemMedChem*, vol. 1, no. 9, pp. 920–937, 2006.

[75] J. C. Dearden, "In silico prediction of drug toxicity," *Journal of Computer-Aided Molecular Design*, vol. 17, no. 2-4, pp. 119–127, 2003.

[76] G. Idakwo, J. Luttrell, M. Chen et al., "A review on machine learning methods for in silico toxicity prediction," *Journal of Environmental Science and Health, Part C*, vol. 36, no. 4, pp. 169–191, 2018.

[77] N. L. Kruhlak, R. D. Benz, H. Zhou, and T. J. Colatsky, "(Q) SAR modeling and safety assessment in regulatory review," *Clinical Pharmacology & Therapeutics*, vol. 91, no. 3, pp. 529–534, 2012.

[78] X. Xia, E. G. Maliski, P. Gallant, and D. Rogers, "Classification of kinase inhibitors using a Bayesian model," *Journal of Medicinal Chemistry*, vol. 47, no. 18, pp. 4463–4470, 2004.

[79] BIOVIA. QSAR, ADMET and Predictive Toxicology, 2020, https://www.3dsbiovia.com/products/collaborative-science/biovia-discovery-studio/qsar-admet-and-predictive-toxicology.html.

[80] R. Venkatapathy, N. C. Y. Wang, T. M. Martin, P. F. Harten, and D. Young, "Structure–activity relationships for carcinogenic potential," *General, Applied and Systems Toxicology*, Wiley, Hoboken, NJ, USA, 2009.

[81] G. Goodrnan and R. Wilson, "Comparison of the dependence of the TD50 on maximum tolerated dose for mutagens and nonmutagens," *Risk Analysis*, vol. 12, no. 4, pp. 525–533, 1992.

[82] N. R. Council, "Correlation between carcinogenic potency and the maximum tolerated dose: implications for risk assessment," in *Issues in Risk Assessment*National Academies Press, Washington, DC, USA, 1993.

[83] R. Gonella Diaza, S. Manganelli, A. Esposito, A. Roncaglioni, A. Manganaro, and E. Benfenati, "Comparison of in silico tools for evaluating rat oral acute toxicity," *SAR and QSAR in Environmental Research*, vol. 26, pp. 1–27, 2015.

[84] F. Pizzo and E. Benfenati, "In silico models for repeated-dose toxicity (RDT): prediction of the no observed adverse effect level (NOAEL) and lowest observed adverse effect level (LOAEL) for drugs," *Silico Methods for Predicting Drug Toxicity*, pp. 163–176, Springer, Berlin, Germany, 2016.

[85] R. Venkatapathy, C. J. Moudgal, and R. M. Bruce, "Assessment of the oral rat chronic lowest observed adverse effect level model in TOPKAT, a QSAR software package for toxicity prediction," *Journal of Chemical Information and Computer Sciences*, vol. 44, no. 5, pp. 1623–1629, 2004.

[86] K. R. Wilhelmus, "The Draize eye test," *Survey of Ophthalmology*, vol. 45, no. 6, pp. 493–515, 2001.

[87] S. F. Sousa, P. A. Fernandes, and M. J. Ramos, "Protein–ligand docking: current status and future challenges," *Proteins: Structure, Function, and Bioinformatics*, vol. 65, no. 1, pp. 15–26, 2006.

[88] S. A. Hollingsworth and R. O. Dror, "Molecular dynamics simulation for all," *Neuron*, vol. 99, no. 6, pp. 1129–1143, 2018.

[89] X. Liu, D. Shi, S. Zhou, H. Liu, H. Liu, and X. Yao, "Molecular dynamics simulations and novel drug discovery," *Expert Opinion on Drug Discovery*, vol. 13, no. 1, pp. 23–37, 2018.

[90] T. Hansson, C. Oostenbrink, and W. van Gunsteren, "Molecular dynamics simulations," *Current Opinion in Structural Biology*, vol. 12, no. 2, pp. 190–196, 2002.

[91] J. A. McCammon, B. R. Gelin, and M. Karplus, "Dynamics of folded proteins," *Nature*, vol. 267, no. 5612, pp. 585–590, 1977.

[92] R. Salomon-Ferrer, A. W. Gotz, D. Poole, S. Le Grand, and R. C. Walker, "Routine microsecond molecular dynamics simulations with AMBER on GPUs. 2. Explicit solvent particle mesh Ewald," *Journal of Chemical Theory and Computation*, vol. 9, pp. 3878–3888, 2013.

[93] J. D. Durrant and J. A. McCammon, "Molecular dynamics simulations and drug discovery," *BMC Biology*, vol. 9, pp. 71–79, 2011.

[94] S. Kalyaanamoorthy and Y.-P. P. Chen, "Modelling and enhanced molecular dynamics to steer structure-based drug discovery," *Progress in Biophysics and Molecular Biology*, vol. 114, no. 3, pp. 123–136, 2014.

[95] A. Kuzmanic and B. Zagrovic, "Determination of ensemble-average pairwise root mean-square deviation from experimental B-factors," *Biophysical Journal*, vol. 98, no. 5, pp. 861–871, 2010.

[96] P. Liu, J. Lu, H. Yu, N. Ren, F. E. Lockwood, and Q. J. Wang, "Lubricant shear thinning behavior correlated with variation of radius of gyration via molecular dynamics simulations," *The Journal of chemical physics*, vol. 147, no. 8, Article ID 084904, 2017.

[97] K. M. Kumar, A. Anbarasu, and S. Ramaiah, "Molecular docking and molecular dynamics studies on β-lactamases and penicillin binding proteins," *Molecular BioSystems*, vol. 10, no. 4, pp. 891–900, 2014.

[98] N. Homeyer and H. Gohlke, "Free energy calculations by the molecular mechanics Poisson–Boltzmann surface area method," *Molecular Informatics*, vol. 31, no. 2, pp. 114–122, 2012.

[99] H. Sun, Y. Li, M. Shen et al., "Assessing the performance of MM/PBSA and MM/GBSA methods. 5. Improved docking performance using high solute dielectric constant MM/GBSA and MM/PBSA rescoring," *Physical Chemistry Chemical Physics*, vol. 16, no. 40, pp. 22035–22045, 2014.

[100] J. Ren, X. Yuan, J. Li et al., "Assessing the performance of the g_mmpbsa tools to simulate the inhibition of oseltamivir to influenza virus neuraminidase by molecular mechanics Poisson–Boltzmann surface area methods," *Journal of the Chinese Chemical Society*, vol. 67, no. 1, pp. 46–53, 2020.

[101] I. H. Eissa, M. S. Alesawy, A. M. Saleh, E. B. Elkaeed, B. A. Alsfouk, and A.-A. M. M. El-Attar, "Silico determination of the most promising SARS-CoV-2 nsp16-nsp10 2′-o-methyltransferase complex inhibitors among 3009 FDA approved drugs," *Molecules*, vol. 27, p. 2287, 2022.

[102] Y. M. Suleimen, R. A. Jose, R. N. Suleimen et al., "Jusanin, a new flavonoid from *Artemisia commutata* with an in silico inhibitory potential against the SARS-CoV-2 main protease," *Molecules*, vol. 27, no. 5, p. 1636, 2022.

[103] Y. M. Suleimen, R. A. Jose, R. N. Suleimen et al., "Isolation and in silico SARS-CoV-2 main protease inhibition potential of jusan coumarin, a new dicoumarin from *Artemisia glauca*," *Molecules*, vol. 27, no. 7, p. 2281, 2022.

[104] E. B. Elkaeed, H. Elkady, A. Belal et al., "Multi-phase in silico discovery of potential SARS-CoV-2 RNA-dependent RNA polymerase inhibitors among 3009 clinical and FDA-approved related drugs," *Processes*, vol. 10, no. 3, p. 530, 2022.

[105] R. P. D. Bank, 2020, https://www.rcsb.org/structure/4OW0.

[106] Y. M. Suleimen, R. A. Jose, R. N. Suleimen et al., "Isolation and in silico anti-SARS-CoV-2 papain-like protease potentialities of two rare 2-phenoxychromone derivatives from Artemisia spp," *Molecules*, vol. 27, no. 4, p. 1216, 2022.

[107] S. O. Mohammed, S. H. E. El Ashry, A. Khalid et al., "Expression, purification, and comparative inhibition of *Helicobacter pylori* urease by regio-selectively alkylated benzimidazole 2-thione derivatives," *Molecules*, vol. 27, no. 3, p. 865, 2022.

[108] R. G. Yousef, H. M. Sakr, I. H. Eissa et al., "New quinoxaline-2 (1H)-ones as potential VEGFR-2 inhibitors: design, synthesis, molecular docking, ADMET profile and anti-

proliferative evaluations," *New Journal of Chemistry*, vol. 45, no. 36, pp. 16949–16964, 2021.

[109] H. H. Amer, S. H. Alotaibi, A. H. Trawneh, A. M. Metwaly, and I. H. Eissa, "Anticancer activity, spectroscopic and molecular docking of some new synthesized sugar hydrazones, Arylidene and α-Aminophosphonate derivatives," *Arabian Journal of Chemistry*, vol. 14, no. 10, Article ID 103348, 2021.

[110] M. S. Alesawy, A. A. Al-Karmalawy, E. B. Elkaeed et al., "Design and discovery of new 1, 2, 4-triazolo [4, 3-c] quinazolines as potential DNA intercalators and topoisomerase II inhibitors," *Archiv der Pharmazie*, vol. 354, no. 3, Article ID 2000237, 2021.

[111] S. Jo, T. Kim, V. G. Iyer, and W. Im, "CHARMM-GUI: a web-based graphical user interface for CHARMM," *Journal of Computational Chemistry*, vol. 29, no. 11, pp. 1859–1865, 2008.

[112] B. R. Brooks, C. L. Brooks III, A. D. Mackerell Jr. et al., "CHARMM: the biomolecular simulation program," *Journal of Computational Chemistry*, vol. 30, no. 10, pp. 1545–1614, 2009.

[113] J. Lee, X. Cheng, J. M. Swails et al., "CHARMM-GUI input generator for NAMD, GROMACS, AMBER, OpenMM, and CHARMM/OpenMM simulations using the CHARMM36 additive force field," *Journal of Chemical Theory and Computation*, vol. 12, no. 1, pp. 405–413, 2016.

[114] R. B. Best, X. Zhu, J. Shim et al., "Optimization of the additive CHARMM all-atom protein force field targeting improved sampling of the backbone ϕ, ψ and side-chain χ_1 and χ_2 dihedral angles," *Journal of Chemical Theory and Computation*, vol. 8, no. 9, pp. 3257–3273, 2012.

[115] J. C. Phillips, R. Braun, W. Wang et al., "Scalable molecular dynamics with NAMD," *Journal of Computational Chemistry*, vol. 26, no. 16, pp. 1781–1802, 2005.

Review Article

Metal Complexes in Target-Specific Anticancer Therapy: Recent Trends and Challenges

Gemechu Shumi [1], **Tegene Desalegn** [1], **Taye B. Demissie** [2],
Venkatesha Perumal Ramachandran [1], **and Rajalakshmanan Eswaramoorthy** [1,3]

¹*Department of Applied Chemistry, School of Applied Natural Sciences, Adama Science and Technology University,
Adama, P.O. Box 1888, Ethiopia*
²*Department of Chemistry, University of Botswana, Notwane Rd, P/bag UB 00704, Gaborone, Botswana*
³*Department of Biomaterials, Saveetha Dental College and Hospitals,
Saveetha Institute of Medical and Technical Sciences (SIMATS), Saveetha University, Chennai, India*

Correspondence should be addressed to Gemechu Shumi; gameshumi@gmail.com and Tegene Desalegn; tehtegened@yahoo.com

Cancer is characterized by abnormal cell differentiation in or on the part of the body. The most commonly used chemotherapeutic drugs are developed to target rapidly dividing cells, such as cancer cells, but they also damage healthy epithelial cells. This has serious consequences for normal cells and become responsible for the development of various disorders. Several strategies for delivering the cytotoxic drugs to cancerous sites that limit systemic toxicity and other adverse effects have recently been evolved. Among them, biomolecule-conjugated metal complexes-based cancer targeting strategies have shown tremendous advantages in cancer therapy. This review focuses on several chemoselective biomolecules-bound metal complexes as prospective cancer therapy-targeted agents. In this review, we presented the details of the various extra- and intracellular targeting mechanisms in cancer therapy. We also addressed the current clinical issues and recent therapeutic strategies in targeted cancer therapy that may pave a way for the future direction of metal complexes-based targeted cancer therapy.

1. Introduction

1.1. Introduction to Cancer Therapy. Cancer is a more complicated and fatal disease that poses a threat to human health all over the world. It involves multiple genes and crosstalk between signaling networks, changes in DNA, and/or gene transcription and/or translation [1]. Cancer is caused by the malfunctioning of normal cell genes, which promotes uncontrolled proliferation, metastasis, and the rapid expansion of aberrant cells that grow beyond their normal limits. In the year 2020, the US was anticipated to witness 606,520 deaths and 1.8 million new cases [2]. About 4.5 million premature cancer-caused deaths were reported worldwide in 2016 [3]. Based on current data, the International Agency for Research on Cancer (IARC) forecasts that around 13 million cancer-related deaths would occur by

2030, prompting researchers to continue their hunt for an effective anticancer medicine [4, 5]. The most common clinical approaches for cancer treatment are chemotherapy, radiation therapy, surgery, hormone therapy, and targeted therapy with anticancer drugs [6]. All cancer therapies have the potential to harm normal cells while destroying cancer cells [7]. Targeted therapy, on the other hand, is a potential choice since normal cells can survive when cancer cell proliferation is reduced during targeted therapy [8]. The damaged proteins produced by these mutated genes could be treated with targeted therapy [9, 10].

1.2. Challenges in Recent Cancer Chemotherapy. The finding of the anticancer drug cisplatin is a noticeable breakthrough in cancer chemotherapy [11]. Cisplatin, also known as *cis-*

diamminedichloroplatinum(II), is an antitumor drug used in the treatment of a range of malignancies, including testicular, ovarian, bladder, cervix, lung, head and neck, and breast cancers [12]. However, cisplatin's clinical use is limited due to the appearance of hazardous side effects like nephrotoxicity, neurotoxicity, and cytotoxicity [13, 14]. The primary drawbacks of cancer therapy are mainly the lack of specificity of drugs and ineffective accumulation of drugs at tumor sites, as well as development of drug resistance [15, 16]. As a result, second-generation anticancer medicines, such as metal-based compounds with a tailored drug delivery mechanism, are being developed as potential alternatives [17, 18]. TDDS is a promising field of study that requires an interdisciplinary approach to deliver drugs to target sites while avoiding damage to healthy tissues and organs [19, 20].

Many research groups have demonstrated delivery systems based on target-specific groups, primarily peptide substrates, heterocyclics, oligonucleotides, and monoclonal antibodies [21, 22]. However, their unreducible mass makes it difficult to penetrate solid tumors, and the excretion of unbound reagent is a disadvantage for future use [23]. Only cancer cells would be affected by targeted therapeutic medications that inhibit the mutated form of the protein while maintaining activity of the normal version. Agents that do not contain metals as well as metal complexes are the active agents in medicinal inorganic chemistry. Since the nonemitting ligands are biomolecules (protein or peptide, lipids, vitamins, and nucleic acid), metal complex fragments that keep a part of the carrier ligands are essential because they can help with conjugation and provide selectivity or controlled release activity [24, 25]. There are seven different types of metal-based drugs: (i) one or more ligands are involved in biological activity [26], (ii) a fragment of the complex [27], (iii) the entire reactive complex [28], (iv) the metal is a radiation enhancer [29], (v) the metal ion or its biotransformation product is the active ingredient [30], (vi) the metal is radioactive [31], and (vii) the entire inert complex [32]. Understanding how metals interact with biomolecules raises the potential for modifying metal characteristics, speciation, reactivity, and, ultimately, biological function [33, 34].

Currently, researchers are focusing their efforts on ligand-targeted delivery of medicines. Franz and Metzler-Nolte [35] have reported many biomolecule ligands such as peptides, carbohydrates, lipids, and vitamins, which act as ligand-targeted delivery of drugs. This review attempts to investigate the anticancer metal complexes bound to folic acid, albumin, biotin, and hyaluronic acid, as well as folic acid-human serum albumin, erlotinib, suberoylanilide hydroxamic acid, and valproic acid. The capacity to serve as drug-carriers delivering drugs to receptors and their high selectivity and affinity are the two advantages of these biomolecules [35]. There is a pressing need to develop carriers (vectors) and delivery methods that can carry chemotherapeutic medicines only to the precise target site, thereby improving treatment efficiency and reducing undesirable systemic side effects [19, 20, 36]. The other approach makes use of the fact that malignant cells have more receptors on their surface than healthy cells, allowing cytotoxic drugs to be targeted more effectively at tumor cells. As a result, therapeutic efficacy enhances while side effects diminish [37].

The targeting ligands are biomolecules that include folic acid, biotin, albumin, and hyaluronic acid. Folic acid (FA) is a targeted molecule that has been studied extensively in the fields of imaging, diagnostics, and cancer treatment [35]. Because of their rapid development and cell division, several cancer cell lines overexpress FA receptors (FARs), including ovary, prostate, lung, nose, brain, and colon cancer. Normal cells, on the other hand, express very little folate receptors (FARs). Therefore, some of the anticancer drugs conjugated with biomolecules and metal complexes can selectively accumulate in tumor tissues. By utilizing specific or overexpressed receptors, anticancer drugs can be delivered to cancerous cells and tissues in a targeted manner. However, the use of biomolecules-conjugated metal complexes remains a challenge in the realm of cancer treatment [38, 39].

1.3. Methodology of the Review. Web-based literature searching tools, such as SciFinder, PubMed, and Google Scholar, were used to carefully select articles. The literature survey mainly covers the years from 2010 to 2021. However, some relevant literatures out of the interval were also highlighted. The review emphasized on reports on metal complexes in cytotoxic target-specific anticancer therapy, cellular targeting and mechanisms, metal complex-conjugated biomolecules, and folate-conjugated metal-nanoparticles for target drug delivery. By unbalancing the cellular redox state, the metal complex takes up the cell membrane through a receptor on the cell's surface and interacts with organelles, causing cellular death. This review also looks at how biomolecules like folic acid, biotin, and hyaluronic acid can be used to selectively interact with and accumulate metallodrugs in cells.

2. Mechanism of Cellular Targeting and Targeted Cancer Therapy

2.1. Intracellular Targets

2.1.1. Nucleic Acids. The nucleus, the cell's largest organelle, was initially found in the early 1800s. It functions as the cell's brain since it contains the most genetic components, such as chromosomes made up of lengthy DNA strands and nucleoproteins like histones that regulate gene expression [40–42]. Transcription from rDNA to rRNA that occurs in the nucleolus, which includes both nucleic acid and proteins, is one of the most important phases in the gene expression process [43].

Metal complexes are appealing candidates in cancer research, due to their enormous range of structures and activities, as well as the metals' various oxidation state and coordination geometry, among large range of organic ligands attached to the metal center [44]. They are modular systems with a great deal of adaptability. Functionalization of ligands can alter cellular absorption, accumulation, and

biomolecule targeting (Figure 1). With ligand alterations, the metal core can have photophysical, electrochemical, and spectroscopic properties that can be tuned. These features can be used to improve diagnosis and treatment of diseases. Metal complexes bind to nucleic acids in two ways: covalent bonds via direct coordination of metal ions (e.g., platinum agents) or noncovalent bonds via supermolecular interactions of organic ligands (for instance, numerous metal complexes used in bioimaging). As seen in platinum drugs, the metal center attaches directly to the nitrogen atoms of the nucleobases in the first case [45]. The organic ligands, on the other hand, determine the interaction that can be hydrophobic groove bonding, hydrogen bonding, electrostatic interaction, intercalation, insertion, or a mix of these. Due to these, metal complexes that interact with nucleic acids have been proposed for a variety of applications such as pharmaceuticals, fluorescent imaging probes, foot printing agents, and nanotechnology [23, 40, 46].

In addition, recent research has focused on the development of metal compounds capable of targeting DNA noncanonical configurations, even though DNA is generally found as a duplex structure. Target specific sequences using tailored compounds to target certain structural features allows metal complexes to attach to nucleic acids [47, 48]. Ruthenium(II) complexes that can bind to extended DNA; iron(II) that binds to DNA in three-way junctions; and various metal-containing polycyclic planar aromatic compounds that bind to G-quadruplex DNAs, such as metal-salphen and platinum(II) terpyridine complexes, were reported [49–51]. All of these noncanonical structures are found to be potential targets for structure- and shape-specific binders. Moreover, RNA has even more noncanonical structural components than DNA, but it has been less investigated as a metal complex target. RNA is an important molecule: in recent decades, messenger ribosomal and transfer RNA have been discovered, permitting the passage of genetic material from DNA to proteins in enormous quantities of noncoding RNAs [52, 53]. Examples include short microRNAs (miRNA) and ribo-switches, which both play a role in gene regulation, as do ribozymes, which are catalytically active RNAs that can catalyze reactions without the use of a protein. They target noncanonical elements, which is a difficult but effective technique to disrupt RNA function [54, 55]. Also, various small compounds that target RNAs have been developed [46].

2.1.2. Mitochondria.

The mitochondrion is a semi-independent organelle with a double membrane that controls most the cell's metabolic functions. The electron transport chain is stored within the inner mitochondrial membrane, where electrons are moved from NADH to oxygen in redox processes and energy is used to pump H^+ out of the matrix, resulting in a negative charge within [56]. Mitochondria control cell metabolism, the production of reactive oxygen species (ROS), cell death, and calcium, the second universal messenger. Mitochondria, the cell's powerhouses and energy centers, are essential for cancer metabolism. The phrase "aerobic glycolysis," known as the Warburg effect, was used
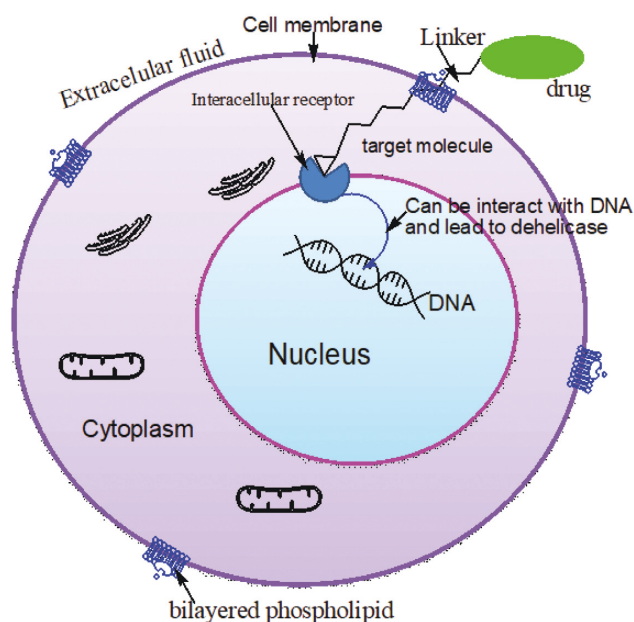
FIGURE 1: General model of intracellular targeting mechanism (adapted from Ref. [44]).

to explain mitochondria's role in carcinogenesis. This is because tumor cells create energy via glycolysis rather than the tricarboxylic acid (TCA) cycle. This phenomenon was linked by Warburg to tumor cell mitochondrial malfunction, and he suggested that tumor cells were forced to rely on glycolysis due to the loss of the mitochondrial respiratory chain [57, 58].

Anticancer drugs that directly target mitochondrial functionality have significant benefits over traditional chemotherapy drugs that cause mitochondrial dysfunction in an indirect manner by employing damaged DNAs to generate apoptosis-initiating signals. Many transition-metal complexes that accumulate within mitochondria are emissive, and the fluorescence of these complexes can be used to demonstrate both cellular uptake and organelle-specific distribution. The contribution of the Au(I) (phosphine) moiety to mitochondria has been described, with an emphasis on di- and tetrapeptides. The cause is an increase in reactive oxygen species (ROS) within the cells [59]. Hao and coworkers described three novel Ir metallic complexes containing cdppz (11-chlorodipyrido[3,2-a,2′,3′-c]phenazine) as mitochondrial-targeting anticancer agent: [Ir(ppy)2(cdppz)] (PF6) (ppy = 2-phenylpyridine), [Ir(bzq)2(cdppz)](PF6) (2) (bzq = benzo[h]quinolone), and [Ir(piq)2(cdppz)](PF6) (3) (piq = 1-phenylisoquinoline). These complexes increase intracellular ROS levels, diminish mitochondrial membrane capacity, and cause apoptosis by regulating the stages of apoptosis-related proteins, preventing colony formation, and slowing the cellular cycle at G0/G1 phase [60].

2.1.3. Lysosome.

Lysosomes are dense granular structures with hydrolytic enzymes that are mainly responsible for intracellular and extracellular digestion. A hydrogen proton

pump is located on the lysosomal membrane and is responsible for maintaining the pH of the enzymes. The lysosomal enzymes' functionality is ensured by the acidic media maintained by the proton pump, which pumps H$^+$ into the lumen. Lysosomes, which are loaded with enzymes known as hydrolases, are responsible for the breakdown of extracellular and intracellular materials. It contains around 40 different enzymes that are divided into five categories: proteases, lipases, amylase, nucleases, and phosphoric acid monoesters. Hydrolases are a class of enzymes that use water molecules to cleave substrates. Most lysosomal enzymes work in an acidic environment [61].

Cancer growth, invasion, and metastasis all require lysosome migration toward the cell periphery. Lysosomes alter in number, shape, hydrolase concentration, luminal pH, and intracellular distribution during neoplastic transformation. The population of lysosomes has migrated from the center to the periphery of the cytoplasm, which is a particularly noticeable modification. Changes in the tumor microenvironment, such as acidity, or changes in the expression of genes that control lysosome location and motility, which occur during oncogenic transformation, could trigger this redistribution. Lysosome's exocytosis, extracellular matrix breakdown, cell adhesion, and migration are facilitated by centrifugal transport of lysosomes, all of which lead to cancer. Anticancer treatments should investigate targeting the regulation of lysosome placement and motility [58, 61].

Yang and coauthors [62] synthesized lysosome-targeted cyclometalated iridium(III) anticancer complexes containing imine-N-heterocyclic carbene ligands [Ir(ppy)$_2$(CN)] PF$_6^-$ (wherein CN are imine-N-heterocyclic carbene ligands with diverse substituents and ppy is 2-phenylpyridine). Iridium complexes cause cellular autolysis and cell death by destroying the lysosomal membrane in which lysosomal damage changes accountable for the cell apoptosis. Moreover, rhodamine-modified metalated Ir(III) complexes that target lysosomes exert effective anticancer outcomes through unique mechanisms, along with targeting subcellular organelles and inhibiting protein activities [63]. Ru-1@TPP-PEG-biotin has also been used in targeting lysosomes as a brand new anticancer therapeutic strategy, and it was also stated that it contributed to the instability of the lysosomal membrane through the reduced expression of ceramide [64].

2.2. Extracellular Targeted Therapy

2.2.1. Cell Membrane.
The cell membrane is vital for its receptors, signal transmission, enzymatic activity, fusion-fission, endocytosis, and transport, in addition to its structural function. It is responsible for cell-environment interaction. Specific bilayer activities are linked to high lipid compositional diversity, flexibility, interactions, and dispersion, impacting membrane or cell characteristics. Lipid research has shown to be critical in better understanding the intricacies of biological systems and disorders. Lipids feature a lengthy hydrophobic tail and a polar head. Due to thermodynamic factors, hydrophobic tails are covered by a layer

of hydrophilic heads, forming micelles or bilayered sheets that are thought to be the origin of cell membranes and spontaneously associate in aqueous conditions. These components facilitate noncovalent interactions with other biomolecules including proteins and lipids, which help to shape cellular and organelle membranes. Membranes' lipid composition and distribution are not uniform. Lipid asymmetry between the inner and outer membrane leaflets is caused by phospholipid enrichment with amine or serine moieties in the inner leaflet, whereas choline and sphingomyelins (SMs) predominate on the exterior. For millennia, people have used lipids in their meals and supplements to improve their health and avoid illness [65]. Mono- and polyunsaturated fatty acids, together with oleic acid, linoleic acid, and fish oils, are thought to prevent colon cancer. The cellular membrane may be used alone or in combination with current chemotherapeutics and small compounds to deal with cancer. The cellular membrane and its components ought to be considered in cancer treatment, and clean therapeutic techniques need to be advanced [66, 67].

2.2.2. Cellular Receptors.
A cell receptor structure (CRS) is a structure on a cell's surface that permits it to admit outside molecules like nutrients and hormones, as depicted in Figure 2. There are many different types of receptors, but they can be categorized into two groups: intracellular receptors (found in the cytoplasm or nucleus) and extracellular or cell surface receptors (found in the plasma membrane) [68]. The CRS plays a role in a wide range of physiological and pathological processes, such as the extracellular matrix, growth factor signaling, and cell activation in response to microbial invasion. The progression of degenerative diseases such as cancer, atherosclerosis, and neurological disorders is dependent on cell surface receptors [69].

The main goal of cancer detection and/or treatment is to develop drugs that can target the tumor microenvironment. Some overexpressed receptors, such as αVβ3 integrin, folate receptor (FAR-α), epidermal growth factor receptor (EGFR), vascular endothelial cell growth factor receptor 2 (VEGFR2), and neuropilin-1 (NRP1), are commonly exploited as targets for cancer applications [69]. Overexpression of the human epidermal receptor 2 (*HER2*) proteins is frequently seen in a variety of primary tumors and contributes to carcinogenesis, particularly in breast cancer [71, 72].

The cell membrane, which separates the interior of cells from the outside environment, is engaged in a number of cellular functions, including selectively identifying and transporting specific molecules, as well as cell signaling transmission. Deng and coauthors [73] discovered that Ru complexes containing phenylterpyridine derivatives had anticancer properties and identified their cell membrane target receptors. The coupling of ruthenium polypyridyl subunits and EGFR-inhibiting 4-anilinoquinazoline ligands results in a class of extremely active dual-targeting anticancer drugs. The anticancer potency of the most active Ru(II) polypyridyl complexes is similar to that of cisplatin and higher than that of gefitinib, according to an *in vitro* antiproliferation experiment
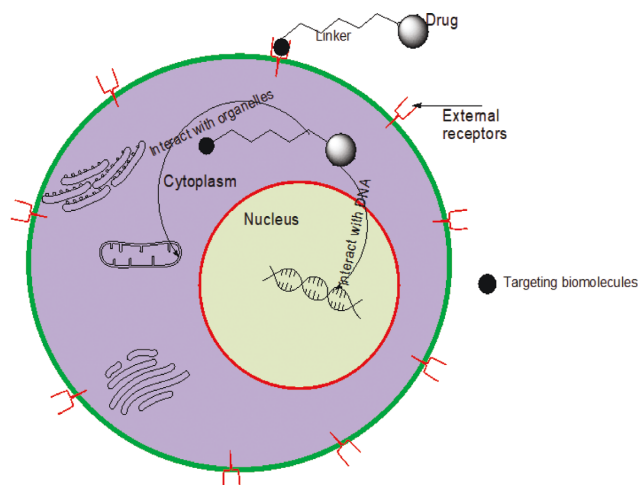
FIGURE 2: Model of extracellular/surface cell target mechanism (adapted from Ref. [70]).

against a range of EGRF-overexpressing cancer cell lines [73].

3. Metal Complexes-Biomolecule Conjugation in Targeted Cancer Therapy and Their Challenges

The production of metal complexes as medications or diagnostic agents has piqued the interest of medicinal chemistry. A metal complex, also known as a coordination compound, is made up of a core metal atom and an array of molecules or anions known as ligands. Metal compounds provide therapeutic action mechanisms that organic agents cannot achieve due to their vast range of coordination numbers, geometries, and their kinetic properties (Figure 3) [74]. Preclinical studies *in vitro* and *in vivo* have investigated various metal compounds as antitumor medicines. Complexes with ionic organic ligands, classical inorganic agents, and increasingly organometallic species are all present in the various agents examined. Main group metals (such as bismuth, tin, antimony), transition metals (such as rhodium, vanadium, iron, cobalt, and gold), and cerium are among the metals studied. In contrast to organic molecules, metals provide accessible redox states, a wide range of coordination numbers, and ligand substitution kinetics for the design of anticancer medicines [75, 76].

Metallocomplexes have created new challenges in terms of pharmacological limitations including low water solubility and reduced bioavailability. In order to attain a greater therapeutic index, breakthrough metal complexes must boost the selectivity of tumor cells over healthy cells, in addition to improving solubility. Targeting ligands, which are coupled to metal and carry the medicine to the interesting cells, can provide precise delivery. A targeted delivery system is defined as the ability of a molecule (ligands or metal complexes) to be recognized by membrane receptors on tumor cells, resulting in efficient accumulation into tumor tissue. This build-up can also be caused by tumor cells'

high need for a substance that is not or lesser required by normal cells, like vitamins and sugars [77, 78].

Metals have distinct properties such as various coordination modes, redox activity, and reactivity and are required for a variety of metabolic activities in cells. Their concentration is tightly regulated inside the cells due to their reactivity. These metals all could produce reactive oxygen species (ROS), which are important in cell metabolism, signaling for proliferation, differentiation, and cell death, and are a part of the cellular redox balance. Furthermore, ligand substitution and modification of existing chemical structures resulted in the synthesis of a wide spectrum of metal-based compounds, some of which have a better cytotoxic and pharmacokinetic profile than others. Figure 4 depicts the mechanism and specific function of metal complexation in increased drug-metal complex efficacy or potency [79].

Many anticancer drug applications had been designed to apply as cancer cell reductase enzymes for target-specific activation. Some may also comprise metal complexes as prodrugs for bioreductive activation [80]. For instance, cobalt complexes are reported to be bioreductive prodrugs, having a completely inert oxidized cobalt(III) state and really labile reduced cobalt(II) state [81]. The Pt(IV) metal complex is an inert prodrug, and its reduction yields an active Pt(II) complex and equivalents of active ligands. Metal complex-drug conjugation can grow the potency and the performance of the drug. Besides these, curcumin is a bioactive ligand; however, it has poor stability and bioavailability [82]. The coordination of curcumin to an oxovanadium(IV) dipyridophenazine (dppz) complex was found to prevent the hydrolytic cleavage of curcumin under physiological conditions and increases the efficiency of curcumin to target DNA cleavage [83]. The metal complex can itself be biologically active. With the active metal complex and active organic molecules from a single prodrug, more than one way of acting upon a target can be realized. Synergy action drugs can be more potent than the parent organic drug and be able to avoid drug resistance mechanisms [84].

Conjugation of a drug to a positively charged metal complex has been shown to greatly enhance the aqueous solubility of the drug because of its hydrophilicity. Alternatively, conjugation of metal to negatively charged groups can reduce the negative charge of a drug, enhancing passive cellular uptake and absorption [79]. Those are effective approaches to enhancing both the pharmacokinetic and pharmacodynamic properties of the parental drug and metal-conjugated drugs to enter the cell. Reducing side effects and booming of the bioavailability of the metal-drug complexes can mainly depend on changes in environmental situations, which include the redox status of the metals and the pH conditions [85–87].

3.1. Folic Acid-Conjugated Metal Complexes. Folic acid belongs to a category of water-soluble vitamins that function as a coenzyme in the production of DNA, RNA, and protein constituents, as well as numerous single carbon transfer processes [88]. Hamed and coauthor [89] investigated the
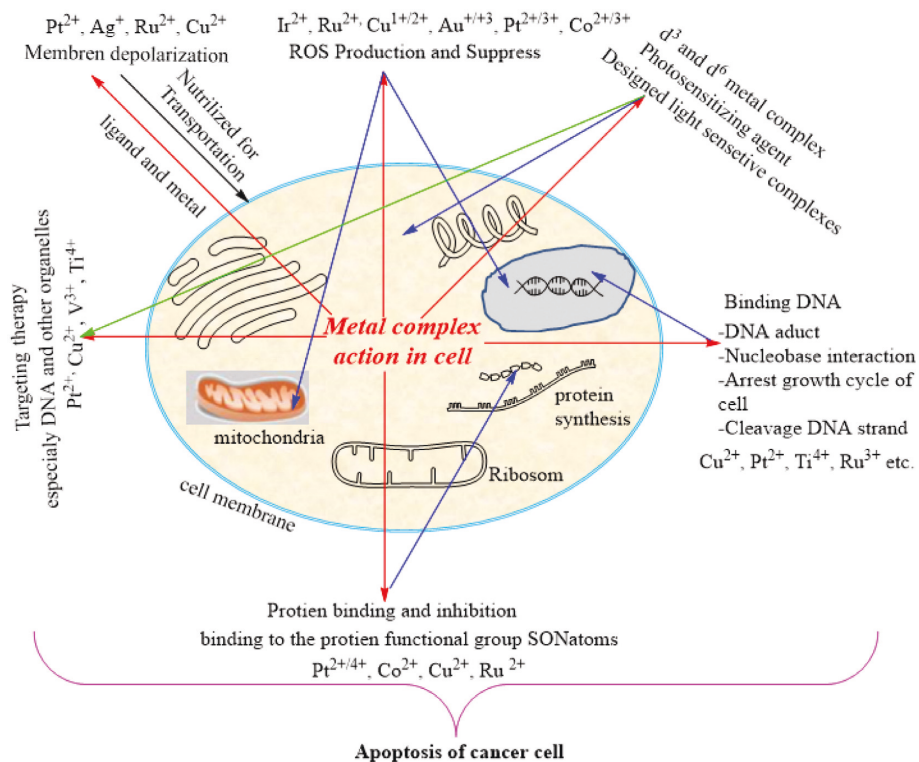
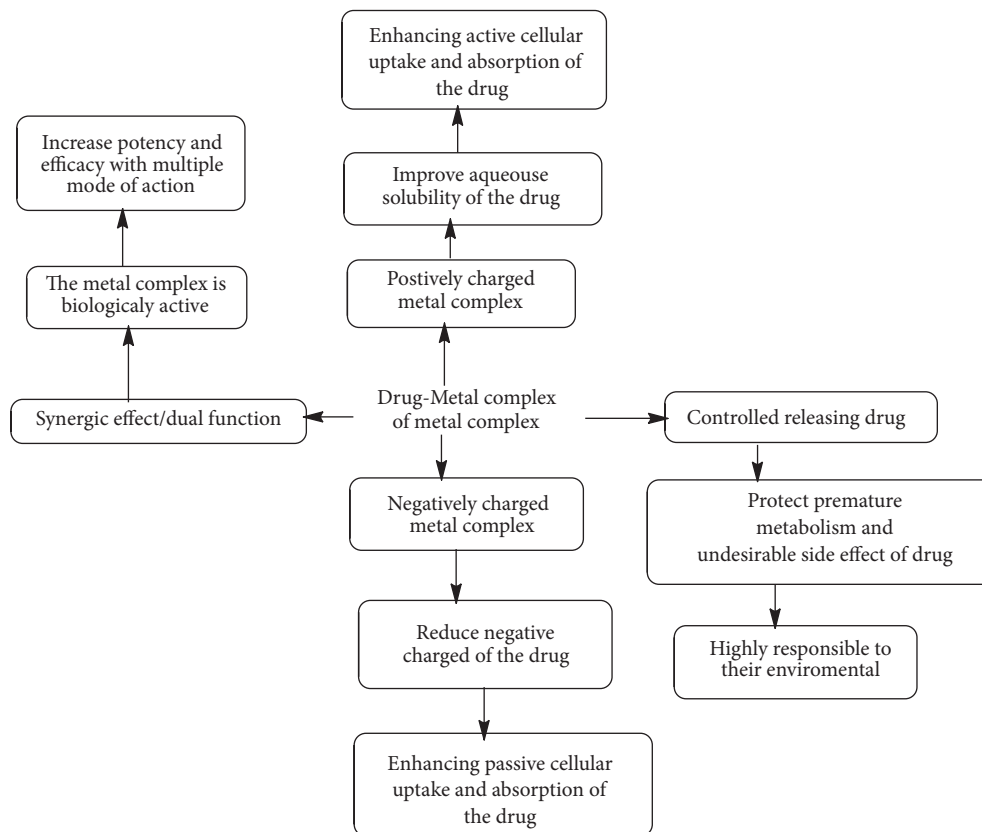FIGURE 3: Mechanism of metal complex targeting cellular structure. Adapted from Ref. [74].

FIGURE 4: Illustration the mechanism and potency of drug-metal complex.

absorption efficiencies of folic acid alone and in complexes with metals like Fe(III) and Cu(I), finding that the metal complexes were substantially more absorbed in the blood than folic acid. Therefore, they have concluded that folic acid-transition metal complexes are preferential over folic acid alone because of their higher absorption efficiency than folic acid. On the other hand, folic acid serves as a bidentate ligand, allowing it to extract or withdraw important metals from the blood serum [89].

Yang and coauthors [39] reported the platinum porphyrin complex (PPC) coupled with folic acid can selectively accumulate in tumor tissue. PPC is an efficient photosensitizer for tumor-targeted photodynamic treatment (PDT) [90]. The folic acid used as a targeting biomolecule is bonded to PPC to improve the photosensitizer's tumor-targeting competency via folate receptor mediated. Through the heavy atom impact, platinum is coordinated with the porphyrin conjugate to boost the photodynamic therapeutic efficacy of the drug [91]. As a result, the folate-conjugated PPC demonstrated remarkable therapeutic efficacy in a dose-dependent manner against HeLa cells, with an IC_{50} of roughly $5.78\,\mu M$ after irradiation. The surviving rate of HeLa cells (positive folate receptor) was only $22.25 \pm 4.75\%$; when the concentration of sample was increased to $20\,\mu M$, the survival rate of A549 cells (negative folate receptor) was $75.25 \pm 4.75\%$, indicating that PPC accumulates selectively in cancerous cells with high folate receptor expression. As PPC is one of the photo sensors, even if it accumulated in the cell due to folic acid, it is not active in the absence of radiation. These findings showed that the synthesized platinum-porphyrin with folate might be employed as an effective photosensitizing agent for cancer treatment.

Targeted therapy medications are gaining popularity because most cancer-killing drugs lack specificity for tumor cells, causing significant toxic effects in healthy organs during treatment. Ru-NO@FA@CDs is a NO-delivery nanoplatform in which a folic acid (FA), a Ru-NO donor, and ruthenium nitrosyl molecules are covalently bound to the surface of carbon dots (CDs) was described as a targeted medication (Scheme 1). Confocal laser scanning microscopy was used to confirm the specific binding of Ru NO@FA@CDs to the folate receptor (FAR) human cervical cancer cell. The Ru-NO@FA@CDs nanoplatform exhibited targeted NO delivery to several cell lines, which was monitored using fluorescence under complete control of visible light irradiation [92].

To create a multifunctional NO-delivery nanoplatform, ruthenium nitrosyls were covalently linked onto the surface of a CD carrier, together with cancer-cell-guiding FA molecules. The RF-overexpressed cancer cell lines are preferentially targeted by the Ru-NO@FA@CDs nanoplatform, which allows for intracellular delivery of NO under the control of light to kill cancer cells. The Ru-NO@FA@CDs nanoplatform could be monitored by fluorescence as it was utilized and absorbed by cells since CDs have inherent fluorescence. Furthermore, the amount of NO released from the Ru-NO@FA@CDs nanoplatform may be regulated by altering the exposure of the nanoplatform to visible light, allowing for spatiotemporal delivery of NO at concentrations ranging from nM to M. This opened the possibility of using it to treat disorders caused by a lack of NO, as well as cancer therapy mediated by NO [39].

Folates (also known as vitamin B9) play a crucial role in metabolic activities like RNA and DNA synthesis, making them vital for the human genome and cell health. The decreased tetrahydrofolate form of folate, which plays a critical role in rapid cell division and growth, has been associated with the pivotal role of folates in DNA synthesis, repair, and methylation. Reduced folate levels have been linked to the development of cancers like colorectal, lung, and breast cancers, possibly due to higher DNA damage and mutation rates. The reduced folate carrier (RFC) is an anion exchanger that primarily carries reduced folate; the proton-coupled folate transporter (PCFT) can carry folate in an acidic environment; and the folate receptors (FARs), which have a high affinity for folic acid (FA), can transport it into cells via endocytosis [93].

Kidney, lung, breast, ovarian, colorectal, cervical, brain, and nasopharyngeal carcinomas all show elevated expression of the FARs, and this enhanced expression has been associated with tumor growth. The FA, which is stable across a wide pH and temperature range, can be employed as a nonimmunogenic and biocompatible targeting motif to covalently conjugate with an optical imaging or therapeutic agent, making the FAR a possible target for cancer diagnostics and treatment [38].

Eu-FA, Eu-MTX, Tb-FA, and Tb-MTX are the visual probes (lanthanide(III)) developed by Du and coauthors [94] to make it possible to image folate receptors in cancer cells. Each complex consists of a high-intensity antenna complex covalently coupled to FA or methotrexate (MTX) (Figure 5). A crucial enzyme in the conversion of folate to its tetrahydrofolate form is dihydrofolate reductase; it is inhibited by MTX, causing cell death by reducing DNA and RNA synthesis. Folates and antifolates have also been utilized as targeting agents in a range of imaging applications. The scientists were able to effectively create four luminous lanthanide complexes that are extremely stable in a wide range of environments. Nonmalignant cells do not readily absorb the folate- and MTX-tethered complexes. FAR-positive cancer cell lines, on the other hand, internalized all four complexes, showing that both FA and MTX can be employed as folate receptor-targeting groups (Table 1). As expected, the complex bound to MTX turned out to be more dangerous than FA, even though the MTX complexes allowed for imaging of the therapeutic activity location. Significantly, Eu(III) complexes were discovered to be considerably more hazardous than Tb(III) complexes. By incubating cells with both Eu-MTX and Tb-FA, cell biologists can investigate MTX toxicity coupled with FA action. This is due to the fact that the emission from these compounds is solved easily. The fact that FA- and MTX-labeled complexes differ in the oral adenosquamous cell line (CAL-27) indicates that folate and antifolate imaging can be utilized to evaluate changes in folate receptors [94].

3.2. FA-HSA-Conjugated Metallodrugs.

When 9–10 FA groups for each HSA molecule were introduced, it was possible to preferentially target tumor cells and tissues while
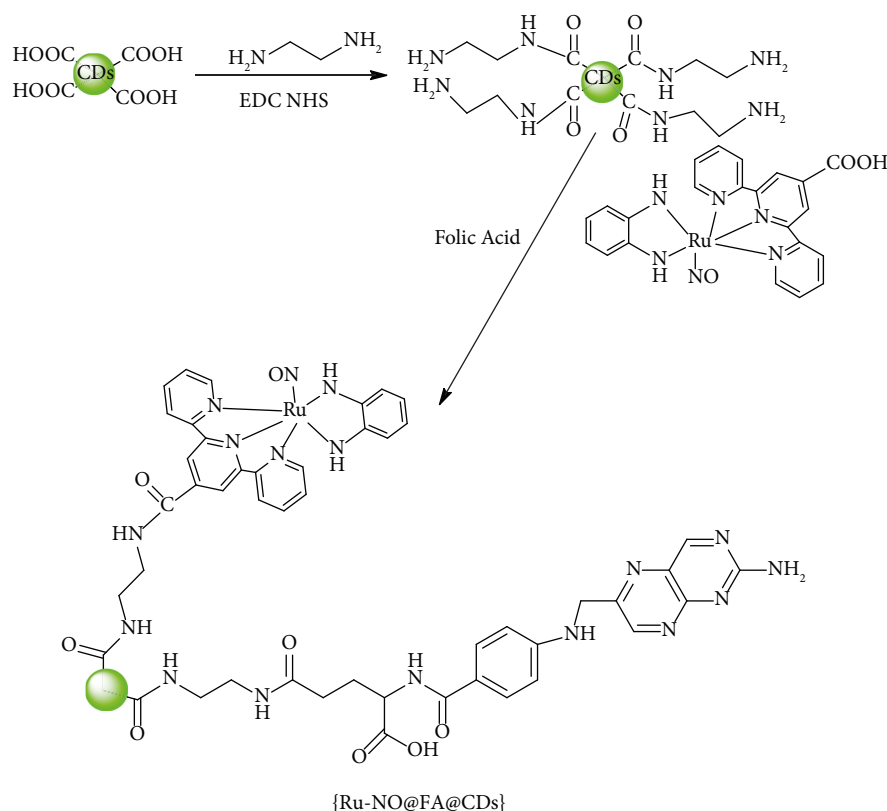
Scheme 1: Synthesis of {Ru-NO@FA@CDs} nanoplatform.

reducing nonspecific damage to normal cells. Molecular or biomaterial FA-conjugated drug delivery techniques include copolymer nanoparticles, albumin, and liposomes [95]. Drug delivery systems based on human serum albumin (HSA) may be the most effective of them due to their unique properties. HSA is a biopolymer with several desirable characteristics, including water solubility, biocompatibility, biodegradability, and high safety. More importantly, HSA possesses a large number of surface functional groups that are easily conjugated to FA. At the stage, the target carriers were FA-functionalized human serum albumin (FA-HSA) conjugates [96–98]. Human serum albumin (HAS) carriers for Cu(II) complexes (Figure 6) were produced by conjugating folic acid (FA) with HAS, as reported by Gou *et al.* [99]. C3 and C4 have a significant cytotoxic effect against both cancerous and noncancerous cells.

On the other hand, in cancer cells, the cytotoxic activity of the FA-HAS metallodrug complexes is three times higher, whereas no such effects are detected in normal cells (Table 2). In comparison to Cu(II) complexes alone, FA-HSA metallodrugs complex have the potential to target FAR-positive tumor cells preferentially while causing minimal cytotoxicity in normal cells. The intrinsic ROS-mediated mitochondrial pathway may play a role in cancer cell death caused by FA-HSA-Cu(II) complexes. In addition, targeting FA-HSA carriers enhances anticancer activity, arrests the cell cycle during the G2/M phase of cancer cells (HeLa), and downregulates cyclin-dependent kinase 1 (CDK1) and cyclin B1. Furthermore, HeLa cells are killed by the FA-HSA metallodrug combination through an endogenous

ROS-mediated mitochondrial pathway, which is aided by Bcl-2 family gene regulation [99, 100].

3.3. Albumin-Conjugated Metal Complexes.

Cancer cells' redox metabolism differs from that of normal cells in that they have higher intracellular ROS concentrations. In addition to intercalation, metal-based drugs seem to increase ROS levels in cancer cells and/or block ROS-detoxifying enzymes (e.g., glutathione) as an anticancer mechanism [101]. Certainly, metal-based drugs' redox cycling is suggested to be a vital factor for enhanced ROS generation, which can damage DNA and contribute to cancer cell death. In blood plasma, human serum albumin (HSA) is the most abundant protein in millimolar quantities [102, 103]. HSA transports fatty acids, drugs, metal ions, and metal complexes and includes amino acid tryptophan at the position 214, which fluoresces intensely at 347 nm when excited at 295 nm. In the presence of the complex, the quenching of HSA fluorescence was evaluated [104]. When the complex binds to the tryptophan residue of HSA, fluorescence quenching occurs, resulting in albumin conformational change, subunit interactions, denaturation, and substrate binding [105, 106].

Simunkova and collaborators investigated the anticancer properties of copper(II) complexes containing flufenamic acid, mefenamic acid, tolfenamic acid, and 1,10-phenathroline (Figure 7). The complexes interact with albumin as targeting biomolecules, and the targeted drug delivery vehicles for Cu(II) complexes have a high affinity binding constant ($K = 106$). Once the albumin-bound complexes
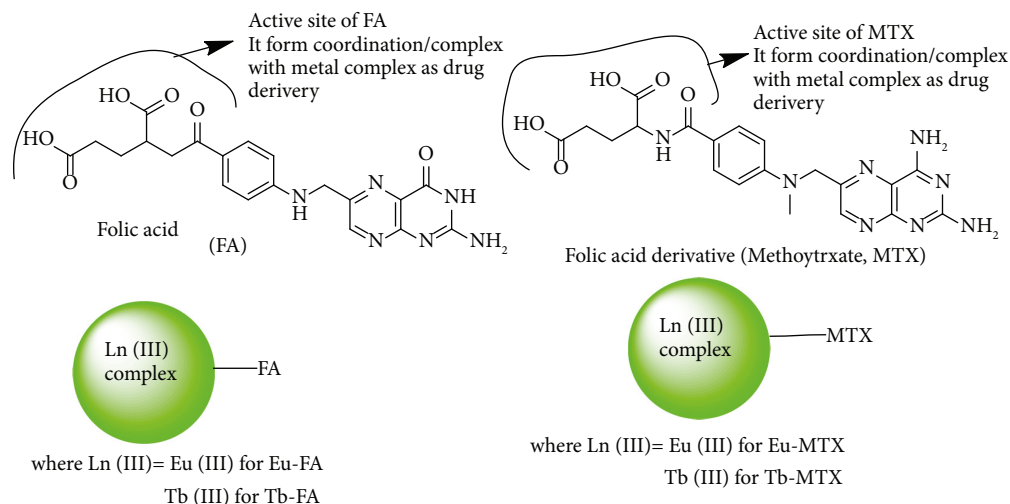
FIGURE 5: The chemical structures of folic acid (FA), methotrexate (MTX), and the four lanthanide complexes Eu-FA, Tb-FA, Eu-MTX, and Tb-MTX.

TABLE 1: The cytotoxic effects of Ln-tethered complexes.

As synthesis agents	MDA-MB-231 (IC_{50}, mM)	HeLa (IC_{50}, mM)	MLO-Y4 (IC_{50}, mM)
Eu-FA	3.59 ± 1.33	1.67 ± 0.52	12.86 ± 4.61
Tb-FA	5.24 ± 1.27	2.25 ± 0.86	12.79 ± 3.56
Eu-MTX	0.26 ± 0.06	0.58 ± 0.79	9.07 ± 3.25
Tb-MTX	1.90 ± 0.32	1.64 ± 0.79	9.22 ± 4.17
MTX	1.60 ± 0.22	1.91 ± 0.17	2.91 ± 0.25

(adapted from [94]).
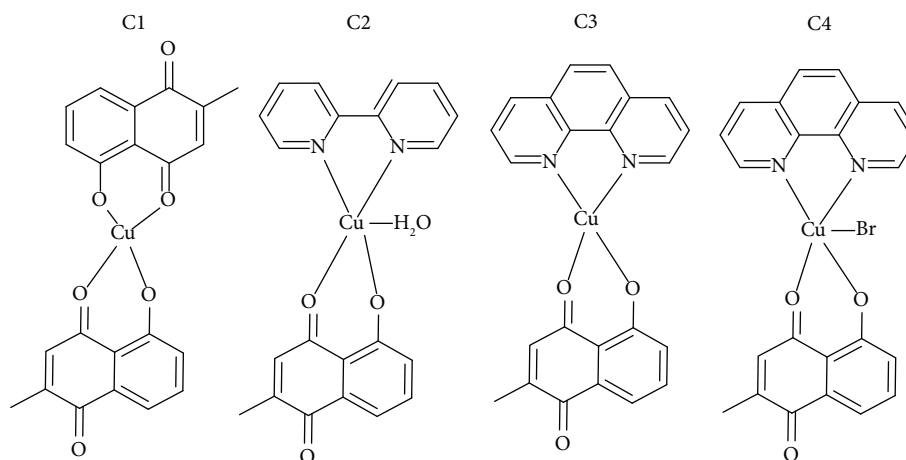
FIGURE 6: Chemical structure of Cu (II) complexes.

arrive at their destination, then the metal complex is freed from the carrier and binds to DNA. Cu(II) complexes are thus good superoxide dismutase (SOD) mimics as well as effective DNA intercalating agents. Furthermore, their ability to promote DNA damage is due to a redox cycling mechanism that produces hydroxyl radicals, singlet oxygen, and superoxide radical anions [107, 108].

3.4. Erlotinib-Conjugated Metal Complexes.
In some malignancies, epidermal growth factor and its receptor (EGFR)

overexpression is viewed as a prospective chemotherapeutic target. EGFR signaling activation has been linked to enhanced proliferation and reduced apoptosis, angiogenesis, and metastasis in tumor cells. Therefore, the EGFR gene is a promising target for the development of anticancer drugs. An EGFR-targeting drug, erlotinib, has shown promise in cancer therapy in clinical studies. It is a suitable organic pharmacophore and has good inhibitory capability. Erlotinib works by inhibiting the activity of the EGFR tyrosine kinase by binding to the kinase domain in an ATP-competitive manner. Erlotinib conjugates are made by

TABLE 2: Inhibition of human cancer cell lines growth ($IC_{50} \mu M$) for C1–C4 and their HSA-FA complexes.

Compound	Cell growth inhibition, $IC_{50} \pm SD$ (mM)	
	MCF-7	HeLa
PLN	14.15 ± 0.59	18.36 ± 1.75
PLN-HSA_FA	6.75 ± 1.27	8.25 ± 0.86
C1	6.62 ± 0.72	7.58 ± 0.95
C1-HSA_FA	3.57 ± 0.21	3.67 ± 0.34
C2	13.86 ± 0.35	4.68 ± 0.47
C2-HSA_FA	1.39 ± 0.16	1.45 ± 0.15
C3	3.32 ± 0.31	3.71 ± 0.27
C3-HSA_FA	1.24 ± 0.13	0.98 ± 0.11
C4	3.22 ± 0.29	3.68 ± 0.15
C4-HSA_FA	1.21 ± 0.16	1.01 ± 0.03
Cisplantin	20.15 ± 1.91	10.62 ± 1.12
Cisplantin-HSA_FA	45.64 ± 4.62	38.29 ± 2.47
HSA_FA	>50	>50

FIGURE 7: Structure of active anticancer fenamic acid derivatives and phenathroline.

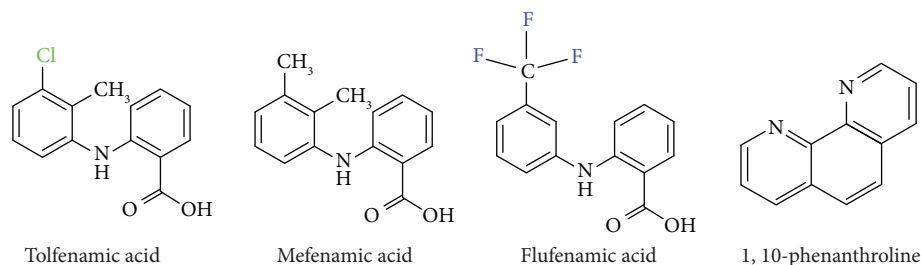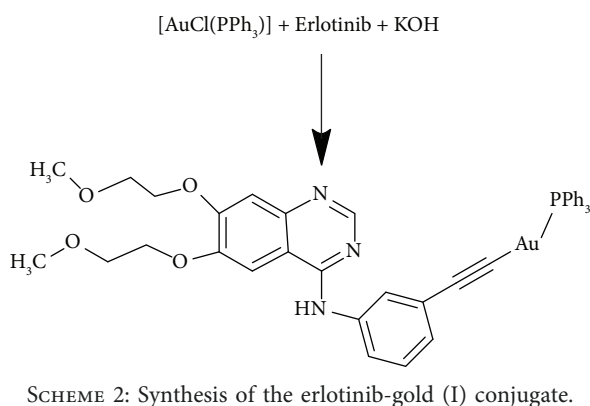combining erlotinib with a metal center that binds to a known biological target EGFR or a reactive gold complex that promotes erlotinib transfer. Indeed, Erlotinib-targeted zinc(II) phthalocyanine had show selective photodynamic activity in EGFR + HepG2 cancer cells [109–111].

Ortega and coauthor [110] used X-ray diffraction to characterize erlotinib triphenylphosphane gold(I) conjugate (Scheme 2), which is designed to bind to the well-known biological target EGFR with high affinity. In the tumorigenic and triple-negative MDA-MB-231 cell line, the gold compound showed 68-fold higher cytotoxicity than erlotinib. Studies using contrast phase inverted microscopy revealed that the conjugate caused significant alterations in cellular morphology. The compound can raise intracellular ROS levels, according to flow cytometry and cell-based fluorescence tests. The conjugate caused mitochondrial malfunction and DNA damage after producing ROS in cancer cells, resulting in S and G2/M arrest as well as apoptotic activation. While erlotinib is known to suppress EGFR tyrosine kinase efficacy and cause the arrest of G1-phase, this study discovered that adding a phosphane gold(I) substrate to the erlotinib pharmacophore modified the bioactivity of the resultant molecule substantially. When employing new erlotinib-gold(I) conjugates, it was studied whether changing the property of the co-ligand (i.e., phosphane and N-heterocyclic carbene-type ligands with varying electronic characteristics and/or lipophilicity) could increase selectivity for cancer than noncancer cells. Consequently, the complexes easily enter the cancer cell and generate ROS, which

leads to apoptosis of cancer cells as well as decrease the side effect of the drug on normal cells [110].

To and coauthors [112] reported *in vitro* and *in vivo* effects of the gold(III)-porphyrin complex [Au(III)(TPP)]Cl in inhibiting proliferation of cisplatin-sensitive, cisplatin-resistant, and Epstein-Barr virus (EBV)-carrying nasopharyngeal carcinoma (NPC) cells through the induction of cellular apoptosis. [Au(TPP)]Cl showed 100-fold higher potency than cisplatin in killing NPC cells, including cisplatin-sensitive and cisplatin-resistant variants and also a variant harboring the EBV. [Au(TPP)]Cl has the capability of noncovalently binding to DNA and targeting tumor activities as antitumor and has no major side effects, and hence it is a promising chemotherapeutic agent against NPC cells. In this work, a very important point is the porphyrin ring and its derivatives should be recommended for complexing Au(III); otherwise it is decomposed to Au(I), which is less effective and has side effects on normal cells [112].

3.5. SAHA- and VPA-Conjugated Metal Complexes. Grift and coauthors [44] studied the histone deacetylase (HDAC) enzyme-targeting molecules such as suberoylanilide hydroxamic acid (SAHA) and valproic acid (VPA), which are substitutes for the chlorido of trans-platinum planar amine (TPA) complex (Figure 8). Histones are perhaps the most significant protein constituent of chromatin, which is responsible for wrapping DNA around it. HDACs are zinc-containing enzymes or metalloenzymes that result in

[AuCl(PPh₃)] + Erlotinib + KOH

SCHEME 2: Synthesis of the erlotinib-gold (I) conjugate.

FIGURE 8: Structures of SAHA and VPA (HDAC inhibitors) and cis-[Pt(NH₃)₂(malSAHA-₂H)].

FIGURE 9: Chemical structural relationship of suberoylanilide hydroxamic acid (SAHA).

chromatin constriction and transcriptional suppression by deacetylating core histone lysine residues. Therefore, inhibiting HDAC activity has a significant impact on chromatin structure and its functions. As a result, cis-[Pt(NH3) 2(malSAHA-2H)], a bifunctional anticancer Pt therapeutic candidate with dual DNA binding and HDAC inhibitory action, was developed, and the IC$_{50}$ was calculated as shown in the aforementioned study [43] (Table 3).

SAHA (Figure 9) is composed of a hydroxamic acid group that chelates Zn^{2+} in the enzyme's active site cavity, a hydrophobic chain that passes through the narrow cavity, and a phenyl head group at the cavity's entrance. This head group's structural changes may result in a change in binding affinity 34 or an expansion of inhibitor activity. For example, SAHA analogues with fluorescent head groups have been developed and could be utilized in optical microscopy to track HDAC-dependent events in real time [113].

3.6. Biotin-Conjugated Metal Complexes. Among vitamin compounds, biotin is the most promising targeting agent. Biotin absorbed by human peripheral blood mononuclear cells (PBMCs) is dependent on the regular activity of the Na-K-ATPase enzyme. Biotin is transported with Na ions in and out of the cell [114]. Babak and

co-authors [115] synthesized ruthenium(II)-arene complexes bearing biotin-containing ligands. As a result, a new drug delivery system based on endocytosis through tumor-specific vitamin receptors has emerged (Scheme 3). Ruthenium coordination resulted in dramatically increased cytotoxicity, despite the fact that Ru(II)-biotin complexes had a lower affinity for avidin than unmodified biotin. According to in vitro anticancer activity data, these unique half-sandwich ruthenium(II)-biotin conjugates may operate as biological vectors to cancer cells, notwithstanding the lack of a strong link between the existence of cellular metal complexes, cytotoxicity, and the biotin moiety. The purpose of this vector is to limit toxicity by targeting and accumulating the complex in cancer cells [115].

Biotin (vitamin H) is required for cell proliferation, and many rapidly increasing cancer cells have a high concentration of a particular vitamin receptor on their surface (sodium-dependent multivitamin transporter, SMVT). Ferrocenyl-biotin conjugates may have improved anticancer effects. As a result, biotin could be used as a biological vector
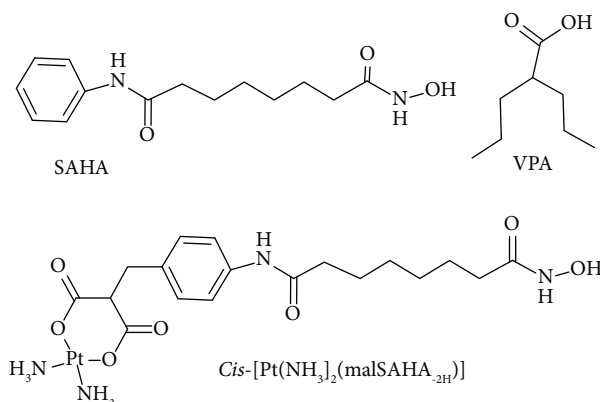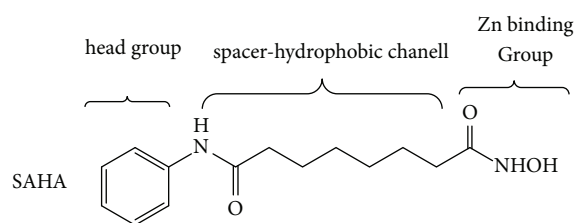
TABLE 3: IC$_{50}$ values (μM) for test agents determined using A2780 and A2780*cis*R following 72 h of incubation.

Cytotoxicity mean IC$_{50}$ ± SEM		
Test agent	A2780	A2780*cis*R
Cisplatin	2.9 ± 0.1	28.5 ± 1.5
Transplatin	>100	>100
Sodium valproate	>100	>100
Trans-[PtCl₂(py)₂]	>100	>100
Trans-[Pt(VPA-1H)₂(py)₂].	>100	95.1 ± 7.30
Trans-[PtCl₂(NH₃)(py)].	>100	>100
Trans-[Pt(VPA-1H)₂NH₃(py)].	86.5 ± 1.20	76.3 ± 04.20

to transport deadly chemicals to cancer cells selectively. Desthiobiotin and biotin-derived acids with aminoacyl linkers are used to the acylation of ferrocene. The conjugates and molecules produced by the acylation of ferrocene with biotin (Figure 10) have a high affinity for avidin and are cytotoxic to cancer cell lines, demonstrating that the biotin receptor is well expressed. This suggests that the biotin moiety could be employed as a biological vector to carry cancer cells with lethal ferrocenyl groups [116].

Kallus and coauthors [117] described the anticancer effects of triapine- and biotin-conjugated copper(II) and iron(III) complexes (Figure 11), in which triapine is the most well-known anticancer drug of thiosemicarbazone chemical class. The biotin metal complexes of the biotinylated derivative exhibited dramatically lowered anticancer activity. This phenomenon might be due to the metals utilized (Cu and Fe), and biotins are very important elements/molecules for cancer cell proliferation, which leads to cancer cell
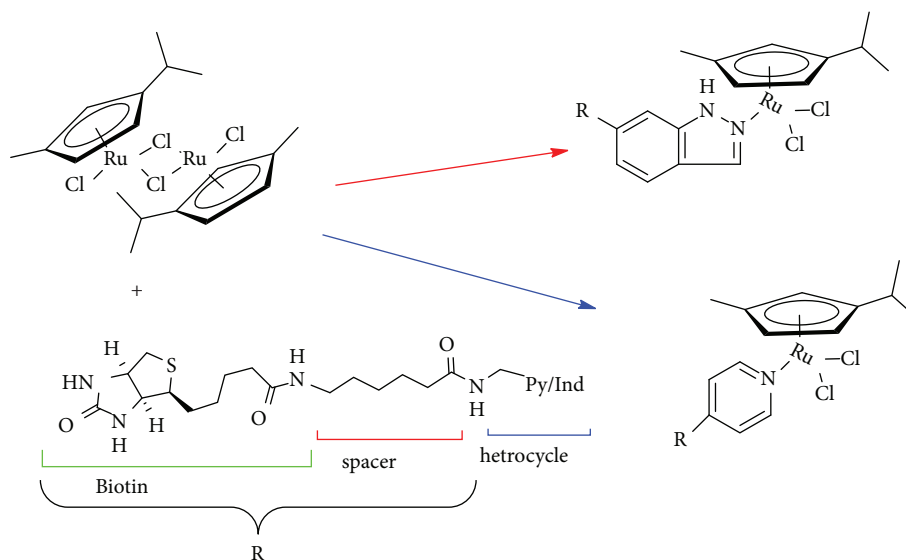
Scheme 3: Biotinylation of half-sandwich Ru (II) complexes (anhydrous DMF, ratio of [{Ru(h6-p-cymene)Cl$_2$}$_2$] to ligand.

Figure 10: Chemical structure of acylation of ferrocene with biotin.

resistance to death. On the other hand, the metal-free biotin-conjugated ligands were comparable to the reference drug triapine in terms of activity [117].

A tumor-targeting compound might be linked to Pt complexes to develop targeted therapies, potentially improving efficacy while reducing negative effects. Some vitamins are highly sought after by cancer cells, and vitamin uptake receptors are overexpressed on the cell surface. As a result, v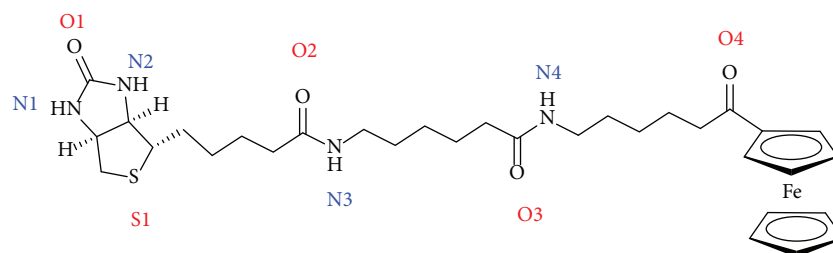itamin-bound Pt compounds can enter easily into cancerous cells and could be used as anticancer agents that lead the cancer cell apoptosis. Biotin (vitamin H or B7) has recently gained a lot of interest because cancer cells absorb it more than normal cells. Biotin can be synthesized from an ureido, tetrahydrothiophene, and valeric acid. It is a coenzyme for carboxylases, which are involved in the synthesis of amino acids and fatty acids as well as signal transduction and gene expression. Biotin is largely absorbed by the SMVT, which has previously been discovered to be overexpressed in cancer cells from the kidney, lung, breast, and ovary. Biotin-bound drug delivery methods boost drug cellular absorption while also allowing for safer and more focused medication administration to tumor areas [115, 118].

Muhammad and coauthors [119] developed and investigated mono- and dibiotinylated Pt(IV) complexes for cancer treatment (Figure 12). Pt cellular absorption in breast cancer cells is greatly improved by tethering the biotin

moiety to the Pt(IV) scaffold, but Pt accumulation in breast epithelial cells is significantly reduced. The mono-biotinylated Pt(IV) complex is more active than the dibiotinylated Pt(IV) complex in terms of reactivity and cytotoxicity. Pt-Bio-I inhibits cisplatin-resistant MDA-MB-231 cells much more effectively than cisplatin and inhibits MCF-7 cancer cells similarly to cisplatin. Due to its low toxicity to mammary epithelial cells, Pt-Bio-I may offer certain advantages over cisplatin in the breast cancer treatment. One hydroxyl ligand in axial position of Pt(IV) complexes appears to enhance DNA response and cancer cell cytotoxicity [119].

3.7. Hyaluronic Acid (HA)-Conjugated Metal Complexes.
Hyaluronic acid (HA) is a sequential anionic polymer composed of 1,4-D-glucuronic acid and 1,3-N-acetyl-D-glucosamine repeating disaccharide units (Figure 13). It is a nonsulfated glycosaminoglycan present in neuronal, epithelial, and connective tissues. HA is made up of hydroxyl, carboxylic acid, and N-acetyl groups and can be coupled with a variety of different compounds [120]. HA has a variety of applications in medicine, cosmetics, and nutraceuticals due to its outstanding viscoelasticity, high moisture holding capacity, and high biocompatibility. It is frequently utilized for ophthalmology surgery, arthritis treatment, tissue
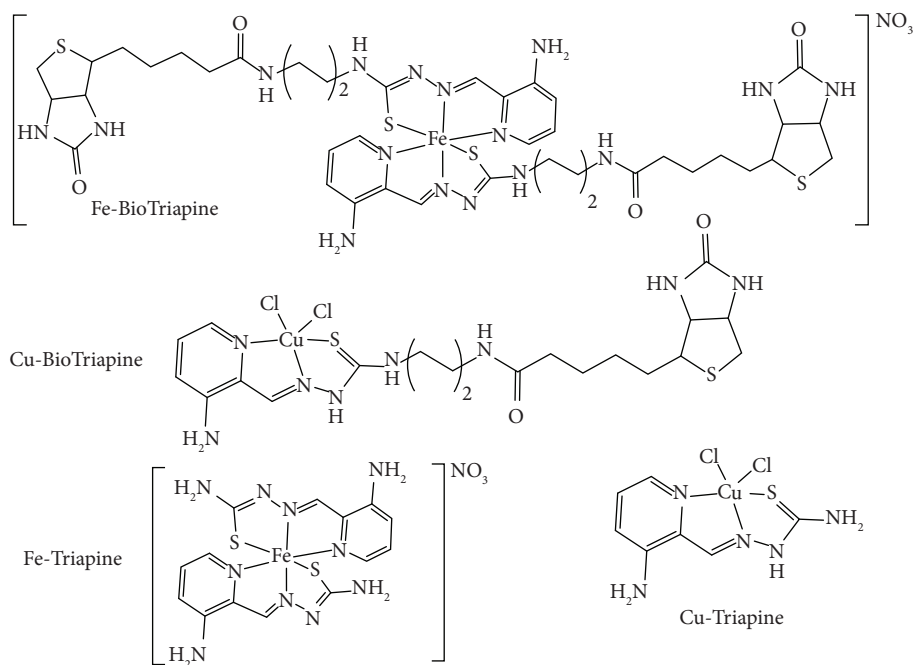
FIGURE 11: Chemical structure of Fe and Cu complexes with biotin and triapine.

engineering, and drug delivery since it is nonimmunogenic, nontoxic, noninflammatory, biocompatible, and biodegradable. As a drug delivery mechanism, HA has been combined with a range of drugs, such as paclitaxel (PTX) and doxorubicin (Dox), and other biopharmaceuticals. The enhanced permeability and retention (EPR) effect selectively transfers nanoparticles of HA medicine to cancer cells [121]. Furthermore, the interaction of HA with several receptors, such as cluster determinant44 (CD44), receptor for HA-mediated motility (RHAMM), and lymphatic vascular endothelial receptor-1, improves selective delivery (LYVE-1). The reticuloendothelial system (RES) cannot clear HA nanomedicines due to their negative surface charge. As a result, HA conducted research in the realm of drug delivery to improve material biocompatibility and drug delivery by passive and active targeting [122].

For drug administration and magnetic resonance imaging, Shu and coauthors [123] developed doxorubicin (DOX) loaded into a zeolitic imidazolate framework (ZIF) lined with polydopamine (PDA), chelated with Fe^{3+}, and coupled with hyaluronic acid (HA) (Figure 14). A Fe^{3+}-mediated coordination process linked the target molecule HA to DOX@ZIF-8. The integrated DOX might be released from the nanocarrier in a pH-dependent and sustained way. The inhibition experiment also revealed that DOX@ZIF-8-HA's ability to target CD44-overexpressed PC-3 cells effectively increased intracellular absorption and improved in vitro chemotherapeutic efficacy when compared with DOX. Furthermore, the Fe^{3+} chelation provided DOX@ZIF-HA a high contrast potential for MR imaging. The developed DOX@ZIF-HA might be used as a possible theranostic agent for chemotherapy and MR imaging of CD44-overexpressed PC-3 cells [123, 124].

4. Folate-Conjugated Metal Nanomaterials in Targeted Cancer Therapy

Folate (FA, pteroyl-L-glutamic acid) is a tiny organic biomolecule with unique properties. FA offers various advantages as a member of the vitamin B family, including cheap cost, immunogenicity, biocompatibility, molecular weight, and strong affinity for the folate receptor (FAR), a highly selective tumor marker overexpressed in over 90% of ovarian carcinomas. Moreover, the FA molecule contains many active sites, making it a typical ligand for metal coordination. FA was able to coordinate with metallic elements such as Fe(III) and Cu(II) via –COOH; however, the topologies and dimensions of these coordination complexes were erratic and unpredictable, which had a strong link to the coordination state [125–127].

Liu and coauthors [128] used FA as a ligand to make metal complexes in the nanoscale, such as folate-nickel nanotubes (FA-Ni NTs) and folate-cobalt nanotubes (FA-Co NTs) and studied their anticancer effects in vivo and in vitro. Unlike the widely used folate-drug conjugates, this complex nanotube's production technique is easy and straightforward, yielding in a constant form and uniform morphology. According to in vitro studies, folate-cobalt nanotubes (FA-Co NTs) exhibit remarkable anticancer effects against tumor cells with high rates of FAR expression, while causing minimal damage to normal cells. Furthermore, when encapsulating the anticancer medication doxorubicin via cell surface receptor-mediated endocytosis, certain types of NTs had a stronger antitumor capacity. Furthermore, pharmacokinetic parameters of FA-Co NTs in mice were explored, as well as its capacity to target tumor tissues in tumor-bearing animals. When administered separately in vivo, FA-
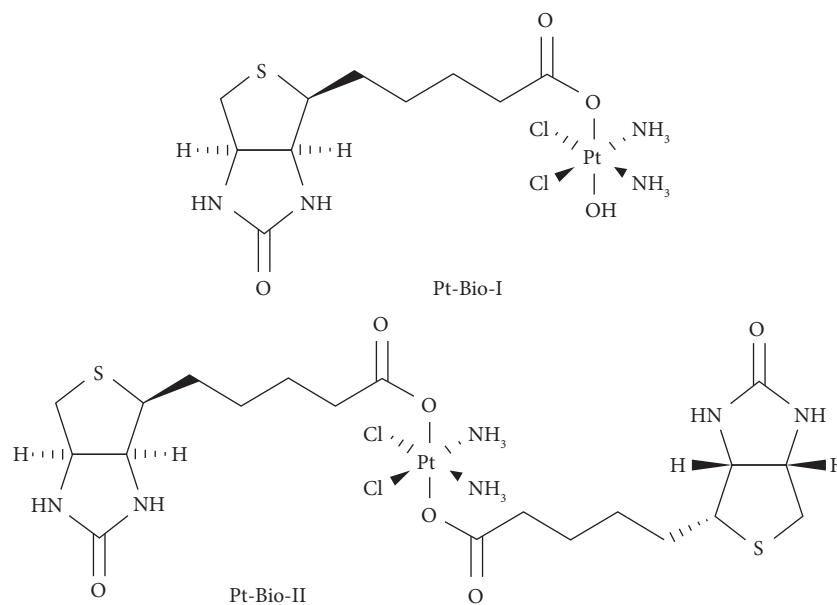
FIGURE 12: The structure Pt-Bio-I and Pt-Bio-II complexes.
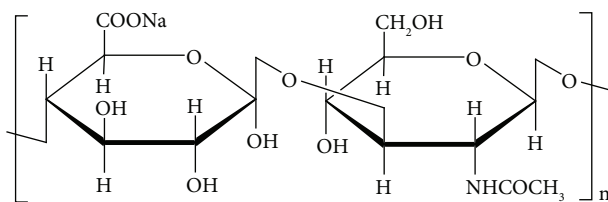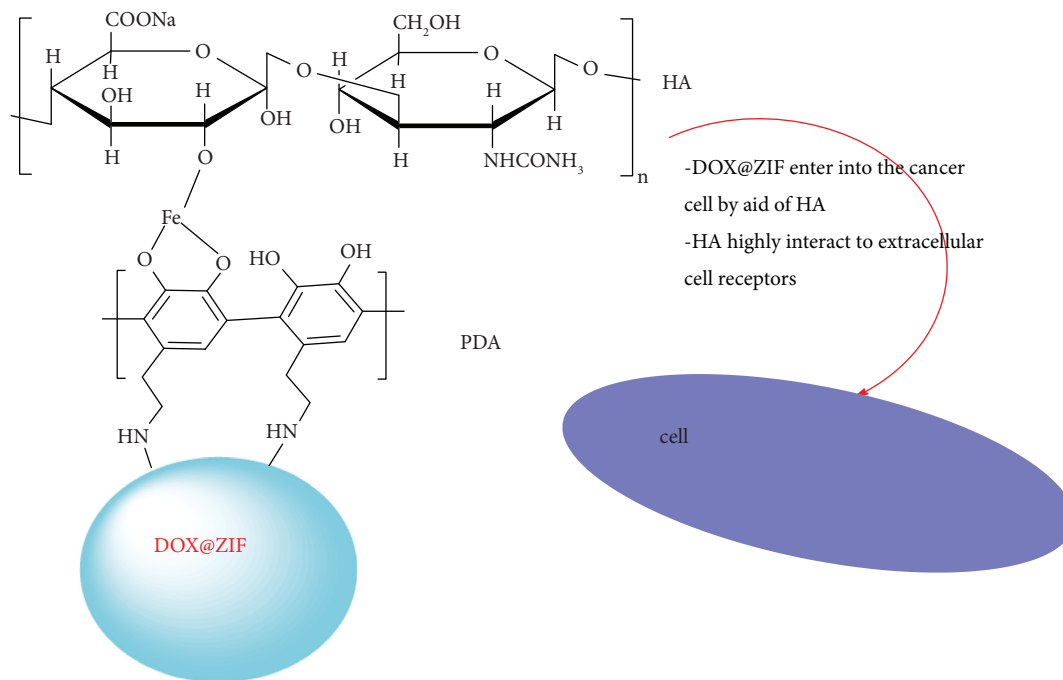

FIGURE 13: Chemical structure of hyaluronic acid (HA).

FIGURE 14: Mechanism of actions of the HA conjugated the DOX@ZIF through Fe3+ complexed dopamine on cell (adapted from Ref. [123]).

TABLE 4: Anticancer activities of folate-cobalt nanotubes (FA-Co NTs).

Drug	IC$_{50}$ (mM)		
	HeLa	A549	L-O2
DOX	1.05		4.51
FA-Co NTs	1.49	5.43	20.32

Co NTs can significantly slow tumor growth with little side effects. As indicated, the IC$_{50}$ capacity of cancer cells HeLa and A54, as well as a normal cell, L-O2, was investigated (Table 4). These findings will help researchers learn more about FA-based metal complex nanomaterials as a possible anticancer nanomedicine and targeted drug carrier [128, 129].

5. Conclusions

Anticancer medicines based on platinum (Pt) have received a lot of attention. However, substantial side effects, lack of target-specific actions, and drug resistance have restricted their use. Without promoting side effects and/or cancer cell resistance, cancer will continue to be one of the leading causes of death in humans around the world. Some of the receptors attach to biomolecule ligands such as biotin, folic acid, hyaluronic acid, and others, allowing them to enter the cell and promote cancer cell proliferation. Overexpressed receptors, such as EGFR, FAR, and biotin receptors, are known to play a role in cell differentiation, proliferation, and migration and have been identified as critical tumor-specific targets. In this aspect, metal complexes can engage in a wide range of different and novel modes of action, such as ligand exchange reactions, the generation of ROS, and the release of bioactive molecules, as well as interacting with cell membranes, nucleic acids, and organelles. As anticancer drugs, nonplatinum complexes containing metal ions (Zn, Fe, Ru, Cu, Au, and Ir) and lanthanide complexes must be utilized. Metal complexes that are more easily reduced are more cytotoxic. In the presence of biological reductants, the anticancer activities of ruthenium(III), cobalt(III), copper(II), and iron(III) complexes are thought to be dependent on their reduction to the next oxidation state, which improves their antimetastatic activity. Similarly, a combination of metal prodrugs with nano-vehicles can mediate transport of drug molecules to active targets of the cancer tissue. Metal-drug complex activation by light could become the most promising approach, allowing the use of highly inert complexes that are only activated where a light source is applied. In addition to drug development, conjugated biomolecules drug delivery systems with better pharmacokinetic and pharmacodynamic features, such as higher bioavailability, have emerged as viable options for the requisite therapeutic efficacy over the previous decade. Combining novel anticancer metal complexes with biomolecules that target the cancer cellular metabolomics pathway could open a new route for cancer treatment, that is, both effective and safe. It is clear that future research will focus on finding new molecular targets and thereby improving bioavailability, reducing adverse side effects, and improving the structural components of metal-drug complexes conjugated to biomolecules for cancer therapy.

Data Availability

The data used in this study can be accessed from the corresponding author upon request.

Conflicts of Interest

The authors declare that they have no conflicts of interest.

Authors' Contributions

The literature collection and the first draft writing were carried out by Gemechu Shumi. Dr Rajalakshmanan Eswaramoorthy, Dr Tegene Dessalegn, and Dr Taye B. Demissie supervised and edited the manuscript. All the coauthors participated in reviewing and editing the manuscript.

Acknowledgments

References

[1] N. C. Coleman, R. T. Burnett, J. D. Higbee et al., "Cancer mortality risk, fine particulate air pollution, and smoking in a large, representative cohort of US adults," *Cancer Causes & Control*, vol. 31, no. 8, pp. 767–776, 2020.

[2] S. K. Clinton, E. L. Giovannucci, and S. D. Hursting, "The world cancer research fund/American institute for cancer research third expert report on diet, nutrition, physical activity, and cancer: impact and future directions," *Journal of Nutrition*, vol. 150, no. 4, pp. 663–671, 2019.

[3] B. Karimi and B. Shokrinezhad, "Air pollution and the number of daily deaths due to respiratory causes in Tehran," *Atmospheric Environment*, vol. 246, Article ID 118161, 2021.

[4] S. Y. Lee, M. S. Kang, W. Y. Jeong, D. W. Han, and K. S. Kim, "Hyaluronic acid-based theranostic nanomedicines for targeted cancer therapy," *Cancers*, vol. 12, no. 4, pp. 940–1017, 2020.

[5] P. Yu, S. Guo, R. Xu et al., "Cohort studies of long-term exposure to outdoor particulate matter and risks of cancer: a systematic review and meta-analysis," *Innovation*, vol. 2, no. 3, Article ID 100143, 2021.

[6] A. Bergal, A. Elmas, and G. Akyüz, "A new type and effective approach for anti-cancer drug delivery application: nanosponge cyclodextrin based nanosponges (Cd- nss)," *Nano Research and Applications*, vol. 5, no. 3, pp. 1–10, 2019.

[7] B. Liu, L. Ezeogu, L. Zellmer, B. Yu, N. Xu, and D. Joshua Liao, "Protecting the normal in order to better kill the cancer," *Cancer Medicine*, vol. 4, no. 9, pp. 1394–1403, 2015.

[8] S. Pan, Y. Zhang, A. Natalia et al., "Extracellular vesicle drug occupancy enables real-time monitoring of targeted cancer therapy," *Nature Nanotechnology*, vol. 16, no. 6, pp. 734–742, 2021.

[9] J.-H. Lee and T. T. Paull, "Cellular functions of the protein kinase ATM and their relevance to human disease," *Nature*

Reviews Molecular Cell Biology, vol. 22, no. 12, pp. 796–814, 2021.

[10] M. P. Dias, S. C. Moser, S. Ganesan, and J. Jonkers, "Understanding and overcoming resistance to PARP inhibitors in cancer therapy," *Nature Reviews Clinical Oncology*, vol. 18, no. 12, pp. 773–791, 2021.

[11] M. Santi, A. K. Mapanao, L. Biancalana, F. Marchetti, and V. Voliani, "Ruthenium arene complexes in the treatment of 3D models of head and neck squamous cell carcinomas," *European Journal of Medicinal Chemistry*, vol. 212, Article ID 113143, 2021.

[12] B. Köberle and S. Schoch, "Platinum complexes in colorectal cancer and other solid tumors," *Cancers*, vol. 13, no. 9, p. 2073, 2021.

[13] U. Ndagi, N. Mhlongo, and M. Soliman, "Metal complexes in cancer therapy – an update from drug design perspective," *Drug Design, Development and Therapy*, vol. 11, pp. 599–616, 2017.

[14] B. A. Aderibigbe, A. Mugogodi, M. Nwamadi et al., "Poly-amidoamine-drug conjugates containing metal-based anti-cancer compounds," *Journal of Inorganic and Organometallic Polymers and Materials*, vol. 30, no. 5, pp. 1503–1518, 2020.

[15] A. Ulldemolins, J. Seras-Franzoso, F. Andrade et al., "Perspectives of nano-carrier drug delivery systems to overcome cancer drug resistance in the clinics," *Cancer Drug Resistance*, vol. 4, no. 1, pp. 44–68, 2021.

[16] A. M. Dos Santos, S. G. Carvalho, A. B. Meneguin, R. M. Sábio, M. P. D. Gremião, and M. Chorilli, "Oral delivery of micro/nanoparticulate systems based on natural polysaccharides for intestinal diseases therapy: challenges, advances and future perspectives," *Journal of Controlled Release*, vol. 334, pp. 353–366, 2021.

[17] X. Wei, L. Liu, X. Li et al., "Selectively targeting tumor-associated macrophages and tumor cells with polymeric micelles for enhanced cancer chemo-immunotherapy," *Journal of Controlled Release*, vol. 313, pp. 42–53, 2019.

[18] S. Dissanayake, W. A. Denny, S. Gamage, and V. Sarojini, "Recent developments in anticancer drug delivery using cell penetrating and tumor targeting peptides," *Journal of Controlled Release*, vol. 250, pp. 62–76, 2017.

[19] M. Pandey, H. Choudhury, B. Gorain et al., "Site-specific vesicular drug delivery system for skin cancer: a novel approach for targeting," *Gels*, vol. 7, no. 4, pp. 218–237, 2021.

[20] A. N. Singh, B. Mahanti, and K. Bera, "Novel drug delivery system & it's future: an overview," *International Journal of Pharmacy and Engineering*, vol. 9, no. 2, pp. 1070–1088, 2021.

[21] M. C. P. Mendonça, A. Kont, M. R. Aburto, J. F. Cryan, and C. M. O'Driscoll, "Advances in the design of (Nano) Formulations for delivery of antisense oligonucleotides and small interfering RNA: focus on the central nervous system," *Molecular Pharmaceutics*, vol. 18, no. 4, pp. 1491–1506, 2021.

[22] A. Emery, B. S. Hardwick, A. T. Crooks et al., "Target identification for small-molecule discovery in the FOXO3a tumor-suppressor pathway using a biodiverse peptide library," *Cell Chemical Biology*, vol. 28, no. 11, pp. 1602–1615.e9, 2021.

[23] S. Maniganda, V. Sankar, J. B. Nair, K. G. Raghu, and K. K. Maiti, "A lysosome-targeted drug delivery system based on sorbitol backbone towards efficient cancer therapy," *Organic and Biomolecular Chemistry*, vol. 12, no. 34, pp. 6564–6569, 2014.

[24] J. R. Junutula, H. Raab, S. Clark et al., "Site-specific conjugation of a cytotoxic drug to an antibody improves the therapeutic index," *Nature Biotechnology*, vol. 26, no. 8, pp. 925–932, 2008.

[25] X. Jiang, X. Fan, W. Xu et al., "Self-assembled peptide nanoparticles responsive to multiple tumor microenvironment triggers provide highly efficient targeted delivery and release of antitumor drug," *Journal of Controlled Release*, vol. 316, pp. 196–207, 2019.

[26] A. Gaber, M. S. Refat, A. A. M. Belal et al., "New mononuclear and binuclear Cu (II), Co (II), Ni (II), and Zn (II) thiosemicarbazone complexes with potential biological activity: antimicrobial and molecular docking study," *Molecules*, vol. 26, no. 8, p. 2288, 2021.

[27] S. R. Alves, R. L. S. R. Santos, B. Fornaciari, A. Colquhoun, and D. de Oliveira Silva, "A novel μ-oxo-diruthenium (III, III)-ibuprofen-(4-aminopyridine) chloride derived from the diruthenium (II, III)-ibuprofen paddlewheel metallodrug shows anticancer properties," *Journal of Inorganic Biochemistry*, vol. 225, Article ID 111596, 2021.

[28] R. K. Mohapatra, M. M. El-ajaily, F. S. Alassbaly et al., "DFT, anticancer, antioxidant and molecular docking investigations of some ternary Ni (II) complexes with 2-[(E)-[4-(dimethylamino)phenyl]methyleneamino]phenol," *Chemical Papers*, vol. 75, no. 3, pp. 1005–1019, 2020.

[29] Y. Deswal, S. Asija, D. Kumar et al., "Transition metal complexes of triazole-based bioactive ligands: synthesis, spectral characterization, antimicrobial, anticancer and molecular docking studies," *Research on Chemical Intermediates*, vol. 48, no. 2, pp. 703–729, 2022.

[30] A. Levina, J. B. Aitken, Y. Y. Gwee et al., "Biotransformations of anticancer ruthenium (III) complexes: an X-ray absorption spectroscopic study," *Chemistry—A European Journal*, vol. 19, no. 11, pp. 3609–3619, 2013.

[31] R. A. Nadar, K. Farbod, K. C. v. der Schilden et al., *Scientific Reports*, vol. 10, no. 1, p. 5889, 2020.

[32] T. W. Hambley, "Developing new metal-based therapeutics: challenges and opportunities," *Dalton Transactions*, vol. 43, pp. 4929–4937, 2007.

[33] J. L Arias, "Drug targeting strategies in cancer treatment: an overview," *Mini Reviews in Medicinal Chemistry*, vol. 11, no. 1, pp. 1–17, 2011.

[34] K. J. Franz and N. Metzler-Nolte, "Introduction: metals in medicine," *Chemical Reviews*, vol. 119, no. 2, pp. 727–729, 2019.

[35] F. Thoreau, L. Vanwonterghem, M. Henry, J. L. Coll, and D. Boturyn, "Design of RGD–ATWLPPR peptide conjugates for the dual targeting of $\alpha_V\beta_3$ integrin and neuropilin-1," *Organic and Biomolecular Chemistry*, vol. 16, no. 22, pp. 4101–4107, 2018.

[36] N. Brodyagin, M. Katkevics, V. Kotikam, C. A. Ryan, and E. Rozners, "Chemical approaches to discover the full potential of peptide nucleic acids in biomedical applications," *Beilstein Journal of Organic Chemistry*, vol. 17, no. 116, pp. 1641–1688, 2021.

[37] Y. Zhou, S. Liu, M. Zhao et al., "Injectable extracellular vesicle-released self-assembling peptide nanofiber hydrogel as an enhanced cell-free therapy for tissue regeneration," *Journal of Controlled Release*, vol. 316, pp. 93–104, 2019.

[38] G. M. L. Consoli, L. Consoli, G. Granata et al., "Design and synthesis of a multivalent fluorescent folate–calix[4] arene conjugate: cancer cell penetration and intracellular localization," *Organic and Biomolecular Chemistry*, vol. 13, no. 11, pp. 3298–3307, 2015.

[39] M. Yang, J. Deng, D. Guo, J. Zhang, L. Yang, and F. Wu, "A folate-conjugated platinum porphyrin complex as a new

cancer-targeting photosensitizer for photodynamic therapy," *Organic and Biomolecular Chemistry*, vol. 17, no. 21, pp. 5367–5374, 2019.

[40] F. Hu and B. Liu, "Organelle-specific bioprobes based on fluorogens with aggregation-induced emission (AIE) characteristics," *Organic and Biomolecular Chemistry*, vol. 14, no. 42, pp. 9931–9944, 2016.

[41] A. M. Lenkiewicz, M. Krakowczyk, and P. Bragoszewski, "Cytosolic quality control of mitochondrial protein precursors—the early stages of the organelle biogenesis," *International Journal of Molecular Sciences*, vol. 23, no. 1, pp. 7–27, 2021.

[42] M. F. Shishova and V. V. Yemelyanov, "Proteome and lipidome of plant cell membranes during development," *Russian Journal of Plant Physiology*, vol. 68, no. 5, pp. 800–817, 2021.

[43] D. M. Griffith, B. Duff, K. Y. Suponitsky et al., "Novel trans -platinum complexes of the histone deacetylase inhibitor valproic acid ; synthesis , in vitro cytotoxicity and mutagenicity," *Journal of Inorganic Biochemistry*, vol. 105, no. 6, pp. 793–799, 2011.

[44] N. Z. Fantoni, A. H. El-Sagheer, and T. Brown, "A hitchhiker's guide to click-chemistry with nucleic acids," *Chemical Reviews*, vol. 121, no. 12, pp. 7122–7154, 2021.

[45] L. O. Alimi, M. Z. Alyami, S. Chand, W. Baslyman, and N. M. Khashab, "Coordination-based self-assembled capsules (SACs) for protein, CRISPR–Cas9, DNA and RNA delivery," *Chemical Science*, vol. 12, no. 7, pp. 2329–2344, 2021.

[46] E. Alberti, M. Zampakou, and D. Donghi, "Covalent and non-covalent binding of metal complexes to RNA," *Journal of Inorganic Biochemistry*, vol. 163, pp. 278–291, 2016.

[47] G. Sundaraselvan and S. Darlin Quine, "Green synthesis of zinc oxide nanoparticles using seed extract of murraya koenigii and their antimicrobial activity against some human pathogens," *Journal of Nanoscience and Technology*, vol. 3, no. 4, pp. 289–292, 2017.

[48] F. Y. Teng, Z. Z. Jiang, M. Guo et al., "G-quadruplex DNA: a novel target for drug design," *Cellular and Molecular Life Sciences*, vol. 78, no. 19-20, pp. 6557–6583, 2021.

[49] L. Conti, A. Mengoni, G. E. Giacomazzo et al., "Exploring the potential of highly charged Ru (II)- and heteronuclear Ru (II)/Cu (II)-polypyridyl complexes as antimicrobial agents," *Journal of Inorganic Biochemistry*, vol. 220, Article ID 111467, 2021.

[50] E. Palma, J. Carvalho, C. Cruz, and A. Paulo, "Metal-based G-quadruplex binders for cancer theranostics," *Pharmaceuticals*, vol. 14, no. 7, p. 605, 2021.

[51] J. Shao, Z.-Y. Yan, M. Tang et al., "Potent oxidation of DNA by Ru (ii) tri (polypyridyl) complexes under visible light irradiation via a singlet oxygen-mediated mechanism," *Inorganic Chemistry Frontiers*, vol. 8, no. 14, pp. 3421–3432, 2021.

[52] S. Kumar and T. Mohapatra, "Deciphering epitranscriptome: modification of mRNA bases provides a new perspective for post-transcriptional regulation of gene expression," *Frontiers in Cell and Developmental Biology*, vol. 9, no. 15, pp. 1–22, 2021.

[53] A. Ohkubo, L. Van Haute, D. L. Rudler et al., "The FASTK family proteins fine-tune mitochondrial RNA processing," *PLoS Genetics*, vol. 17, no. 11, pp. e1009873–27, 2021.

[54] N. Pandya, S. R. Bhagwat, and A. Kumar, "Regulatory role of Non-canonical DNA Polymorphisms in human genome and their relevance in Cancer," *Biochimica et Biophysica Acta (BBA)—Reviews on Cancer*, vol. 1876, no. 2, Article ID 188594, 2021.

[55] S. L. Sanford, G. A. Welfer, B. D. Freudenthal, and P. L. Opresko, "how DNA damage and non-canonical nucleotides alter the telomerase catalytic cycle," *DNA Repair*, vol. 107, Article ID 103, 2021.

[56] J. Ramón, F. Vila-Julià, D. Molina-Granada et al., "Therapy prospects for mitochondrial DNA maintenance disorders," *International Journal of Molecular Sciences*, vol. 22, no. 12, p. 6447, 2021.

[57] W. Kühlbrandt, "Structure and function of mitochondrial membrane protein complexes," *BMC Biology*, vol. 13, no. 1, p. 89, 2015.

[58] M. Xia, Y. Zhang, K. Jin, Z. Lu, Z. Zeng, and W. Xiong, "Communication between mitochondria and other organelles: a brand - new perspective on mitochondria in cancer," *Cell & Bioscience*, vol. 9, no. 1, p. 27, 2019.

[59] A. Erxleben, "Mitochondria-targeting anticancer metal complexes," *Current Medicinal Chemistry*, vol. 25, 2018.

[60] J. Hao, H. Zhang, L. Tian et al., "Evaluation of anticancer effects in vitro of new iridium (III) complexes targeting the mitochondria," *Journal of Inorganic Biochemistry*, vol. 221, Article ID 111465, 2021.

[61] J. Pu, C. M. Guardia, T. Keren-kaplan, and J. S. Bonifacino, "Mechanisms and functions of lysosome positioning," *Journal of Cell Science*, vol. 129, 2016.

[62] Y. Yang, L. Guo, X. Ge et al., "Novel lysosome-targeted cyclometalated Iridium (III) anticancer complexes containing imine-N-heterocyclic carbene ligands: synthesis, spectroscopic properties and biological activity," *Dyes and Pigments*, vol. 161, pp. 119–129, 2019.

[63] B. Purushothaman, J. Lee, S. Hong, and J. M. Song, "Multifunctional TPP-PEG-biotin self-assembled nanoparticle drug delivery-based combination therapeutic approach for co-targeting of GRP78 and lysosome," *Journal of Nanobiotechnology*, vol. 18, no. 1, p. 102, 2020.

[64] W. Ma, X. Ge, Z. Xu et al., "Theranostic lysosomal targeting anticancer and antimetastatic agents: half-sandwich iridium (III) rhodamine complexes," *ACS Omega*, vol. 4, no. 12, pp. 15240–15248, 2019.

[65] S. Zalba and T. L. M. ten Hagen, "Cell membrane modulation as adjuvant in cancer therapy," *Cancer Treatment Reviews*, vol. 52, pp. 48–57, 2017.

[66] P. Corsetto, I. Colombo, J. Kopecka, A. Rizzo, and C. Riganti, "ω-3 long chain polyunsaturated fatty acids as sensitizing agents and multidrug resistance revertants in cancer therapy," *International Journal of Molecular Sciences*, vol. 18, no. 12, p. 2770, 2017.

[67] M. Volpato and M. A. Hull, "Omega-3 polyunsaturated fatty acids as adjuvant therapy of colorectal cancer," *Cancer and Metastasis Reviews*, vol. 37, no. 2-3, pp. 545–555, 2018.

[68] K. Varini, P. Lécorché, R. Sonnette et al., "Target engagement and intracellular delivery of mono- and bivalent LDL receptor-binding peptide-cargo conjugates: implications for the rational design of new targeted drug therapies," *Journal of Controlled Release*, vol. 314, pp. 141–161, 2019.

[69] A. S. Semkina, M. A. Abakumov, A. S. Skorikov et al., "Multimodal doxorubicin loaded magnetic nanoparticles for VEGF targeted theranostics of breast cancer," *Nanomedicine: Nanotechnology, Biology and Medicine*, vol. 14, no. 5, pp. 1733–1742, 2018.

[70] S. Gandham, X. Su, J. Wood et al., "Technologies and standardization in research on extracellular vesicles," *Trends in Biotechnology*, vol. 38, no. 10, pp. 1066–1098, 2020.

[71] T. Kubota, S. Kuroda, N. Kanaya et al., "HER2-targeted gold nanoparticles potentially overcome resistance to trastuzumab in gastric cancer," *Nanomedicine: Nanotechnology, Biology and Medicine*, vol. 14, no. 6, pp. 1919–1929, 2018.

[72] Y. Mesbahi, A. Zekri, S. Ahmadian, K. Alimoghaddam, A. Ghavamzadeh, and S. H. Ghaffari, "Targeting of EGFR increase anti-cancer e ffects of arsenic trioxide: promising treatment for glioblastoma multiform," *European Journal of Pharmacology*, vol. 820, pp. 274–285, 2018.

[73] J. Du, Y. Kang, Y. Zhao et al., "Synthesis, characterization, and in vitro antitumor activity of ruthenium (II) polypyridyl complexes tethering EGFR-inhibiting 4-anilinoquinazolines," *Inorganic Chemistry*, vol. 55, no. 9, pp. 4595–4605, 2016.

[74] P. C. A. Bruijnincx and P. J. Sadler, "New trends for metal complexes with anticancer activity," *Current Opinion in Chemical Biology*, vol. 12, no. 2, pp. 197–206, 2008.

[75] A. Chaudhary, A. K. Singh, and R. V. Singh, "Investigations of the possible pharmacological effects of organotin (II) complexes," *Journal of Inorganic Biochemistry*, vol. 100, no. 10, pp. 1632–1645, 2006.

[76] P. Chellan and P. J. Sadler, "The elements of life and medicines," *Philosophical Transactions of the Royal Society A: Mathematical, Physical & Engineering Sciences*, vol. 373, no. 2037, Article ID 20140182, 2015.

[77] A.-L. Lainé and C. Passirani, "Novel metal-based anticancer drugs: a new challenge in drug delivery," *Current Opinion in Pharmacology*, vol. 12, no. 4, pp. 420–426, 2012.

[78] K. D. Mjos and C. Orvig, "Metallodrugs in medicinal inorganic chemistry," *Chemical Reviews*, vol. 114, no. 8, pp. 4540–4563, 2014.

[79] A. K. Renfrew, "Transition metal complexes with bioactive ligands: mechanisms for selective ligand release and applications for drug delivery," *Metallomics*, vol. 6, no. 8, pp. 1324–1335, 2014.

[80] Y. Chen and L. Hu, "Design of anticancer prodrugs for reductive activation," *Medicinal Research Reviews*, vol. 29, no. 1, pp. 29–64, 2009.

[81] M. Mathuber, H. Schueffl, O. Dömötör et al., "Improving the stability of EGFR inhibitor cobalt (III) prodrugs," *Inorganic Chemistry*, vol. 59, no. 23, pp. 17794–17810, 2020.

[82] S. Banerjee, I. Pant, I. Khan et al., "Remarkable enhancement in photocytotoxicity and hydrolytic stability of curcumin on binding to an oxovanadium (iv) moiety," *Dalton Transactions*, vol. 44, no. 9, pp. 4108–4122, 2015.

[83] B. Banik, K. Somyajit, G. Nagaraju, and A. R. Chakravarty, "Oxovanadium (iv) complexes of curcumin for cellular imaging and mitochondria targeted photocytotoxicity," *Dalton Transactions*, vol. 43, no. 35, Article ID 13358, 2014.

[84] D. Cirri, F. Bartoli, A. Pratesi, E. Baglini, E. Barresi, and T. Marzo, *Biomedicines*, vol. 9, no. 5, p. 504, 2021.

[85] K. T. Savjani, A. K. Gajjar, and J. K. Savjani, "Drug Solubility: Importance and Enhancement Techniques," *International Scholarly Research Notices*, vol. 2012, Article ID 195727, 10 pages, 2012.

[86] S. Senapati, A. K. Mahanta, S. Kumar, and P. Maiti, *Signal Transduction and Targeted Therapy*, vol. 3, no. 1, p. 7, 2018.

[87] G. C. M'bitsi-Ibouily, T. Marimuthu, P. Kumar et al., "Synthesis, characterisation and in vitro permeation, dissolution and cytotoxic evaluation of ruthenium (II)-Liganded sulpiride and amino alcohol," *Scientific Reports*, vol. 9, no. 1, p. 4146, 2019.

[88] S. Ghosh, K. Datta, and S. K. Datta, *Rice Vitamins*, University of Calcutta, Kolkata, India, 2019.

[89] E. Hamed, M. S. Attia, and K. Bassiouny, "Synthesis, spectroscopic and thermal characterization of copper (II) and iron (III) complexes of folic acid and their absorption efficiency in the blood," *Bioinorganic Chemistry and Applications*, vol. 2009, Article ID 979680, 6 pages, 2009.

[90] S. Zhu, S. Yao, F. Wu et al., "Platinated porphyrin as a new organelle and nucleus dual-targeted photosensitizer for photodynamic therapy," *Organic and Biomolecular Chemistry*, vol. 15, no. 27, pp. 5764–5771, 2017.

[91] Z. Lei, X. Zhang, X. Zheng, S. Liu, and Z. Xie, "Porphyrin–ferrocene conjugates for photodynamic and chemodynamic therapy," *Organic and Biomolecular Chemistry*, vol. 16, no. 44, pp. 8613–8619, 2018.

[92] Q. Deng, H. J. Xiang, W. W. Tang et al., "Ruthenium nitrosyl grafted carbon dots as a fluorescence-trackable nanoplatform for visible light-controlled nitric oxide release and targeted intracellular delivery," *Journal of Inorganic Biochemistry*, vol. 165, pp. 152–158, 2016.

[93] P. Kumar, S. Swagatika, S. Dasari, R. S. Tomar, and A. K. Patra, "Modulation of ruthenium anticancer drugs analogs with tolfenamicacid: reactivity, biological interactions and growth inhibition of yeast cell," *Journal of Inorganic Biochemistry*, vol. 199, Article ID 110769, 2019.

[94] Z. Du, J. Sun, C. A. Bader et al., "Synthesis, photophysical and cellular characterisation of folate and methotrexate labelled luminescent lanthanide complexes," *Journal of Inorganic Biochemistry*, vol. 178, pp. 32–42, 2018.

[95] Y. T. Lee, Y. J. Tan, and C. E. Oon, "Molecular targeted therapy: treating cancer with speci fi city," *European Journal of Pharmacology*, vol. 834, pp. 188–196, 2018.

[96] F. Shiri, S. Shahraki, A. Shahriyar, and M. H. Majd, "Exploring isoxsuprine hydrochloride binding with human serum albumin in the presence of folic acid and ascorbic acid using multispectroscopic and molecular modeling methods," *Journal of Photochemistry and Photobiology B: Biology*, vol. 170, pp. 152–163, 2017.

[97] W. Gao, X. Jia, J. Wu et al., "Preparation and evaluation of folate-decorated human serum albumin nanoparticles for the targeted delivery of sorafenib to enhance anti-hepatocarcinoma efficacy," *Journal of Drug Delivery Science and Technology*, vol. 54, Article ID 101349, 2019.

[98] Y. Sun, Y. Zhao, S. Teng et al., "Folic acid receptor-targeted human serum albumin nanoparticle formulation of cabazitaxel for tumor therapy," *International Journal of Nanomedicine*, vol. 14, pp. 135–148, 2018.

[99] Y. Gou, Z. Zhang, J. Qi et al., "Folate-functionalized human serum albumin carrier for anticancer copper (II) complexes derived from natural plumbagin," *Journal of Inorganic Biochemistry*, vol. 153, pp. 13–22, 2015.

[100] Q. Xu and C. C. Chu, "Development of ROS-responsive amino acid-based poly(ester amide) nanoparticle for anticancer drug delivery," *Journal of Biomedical Materials Research Part A*, vol. 109, no. 4, pp. 524–537, 2021.

[101] M. C. Khan, J. Deng, P. Yu, H. Liang, and F. Yang, "Anticancer function and ROS-mediated multi-targeting anticancer mechanisms of copper (II) 2-hydroxy-1-naphthaldehyde complexes," *Molecules*, vol. 24, 2019.

[102] M. J. Matos, C. Labão-Almeida, O. Dada, M. Tacke, and G. J. L. Bernardes, "Synthesis and biological evaluation of homogeneous thiol-linked NHC -Au-albumin and TrastuzumabBioconjugates," *Chemistry—A European Journal*, vol. 24, no. 47, pp. 12250–12253, 2018.

[103] I. Almi, S. Belaidi, E. Zerroug et al., "QSAR investigations and structure-based virtual screening on a series of nitro

benzoxadiazole derivatives targeting human glutathione-S-transferases," *Journal of Molecular Structure*, vol. 1211, pp. 128015–128025, 2020.

[104] R. Pereira, S. G. Silva, M. Pinheiro, S. Reis, and M. L. Vale, "Current status of amino acid-based permeation enhancers in transdermal drug delivery," *Membranes*, vol. 11, no. 5, p. 343, 2021.

[105] A. A. Sharfalddin, A.-H. Emwas, M. Jaremko, and M. A. Hussien, "Synthesis and theoretical calculations of metal-antibiotic chelation with thiamphenicol: in vitro DNA and HSA binding, molecular docking, and cytotoxicity studies," *New Journal of Chemistry*, vol. 45, no. 21, pp. 9598–9613, 2021.

[106] T. Wang and D. Xiao, "Rapid synthesis of fluorescent bovine serum albumin-gold nanoclusters complex for glutathione determination," *Microchimica Acta*, vol. 188, no. 6, pp. 193–198, 2021.

[107] M. Simunkova, P. Lauro, K. Jomova et al., "Redox-cycling and intercalating properties of novel mixed copper (II) complexes with non-steroidal anti-inflammatory drugs tolfenamic, mefenamic and flufenamic acids and phenanthroline functionality: structure, SOD-mimetic activity, interaction with albumin, DNA damage study and anticancer activity," *Journal of Inorganic Biochemistry*, vol. 194, pp. 97–113, 2019.

[108] A. B. M. Ibrahim, M. K. Farh, and P. Mayer, "Copper complexes of new thiosemicarbazone ligands: synthesis, structural studies and antimicrobial activity," *Inorganic Chemistry Communications*, vol. 94, pp. 127–132, 2018.

[109] B. K. Erickson, B. Zeybek, A. D. Santin, A. N. Fader, and N. Haven, "Targeting human epidermal growth factor receptor 2 (HER2) in gynecologic malignancies," *Current Opinion in Obstetrics and Gynecology*, vol. 32, no. 1, pp. 57–64, 2020.

[110] E. Ortega, A. Zamora, U. Basu et al., "An Erlotinib gold (I) conjugate for combating triple-negative breast cancer," *Journal of Inorganic Biochemistry*, vol. 203, Article ID 110910, 2020.

[111] J. Palle, A. Rochand, S. Pernot, C. Gallois, J. Taïeb, and A. Zaanan, "Human epidermal growth factor receptor 2 (HER2) in advanced gastric cancer: current knowledge and future perspectives," *Drugs*, vol. 80, no. 4, pp. 401–415, 2020.

[112] Y. F. To, R. W.-Y. Sun, Y. Chen et al., "Gold (III) porphyrin complex is more potent than cisplatin in inhibiting growth of nasopharyngeal carcinomain vitroand in vivo," *International Journal of Cancer*, vol. 124, no. 8, pp. 1971–1979, 2009.

[113] J. W. Walton, J. M. Cross, and T. Riedel, "Perfluorinated HDAC inhibitors as selective anticancer agents," *Organic and Biomolecular Chemistry*, vol. 15, no. 43, pp. 9186–9190, 2017.

[114] G. Tripodo, D. Mandracchia, S. Collina, M. Rui, and D. Rossi, "New perspectives in cancer therapy: the biotin-antitumor molecule conjugates," *Medicinal Chemistry*, vol. S1, 2014.

[115] M. V. Babak, D. Plażuk, S. M. Meier et al., "Half-sandwich ruthenium (II) biotin conjugates as biological vectors to cancer cells," *Chemistry—A European Journal*, vol. 21, no. 13, pp. 5110–5117, 2015.

[116] D. Plażuk, J. Zakrzewski, M. Salmain et al., "Ferrocene–biotin conjugates targeting cancer cells: synthesis, interaction with avidin, cytotoxic properties and the crystal structure of the complex of avidin with a biotin–linker–ferrocene conjugate," *Organometallics*, vol. 32, no. 20, pp. 5774–5783, 2013.

[117] S. Kallus, L. Uhlik, S. van Schoonhoven et al., "Synthesis and biological evaluation of biotin-conjugated anticancer thiosemicarbazones and their iron (III) and copper (II) complexes," *Journal of Inorganic Biochemistry*, vol. 190, pp. 85–97, 2019.

[118] S. Roy and P. K. Das, "Antibacterial hydrogels of amino acid-based cationic amphiphiles," *Biotechnology and Bioengineering*, vol. 100, no. 4, pp. 756–764, 2008.

[119] N. Muhammad, N. Sadia, C. Zhu, C. Luo, Z. Guo, and X. Wang, "Biotin-tagged platinum (iv) complexes as targeted cytostatic agents against breast cancer cells," *Chemical Communications*, vol. 53, no. 72, pp. 9971–9974, 2017.

[120] H. Lin, J. Liu, G. Fan et al., "A dual-responsive, hyaluronic acid targeted drug delivery system based on hollow mesoporous silica nanoparticles for cancer therapy," *Journal of Materials Chemistry B*, vol. 6, no. 28, pp. 4618–4629, 2018.

[121] J. Zugazagoitia, C. Guedes, S. Ponce, I. Ferrer, S. Molina-pinelo, and L. Paz-ares, "Current challenges in cancer treatment," *Clinical Therapeutics*, vol. 38, no. 7, pp. 1551–1566, 2016.

[122] K. Kim, H. Choi, E. S. Choi, and M. Park, "Hyaluronic acid-coated nanomedicine for targeted cancer therapy," *Pharmaceutics*, vol. 11, no. 7, p. 301, 2019.

[123] F. Shu, D. Lv, X.-L. Song et al., "Fabrication of a hyaluronic acid conjugated metal organic framework for targeted drug delivery and magnetic resonance imaging," *RSC Advances*, vol. 8, no. 12, pp. 6581–6589, 2018.

[124] N. Pramanik and S. K. Jagirdar, *Hyaluronic Acid Derivatives for Targeted Cancer Therapy*, IntechOpen, London, UK, 2012.

[125] D. Liu, F. Yang, F. Xiong, and N. Gu, "The smart drug delivery system and its clinical potential," *Theranostics*, vol. 6, no. 9, pp. 1306–1323, 2016.

[126] A. Gandioso, A. Rovira, H. Shi, P. J. Sadler, and V. Marchán, "Unexpected photoactivation pathways in a folate-receptor-targeted trans-diazido Pt (iv) anticancer pro-drug," *Dalton Transactions*, vol. 49, no. 34, pp. 11828–11834, 2020.

[127] T. S. Sheena, R. Dhivya, V. Rajiu et al., "Folate-engineered mesoporous silica-encapsulated copper (II) complex $[Cu(L)(dppz)]^+$: an active targeting cell-specific platform for breast cancer therapy," *Inorganica Chimica Acta*, vol. 510, no. 2, Article ID 119783, 2020.

[128] S. Thota, D. A. Rodrigues, D. C. Crans, and E. J. Barreiro, "Ru (II) compounds: next-generation anticancer metallotherapeutic," *Journal of Medicinal Chemistry*, vol. 61, no. 14, pp. 5805–5821, 2018.

[129] L. X. Liu, B. X. Li, Q. Y. Wang et al., "An integrative folate-based metal complex nanotube as a potent antitumor nanomedicine as well as an efficient tumor-targeted drug carrier," *Bioconjugate Chemistry*, vol. 27, no. 12, pp. 2863–2873, 2016.

Research Article

Computational Study of the Phytochemical Constituents from *Uncaria tomentosa* Stem Bark against SARS-CoV-2 Omicron Spike Protein

Oscar Herrera-Calderon [ID],[1] Abdulrahman M. Saleh [ID],[2] Andres F. Yepes-Perez [ID],[3] Nada H. Aljarba [ID],[4] Saad Alkahtani [ID],[5] Gaber El-Saber Batiha [ID],[6] Renan Dilton Hañari-Quispe [ID],[7] Haydee Chavez [ID],[8] Josefa Bertha Pari-Olarte [ID],[8] Eddie Loyola-Gonzales [ID],[9] José Santiago Almeida-Galindo [ID],[10] José Francisco Kong-Chirinos [ID],[11] and Taoufiq Benali [ID][12]

[1]*Department of Pharmacology, Bromatology and Toxicology, Faculty of Pharmacy and Biochemistry, Universidad Nacional Mayor de san Marcos, Lima, Peru*

[2]*Pharmaceutical Medicinal Chemistry & Drug Design Department, Faculty of Pharmacy (Boys), Al-Azhar University, Cairo 11884, Egypt*

[3]*Chemistry of Colombian Plants, Institute of Chemistry, Faculty of Exact and Natural Sciences, University of Antioquia-UdeA, Calle 70 No. 52-21, A.A 1226, Medellin, Colombia*

[4]*Department of Biology, College of Science, Princess Nourah bint Abdulrahman University, P. O. Box 84428, Riyadh 11671, Saudi Arabia*

[5]*Department of Zoology, College of Science, King Saud University, P. O. Box 2455, Riyadh 11451, Saudi Arabia*

[6]*Department of Pharmacology and Therapeutics, Faculty of Veterinary Medicine, Damanhour University, Damanhour 22511, AlBeheira, Egypt*

[7]*Clinical Pathology Laboratory, Faculty of Veterinary Medicine and Zootechnics, Universidad Nacional del Altiplano, Av Floral 1153, Puno 21001, Peru*

[8]*Department of Pharmaceutical Chemistry, Faculty of Pharmacy and Biochemistry, Universidad Nacional San Luis Gonzaga, Ica, Peru*

[9]*Department of Pharmaceutical Sciences, Faculty of Pharmacy and Biochemistry, Universidad Nacional San Luis Gonzaga, Ica, Peru*

[10]*Department of Basic Sciences, Faculty of Human Medicine, Universidad Nacional San Luis Gonzaga, Ica, Peru*

[11]*Department of Surgical Clinical Sciences, Faculty of Human Medicine, Universidad Nacional San Luis Gonzaga, Ica, Peru*

[12]*Environment and Health Team, Polydisciplinary Faculty of Safi, Cadi Ayyad University, Sidi Bouzid B.P. 4162, Morocco*

Correspondence should be addressed to Oscar Herrera-Calderon; oherreraca@unmsm.edu.pe

The SARS-CoV-2 Omicron variant has spread rapidly and is considered the predominant variant in the world, and its main characteristic is related to evade immunity from natural infection or vaccines, due to its multiple mutations in the spike protein. On the other hand, medicinal plants have been used as alternatives therapies to ameliorate some signs and symptoms in COVID-19, and in our previous work, the cat's claw (*Uncaria tomentosa*) stem bark has been studied in vitro and showed antiviral activity on SARS-CoV-2 as well as in silico studies on the 3CL^{pro} protein and as disruptor between the ACE-2 human receptor and the spike protein. The aim in this computational study was to determine the main phytochemical constituents from *U. tomentosa* stem bark against the SARS-CoV-2 Omicron spike protein based on molecular modeling. A molecular docking was carried out on the isolated phytochemicals in a previous work against the SARS-CoV-2 Omicron spike protein-

binding domain (PDB ID: 7T9K). Next, a molecular dynamic study was carried out to monitor the stability during the MD simulations. As results proanthocyanidin-C1 (-10.76 kcal/mol), quinovic acid-type 2 (-9.86 kcal/mol), and proanthocyanidin-B2 (-9.82 kcal/mol) were the constituents with the best binding free energy on the SARS-CoV-2 Omicron spike protein, and the best compound was stable during the dynamic simulation under physiological conditions. It is concluded that the anthocyanidin-based compounds determined in the stem bark ethanol extract could be responsible for the potential antiviral activity on SARS-CoV-2 Omicron variant, and the proanthocyanidin-C1 emerged as a powerful candidate to combat new variants.

1. Introduction

Since November 2021, the World Health Organization (WHO) declared the variant of COVID-19 named Omicron (B.1.1.529) as a variant of concern after its detection for the first time in South Africa [1]. S. S. A. Karim and Q. A. Karim [2] demonstrated that the Omicron variant was characterized by the highest number of spike (S) protein mutations compared to Alpha, Beta, Gamma, and Delta variant of concerns. The fifth variant of SARS-CoV-2 has become dominant in countries Africa, Asia, North America, the United States, and Europe [3]. Indeed, on December 3, the number of confirmed Omicron cases was 219, while on December 9, 2021, 2152 people were affected, which a large number of this variant was described in Denmark, the United Kingdom, and South Africa [4]. The Office for National Statistics (ONS) of the United Kingdom showed that in the week ending January 14, 2022, with omicron as the dominant variant, 1382 deaths were registered in England and Wales [5]. According to Omicron variant, the spike protein (S protein) presented 30 mutations in this protein which were identified such as A67V, H69, V70, T95I, G142D, E156, F157, R158G, G339D, S371L, S373P, S375F, Q493R, G496S, Q498R, L452R, T478K, N501Y, Y505H, T547K, D614G, H655Y, N679K, P681R, N764K, D796Y, N856K, Q954H, N969K, and L981F, meanwhile, the Delta variant ((B.1.617.2) presented mutations at T19R, T95I, G142D, E156, F157, R158G, L452R, T478K, D614G, P681R, P812R, and D950N [6].

On the one hand, the vaccine successes against omicron variant remain unclear compared to their power versus infection with SARS-CoV-2 [3]. Additionally, the emergence of new variants of concern (COV) causes the collapse of the health system especially in developing countries which are unable to ensure the health care offer to their population [7]. Thanks to their effectiveness against viral disease, the plant extracts and their compounds have received increasing attention and might be a hopeful alternative to discover antiviral agents [8–10]. In this context, several research works have attempted to investigate the effect of the plant extracts and natural products against COVID-19. Indeed, in silico study, Alamri and collaborators [11] identified 9 natural compounds including calonysterone, isocodonocarpine, and withanolide A bound strictly to PL^{pro}, while chrysophanol 8-(6-galloylglucoside), luteolin 7-rutinoside, and kaempferol 7-(6″-galloylglucoside) linked strongly with RdRp, and 3,4,5-tri-O-galloylquinic acid, mulberrofuran G, and chrysophanol 8-(6-galloylglucoside) bound efficiently to 3CL^{pro}. In another study, Qamar et al., [12] using in silico approach demonstrated that licoleafol, Calceolarioside B, methyl rosmarinate, myricitrin, and 5,7,3′,4′-tetrahydroxy-2′-(3,3-dimethylallyl) isoflavone from *Glycyrrhiza uralensis*, *Hyptis atrorubens* Poit, *Myrica cerifera*, and *Psorothamnus arborescens*, respectively, exert an inhibition of SARS-CoV-2 3CL^{pro} effect. These products showed better linking affinity and better docking scores compared to the nelfinavir and prulifloxacin a control drug. Similarly, Yepes-Pérez et al. [13] reported the potential therapeutic activities, in silico, of cadambine, speciophylline, and proanthocyanidin-B2 against SARS-CoV-2 by strong interaction with 3CL^{pro}. Another study showed the inhibition effect of angiotensin-converting enzyme 2 (ACE$_2$) receptor caused by isothymol isolated from *Ammoides verticillata* plant [14]. A study conducted, in vitro, by Yepes-Pérez and colleagues found an interesting inhibition of 92.7% of SARS-CoV-2 at 25.0 μg/mL and an important reduction the cytopathic effect induced by SARS-CoV-2, after 48 h hydroalcoholic extract of *Uncaria tomentosa* treatment on Vero E6 cells [15]. In recent study, Nair et al. [16] investigated, in vivo, the antiviral activity of *Artemisia annua* L. hot-water extracts on five infectious variants of SARS-CoV-2 including alpha (B.1.1.7), beta (B.1.351), gamma (P.1), delta (B.1.617.2), and kappa (B.1.617.1) using Vero E6 cells. As results, the extracts of *A. annua* exhibit an important activity versus SARS-CoV-2 and its five variants.

Uncaria tomentosa, a member of Rubiaceae family, commonly called cat's claw or uña de gato is distributed in the Amazon region of Peru and other South American countries such as Colombia, Ecuador, and Brazil [17]. *U. tomentosa* commonly has been used by patients to treat the gastrointestinal disease, inflammatory diseases, and viral infections [18]. Previous papers reported that *U. tomentosa* contains various secondary metabolites including triterpenes, oxindole alkaloids, vegetal steroids, tannin, phenolic compounds, and flavonoids [19, 20]. Concerning the biological proprieties, pharmacological investigations showed that plant extracts exhibit multiple biological properties as antiviral on RNA-type virus like dengue [21], herpes [22], and SARS-CoV-2 [15]. Molecular docking protocols are a valuable computational strategy used in modern drug design which studies the ability of one or a few compounds to bind a given molecular target. In this regard, protein-ligand dockings of the main components of ethanolic extracts of cat's claw were performed against the three-dimensional structure of the SARS-CoV-2 Omicron spike glycoprotein (PDB ID: 7T9K) [23] (Figure 1).

2. Materials and Methods

2.1. Ligand Dataset Preparation of U. tomentosa Stem Bark. Ligands used in this computational study are components
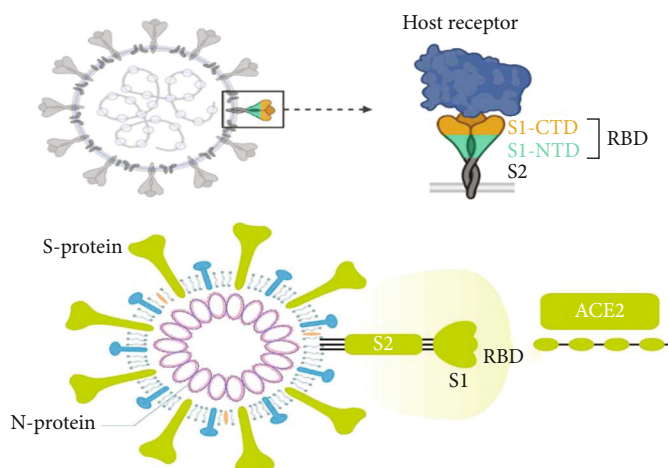
FIGURE 1: Schematic structure of the SARS-CoV-2 Omicron spike protein attached with host ACE2.

TABLE 1: Essential features, fit values, and relative fit values of the tested ligands and Azithromycin based on the generated pharmacophore model.

Ligand	Pharmacophoric queries	Pharmacophore-fit score	Relative fit value
Pteropodine		2.75	0.951
Speciophylline		2.56	0.885
Rhynchophylline		2.43	0.840
Mitraphylline		3.02	1.044
Uncarine F		3.12	1.079
Isorhynchophylline		3.01	1.041
Isomitraphylline		2.56	0.885
Quinovic acid-type 2		2.58	1.107
3-Dihydrocadambine		2.33	0.806
Chlorogenic acid		2.30	0.795
Proanthocyanidin-B4		2.14	0.740
Proanthocyanidin-B2		3.01	1.041
Proanthocyanidin-C1		2.98	1.031
Isopteropodine		1.36	0.470
Epicatechin		2.01	0.695
Azithromycin		2.89	1
∗relative fit value = tested compound fit value/azithromycin fit value			

determined of the cat's claw ethanol extract by HPLC-MS in the antiviral activity in vitro against SARS-CoV-2. These compounds were classified as oxindole alkaloids: isomitraphylline, isopteropodine, isorynchophylline, mitraphylline, pteropodine, rhynchophylline, speciophylline, and uncarine F; indole alkaloid: 3-dihydrocadambine; quinovic acids: quinovic acid-2; and proanthocyanins: chlorogenic acid, epicatechin, proanthocyanidin-B2, proanthocyanidin-B4, and proanthocyanidin-C1.

2.2. Generation of 3D-Pharmacophore Model. SARS-CoV-2 Omicron spike is one of the most essential and promising targets; it is the main part that SARS-CoV-2 virus used to penetrate the host cells. Spike is consisted of two main parts S1 and S2; S1 part contain receptor-binding domain (RBD);

it can recognize and bind with ACE-2 that facilitate the attack of virus against targeted host cells Figure [2]. Azithromycin shows a good inhibitory activity to RBD that can restrict the binding of SARS-CoV-2 spike with host ACE-2 [24]. The structure-based pharmacophore model was generated by BIO-VIA Discovery Studio 2019 client software; the pharmacophore queries was generated depending on the amino acid present in RBD; the best-fitted values and relative fit values were calculated in Table 1. The main objective of the pharmacophore structure-based drug design is to generate a 3D-pharmacophore model based on the known pocket. In this study, the pocket of RBD-SARS-CoV-2 was used to generate the queries (features) based on the amino acids present in target pocket. These features (Figures 2, 3, and 4) are essential for

Speciophylline
$C_{21}H_{24}N_2O_4$
368.1736

isopteropodine
$C_{21}H_{24}N_2O_4$
368.1736

isomitraphylline
$C_{21}H_{24}N_2O_4$
368.1736

Uncarine F
$C_{21}H_{24}N_2O_4$
368.1736

Mitraphylline
$C_{21}H_{24}N_2O_4$
368.1736

Pteropodine
$C_{21}H_{24}N_2O_4$
368.1736

rynchophylline
$C_{22}H_{28}N_2O_4$
384.2049

isorynchophyllin
$C_{22}H_{28}N_2O_4$
384.2049

3-dihydrocadambine
$C_{27}H_{34}N_2O_{10}$
546.2213

Quinovic acid type-2
$C_{48}H_{76}O_{19}$
956.4981

Proanthocyanidin C1
$C_{45}H_{38}O_{18}$
866.2058

Proanthocyanidin B4
$C_{30}H_{26}O_{12}$
578.1424

Proanthocyanidin B2
$C_{30}H_{26}O_{12}$
578.1424

Chlorogenic acid
$C_{16}H_{18}O_9$
354.0951

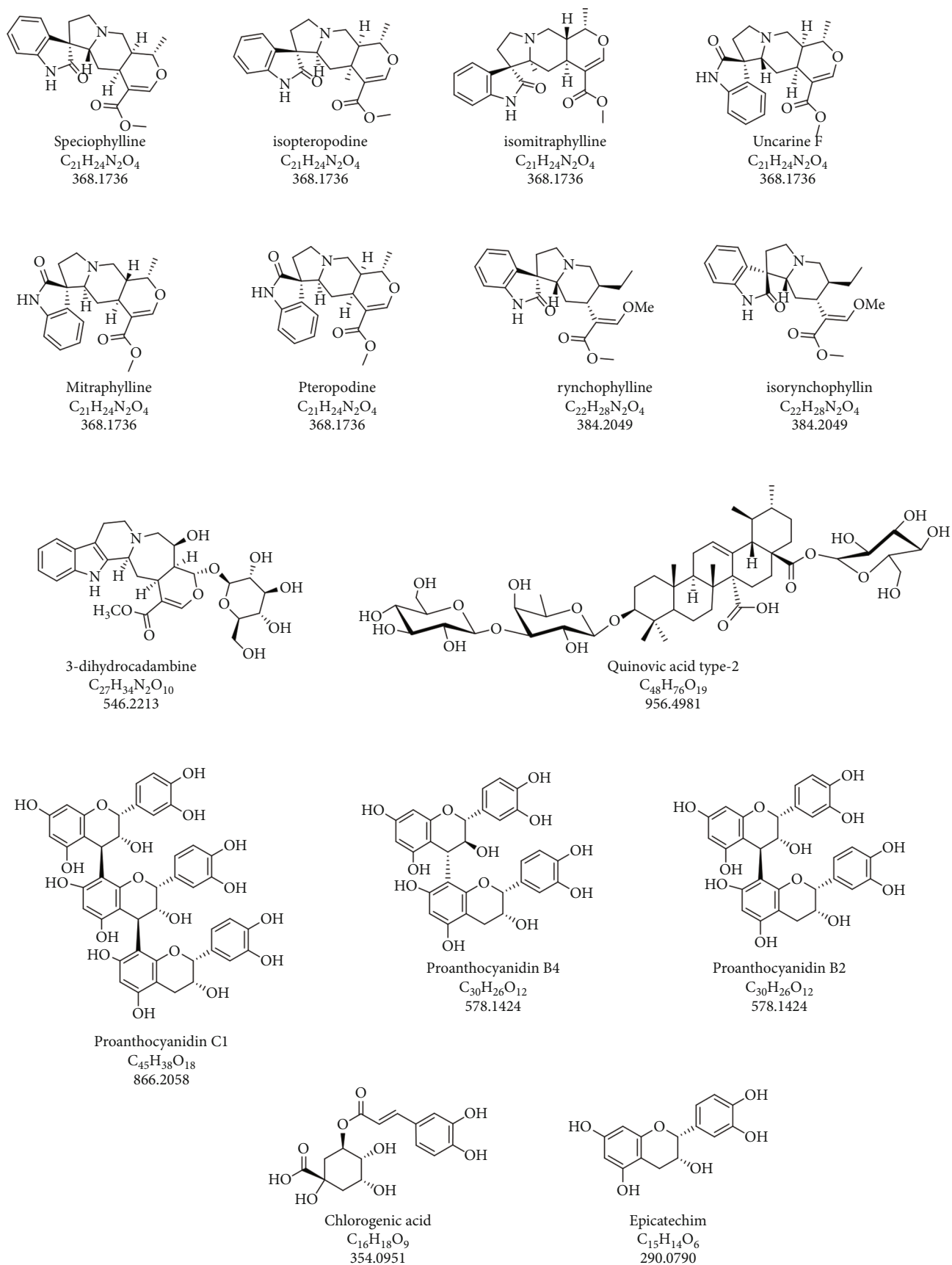Epicatechim
$C_{15}H_{14}O_6$
290.0790

FIGURE 2: Phytochemical components of the ethanolic extract of *U. tomentosa* stem bark.
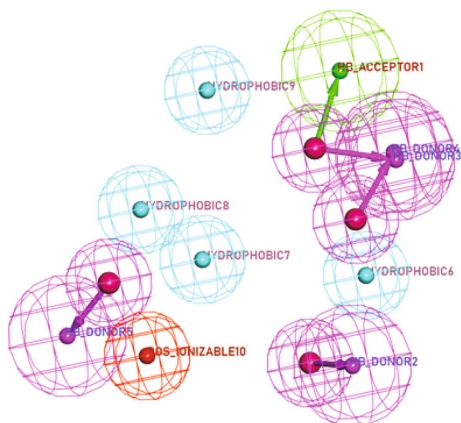
FIGURE 3: The generated hypothetical 3D-pharmacophore geometry with targeted pocket features; aromatic ring or hydrophobic (blue), ionic center (orange), hydrogen bond donor (violet), and acceptor center (green). (a) Queries of generated pharmacophore.

the activity. Consequently, any ligand will match or fit with these features is expected to be active.

2.3. Molecular Docking Studies. After doing the structure-based pharmacophore study for fifteen compounds isolated from *Uncaria tomentosa* (cat's Claw) stem bark, the molecular docking was done inside the pocket of RBD-SARS-CoV-2 Omicron spike protein by using BIOVIA Discovery Studio 2019 client. The SARS-CoV-2 Omicron spike protein crystal protein (PDB code: 7T9K) was downloaded from https://www.rcsb.org, acceded on January 25, 2022. At first water molecules have been removed from the complex. Then, crystallographic disorders and unfilled valence atoms were corrected using protein report and utility and clean protein options. Protein energy was minimized by applying CHARMM force fields. The rigid of binding site was the structure of protein that was obtained by applying fixed atom constraint. The protein essential amino acids were defined and prepared for docking process. 2D structures of tested compounds were drawn using ChemBioDraw Ultra17.0 and saved in MDL-SD file format; from BIOVIA Discovery Studio 2019 client, the saved file was opened, 3D structures were protonated, and energy was minimized by applying 0.05 RMSD kcal/mol CHARMM force field. Then, the minimized structures were prepared for docking using prepared ligand protocol. The molecular docking process was carried out using the CDOCKER protocol. The receptor was held rigid, while the ligands were allowed to be flexible during the refinement in which each molecule was allowed to produce ten different interaction poses with the protein. Then docking scores (-CDOCKER interaction energy) of the best-fitted poses with the active site at RBD-SARS-CoV-2 Omicron spike protein were recorded, and a 3D view was generated [25]. We use all these processes to predict the proposed binding mode, affinity, preferred orientation of each docking pose, and binding free energy (ΔG) of the tested compounds with RBD-SARS-CoV-2 Omicron spike protein Table 2.

2.3.1. Validation of Molecular Docking. The molecular docking was initially validated by redocking of the cocrystallized ligand into the active site of the respective receptor with the calculation of root mean square deviation (RMSD) for reliability and reproducibility of the proposed docking algorithm. In cocrystallized ligand not integrated with SARS-CoV-2 Omicron spike, we used Azithromycin as a guide and as coligand. Azithromycin was redocked on RBD-SARS-CoV-2 Omicron spike protein (PDB ID: 7T9K) and the RMSD 1.46 blew 2.00 A° indicating a validated method.

2.4. Molecular Dynamics Simulation (MD). Molecular dynamics simulation of the protein-ligand complexes was carried on the docked complexes for proanthocyanidin-B2 (the most active in the molecular docking analysis) with the SARS-CoV-2 Omicron spike protein (PDB ID: 7T9K) using GROMACS [26] 2021.1 version and Linux 5.4 package. The GROMOS96 54a7 force field was selected as the force field for proteins, and the ligand topologies were generated from the PRODRG [27] server. All the complexes were solvated using simple point charge (SPC) water molecules in a rectangular box. To make the simulation system electrically neutral, the required number of Na+ and Cl– ions were added, while 0.15 mol/L salt concentrations were set in all the systems. Using the steepest descent method, all the solvated systems were subjected to energy minimization for 5000 steps. Afterwards, NVT (constant number of particles, volume, and temperature) series, NPT (constant number of particles, pressure, and temperature) series, and the production run were conducted in the MD simulation. The NVT and the NPT series were conducted at a 300 K temperature and 1 atm pressure for the duration of 300 ps. V-rescale thermostat and Parrinello-Rahman barostat were selected for the performed simulation. Finally, the production run was performed at 300 K for a duration of 100 ns (nanoseconds). Thereafter, a comparative analysis was performed measuring root mean square deviation (RMSD), root mean square fluctuation (RMSF), radius of gyration (Rg), solvent accessible surface area (SASA), and hydrogen bonds to analyze their stability. The Xmgrace program was used to represent the analyses in the form of plots.

2.5. Molecular Similarity. The molecular similarity is a computational ligand-based calculation that is used to expect the similarity between two molecules. The principle that this study based on that the structurally similar ligands are predicted to have related properties to different molecules. Molecular similarity calculation targets the molecular properties of the examined ligands, such as LogP and molecular weight. Additionally, the molecular similarity mostly depends on the measures of distances in space in both structural and physicochemical descriptors.

3. Results and Discussion

3.1. Selecting of Ligands Based on Phytochemical Constituents of U. tomentosa Ethanol Extract. The ligands selected were established based on our previous study, which 15 metabolites were determined by HPLC-MS [15] in hydroalcoholic
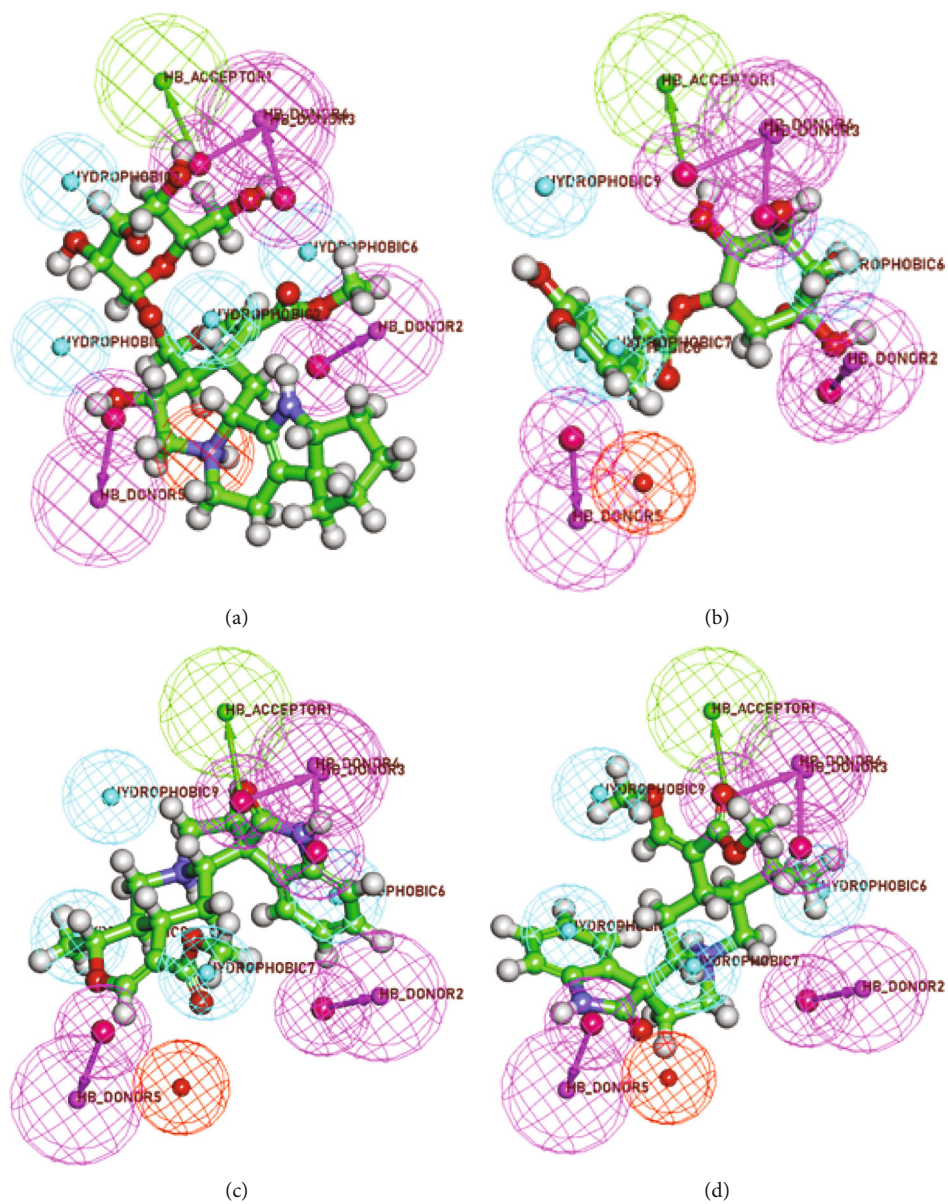
(a)

(b)

(c)

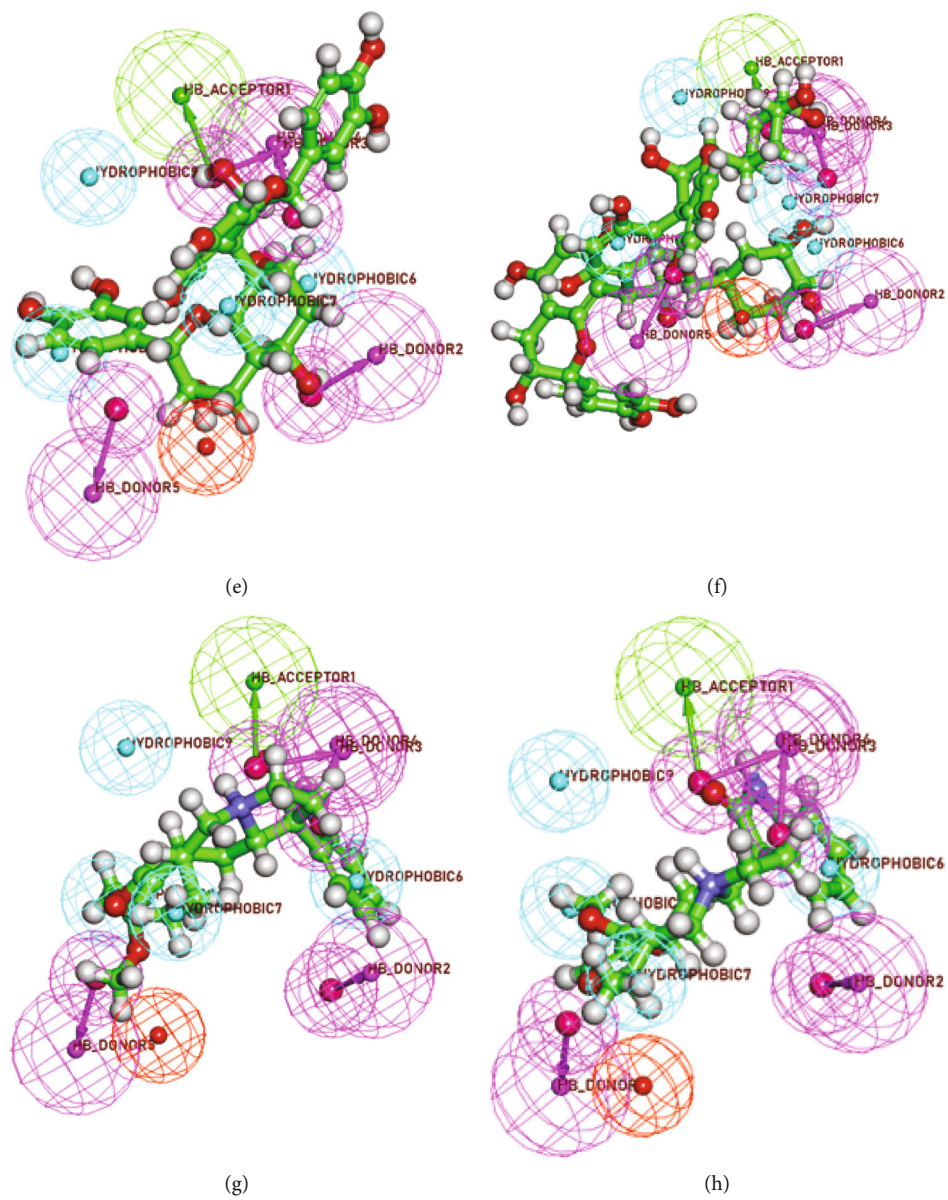(d)

Figure 4: Continued.

(e)
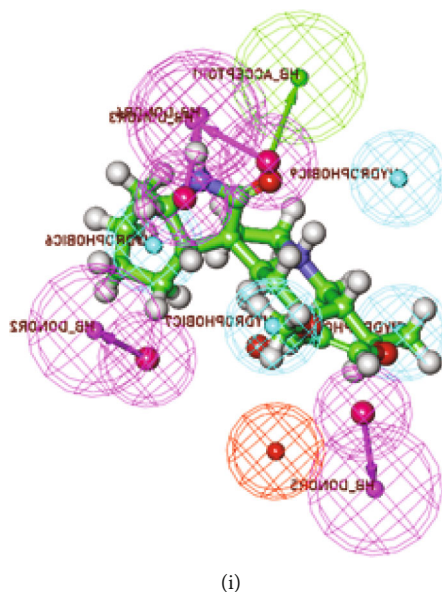
(f)

(g)

(h)

FIGURE 4: Continued.

(i)

FIGURE 4: Mapping of the tested ligands on the generated pharmacophore (a) ligand: 3-dihydrocadambine (fit value = 2.33), (b) ligand chlorogenic acid (fit value = 2.30), (c) ligand isomitraphylline (fit value = 2.56), (d) ligand isorhynchophylline (fit value = 3.01), (e) ligand proanthocyanidin-B2 (fit value = 3.01), (f) ligand proanthocyanidin-C1 (fit value = 2.98), (g) ligand rhynchophylline (fit value = 2.43), (h) ligand uncarine F (fit value = 3.12), and (i) ligand speciophylline (fit value = 2.56).

TABLE 2: Best binding energy (kcal mol^{-1}) based on BIOVIA Discovery Studio scoring of the main constituents of the *U. tomentosa* into SARS-CoV-2 Omicron spike protein-binding domain (PDB ID: 7T9K).

Protein ligand complex	Binding affinity (kcal/mol)	RMSD value
Isomitraphylline	-7.75	1.66
Quinovic acid-type 2	-9.86	1.56
Isopteropodine	-7.66	1.63
Isorhynchophylline	-7.35	0.96
Mitraphylline	-7.67	1.16
Pteropodine	-6.72	1.67
Rhynchophylline	-7.49	1.05
Speciophylline	-6.45	1.06
Uncarine F	-7.11	1.36
3-Dihydrocadambine	-8.58	1.63
Chlorogenic acid	-6.42	1.06
Epicatechin	-6.89	1.69
Proanthocyanidin-B2	-9.82	1.12
Proanthocyanidin-B4	-8.95	1.25
Proanthocyanidin-C1	-10.76	1.56
Azithromycin	-9.32	1.23

extract of *U. tomentosa* (Figure 2). They were identified as oxindole alkaloids, indole alkaloids, quinovic acid, and proanthocyanidins. The total phytoconstituents were classified as spirooxindole alkaloids, indole glycosides alkaloids, quinovic acid, and proanthocyanidins. Other investigations have confirmed our findings based on the phytochemical

profile carried out on different extracts from stem bark, which is traditionally consumed in different forms such as infusions, teas, decoction, macerated, and lately dosage forms like capsules and tablets which can be sold in pharmacies. Although in national hospitals from Peru, bags containing a powder of *U. tomentosa* (uña de gato) are used for rheumatic pain as alternative treatment. Several studies attributed to its alkaloids as the responsible of the biological activity like antiviral. However, other studies revealed the total extract synergisms of the pharmacological effect, acting by different mechanisms. Furthermore, the quality control of *U. tomentosa* is based on the determination of its eight alkaloids as in the American Pharmacopoeia (USP) and corresponds to its fingerprint [28].

3.2. Generation of 3D-Pharmacophore Model

3.2.1. Activity Prediction. The test set of the isolated compounds and Azithromycin were examined against the generated 3D-pharmacophore model. In this process, fit values and relative fit values (that quantitatively represent the existence of that essential features) were calculated. All ligands were proved to have the main essential features of inhibitor (Table 1). Interestingly, some ligands showed high fit values and good matching with 3D-pharmacophore queries.

3.3. Docking Studies. Molecular docking protocol is a valuable computational strategy used in modern drug design which study the ability of one or a few compounds to bind a given molecular target. In this regard, protein-ligand dockings of the main components of ethanolic extracts of cat's claw were performed against the three-dimensional structure Omicron spike glycoprotein-RBD of SARS-CoV-2 (PDB ID: 7T9K) [23].
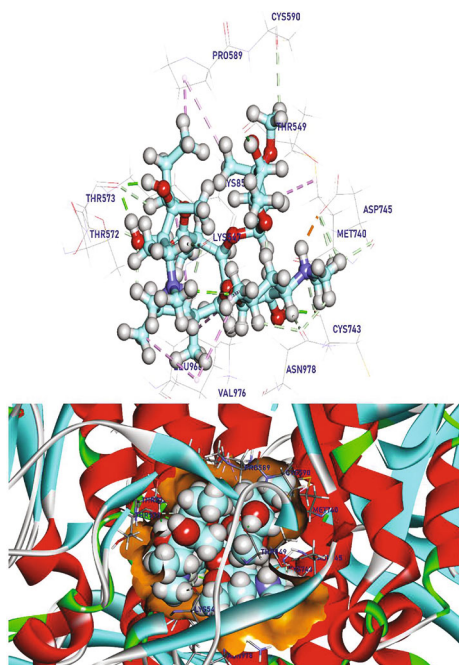
FIGURE 5: (Azithromycin) docked in RBD-SARS-CoV-2 Omicron spike protein, hydrogen bonds (green), and the pi interactions are represented in purple lines with mapping surface showing Azithromycin occupying the active pocket of RBD-SARS-CoV-2 Omicron spike protein.

FIGURE 6: 3-Dihydrocadambine docked in RBD-SARS-CoV-2 Omicron spike protein, hydrogen bonds (green), and the pi interactions are represented in purple lines with mapping surface showing 3-dihydrocadambine occupying the active pocket of RBD-SARS-CoV-2 Omicron spike protein.

The binding mode of Azithromycin exhibited an energy binding of -9.32 kcal/mol-1 against RBD-SARS-CoV-2 Omicron spike protein, which formed nine Pi-Alkyl interactions

FIGURE 7: Isomitraphylline docked in RBD-SARS-CoV-2 Omicron spike protein, hydrogen bonds (green), and the pi interactions are represented in purple lines with mapping surface showing isomitraphylline occupying the active pocket of RBD-SARS-CoV-2 Omicron spike protein.

with Val976, Met740, Leu966, Pro589, and Lys856; moreover, four hydrogen bonds was created with Thr573, Thr549, and Cys743 with a distance of 1.78, 1.82, 1.84, and 1.87 Å, respectively, additionally the cationic NH2 center binding with Asp745 ionic interaction (Figure 5).

The binding mode of 3-dihydrocadambine exhibited an energy binding of -8.58 kcal/mol-1 against RBD-SARS-CoV-2 Omicron spike protein, which interacted with Lys547, Cys590, Gly744, Asp745, Thr549, and Lys856 by eleven hydrogen bonds with a distance of 2.72, 2.77, 2.60, 2.50, 2.59, 1.86, 2.16, 2.60, 2.51, 2.29, and 2.68°A, and additionally formed two Pi-Alkyl interactions with Val976 and Lys856 (Figure 6).

The binding mode of chlorogenic acid exhibited an energy binding of -6.42 kcal/mol-1 against RBD-SARS-CoV-2 Omicron spike protein, which creates one Pi-alkyl interaction with Leu966 and additionally interacts with Lys856, Tyr741, Met740, Lys547, Gly744, Asp745, Thr549, Leu977, and Asn978 by eleven hydrogen bonds with a distance range of 1.91 and 2.90°A (Figure S1). The binding mode of isomitraphylline exhibited an energy binding of -7.75 kcal/mol-1 against RBD-SARS-CoV-2 Omicron spike protein, which created three Pi-Alkyl interactions with Val976, Lys856, and Pro589; additionally interacted with Leu966, Gly744, Asn978, Asp745, and Thr549 by seven hydrogen bonds; and moreover, interacted with Asp745 by ionic interaction with cationic amino group. (Figure 7).

The binding mode of isopteropodine exhibited an energy binding of -7.66 kcal/mol-1 against RBD-SARS-CoV-2 Omicron spike protein. The hydrophilic centers create four conventional hydrogen bonds and seven nonconventional hydrogen bonds with Gly548, Thr549, Asn540, Asp745, Glu748, and Asn978 and additionally interact with Leu977

FIGURE 8: Isopteropodine docked in RBD-SARS-CoV-2 Omicron spike protein, hydrogen bonds (green), and the pi interactions are represented in purple lines with mapping surface showing isopteropodine occupying the active pocket of RBD-SARS-CoV-2 Omicron spike protein.
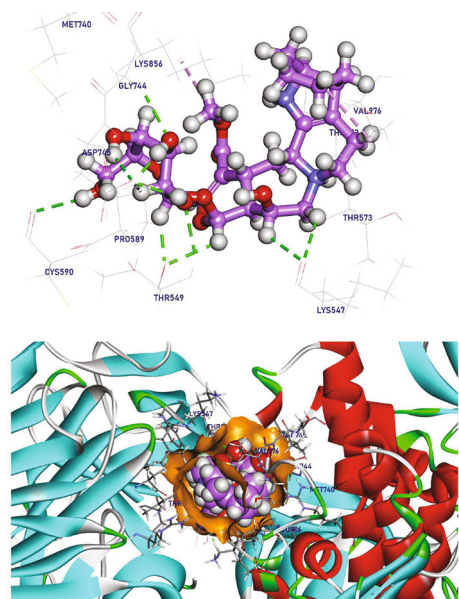

FIGURE 9: Isorhynchophylline docked in RBD-SARS-CoV-2 Omicron spike protein, hydrogen bonds (green), and the pi interactions are represented in purple lines.

and Val976 by two Pi-alkyl interactions and form ionic interactions with Glu748 and Asp745 (Figure 8).

The binding mode of isorhynchophylline exhibited an energy binding of -7.35 kcal/mol-1 against RBD-SARS-CoV-2 Omicron spike protein, which creates five Pi-Alkyl and Pi-Sigma interactions with Ile587, Pro589, Phe541, and Val976. Besides that, it was interacted with Thr572,
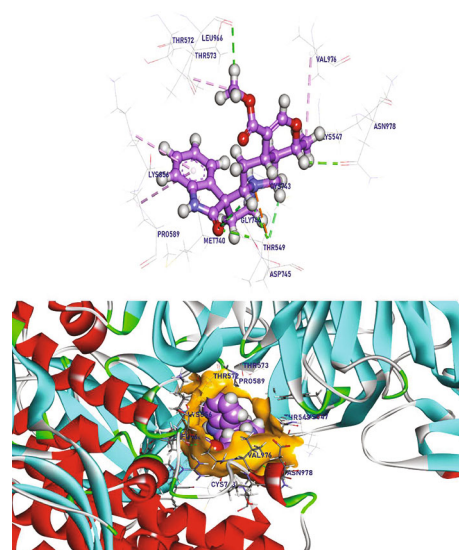

FIGURE 10: Mitraphylline docked in RBD-SARS-CoV-2 Omicron spike protein, hydrogen bonds (green), and the pi interactions are represented in purple lines.

Thr573, and Lys 856 by four hydrogen bonds with a distance of 2.05 to 2.68°A (Figure 9).

The binding mode of mitraphylline exhibited an energy binding of -7.67 kcal/mol-1 against RBD-SARS-CoV-2 Omicron spike protein, which creates two Pi-Alkyl interactions with Pro589 and Leu977 and, moreover, interacts with Gly744, Asp745, Thr549, and Lys547 by five hydrogen bonds with a distance range of 2.09 to 2.68°A (Figure 10).

The binding mode of proanthocyanidin-B2 exhibited an energy binding of -9.82 kcal/mol-1 against RBD-SARS-CoV-2 Omicron spike protein. This complex was stabilized by creating four strong Pi-Alkyl, Pi-amide, and Pi-sigma interactions with Lys547, Gly548, Pro589 and Thr572 and, moreover, interacted with Arg567, Thr573, Gly744, Asn978, Asp745, Thr549, Ile587, and Thr572 by nine hydrogen bonds with a distance range of 2.00 to 3.07°A (Figure 11A), while proanthocyanidin-B4 exhibited an energy binding of -8.95 kcal/mol-1 against RBD-SARS-CoV-2 Omicron spike protein. It creates three Pi-Alkyl and Pi-amide interactions with Cys743, Met740, and Val976 and additionally interacts with Thr573, Cys590, Thr549, Pro589, Asp745, Gly744, Ser975, and Lys547 by eight hydrogen bonds with a distance range of 1.8 to 3.02°A (Figure 11(b)).

The binding mode of proanthocyanidin-C1 exhibited an energy binding of -10.76 kcal/mol-1 against RBD-SARS-CoV-2 Omicron spike protein. The complex was stabilized by creating four Pi-Alkyl and Pi-Sigma interactions with Lys856, Pro589, and Val976 and, moreover, interacted with Gly744, Pro589, Ser967, Thr549, Asp745, Tr572, and Thr573 by nine hydrogen bonds with a distance range of 2.11 to 2.99°A.(Figure 12).

The binding mode of quinovic acid exhibited an energy binding of -9.86 kcal/mol-1 against RBD-SARS-CoV-2
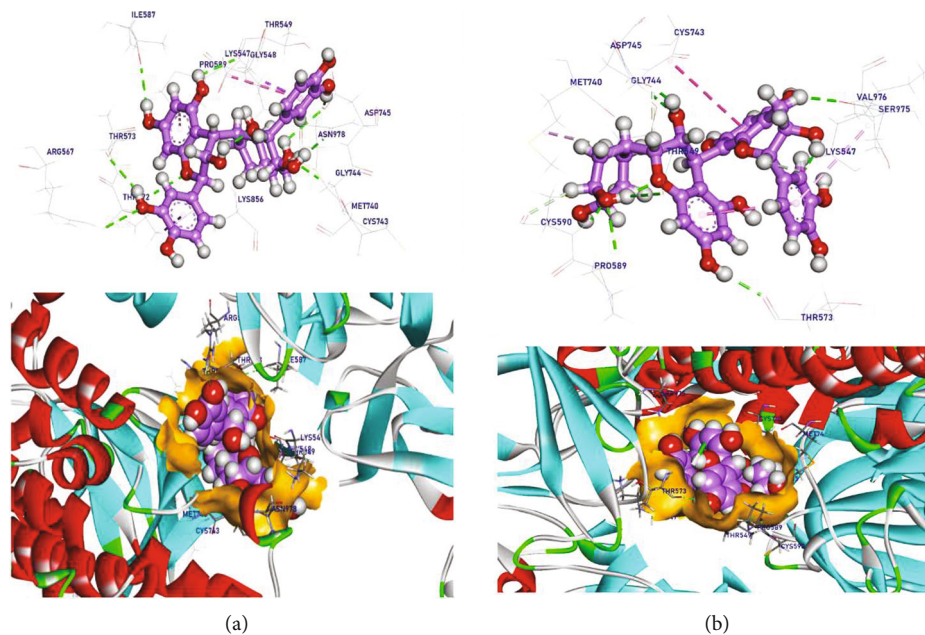
(a)   (b)

FIGURE 11: (a) Proanthocyanidin-B2 docked in RBD-SARS-CoV-2 Omicron spike protein and (b) proanthocyanidin-B4 docked in RBD-SARS-CoV-2 Omicron spike protein, hydrogen bonds (green), and the pi interactions are represented in purple lines with mapping surface showing the ligands occupying the active pocket of RBD-SARS-CoV-2 Omicron spike protein.
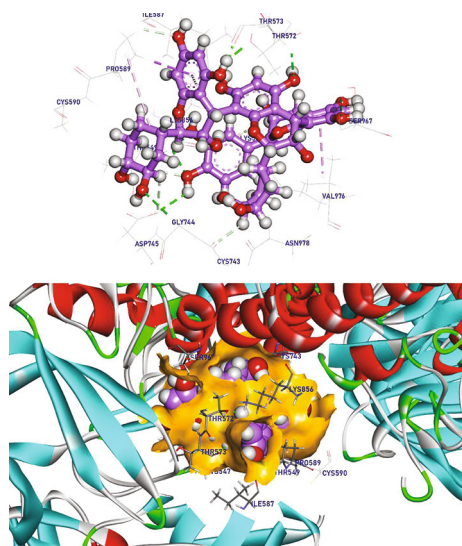

FIGURE 12: Proanthocyanidin-C1 docked in RBD-SARS-CoV-2 Omicron spike protein, hydrogen bonds (green), and the pi interactions are represented in purple lines.

Omicron spike protein, which creates three Pi-Alkyl interactions with Lys547 and Val976 and moreover interacts with Asp745, Gln321, Cys743, Arg1000, Tyr741, and Thr573 by seven hydrogen bonds with a distance range of 1.68 to 2.52 Å (Figure 13).

The binding mode of rhynchophylline exhibited an energy binding of -7.49 kcal/mol-1 against RBD-SARS-CoV-2 Omicron spike protein. It creates four Pi-Alkyl interactions with Leu966, Met740, Phe592, and Pro589 and, additionally, interacts with Gly458 and Thr549 by two hydrogen bonds with a

distance of 2.57 and 2.58 Å (Figure 14). The binding mode of pteropodine exhibited an energy binding of -6.72 kcal/mol-1 against RBD-SARS-CoV-2 Omicron spike protein, which creates four Pi-Alkyl interactions with Leu546, Phe541, Val976, and Leu966 and moreover interacts with Gly548, Val976, and Ser975 by three hydrogen bonds (Figure S2).

The binding mode of speciophylline exhibited an energy binding of -6.45 kcal/mol-1 against RBD-SARS-CoV-2 Omicron spike protein, which creates three Pi-Alkyl interactions with Leu966, Leu977, and Met740 and moreover interacts with Arg1000 and Thr549 by two hydrogen bonds (Figure S3A), while uncarine F exhibited an energy binding of -7.11 kcal/mol-1 against RBD-SARS-CoV-2 Omicron spike protein. It forms two Pi-Alkyl interactions with Pro589 and Leu977 and moreover interacts with Asp745, Gly744, Thr549, and Lys547 by four hydrogen with a distance range of 2.09 to 2.68 Å (Figure S3B). The binding mode of epicatechin exhibited an energy binding of -6.89 kcal/mol-1 against RBD-SARS-CoV-2 Omicron spike protein. It creates one Pi-Alkyl interaction with Pro589 and additionally interacts with Ile578, Lys856, and Asp745 by three hydrogen bonds (Figure S4).

These facts are in good agreement with our previous report which computational and in vitro experiments confirmed that the hydroalcoholic fraction from cat's claw inhibited the release of SARS-CoV-2 infectious particles and reduced the cytopathic effect caused by the virus [15]. Therefore, virtual screening suggests that some components in hydroalcoholic extract of *U. tomentosa* stem bark could positively modulates the recently emerged SARS-CoV-2 Omicron infection. However, experimental assays are needed to support these computational predictions. In addition, as can be seen in a previous report [28], calculated
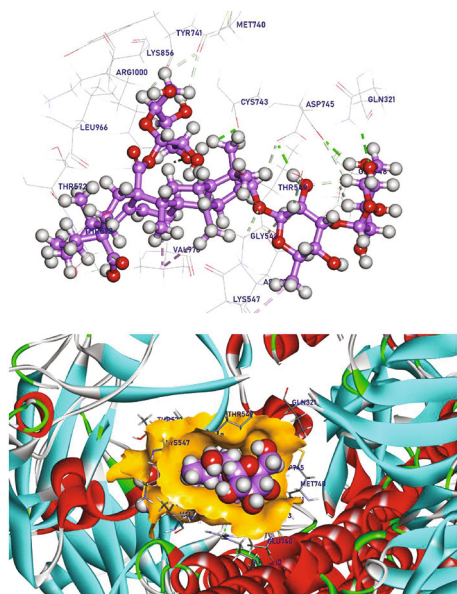
FIGURE 13: Quinovic acid docked in RBD-SARS-CoV-2 Omicron spike protein, hydrogen bonds (green), and the pi interactions are represented in purple lines.
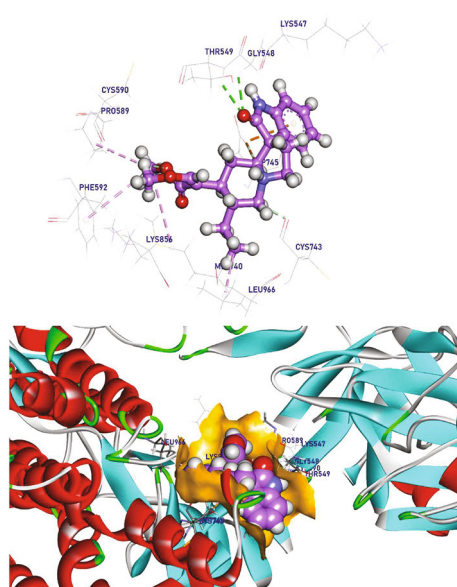

FIGURE 14: Rhynchophylline docked in RBD-SARS-CoV-2 Omicron spike protein, hydrogen bonds (green), and the pi interactions are represented in purple lines.

pharmacokinetic indices for the most qualified cat's claw components showed the druggability of the selected components and their potential as likely orally active antiviral. Calculated parameters revealed that most of components exhibited favorable characteristics as the drug like; hence, *U. tomentosa* may constitute itself a promissory option to fight against COVID-19 infection.

3.4. Molecular Dynamics Simulation (MD). Molecular dynamics and simulation (MD) studies were carried out in

order to determine the stability and convergence of 7T9K/proanthocyanidin-B2, 7T9K/proanthocyanidin-C1, and 7T9K/quinovic acid complexes. According to 7T9K/Pproanthocyanidin-B2, the dynamic movements of atoms and conformational variations of backbone atoms of the protein-ligand complex were calculated by RMSD to detect their stability upon apo and ligand bonded state. It is observed that the protein and ligand exhibit very lower RMSD with no major fluctuations indicating their greater stability. The complex was slightly stable until 25 ns~ and showed more stability later. The flexibility of each residue was calculated in terms of RMSF to get better insight on the region of proteins that are being fluctuated during the simulation. It can be understood that the binding of ligand does not make the protein in any areas. The compactness of the complex was represented by the radius of gyration (Rg). The lower degree of fluctuation throughout the simulation period indicates the greater compactness of a system. The Rg of the complex was found to be slightly lower than the starting period. Interaction between protein-ligand complexes and solvents was measured by solvent accessible surface area (SASA) over the simulation period. So, SASA of the complex was calculated to analyze the extent of the conformational changes occurred during the interaction. Interestingly, the protein featured a slight reduction of the surface area showing relatively lower SASA value than the starting period. Hydrogen bonding between a protein-ligand complex is essential to stabilize the structure. It was observed that the highest number of conformations of the protein formed up to six hydrogen bonds with the ligand (Figures 15, 16, 17, 18, 19, and 20). Additionally, we calculated the binding free energy of the last 20 ns of MD production run of the protein-ligand complex with an interval of 100 ps from MD trajectories using MM/PBSA method. We also utilized the MmPbSaStat.py script that calculated the average free binding energy and its standard deviation/error from the output files that were obtained from g_mmpbsa. The ligand showed less binding free energy of -121 KJ/mol with the protein. Further, we identified the contribution of each residue of the protein in terms of binding free energy to the interaction with the ligand. By decomposing the total binding free energy of the system into per residue contribution energy, the contribution of each residue was calculated. This gave us an insight into the "crucial" residues that contributes favorably to the binding of this molecule to the protein. It was found that THR-549, ARG-567, THR-573, ILE587, GLY-744, ASP745, and ASN-978 residues of the protein contributed higher than -5 KJ/mol binding energy and thereby are hotspot residues in binding with the ligand.

According to 7T9K/proanthocyanidin-C1 complex, it is observed that the protein and ligand exhibit very lower RMSD with no major fluctuations indicating their greater stability. The complex was unstable until 10 ns~, and it becomes stable until 40 ns~ with minor fluctuation and showed stability later. The flexibility of each residue was calculated in terms of RMSF to get better insight on the region of proteins that are being fluctuated during the simulation. It can be understood that the binding of ligand makes the protein slightly flexible in 1700-1800 residue areas. The compactness of the complex was represented by the radius of gyration (Rg). The lower degree of fluctuation throughout
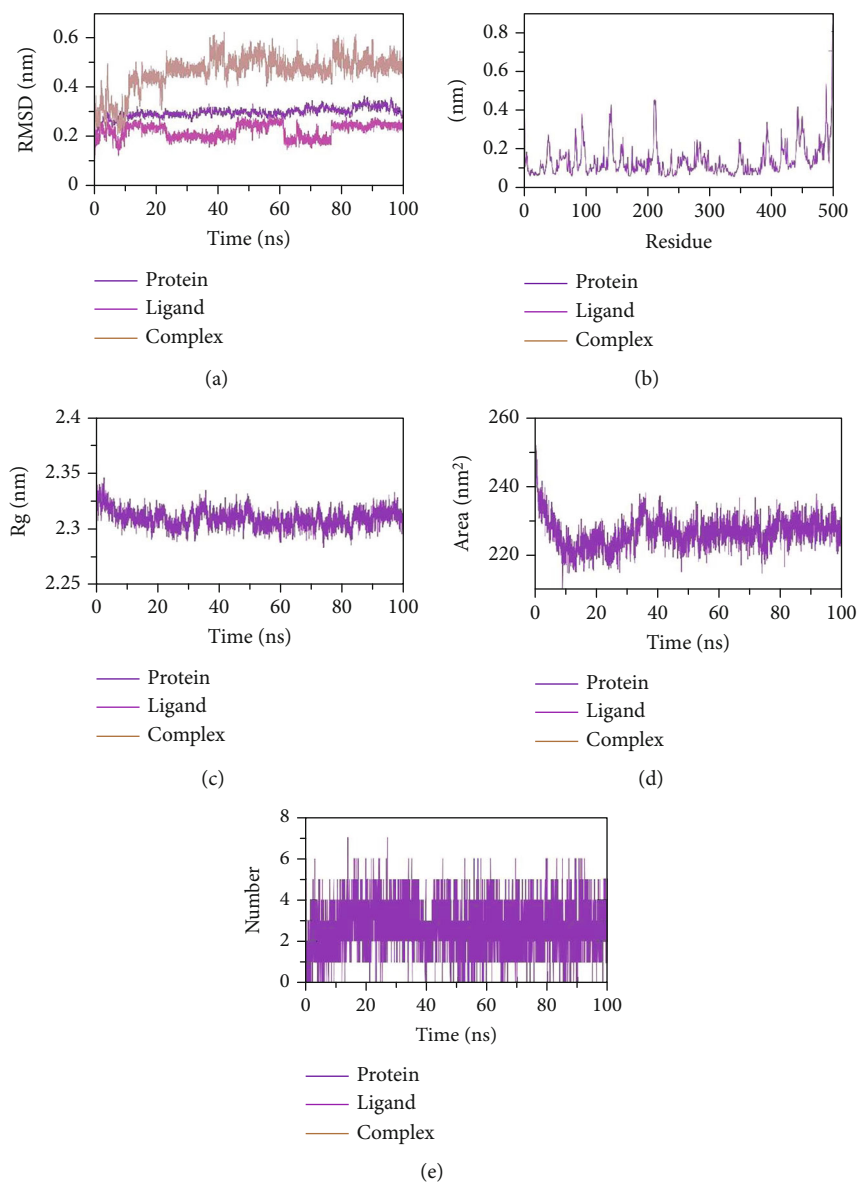
(a)

(b)

(c)

(d)

(e)

Figure 15: MD simulation trajectory analysis of (a) root mean square deviation (RMSD) of proanthocyanidin-B2 bound with 7T9K at 100-ns time frame, (b) root mean square fluctuation (RMSF), (c) radius of gyration (Rg), (d) solvent accessible surface area plot of proanthocyanidin-B2 bound with 7T9K at 100-ns time frame, and (e) number of H-Bond plot of proanthocyanidin-B2 bound with 7T9K at 100 ns time frame.
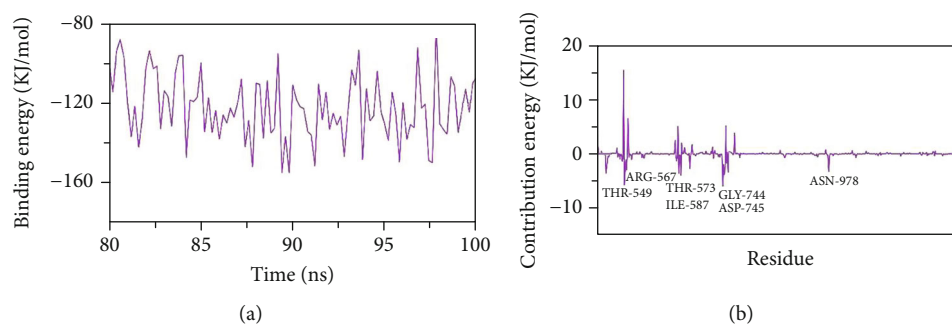

(a)

(b)

Figure 16: (a) Total binding energy plot of proanthocyanidin-B2 bound with 7T9K at 100-ns time frame. (b) Contribution energy plot with interacting amino acids.
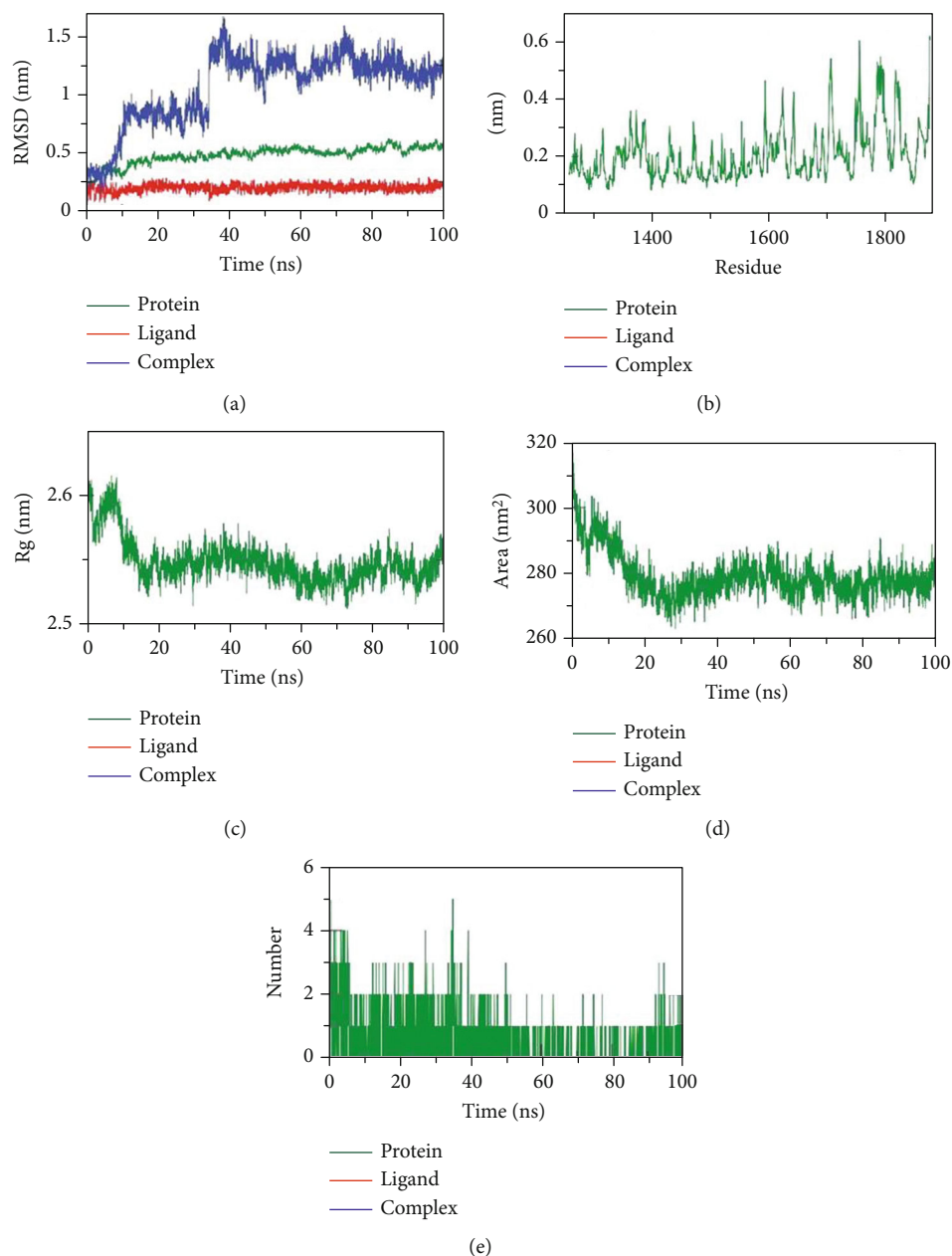
(a)

(b)

(c)

(d)

(e)

Figure 17: MD simulation trajectory analysis of (a) root mean square deviation (RMSD) of proanthocyanidin-C1 bound with 7T9K at 100-ns time frame, (b) root mean square fluctuation (RMSF), (c) radius of gyration (Rg), (d) solvent accessible surface area plot of proanthocyanidin-C1 bound with 7T9K at 100-ns time frame, and (e) number of H-Bond plot of proanthocyanidin-C1 bound with 7T9K at 100 ns time frame.

the simulation period indicates the greater compactness of a system. The Rg of the complex was found to be slightly lower than the starting period. The interaction between protein-ligand complexes and solvents was measured by solvent accessible surface area (SASA) over the simulation period. So, SASA of the complex was calculated to analyze the extent of the conformational changes occurred during the interaction. Interestingly, the protein featured a slight reduction of the surface area showing relatively lower SASA value than the starting period. Hydrogen bonding between a protein-ligand complex is essential to stabilize the structure. It was observed that the highest number of conformations of the

protein formed up to two hydrogen bonds with the ligand. Moreover, we calculated the binding free energy of the last 20 ns of MD production run of the protein-ligand complex with an interval of 100 ps from MD trajectories using MM/PBSA method. We also utilized the MmPbSaStat.py script that calculated the average free binding energy and its standard deviation/error from the output files that were obtained from g_mmpbsa. The ligand showed less binding free energy of -96 KJ/mol with the protein. Further, we identified the contribution of each residue of the protein in terms of binding free energy to the interaction with the ligand. By decomposing the total binding free energy of the system into per
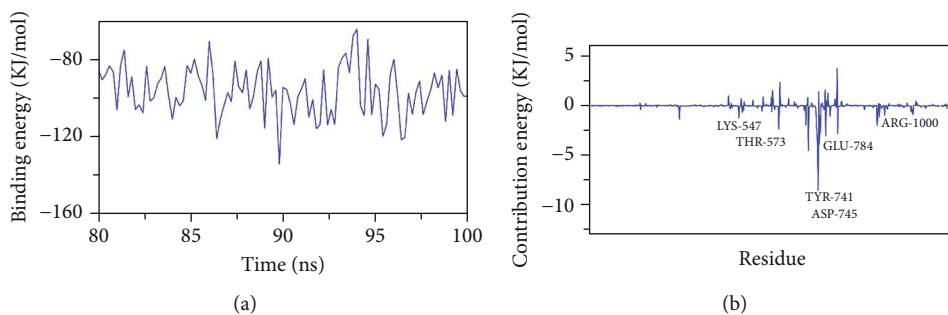
(a)

(b)

FIGURE 18: (a) Total binding energy plot of proanthocyanidin-C1 bound with 7T9K at 100-ns time frame. (b) Contribution energy plot with interacting amino acids.

(a)

(b)

(c)

(d)

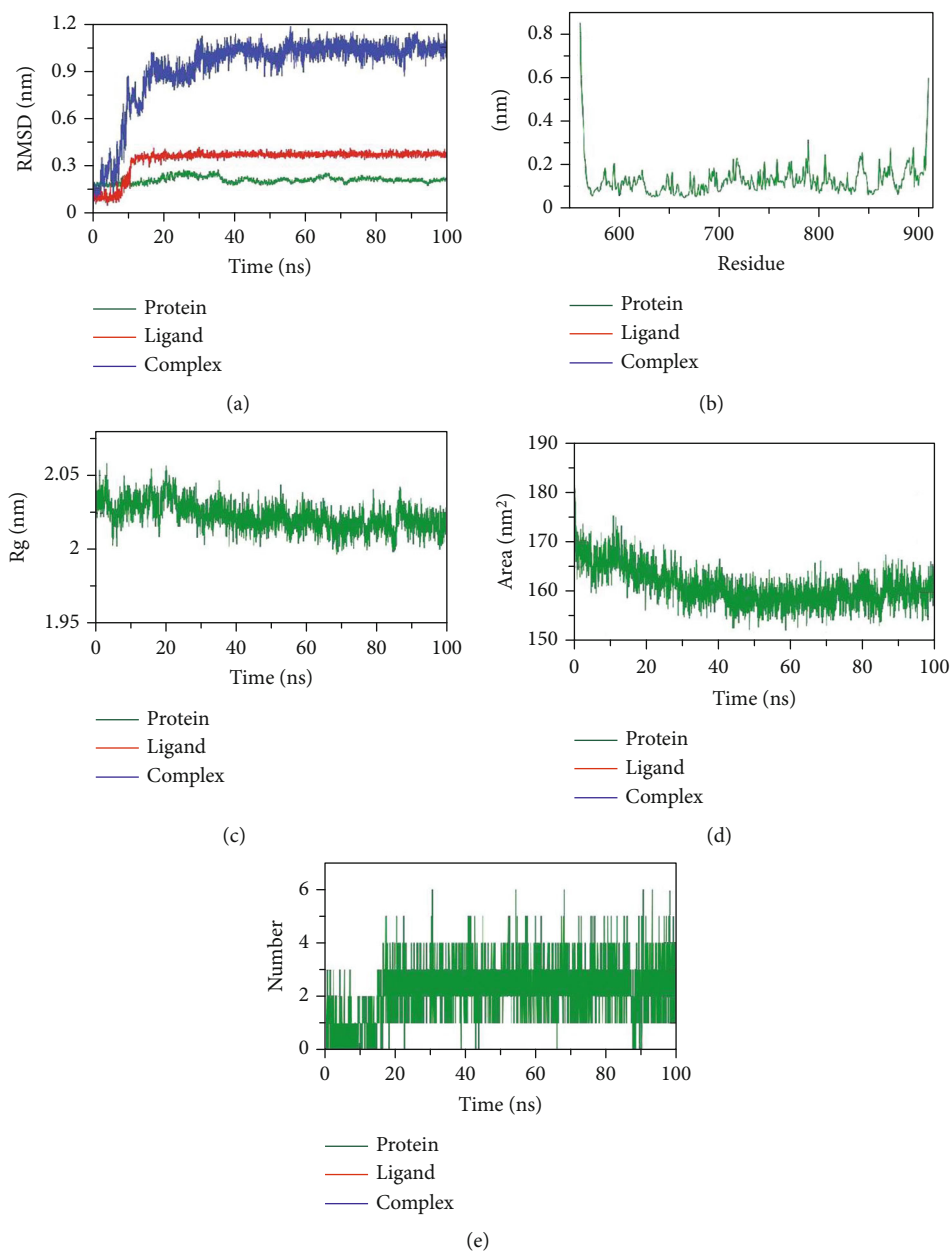
(e)

FIGURE 19: MD simulation trajectory analysis of (a) root mean square deviation (RMSD) of quinovic acid bound with 7T9K at 100-ns time frame, (b) root mean square fluctuation (RMSF), (c) radius of gyration (Rg), (d) solvent accessible surface area plot of quinovic acid bound with 7T9K at 100-ns time frame, and (e) number of H-Bond plot of quinovic acid bound with 7T9K at 100-ns time frame.

(a)   (b)
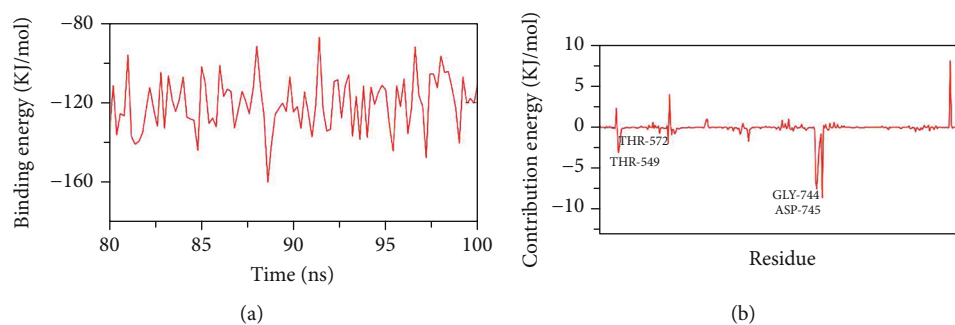
FIGURE 20: (a) Total binding energy plot of quinovic acid bound with 7T9K at 100-ns time frame. (b) Contribution energy plot with interacting amino acids.

TABLE 3: Ligands with Azithromycin and their molecular properties.

Comp.	ALog p	M. Wt	HBA	HBD	Rotatable bonds	Rings	Aromatic rings	MFPSA	Minimum distance	Is similar to Azithromycin
Rhynchophylline	0.542	385.477	4	2	5	4	1	0.174	1.16308	True
Isorhynchophylline	0.542	385.477	4	2	5	4	1	0.174	1.16308	True
Proanthocyanidin-B4	2.45	584.568	12	10	3	6	3	0.423	1.52546	True
Quinovic acid	1.101	957.106	19	11	10	8	0	0.328	1.4189	True
Proanthocyanidin-B2	1.224	584.568	12	10	3	6	3	0.425	1.54092	True
Speciophylline	-0.284	375.482	4	2	2	5	0	0.189	1.45461	False
Proanthocyanidin-C1	2.879	878.868	18	15	5	9	4	0.426	2.11191	False
Epicatechin	2.021	290.268	6	5	1	3	2	0.415	1.61445	False
Chlorogenic acid	-0.34	354.309	9	6	5	2	1	0.487	1.41617	True
3-Dihydrocadambine	-2.649	553.622	11	7	5	6	0	0.334	1.51574	False
Uncarine F	-0.399	369.434	4	2	2	5	1	0.196	1.5013	False
Isomitraphylline	-0.399	369.434	4	2	2	5	1	0.196	1.5013	False
Isopteropodine	-0.399	369.434	4	2	2	5	1	0.196	1.5013	False
Pteropodine	-0.407	373.466	4	2	2	5	0	0.191	1.46941	False
Mitraphylline	-0.399	369.434	4	2	2	5	1	0.196	1.5013	False
Azithromycin	2.078	748.984	14	5	7	3	0	0.209	—	Reference

residue contribution energy, the contribution of each residue was calculated. This gave us an insight into the "crucial" residues that contributes favorably to the binding of this molecule to the protein. It was found that LYS-547, THR573, TYR-741, ASP745, GLU-784, and ARG-1000 residues of the protein contributed higher than -8 KJ/mol binding energy and thereby are hotspot residues in binding with the ligand.

According to 7T9K/quinovic acid complex, the dynamic movements of atoms and conformational variations of backbone atoms of the protein-ligand complex were calculated by RMSD to detect their stability upon apo and ligand bonded state. It is observed that the protein, ligand, and complex exhibit very lower RMSD with no major fluctuations indicating their greater stability. The complex was unstable until 17 ns~ and showed stability later. The flexibility of each residue was calculated in terms of RMSF to get better insight on the region of proteins that are being fluctuated during the simulation. The compactness of the complex was represented by the radius of gyration (Rg). The lower degree of fluctuation throughout the simulation period indicates the greater compactness of a system. The Rg of the complex was found to be slightly lower than the starting period. Interaction between protein-ligand complexes and solvents was measured by solvent accessible surface area (SASA) over the simulation period. So, SASA of the complex was calculated to analyze the extent of the conformational changes occurred during the interaction. Interestingly, the protein featured a slight reduction of the surface area showing relatively lower SASA value than the starting period.

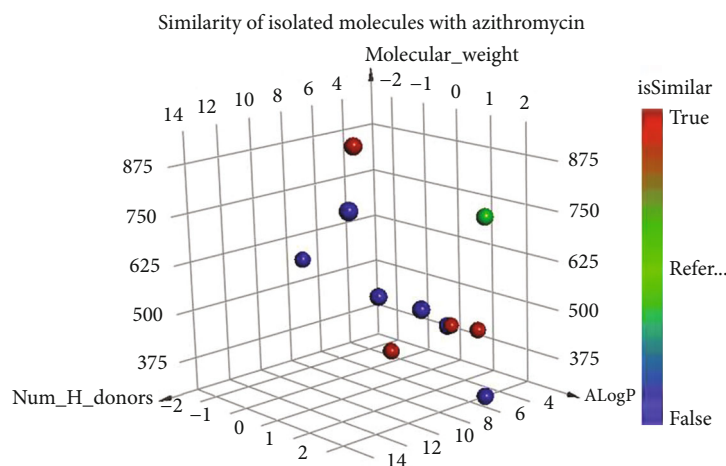Similarity of isolated molecules with azithromycin

Figure 21: The similarity analysis between the tested molecules and (Azithromycin). Green ball = (reference); red balls = similar ligands; blue balls = not similar ligands.

Hydrogen bonding between a protein-ligand complex is essential to stabilize the structure. It was observed that the highest number of conformations of the protein formed up to five hydrogen bonds with the ligand.

Additionally, we calculated the binding free energy of the last 20 ns of MD production run of the protein-ligand complex with an interval of 100 ps from MD trajectories using MM/PBSA method. We also utilized the MmPbSaStat.py script that calculated the average free binding energy and its standard deviation/error from the output files that were obtained from g_mmpbsa. The ligand showed less binding free energy of -120 KJ/mol with the protein. Further, we identified the contribution of each residue of the protein in terms of binding free energy to the interaction with the ligand. By decomposing the total binding free energy of the system into per residue contribution energy, the contribution of each residue was calculated. This gave us an insight into the "crucial" residues that contributes favorably to the binding of this molecule to the protein. It was found that THR-549, THR-572, GLY-744, and ASP745 residues of the protein contributed higher than -7 KJ/mol binding energy and thereby are hotspot residues in binding with the ligand.

Finally, the MD simulation results suggest that (1) the ligands were stable at the binding pocket in the 100-ns MD simulations, (2) ligand does not leave the Omicron receptor-binding domain (RBD) while 100 ns MD run, and (3) 100 ns molecular dynamics simulation suggest the rationality and validity of our docking studies. Accordingly, some chemical components of hydroalcoholic extract of *U. tomentosa*, particularly, proanthocyanidin-B2, proanthocyanidin-C1, and quinovic acid could suppress Omicron viral spike function, which in turn suggest that *U. tomentosa* may interfere with internalization of the Omicron variant in the human host.

Altogether, computational modeling studies showed strong evidence that several chemical components in hydroalcoholic extract of *U. tomentosa*, especially proanthocyanidin-B2, proanthocyanidin-C1, and quinovic acid are able to bind to SARS-CoV-2 Omicron spike protein via key interactions with those critical amino acids which mediates attachment of the virus to the host cell surface in stable com-

plexes. In turn, we firmly believe that these results could open new avenues for treating COVID-19 infection associated with the Omicron variant. However, further studies are needed aiming to validate, support, and extend computational findings, as well as determine the potential benefits of hydroalcoholic extract of *U. tomentosa* against the SARS-CoV-2 Omicron variant.

3.5. Molecular Similarity. In this research, a molecular similarity study has been preceded for fifteen ligands that showed antiviral activities against Azithromycin targeted on RBD-SARS-CoV-2 Omicron spike protein, by using Discovery studio software. The used molecular properties listed in Table 3 [29] include the number of rotatable bonds, number of cyclic rings, number of aromatic rings, number of hydrogen bond donors (HBD), number of hydrogen bond acceptors (HBA), partition coefficient (ALog p), molecular weight (M. Wt), and molecular fractional polar surface area (MFPSA) (Figure 21) which shows that rhynchophylline, isorhynchophylline, proanthocyanidin-B4, proanthocyanidin-B2, and quinovic acid (red balls) are similar to Azithromycin (green ball).

4. Conclusions

U. tomentosa have demonstrated antiviral activity against the SARS-CoV in vitro and also in silico on potential targets such as the RBD in spike protein, the complex SARS-CoV-2/ACE-2 junction, and the 3CL^pro protein. Based on the phytochemicals constituents determined in our previous work, 15 compounds were docked against SARS-CoV-2 Omicron spike protein-binding domain (RBD) (PDB ID: 7T9K) resulting proanthocyanidin-C1 (-10.76 Kcal/mol), quinovic acid-type 2 (-9.86 kcal/mol), and proanthocyanidin-B2 (-9.82 kcal/mol) like the constituents with best binding energy on the SARS-CoV-2 omicron spike protein and proanthocyanidin-C1 which was stable at the binding pocket in the 100-ns of molecular dynamic simulations under physiological parameters. Although in vitro analysis on omicron variant is needed, proanthocyanidin-C1 might be considered

as a candidate molecule against new variants or the total extract of *U. tomentosa*, which all constituents would synergism the antiviral effect.

Data Availability

The data used to support the findings of this study are included within the supplementary information file.

Conflicts of Interest

The authors declare no conflict of interest.

Authors' Contributions

Conceptualization was contributed by O.H.-C., A.M.S., and A.F.Y.-P.; methodology was contributed by N.H.A.; software was contributed by S.A. and H.C.; validation was performed by A.M.S., A.F.Y.-P., E.L.-G., R.D.H.-Q., and J.S.A.-G.; formal analysis was performed by A.M.S. and G.E.-S.B.; investigation was performed by O.H.-C. and J.F.K.-C.; writing—original draft preparation was initiated by O.H.-C., H.C., and J.B.P.-O.; writing—review and editing was initiated by A.M.S. and T.B.; project administration was performed by S.A.; funding acquisition was performed by N.H.A. All authors have read and agreed to the published version of the manuscript.

Acknowledgments

Supplementary Materials

Figure S1: chlorogenic acid docked in RBD-SARS-CoV-2 Omicron spike protein, hydrogen bonds (green), and the pi interactions are represented in purple lines. Figure S2: pteropodine docked in RBD-SARS-CoV-2 Omicron spike protein, hydrogen bonds (green), and the pi interactions are represented in purple lines. Figure S3: (A) speciophylline docked in RBD-SARS-CoV-2 Omicron spike protein and (B) uncarine F docked in RBD-SARS-CoV-2 Omicron spike protein, hydrogen bonds (green), and the pi interactions are represented in purple lines. Figure S4: epicatechin docked in RBD-SARS-CoV-2 Omicron spike protein, hydrogen bonds (green), and the pi interactions are represented in purple lines. *(Supplementary Materials)*

References

[1] C. del Rio, S. B. Omer, and P. N. Malani, "Winter of Omicron-the evolving COVID-19 pandemic," *JAMA*, vol. 327, no. 4, pp. 319-320, 2022.

[2] S. S. A. Karim and Q. A. Karim, "Omicron SARS-CoV-2 variant: a new chapter in the COVID-19 pandemic," *The Lancet*, vol. 398, no. 10317, pp. 2126–2128, 2021.

[3] S. Poudel, A. Ishak, J. Perez-Fernandez et al., "Highly mutated SARS-CoV-2 Omicron variant sparks significant concern among global experts - what is known so far?," *Travel Medicine and Infectious Disease*, vol. 45, article 102234, 2022.

[4] S. A. Meo, A. S. Meo, F. F. Al-Jassir, and D. C. Klonoff, "Omicron SARS-CoV-2 new variant: global prevalence and biological and clinical characteristics," *European Review for Medical and Pharmacological Sciences*, vol. 25, no. 24, pp. 8012–8018, 2021.

[5] G. Iacobucci, "Covid-19: unravelling the conundrum of omicron and deaths," *BMJ*, vol. 376, article o254, 2022.

[6] D. Barh, S. Tiwari, L. G. Gomes et al., "SARS-CoV-2 variants show a gradual declining pathogenicity and pro-inflammatory cytokine spur, an increasing antigenic and anti-inflammatory cytokine induction, and rising structural protein instability," 2022, *bioRxiv*.

[7] C. Wang, P. W. Horby, F. G. Hayden, and G. F. Gao, "A novel coronavirus outbreak of global health concern," *The Lancet*, vol. 395, no. 10223, pp. 470–473, 2020.

[8] S. C. Bachar, K. Mazumder, R. Bachar, A. Aktar, and M. Al Mahtab, "A review of medicinal plants with antiviral activity available in Bangladesh and mechanistic insight into their bioactive metabolites on SARS-CoV-2, HIV and HBV," *Frontiers in Pharmacology*, vol. 12, p. 3137, 2021.

[9] M. C. M. Ribeiro, T. S. Salles, M. F. Moreira, E. Barbarino, A. F. do Valle, and M. A. P. G. Couto, "Antiviral activity of microalgae extracts against Mayaro virus," *Algal Research*, vol. 61, article 102577, 2022.

[10] W.-K. Cho and J. Y. Ma, "Antiviral activity of Epimedium koreanum Nakai water extract against influenza viruses," *Biomedicine & Pharmacotherapy*, vol. 146, article 112581, 2022.

[11] M. A. Alamri, A. Altharawi, A. B. Alabbas, M. A. Alossaimi, and S. M. Alqahtani, "Structure-based virtual screening and molecular dynamics of phytochemicals derived from Saudi medicinal plants to identify potential COVID-19 therapeutics," *Arabian Journal of Chemistry*, vol. 13, no. 9, pp. 7224–7234, 2020.

[12] M. T. ul Qamar, S. M. Alqahtani, M. A. Alamri, and L. L. Chen, "Structural basis of SARS-CoV-2 3CLpro and anti-COVID-19 drug discovery from medicinal plants," *Journal of Pharmaceutical Analysis*, vol. 10, no. 4, p. 313, 2020.

[13] A. F. Yepes-Pérez, O. Herrera-Calderon, J.-E. Sánchez-Aparicio, L. Tiessler-Sala, J. D. Maréchal, and W. Cardona-G, "Investigating potential inhibitory effect of Uncaria tomentosa (cat's claw) against the main protease 3CLpro of SARS-CoV-2 by molecular modeling," *Evidence-based Complementary and Alternative Medicine*, vol. 2020, Article ID 4932572, 14 pages, 2020.

[14] I. Abdelli, F. Hassani, S. Bekkel Brikci, and S. Ghalem, "In silico study the inhibition of angiotensin converting enzyme 2 receptor of COVID-19 by Ammoides verticillata components harvested from Western Algeria," *Journal of Biomolecular Structure & Dynamics*, vol. 39, no. 9, pp. 3263–3276, 2021.

[15] A. F. Yepes-Perez, O. Herrera-Calderón, C. A. Oliveros et al., "The hydroalcoholic extract of Uncaria tomentosa (cat's claw) inhibits the infection of severe acute respiratory syndrome coronavirus 2 (SARS-CoV-2) in vitro," *Evidence-based Complementary and Alternative Medicine*, vol. 2021, Article ID 6679761, 11 pages, 2021.

[16] M. S. Nair, Y. Huang, D. A. Fidock, M. J. Towler, and P. J. Weathers, "Artemisia annua L. hot-water extracts show potent

activity in vitro against Covid-19 variants including delta," *Journal of Ethnopharmacology*, vol. 284, article 114797, 2022.

[17] G. E. Batiha, A. Magdy Beshbishy, L. Wasef et al., "Uncaria tomentosa (Willd. ex Schult.) DC.: a review on chemical constituents and biological activities," *Applied Sciences*, vol. 10, no. 8, p. 2668, 2020.

[18] R. Aquino, V. de Feo, F. de Simone, C. Pizza, and G. Cirino, "Plant metabolites. New compounds and anti-inflammatory activity of Uncaria tomentosa," *Journal of Natural Products*, vol. 54, no. 2, pp. 453–459, 1991.

[19] G. Laus, D. Brössner, and K. Keplinger, "Alkaloids of peruvian Uncaria tomentosa," *Phytochemistry*, vol. 45, no. 4, pp. 855–860, 1997.

[20] M. Navarro, W. Zamora, S. Quesada, G. Azofeifa, D. Alvarado, and M. Monagas, "Fractioning of proanthocyanidins of Uncaria tomentosa. Composition and structure-bioactivity relationship," *Antioxidants*, vol. 6, no. 3, p. 60, 2017.

[21] S. R. I. N. Reis, L. M. M. Valente, A. L. Sampaio et al., "Immunomodulating and antiviral activities of Uncaria tomentosa on human monocytes infected with dengue virus-2," *International Immunopharmacology*, vol. 8, no. 3, pp. 468–476, 2008.

[22] T. Caon, S. Kaiser, C. Feltrin et al., "Antimutagenic and antiherpetic activities of different preparations from Uncaria tomentosa (cat 's claw)," *Food and Chemical Toxicology*, vol. 66, pp. 30–35, 2014.

[23] D. Mannar, J. W. Saville, X. Zhu et al., "SARS-CoV-2 Omicron variant: antibody evasion and cryo-EM structure of spike protein–ACE2 complex," *Science*, vol. 375, no. 6582, pp. 760–764, 2022.

[24] A. Mostafa, A. Kandeil, Y. AMM Elshaier et al., "FDA-approved drugs with potent in vitro antiviral activity against severe acute respiratory syndrome coronavirus 2," *Pharmaceuticals*, vol. 13, no. 12, p. 443, 2020.

[25] A. S. M. Al-Janabi, A. M. Saleh, and M. R. Hatshan, "Cytotoxicity, anti-microbial studies of M(II)-dithiocarbamate complexes, and molecular docking study against SARS COV2 RNA-dependent RNA polymerase," *Journal of the Chinese Chemical Society*, vol. 68, no. 6, pp. 1104–1115, 2021.

[26] *GROMACS - A PARALLEL COMPUTER FOR MOLECULAR-DYNAMICS SIMULATIONS — the University of Groningen research portal*September 2021, https://research.rug.nl/en/publications/gromacs-a-parallel-computer-for-molecular-dynamics-simulations.

[27] A. W. Schüttelkopf and D. M. Van Aalten, "PRODRG: a tool for high-throughput crystallography of protein-ligand complexes," *Acta Crystallographica. Section D, Biological Crystallography*, vol. 60, no. 8, pp. 1355–1363, 2004.

[28] A. F. Yepes-Pérez, O. Herrera-Calderon, and J. Quintero-Saumeth, "Uncaria tomentosa (cat's claw): a promising herbal medicine against SARS-CoV-2/ACE-2 junction and SARS-CoV-2 spike protein based on molecular modeling," *Journal of Biomolecular Structure and Dynamics*, vol. 40, pp. 1–17, 2022.

[29] I. H. Eissa, M. S. Alesawy, A. M. Saleh et al., "Ligand and structure-based in silico determination of the most promising SARS-CoV-2 nsp16-nsp10 $2'$-o-Methyltransferase complex inhibitors among 3009 FDA approved drugs," *Molecules*, vol. 27, no. 7, p. 2287, 2022.